Physik-Department E11
Lehrstuhl für
Laser- und Röntgenphysik

Advancements of Attosecond Photoelectron Spectroscopy – Streaking Spectroscopy in the Liquid Phase and X-Ray Pulse Characterization

Martin Sebastian Wagner, M.Sc.

Vollständiger Abdruck der von der
Fakultät für Physik der Technischen Universität München
zur Erlangung des akademischen Grades eines

Doktors der Naturwissenschaften

genehmigten Dissertation.

Vorsitzender:
Prof. Dr. Martin Zacharias

Prüfer der Dissertation:
1. Prof. Dr. Reinhard Kienberger
2. Prof. Dr. Katharina Krischer

Die Dissertation wurde am 29.05.2018 bei der
Technischen Universität München eingereicht und durch die
Fakultät für Physik am 05.09.2018 angenommen.

Zusammenfassung

Die Photoelektronen-Streaking Methode, bei der die Photoemission mit Lichtfeldern modifiziert werden kann, ist seit ihrem ersten Einsatz im Jahr 2002 zu einer elementaren Technik im Bereich der Attosekundenspektroskopie geworden. Seitdem ist sie dazu verwendet worden, die Elektronendynamik in Gasen und Molekülen, sowie in reinen und beschichteten Festkörper-Proben zu untersuchen. Um die gewünschte Auflösung von wenigen Attosekunden oder sogar unter einer Attosekunde in modernen Experimenten im Bereich der Streaking-Spektroskopie zu erreichen, müssen extrem hohe experimentelle Anforderungen erfüllt werden. Auf Basis der stetigen Weiterentwicklungen der dazu nötigen Labore und den daraus gewonnenen Erfahrungen wird eine neue und vielseitige Beamline für die Attosekundenspektroskopie an der Technischen Universität München konzipiert und aufgebaut. Das Herzstück dieser Anlage besteht aus einem Hohlfasersystem, das eine spektrale Verbreiterung von Laserpulsen mit Hilfe eines konjugierten Helium-Druckgradienten ermöglicht, sowie einem darauffolgenden Pulskompressor, der mit gechirpten Spiegeln im Hochvakuum betrieben wird. Mit diesem System können Nahinfrarotpulse mit einer Energie von circa 1 mJ und einer Dauer von 2.9 fs — also nur ungefähr einer optischen Periode entsprechend — erzeugt werden. In der darauffolgenden, sogenannten AS101 Beamline, können mit diesen Pulsen wiederum isolierte Attosekundenpulse mit hohem Photonenfluss und einer Photonenenergie zwischen 80 eV und 160 eV erzeugt werden. In dieser Arbeit werden zum einen die einzelnen Komponenten detailliert beschrieben und zum anderen die erzeugten Pulse mit Hilfe der Photoelektronen-Streaking Methode charakterisiert.

Die zentrale Weiterentwicklung im Bereich der Photoelektronen-Streaking Spektroskopie, die in dieser Arbeit behandelt wird, ist die erste Anwendung dieser Methode auf flüssige Proben. Zeitaufgelöste Streaking-Messungen an Wasser (H_2O) werden durchgeführt, um Aufschluss über die Dynamik der Photoionisation und des Elektronentransports in der flüssigen Phase zu erhalten, die sich durch eine komplexe und bewegliche Anordnung der Wassermoleküle auszeichnet. Das außergewöhnliche intermolekulare Netzwerk aus Wasserstoffbrückenbindungen ist der Grund für diese stark dynamische Struktur, die noch immer nicht komplett verstanden ist und deshalb weiterhin ein wichtiges Thema in der wissenschaftlichen Debatte bleibt. Grundlegendes Verständnis in diesem Bereich ist jedoch dringend erforderlich, um Solvatationsprozesse und chemische Reaktionen in Flüssigkeiten und wässrigen Lösungen genauer untersuchen zu können. Genau deswegen wird die Attosekundenspektroskopie zur Untersuchung flüssiger Wasserfilamente angewendet, welche mit Hilfe der „Liquid Microjet“-Technik im Hochvakuum erzeugt werden. Ein dazu geeigneter, experimenteller Aufbau ist an der ETH Zürich entwickelt worden und wird im Zuge dieser Arbeit an die neue AS101 Beamline angeschlossen. In Folge der damit durchgeführten Streaking-Messungen werden erstmalig Verzögerungen in den Photoemissionszeiten von Elektronen aus den inneren und äußeren Valenzschalen von H_2O — sowohl in der flüssigen als auch in der gasförmigen Phase — bestimmt. Diese neuartigen

Ergebnisse werden in dieser Arbeit ausführlich beschrieben und analysiert. Daraufhin wird der physikalische Ursprung dieser Verzögerungen genauer untersucht. Mit Hilfe fortschrittlicher, theoretischer Modelle zur molekularen Photoionisation kann die Elektronendynamik in der Gasphase beschrieben werden. Zur Erklärung der Streuungsdynamik in der flüssigen Phase von H_2O sind zusätzlich neu entwickelte 3D Monte Carlo Simulationen notwendig. Die Kombination dieser leistungsfähigen, theoretischen Methoden mit der experimentellen Attosekundenspektroskopie macht es somit möglich, verlässliche Werte für die mittleren freien Weglängen von Elektronen in Wasser zu extrahieren, die bisher nur mit hohen Fehlertoleranzen bestimmt werden konnten.

Zusätzlich wird im Zuge dieser Arbeit eine technisch anspruchsvolle Methode zur Charakterisierung von Röntgenpulsen an Freie-Elektronen-Lasern (FEL) mit Hilfe der Streaking-Spektroskopie präsentiert. Aufgrund des zugrundeliegenden Prozesses der selbstverstärkenden spontanen Emission (SASE) zur Erzeugung dieser Pulse, treten statistische Schwankungen im zeitlichen Intensitätsprofil auf. Die Folge ist eine variable zeitliche Substruktur für jeden einzelnen FEL-Puls. Anrege-Abfrage-Experimente mit Röntgenpulsen und optischen Laserpulsen haben sich zu einer wichtigen Messtechnik in vielen wissenschaftlichen Bereichen entwickelt. Die Anforderungen an die Zeitauflösung werden dabei immer höher. Inhärente Schwankungen zwischen der Ankunftszeit von Röntgenpulsen und den synchronisierten, optischen Laserpulsen erschweren diese Experimente jedoch und limitieren die Zeitauflösung. Die Probleme können nur mit einer simultanen Einzelschuss-Messung der zeitlichen Struktur und der relativen Ankunftszeit gelöst werden, welche auch während parallel durchgeführten Experimenten angewendet werden kann. Ein wichtiger Schritt in diese Richtung konnte durch die Anwendung einer winkelaufgelösten Streaking-Methode mit zwei Laserpulsen unterschiedlicher Wellenlänge, in Kombination mit einem speziellen 360° Elektronenspektrometer, gemacht werden. Der Streaking-Laserpuls ist dabei zirkular polarisiert. Um die gewünschte Pulscharakterisierung mit Hilfe dieser Messungen zu erreichen, verfolgt diese Arbeit als weiteres Ziel die Entwicklung eines hierfür geeigneten Algorithmus. Ferner wird gezeigt, dass die SASE-bedingte Substruktur und die Pulsdauer der Röntgenpulse, sowie die relative Ankunftszeit mit einer Auflösung von wenigen Femtosekunden bestimmt werden können. Die Kombination einer Einzelschuss-Messung, die den experimentellen Betrieb nicht beeinträchtigt, mit dem schnellen und zuverlässigen Rekonstruktionsalgorithmus bietet also die Möglichkeit, winkelaufgelöste Streaking-Spektroskopie als Mittel zur Echtzeit-Pulsvermessung an neuesten FEL-Anlagen zu verwenden, welche mit Repetitionsraten von bis einem MHz betrieben werden.

Abstract

Optical-field-controlled photoemission — or briefly photoelectron streaking — has become one of the basic tools of attosecond spectroscopy, applied to investigate electron dynamics in gases, molecules, solid-state and adlayer samples since its first demonstration in 2002. High experimental requirements have to be fulfilled to reach the desired attosecond or even sub-attosecond accuracy of advanced streaking spectroscopy experiments. Based on the knowledge gained during the steady evolution of the according experimental setups, a novel, versatile beamline for attosecond spectroscopy has been designed and built up at the Technical University of Munich. The centerpiece is a newly developed helium-supplied, conjugate-gradient hollow-core fiber pulse broadening system and a subsequent in-vacuum chirped-mirror pulse compressor. With this system, single-cycle, near-infrared pulses with an energy of roughly 1 mJ and a duration as short as 2.9 fs are generated and used to create isolated attosecond pulses with high photon flux and photon energies ranging from 80 eV to 160 eV at the so-called AS101 beamline. The detailed description of the single devices, as well as a thorough characterization of the beamline output using photoelectron streaking, is summarized in this thesis.

The main advancement of photoelectron streaking spectroscopy reported in this work has been accomplished with the first-time application of this method to liquid-phase samples. Time-resolved streaking measurements are conducted in order to shed light on the dynamics of photoionization and electron transport within the complex, non-rigid arrangement of water molecules (H_2O) in the liquid phase. This highly-dynamic structure, resulting mainly from the extraordinary intermolecular hydrogen bonding network, is still not fully understood and under great scientific discussion. However, more profound knowledge in this field is urgently required for the study of solvation processes and chemical reactions in liquid substances and aqueous solutions. Thus, attosecond photoelectron spectroscopy has been applied to a liquid water filament — created using the liquid microjet technique — in a high vacuum surrounding. A specially designed apparatus, which has been developed and is routinely operated at the ETH Zurich for this purpose, is used as an end station at the novel AS101 beamline. Photoemission delays between the inner and outer valence shell electrons of both, liquid and gaseous H_2O could be extracted from the conducted streaking measurements. These unprecedented results are comprehensively analyzed and presented in this thesis. Subsequently, the physical origin of these delays is further scrutinized with advanced molecular photoionization calculations for the gas phase and additional, state-of-the-art 3D Monte Carlo simulations for the scattering dynamics in the liquid phase. The combination of attosecond metrology with these powerful theoretical tools will therefore provide the reliable determination of electron mean free paths in liquid H_2O, which are to date only available with high uncertainties.

Additionally, a more technically challenging application of the streaking technique for the characterization of X-ray pulses at free-electron lasers (FEL) is demonstrated in this work.

The self-amplified spontaneous emission (SASE) generation process imprints a statistically varying temporal pulse shape with differing substructures onto every single FEL shot. X-ray/optical pump–probe experiments have evolved to be an important tool for many scientific fields, and the demands on the time resolution are ever increasing. However, an inherent arrival time jitter between the X-ray and the synchronized optical pulse additionally complicates and limits this time resolution. These issues can only be overcome with a simultaneous, single-shot measurement of both, the temporal pulse shape and the relative arrival time in parallel to ongoing experiments. An advancement towards this goal is accomplished by the method of two-color angular streaking using a circularly polarized streaking laser and a special 360° spectrometer array. For the desired pulse characterization, the development of a suitable algorithm has been pursued within the scope of this thesis. It is demonstrated, that the SASE substructure, the pulse duration, as well as the arrival time can be retrieved with a few-femtosecond resolution. The single-shot, non-invasive measurement scheme in combination with the fast, reliable pulse reconstruction algorithm implies that angular streaking spectroscopy provides the capabilities to be used as a real-time diagnostics tool at modern X-ray FEL facilities with high repetition rates up to the MHz regime.

List of Publications

In order of relevance to this work:

R. Heider, **M. S. Wagner**, N. Hartmann, M. Ilchen, J. Buck, G. Hartmann, V. Shirvanyan, A. O. Lindahl, J. Grünert, J. Krzywinski, J. Liu, M. Ossiander, A. A. Lutman, T. Maxwell, A. A. Miahnahri, S. P. Moeller, M. Planas, J. Robinson, J. Viefhaus, T. Feurer, R. Kienberger, R. N. Coffee, W. Helml. "Online, single-shot characterization of few-femtosecond X-ray temporal pulse substructures at free-electron lasers via angular streaking". *submitted to Nat. Commun.* (2018).

N. Hartmann, G. Hartmann, R. Heider, **M. S. Wagner**, M. Ilchen, J. Buck, A. O. Lindahl, C. Benko, J. Grünert, J. Krzywinski, J. Liu, A. A. Lutman, A. Marinelli, T. Maxwell, A. A. Miahnahri, S. P. Moeller, M. Planas, J. Robinson, A. K. Kazansky, N. M. Kabachnik, J. Viefhaus, T. Feurer, R. Kienberger, R. N. Coffee, W. Helml. "Attosecond time–energy structure of X-ray free-electron laser pulses". *Nat. Photonics* **12**, 215–220 (2018).

M. Ossiander, J. Riemensberger, S. Neppl, M. Mittermair, M. Schäffer, A. Duensing, **M. S. Wagner**, R. Heider, M. Wurzer, M. Gerl, M. Schnitzenbaumer, J. V. Barth, F. Libisch, C. Lemell , J. Burgdörfer , P. Feulner, R. Kienberger. "Absolute Timing of the Photoelectric Effect". *Nature* **561**, 374–377 (2018).

K. Hütten, M. Mittermair, S. O. Stock, R. Beerwerth, V. Shirvanyan, J. Riemensberger, A. Duensing, R. Heider, **M. S. Wagner**, A. Guggenmos, S. Fritzsche, N. M. Kabachnik, R. Kienberger, B. Bernhardt. "Ultrafast quantum control of ionization dynamics in krypton". *Nat. Commun.* **9**, 719 (2018).

M. S. Wagner, E. D. Ilieva, P. St. Petkov, R. D. Nikolova, R. Kienberger, H. Iglev. "Ultrafast hydrogen bond dynamics and partial electron transfer after photoexcitation of diethyl ester of 7-(diethylamino)-coumarin-3-phosphonic acid and its benzoxaphosphorin analog". *Phys. Chem. Chem. Phys.* **17**, 9919–9926 (2015).

M. Weiler, M. Althammer, F. D. Czeschka, H. Huebl, **M. S. Wagner**, M. Opel, I.-M. Imort, G. Reiss, A. Thomas, R. Gross, S. T. B. Goennenwein. "Local charge and spin currents in magnetothermal landscapes". *Phys. Rev. Lett.* **108**, 106602 (2012).

Contents

Chapter 1

Introduction

"Time is what the clock says."

Albert Einstein

This famous quote is a rather simplistic and humorous statement on the definition of time, given by Albert Einstein, a brilliant physicist dedicating his life's work to rewriting the laws of space and time in the frame of the special [1] and general relativity theory [2]. Despite giving a valid and detailed description based on his expertise, he addressed a more pragmatic approach to the nature of time with this witticism. It points out that humanity ever since seeks to measure time by means of periodically recurring phenomena defining the intervals of a clock. The oldest example is the definition of the day and the year by the rotation period of our planet around itself and around the sun. During the continuously ongoing process of innovation in natural sciences, tremendous refinements of the accuracy of time measurement could be achieved with clocks based on mechanical oscillations of springs or pendulums, natural vibration frequencies of quartz crystals and nowadays, the characteristic frequencies of radiative decays of electronic states in atoms [3, 4]. Thus, ever shorter timescales have become accessible by comparing the duration of motions to these time normals.

The oscillation periodicity of an electromagnetic wave in the visible spectral range is on the order of 2 femtoseconds ($= 2 \cdot 10^{-15}$ s). One femtosecond equals a millionth of a billionth of a second. It is thus highly desirable to observe the dynamics of suitable systems in time intervals on the order of the oscillation period of light. State-of-the-art laser technology has developed to a level, where highly-intense, ultrashort laser pulses with durations close to this single-cycle period can be generated [5–7]. These femtosecond pulses have been successfully used for time-resolved measurements revealing the ultrafast relaxation processes in molecules, solutions and solids [8–11], studying the nature of the chemical bond, as well as steering and tracing chemical reactions in the so-called field of femtochemistry [12]. For his work in this discipline, Ahmed Zewail has been awarded the Nobel prize in 2000 [13].

The next breakthrough has come up with the generation of laser pulses in the extreme ultraviolet (XUV) spectral regime being shorter than the minimum oscillation cycle of visible light [14–17]. With the first measurement of isolated attosecond (1 as = 10^{-18} s) pulses,

the field of attosecond metrology has emerged [18–20]. Eventually, the exploration of the inner-shell electron dynamics on its characteristic timescale in the attosecond regime has come within experimental reach [19]. Optical-field-controlled photoemission — henceforth briefly called photoelectron streaking [18, 20–22] — has become one of the basic tools of attosecond spectroscopy. This technique is a special pump–probe scheme, where the attosecond pump pulse ionizes a sample and a synchronized, visible pulse modulates the kinetic energy distribution of the generated photoelectrons depending on the varying, relative delay between both pulses [20, 22].

Soon, the application of the streaking technique has been extended to the solid phase unveiling the electron dynamics of the fundamental steps of photoemission in condensed matter: ionization, transport and escape of the photoelectron [23, 24]. It turned out, that the streaking technique is not only capable of characterizing the pulses involved [22, 25], but also to gain insight into the dynamics of the photoemission process. The discovery of relative photoemission delays between different electron species in isolated, gaseous atoms [26] has demonstrated that the streaking technique allows to access the dynamics of the photoionization process. Based on these findings, it has become a powerful spectroscopic tool applied to many other solid-state and adlayer samples [27–31], molecules and nanoparticles [32, 33] and atoms in the gas phase [34, 35] during the last 15 years. In 2017, the precision of optical-field-based metrology could be improved even to the sub-attosecond level [36]. Probably also Einstein would be impressed by the outstanding accuracy of this "clock", which has just recently been enhanced to determine the absolute timing [37] of the photoelectric effect he first proposed and described theoretically [38].

However, high requirements regarding the employed laser sources and the vacuum conditions have to be fulfilled to reach the precision of the described, state-of-the-art experiments at attosecond spectroscopy laboratories. As stated in the title of this thesis, the advancement of the photoelectron streaking technique is the main aim of this thesis. The first steps to achieve this goal have been to plan and establish a novel attosecond experimental facility at the Chair of Laser and X-ray Physics E11 at the Technical University of Munich (TUM). A frontend laser system of the newest generation has been procured and is extended with an advanced, home-built pulse broadening and compression system. The combination of these components constitutes the centerpiece for two newly designed attosecond experimental laboratories. The first of these setups is called the AS101 beamline and is presented within the scope of this work.

The newly established AS101 beamline soon had to prove its versatility by an extension of the attosecond streaking technique to the liquid phase, which has not yet been reported to date. The complexity of this task arises from the high experimental demands to handle high vapor pressure liquid samples in ultra-high vacuum conditions needed for photoelectron detection [39, 40]. With the advent of the liquid microjet technique in 1997 [39], photoelectron and X-ray spectroscopy of liquid samples at synchrotron sources has become

feasible [40–42] and the electronic structure of various liquids and solvated species has been revealed [39, 40, 43]. In the group of Prof. Hans Jakob Wörner at the ETH Zurich, an apparatus for photoelectron spectroscopy of liquids and gases has been assembled and successfully used for attosecond interferometry measurements in gaseous N_2O and H_2O, as well as in liquid H_2O [44–47]. Particularly, inter-species photoemission delays between the same valence band molecular orbitals in the liquid and gaseous phase of H_2O have been measured at low photon excitation energies (< 30 eV). First insights into ultrafast processes exclusively happening in the liquid could be accomplished [45]. With the streaking technique, an extension of these studies to the measurement of intra-species attosecond delays also at higher photon energies (> 80 eV) is feasible and thus the time-resolved tracing of electron transport and scattering within the liquid sample can be achieved, similar as demonstrated in solid-state samples [24]. Therefore, an advancement of attosecond streaking spectroscopy to the gaseous and especially the liquid phase of water has been realized by attaching the described special end station for liquids to the novel AS101 beamline.

Despite the comparatively simple structure of a single water molecule — consisting of only three atoms — the complex, non-rigid arrangement of these molecules in the liquid phase is still not fully understood and under great scientific discussion. The complexity arises from the extraordinary intermolecular hydrogen bonding network [45, 48]. The molecular structure of liquid water, governed by ultrafast H-bonding dynamics, has been studied extensively using X-ray or neutron diffraction techniques [40, 49, 50], Raman spectroscopy and advanced infrared time-resolved pump–probe experiments [40, 48, 51–55]. However, only fragmentary knowledge could be obtained [40], i. e. hydrogen bond lifetimes and a collective structural organization time in the picosecond regime [45, 56, 57] or the pair correlation functions of liquid water [58], which provide access to structural information by means of average atomic distances. With an extension of these efforts to an investigation of the electron dynamics in liquid water on the attosecond timescale, a more holistic picture of the complex structural changes is in reach. Ultimately, solvation processes like solvent reorganization or electron transfer, which are of utmost importance regarding chemical reactions in liquid substances, can be further examined with unprecedented precision. Therefore, a high impact on all life sciences can be expected, since all life on our blue planet is based on chemical and biological processes in aqueous solutions [59].

Besides the measurement of photoemission delays in liquid and gaseous water in the newly constructed laboratories in Munich, a third sub-project is presented that deals with the application of the streaking technique to the characterization of X-ray pulses generated by free-electron lasers (FEL). The Linac Coherent Light Source (LCLS) at the Stanford National Accelerator Center (SLAC) is a state-of-the-art X-ray FEL facility routinely delivering high-brightness, coherent, femtosecond X-ray pulses with a wide range of tunable photon energies in the soft- and hard X-ray regime up to roughly 13 keV [60, 61]. The temporal shape and thus also the pulse duration of these X-ray pulses vary inherently from shot to shot due to the self-amplified spontaneous emission (SASE) generation process [61–63].

Hence, a reliable and non-invasive method for a single-shot characterization is necessary for time-resolved studies at these facilities [64]. Especially X-ray/optical pump–probe experiments have evolved to an important method for fundamental studies in many scientific fields, like materials science [65], atomic and molecular physics [66–69], chemistry [70, 71] and biology [72, 73].

Since the timescale of the aforementioned X-ray/optical pump–probe experiments at FEL facilities already approaches the few-femtosecond regime [74, 75], the demand for profiling X-ray pulse structures with comparable or even better precision in the attosecond regime arises. The X-ray/optical synchronization is limited by an inherent arrival time jitter in the order of 50 fs or larger [76, 77] deteriorating the time resolution of pump–probe experiments additionally. Despite existing, separate techniques to determine the arrival time [78, 79], it is desirable to combine the single-shot measurement of both, the temporal pulse shape and the relative arrival time by using only one pulse diagnostics tool that can be applied in parallel to ongoing experiments. For this goal, the application of the attosecond streak camera with linearly polarized streaking fields has already revealed promising results [80–83]. However, these measurements still suffer from a non-stable overlap of the involved laser pulses due to the arrival time jitter. In order to lift these restrictions, experiments with circularly polarized streaking fields [84, 85] in combination with fully angle-resolved photoelectron detection have been conducted. Due to the novelty of this pulse characterization technique, the development of a suitable retrieval algorithm has been indispensable and pursued within the scope of this thesis.

While all these topics have been investigated in close collaboration and scientific teamwork with my colleague Rupert Heider, I was the responsible scientist for the attosecond photoemission studies in the liquid and gaseous phase of H_2O, whereas Rupert Heider was in the leading role in the FEL pulse characterization project [86]. This is reflected in the emphasis of the two respective theses. The infrastructure for the AS101 beamline has been designed and built up during the first years of our work — a leading position has not been defined. The described division of the responsibilities leads to the composition of my thesis, which is summarized in the following: In chapter 2, the theoretical background for understanding the physics of ultrashort laser pulses and attosecond metrology is introduced in detail, while the fundamentals of free-electron lasers and angular streaking are only shortly summarized. A detailed explanation of the single parts and a benchmark of the output of the novel AS101 beamline is given in chapter 3. In chapter 4, the experimental apparatus for the streaking experiments in water is introduced, the measured photoemission delays of liquid and gaseous H_2O are presented, before a comprehensive discussion of the results within the theoretical framework of electron transport in liquids is given. In chapter 5, the angular streaking measurements at the LCLS, the functionality of the retrieval algorithm and the novel results for a fast retrieval of few-fs SASE-FEL pulse shapes are summarized. Eventually, a concluding summary of the thesis is given in chapter 6, before future applications and perspectives of the applied methods are sketched in chapter 7.

Chapter 2

Theoretical Background

The development of laser sources generating ultrashort pulses has paved the way for revealing the dynamic behavior of matter on the atomic level. Table-top femtosecond sources in the visible and infrared wavelength regime deliver laser pulses with only a few optical cycles and are used for driving the highly nonlinear process of high harmonic generation (HHG). The resulting XUV radiation is the key for exploring electronic processes on the attosecond timescale. Femtosecond X-ray pulses produced by free-electron lasers extend the range of accessible photon energies with a — to date — unrivaled X-ray photon flux, e.g. for studying ultrafast dynamics of deeply-bound electrons. In the following chapter, the theoretical principles for the generation of ultrashort pulses and their interaction with matter are elaborated. The fundamentals of photoelectron streaking are given and the application of this technique as a tool for attosecond time-resolved spectroscopy and for free-electron laser pulse characterization is presented.

2.1 Attosecond Metrology

The classical treatment of the interaction of highly-intense, ultrashort laser pulses with matter is applied to deduce some important effects in the field of nonlinear optics. It is further shown, how these nonlinear phenomena are used to generate isolated attosecond XUV pulses, which are triggering the photoemission in streaking spectroscopy. First, a classical description of attosecond streaking is presented for a better understanding of the main principle. Afterwards, a more sophisticated quantum-mechanical model is introduced being capable of retrieving the most important properties of a streaking experiment: The waveforms of the involved attosecond XUV and the streaking NIR pulse, as well as the attosecond delay between the emission times of electron wave packets originating from different electronic states.

2.1.1 Ultrashort Laser Pulses

The propagation of electromagnetic waves in dielectric, non-magnetic media without free electric currents is described by the wave equation

$$-\nabla^2\vec{E} + \mu_0\frac{\partial^2\vec{D}}{\partial t^2} = 0\ , \tag{2.1}$$

which can be derived from the Maxwell equations [87]. $\vec{E}$ is the electric field and μ_0 the permeability of free space. The dielectric displacement field $\vec{D}$ is defined by

$$\vec{D} = \epsilon_0 \vec{E} + \vec{P} \,, \tag{2.2}$$

where ϵ_0 is the vacuum permittivity and $\vec{P}$ is the macroscopic polarization. Therefore, $\vec{P}$ is the response of the medium to the penetration of an electric field, which is assumed to be linear in a first approximation. In isotropic media, the relation

$$\vec{P} = \epsilon_0 \chi \vec{E} \tag{2.3}$$

defines the linear electric susceptibility χ as constant of proportionality representing the dielectric properties of the medium. One possible, general solution of the wave equation 2.1 are plane waves described by

$$\vec{E}\,(\vec{r}, t) = \frac{1}{2}\left[\vec{A} e^{-i(\vec{k}\cdot\vec{r} - \omega t)} + c.c.\right] \tag{2.4}$$

with the position vector $\vec{r}$, the complex amplitude $\vec{A}$, the wave vector $\vec{k}$ and the oscillation angular frequency ω. For ultrashort laser pulses, mainly the temporal and spectral properties at a fixed position $\vec{r}$ are of interest, which leads to the simplified wave function

$$E(t) = \mathcal{A}(t) e^{-i\omega_0 t} = |\mathcal{A}(t)| e^{i(\omega_0 t + \phi(t))} \,, \tag{2.5}$$

where ω_0 is the central angular frequency and $\mathcal{A}(t)$ is the complex envelope characterized by its magnitude $|\mathcal{A}(t)|$ and phase $\phi(t) = \arg\{\mathcal{A}(t)\}$. The optical intensity is therefore defined by

$$I(t) = |E(t)|^2 = |\mathcal{A}(t)|^2 \,. \tag{2.6}$$

The description of a laser pulse in the frequency domain is obtained by the Fourier transform of equation 2.5

$$V(\omega) = \int E(t) e^{-i\omega t} dt = |V(\omega)| e^{i\varphi(\omega)} \tag{2.7}$$

with the spectral phase $\varphi(\omega)$ and the spectral intensity $S(\omega) = |V(\omega)|^2$ analogous to the time domain expressions. In the following, the temporal and spectral widths Δt and $\Delta\omega$ of the pulse are defined by the full-width at half-maximum (FWHM) of $I(t)$ and $S(\omega)$, respectively. The Fourier transform relation between the expressions 2.5 and 2.7 leads to the time-bandwidth product (TBP)

$$\Delta t \cdot \Delta\omega = 0.44 \,, \tag{2.8}$$

which holds for pulses with a constant phase and Gaussian magnitude of $E(t)$. In this case, Δt has the minimum achievable duration for a given spectral width $\Delta\omega$ and the pulse is called transform-limited [88]. However, several phenomena in the generation and propagation of ultrashort laser pulses induce non-constant phases $\phi(t)$ or $\varphi(\omega)$ leading to a prolongation or distortion of a transform-limited pulse.

Chromatic Dispersion

The dispersion relation — i.e. the frequency-dependent refractive index of media — plays a major role in the description of ultrashort pulses, which are consisting of a large number of spectral components. Therefore, the spectral domain is used to describe the consequences of chromatic dispersion caused by pulse propagation in dispersive media. For this, the spectral phase is represented as a Taylor expansion around the central angular frequency ω_0

$$\varphi(\omega) = \varphi_0 + \varphi_1 \cdot (\omega - \omega_0) + \frac{1}{2}\varphi_2 \cdot (\omega - \omega_0)^2 + \ldots + \frac{1}{n!}\varphi_n \cdot (\omega - \omega_0)^n \,, \tag{2.9}$$

where φ_n is the n-th order derivative of the spectral phase

$$\varphi_n = \left(\frac{\mathrm{d}^n \varphi}{\mathrm{d}\omega^n}\right)\Big|_{\omega=\omega_0} \,. \tag{2.10}$$

The first term φ_0 in this expansion is independent of ω and called absolute phase or carrier-envelope phase φ_{CE} (CE-phase or CEP) [87, 89]. Note, that upon Fourier transformation, φ_{CE} is not affected and can equally be described as the phase shift between the carrier wave and the peak of the envelope of a pulse in the time domain. Whereas φ_{CE} is negligible for laser pulses consisting of many optical cycles, it can dramatically change the waveform of the electric field in the case of few-cycle laser pulses, as can be seen in figure 2.1 a). The shape of the envelope and thus also the pulse duration are nevertheless not sensitive to a change of the CE-phase. In the strong-field regime, where the interaction time of atoms and light waves is in the order of the oscillation period of the field, the electric field determines the evolution of nonlinear effects of light–matter interaction [7]. Therefore, these effects are highly sensitive to the absolute phase of an ultrashort laser pulse, which will be discussed further in section 2.1.3.

The first-order spectral phase φ_1 is the so-called group delay (GD), which is inversely proportional to the group velocity of the wave packet. In the time domain, the pulse is simply shifted by a non-zero group delay and the pulse shape is left unchanged. Higher-order terms of the spectral phase are indeed affecting the pulse shape and duration. φ_2 is often called group delay dispersion (GDD) and leads to linearly changing frequency modulation (linear chirp) throughout the pulse. A positive GDD $\varphi_2 > 0$ means that higher frequency components arrive later with respect to the lower ones, as can be seen in figure 2.1 b). Nevertheless, the Gaussian envelope is preserved for linearly chirped pulses, though the pulse duration in general increases upon propagation in dispersive media. In contrast to that, higher-order terms ($n \geq 3$) of the spectral phase lead to a distortion of a Gaussian envelope. Thus, side-pulses or plateaus near the central peak of the pulse may appear.

For time-resolved experiments with ultrashort laser pulses, where the precise knowledge and reproducibility of the waveform is important, it is crucial to minimize the propagation through dispersive media and also to compensate for unavoidable dispersive effects. The first condition states the requirement of a vacuum setup for beam propagation to

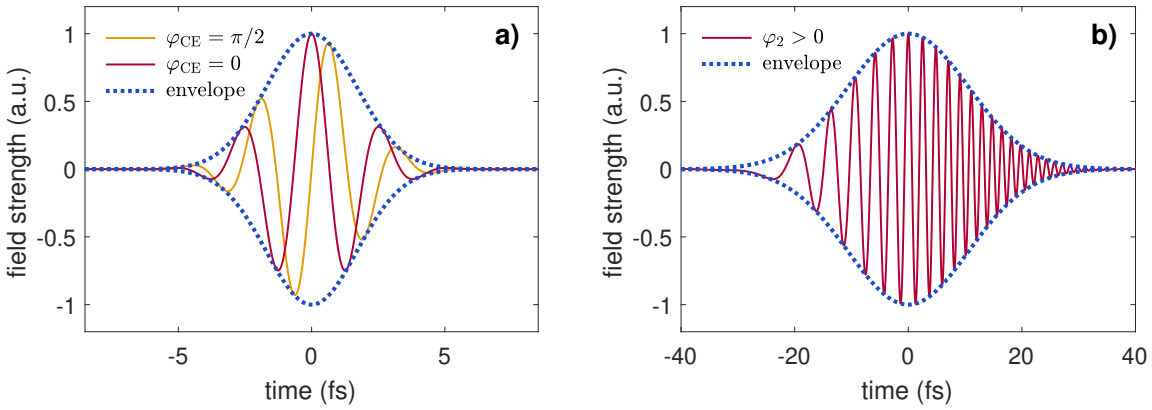

FIGURE 2.1: A few-cycle laser pulse with Gaussian envelope and FWHM duration of 4 fs at a central wavelength of λ = 800 nm is shown in panel a). The electric field is shown for a cosine waveform (φ_{CE} = 0, red) with its maximum overlapping with the maximum of the envelope and for a sine waveform (φ_{CE} = $\pi/2$, orange) with a smaller and shifted maximum of the electric field. The positive GDD ($\varphi_2 > 0$) of a 25 fs laser pulse is sketched in panel b): The lower frequency components are preceding the higher ones.

avoid the dispersion effects of air and the second condition can be fulfilled by introducing and controlling the chirp of a pulse (up to the fourth order) with gratings [90], chirped mirrors [91, 92] or acousto-optical modulation [93, 94]. Further details on these techniques are summarized in the course of this thesis and comprehensively explained in the given references.

2.1.2 Nonlinear Optics

In the previous section, it has been shown that light–matter interaction imprints phase modulations on the light wave. Considering further the extreme intensities of femtosecond laser pulses, the nonlinear response of a dielectric material to these strong electric fields has to be taken into account. For this, the macroscopic polarization, as defined in equation 2.3, can be expressed as a series expansion in the perturbative regime, where the intra-atomic binding fields are much stronger than the electric field applied:

$$\vec{P}(t) = \sum_n \vec{P}^{(n)}(t) = \epsilon_0 \left[\boldsymbol{\chi}^{(1)} \vec{E}(t) + \boldsymbol{\chi}^{(2)} \vec{E}(t)^2 + \boldsymbol{\chi}^{(3)} \vec{E}(t)^3 + \dots \right] = \tag{2.11}$$

$$= \vec{P}^{(1)}(t) + \vec{P}^{(\mathrm{NL})}(t) \, . \tag{2.12}$$

Here, $\boldsymbol{\chi}^{(n)}$ is the n^{th}-order electric susceptibility tensor, $\vec{P}^{(1)}$ is the linear part (n = 1) and $\vec{P}^{(\mathrm{NL})}$ the nonlinear part ($n \geq 2$) of the polarization, respectively. Inserting this expression for $\vec{P}$ into equation 2.1, we get the wave equation for isotropic, dispersion-free materials

$$-\nabla^2 \vec{E} + \frac{n^2}{c^2} \frac{\partial^2 \vec{E}}{\partial t^2} = -\frac{1}{\epsilon_0 c^2} \frac{\partial^2 \vec{P}^{(\mathrm{NL})}}{\partial t^2} \, , \tag{2.13}$$

where n is the refractive index and c is the speed of light. The term on the right hand side represents the time-dependent variation of the nonlinear polarization density and acts as a source of a new, driven wave with a frequency, that differs from the external electric field [87].

Nonlinear effects in dispersive media can be described analogously, but each frequency component ω_j of the laser pulse has to be treated separately in that case:

$$\vec{E}(\vec{r},t) = \sum_{j>0} \vec{E}_j(\vec{r},t) = \sum_{j>0} E_j(\vec{r}) e^{-i\omega_j t} + c.c. \tag{2.14}$$

$$\vec{P}^{(\mathrm{NL})}(\vec{r},t) = \sum_{j>0} \vec{P}_j^{(\mathrm{NL})}(\vec{r},t) = \sum_{j>0} P_j^{(\mathrm{NL})}(\vec{r}) e^{-i\omega_j t} + c.c. \,. \tag{2.15}$$

$E_j(\vec{r})$ and $P_j^{(\mathrm{NL})}(\vec{r})$ are the complex amplitudes for the corresponding frequency components. A wave equation similar to expression 2.13 — valid for each single frequency component — is obtained

$$-\nabla^2 \vec{E}_j + \frac{n(\omega_j)^2}{c^2} \frac{\partial^2 \vec{E}_j}{\partial t^2} = -\frac{1}{\epsilon_0 c^2} \frac{\partial^2 \vec{P}_j^{(\mathrm{NL})}}{\partial t^2} \,, \tag{2.16}$$

with the frequency-dependent refractive index $n(\omega_j)$ [95]. Each frequency component in the spectrum of a broad, ultrashort pulse can therefore induce a driven radiation source in the nonlinear medium with a different frequency distribution. The generated fields are in general very weak compared to the incident driving field ($\chi^{(2)}/\chi^{(1)} \approx 10^{-12}$, $\chi^{(3)}/\chi^{(1)} \approx 10^{-24}$). In summary, the nonlinear, driven oscillations of the polarization are the foundation of a variety of nonlinear optical phenomena like wave-mixing, second harmonic generation, sum and difference frequency generation, parametric amplification, multiphoton effects and the optical Kerr effect. The dominating nonlinear interactions are depending mainly on the intensity and polarization of the incident field, the symmetry of the material and its dielectric properties. The optical Kerr effect and other subsequent self-induced effects will be discussed in more detail in the following, as they play a major for the generation of few-femtosecond pulses, which in turn are necessary to produce isolated attosecond pulses.

Optical Kerr effect

In centrosymmetric media, second-order nonlinear effects are vanishing and the third-order susceptibility $\chi^{(3)}$ becomes the dominating term:

$$\vec{P}^{(\mathrm{NL})}(\omega) = 3\chi^{(3)} |E(\omega)|^2 E(\omega) \,. \tag{2.17}$$

Upon interaction of these so-called Kerr media with intense optical fields, the self-induced nonlinear processes of third-harmonic generation (THG) and the optical Kerr effect emerge. The latter describes the dependence of the refractive index on the intensity of the electric field. This effect is originating from the fast, non-resonant and the resonant electronic response of the dielectric material, as well as from molecular orientation and motion

dynamics (i.e. in liquids) [87]. The polarization component in equation 2.17 gives rise to a change in the susceptibility of

$$\Delta\chi = \frac{P^{(\mathrm{NL})}(\omega)}{E(\omega)} = 3\chi^{(3)}|E(\omega)|^2 = \frac{6\chi^{(3)}\sqrt{\mu_0}}{n\sqrt{\epsilon_0}} \cdot I \ , \tag{2.18}$$

which is equivalent to a change in the refractive index

$$\Delta n = \frac{\Delta\chi}{2n} = \frac{3\sqrt{\mu_0}}{n^2\sqrt{\epsilon_0}}\chi^{(3)} \cdot I \equiv n_2 \cdot I \ . \tag{2.19}$$

Eventually, the overall refractive index can be written in the form

$$n(I) = n + n_2 I \ . \tag{2.20}$$

The intensity-dependence is thus confined to the material constant n_2, which is called second-order nonlinear refractive index [88]. As the intensity of an ultrashort laser pulse is varying temporally and spatially, the nonlinear refraction causes important effects like self-focusing, self-phase modulation (SPM) and self-steepening that have to be considered for high intensities.

Self-focusing

The radial intensity distribution of a laser beam in the TEM_{00} transversal mode is Gaussian-shaped

$$I(r) = \frac{2P}{\pi w^2} \cdot e^{-\frac{2r^2}{w^2}} \ , \tag{2.21}$$

with P being the power and w the waist of the laser beam. According to equation 2.20, it causes a higher refractive index in the peak area than in the weaker outer parts of the beam for nonlinear media with $n_2 > 0$. Analogous to a conventional optical lens, the continuous variation of the optical path length $l_{\mathrm{opt}} = n \cdot d$ along the radial axis leads to a non-uniform phase shift of the wave and thus a change of the beam divergence [96, 97]. Whereas the thickness d of a convex lens is decreasing radially at constant n to achieve beam focusing, the optical Kerr effect induces the variation in n and the thickness of the nonlinear medium is constant. The so-called Kerr lens is self-induced by the laser pulse and its focusing length can be calculated to

$$f_{\mathrm{Kerr}} = \frac{\pi w^4}{8 n_2 P d} \ . \tag{2.22}$$

The critical power for self-focusing is defined by

$$P_{\mathrm{cr}} = \alpha \frac{{\lambda_0}^2}{4\pi n n_2} \ , \tag{2.23}$$

where λ_0 is the wavelength and α is a material-independent factor obtained by a numerical analysis ($\alpha \simeq 1.8$) [98]. For high-power pulses ($P \gg P_{\mathrm{cr}}$), the self-focusing effect can cause very high peak intensities, if the focus is in the medium. This leads to a damage of the

material and a laser beam breakup into filaments. A significant distortion of the temporal and spatial beam profile is the consequence and thus filamentation is undesirable in most cases. In a regime, where $P \simeq P_{\mathrm{cr}}$, the effects of self-focusing and diffraction are balanced and self-trapping of the beam occurs. Consequently, the beam propagates with constant diameter through the nonlinear medium [95, 97].

Self-phase modulation and self-steepening

The change of the phase velocity, caused by the time-dependent nonlinear refraction, results in a change of the temporal phase after a beam propagation length L in a nonlinear medium:

$$\phi_{\mathrm{SPM}}(t) = -n_2 I(t)\omega_0 \frac{L}{c} \,. \tag{2.24}$$

According to the Fourier theorem, the SPM-induced variation of the temporal phase also leads to a modification in the spectral domain, which can be conveniently described with the concept of the instantaneous frequency

$$\omega_{\mathrm{inst}}(t) = \omega_0 + \Delta\omega(t) = \omega_0 + \frac{d\phi(t)}{dt} \,. \tag{2.25}$$

It describes the influence of a change in temporal phase on the frequency in each time frame of a pulse and is valid, if the amplitude varies slowly compared to one optical period $T = 2\pi{\omega_0}^{-1}$ of the central angular frequency. The frequency shift

$$\Delta\omega(t) = \frac{d}{dt}\phi_{\mathrm{SPM}}(t) = -n_2\omega_0 \frac{L}{c}\frac{dI}{dt} \tag{2.26}$$

is therefore proportional to the derivative of the temporal intensity profile [95]. We can estimate the maximum frequency shift induced by a laser pulse with duration τ and amplitude I_0 to

$$\Delta\omega_{\mathrm{max}} \simeq \frac{n_2\omega_0 I_0 L}{c\tau} \,. \tag{2.27}$$

If $\Delta\omega_{\mathrm{max}}$ gets larger than the bandwidth of the incident pulse, SPM leads to the generation of new frequencies and hence symmetrical spectral broadening around the central frequency [95]. The efficiency of this process is obviously enhanced if the pulse gets shorter and for increasing interaction lengths L with nonlinear media of large nonlinear refractive indices n_2. For a Gaussian pulse shape, the situation is illustrated in figure 2.2. For positive values of n_2, the preceding part of the pulse gets shifted to lower frequencies and vice versa, which additionally (to conventional dispersion) imprints positive second-order chirp to the pulse.

Besides SPM, also self-steepening of the pulse upon propagation in a Kerr medium is occurring. It is also a consequence of the time-varying refractive index within the temporal evolution of the laser pulse. The peak of the pulse with its highest intensity propagates with a different group velocity than the lower-intensity parts, which leads to a distortion of the temporal intensity profile. Hence, for positive nonlinear refraction indices $n_2 > 0$, the

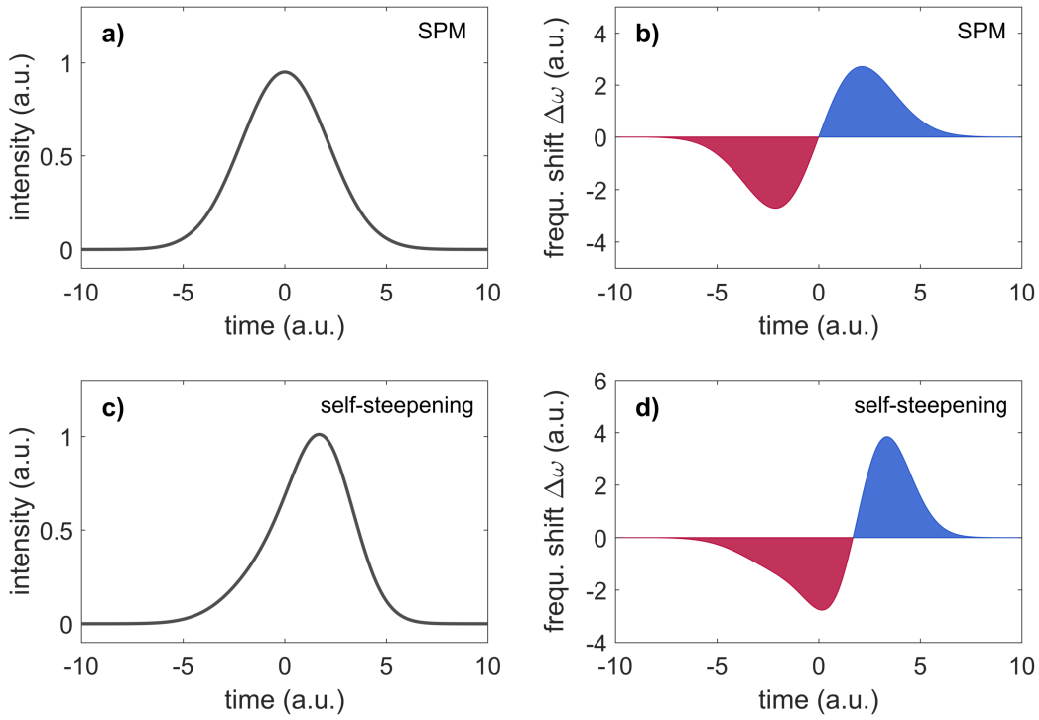

FIGURE 2.2: Influence of SPM and self-steepening on the intensity profile (panel a) and c)) and the frequency shift $\Delta\omega$ (panel b) and d)). In the case of self-steepening, the frequency-shift is enhanced to higher frequencies (indicated by blue filling) compared to the shift to lower frequencies (red filling).

peak of the pulse is retarded stronger by the self-induced refractive index and the leading and trailing edges of the pulses are able to catch up. Consequently, the trailing edge is steepened, while the slope of the preceding parts is flattened (see figure 2.2). As elaborated above, the spectral shift caused by self-phase modulation is proportional to the derivative of the temporal pulse shape $I(t)$, which is now asymmetric. Therefore, the broadening is more efficient for the trailing part of the pulse containing the high-frequency components. The obtained overall spectrum and also the central frequency ω_0 are shifted to higher frequencies accordingly. Self-steepening is dependent on the interaction length L, n_2 and the peak intensity I_0, but also on the interplay of pulse duration and the relaxation time of n_2 [99].

2.1.3 Generation of Isolated Attosecond Pulses

According to the time-bandwidth product, very broad spectra (i.e. $\Delta\lambda \geq 250$ nm at $\lambda_0 = 780$ nm [100]) are necessary to generate few-cycle femtosecond laser pulses, as already discussed before in section 2.1.1 and therefore, self-phase modulation opens up the possibility to further shorten pulses with a large pulse energy [7]. However, a proper compensation of the chirp introduced by the pulse broadening has to be ensured. In the following, the hollow-core fiber pulse compression will be introduced as a technique for maximizing SPM in a controlled way and compressing the broadened pulses to the few-cycle regime (~ 4 fs for $\lambda_0 = 650$ nm). This is already close to the limit in pulse duration, which is given by the

condition that one full oscillation period has to be completed under the envelope of a laser pulse with a central wavelength of λ_0:

$$\tau \geq \frac{\lambda_0}{c} \,. \tag{2.28}$$

The major consequence of this relation is that radiation of shorter wavelength is required to reach the attosecond timescale. We will show, that the generation of high harmonics in the extreme ultraviolet spectral regime is a powerful technique for producing isolated attosecond pulses under the right circumstances.

Hollow-core fiber pulse compressor

In the course of this thesis, a state-of-the-art chirped pulse amplification (CPA) amplifier system has been used as laser source for a newly designed attosecond spectroscopy beamline and is described thoroughly in chapter 3. These sources offer an output pulse energy of up to several millijoules (mJ), but during multiple amplification stages, the effect of gain-narrowing decreases the spectral bandwidth and the pulse duration is typically limited to approximately 20 fs [101].

Spectral broadening of pulses with energies in the nanojoule (nJ) regime with short optical glass-fibers — as demonstrated in references [102, 103] — is not scalable to the millijoule regime. There, the high peak intensities provoke material damage and higher-order nonlinearities, which prevent a proper temporal compression of the broadened pulse. The idea of using a waveguide to enhance SPM by a long propagation path in a nonlinear medium and a small beam diameter (according to relation 2.27) has nevertheless led to the invention of gas-filled hollow-core fibers (HCF) as broadening devices.

Nisoli *et al.* [104] have shown, that hollow-core fused silica fibers are efficiently guiding single modes with large mode diameters and thus are perfectly suited for large pulse energies. The usage of noble gases as nonlinear interaction media offers some major advantages compared to bulk media and glass waveguides: First, plasma generation and filamentation are suppressed, which results from the high threshold for multiphoton ionization ($I_{\mathrm{threshold}} \approx 6 \cdot 10^{13} \frac{\mathrm{W}}{\mathrm{cm}^2}$ for helium [105]). Second, the nonlinearity for moderately high gas pressures originates completely from third-order electronic response and can thus be easier compensated with prisms or chirped mirrors. Finally, by adjusting the gas pressure and switching the gas type (i.e. to argon, neon or krypton), the nonlinearity can be effectively tuned.

The guidance of light along a hollow-core fiber is based on grazing incidence reflection at the inner side of the glass capillary, which has a higher refractive index than the gas inside. This should not be mixed up with the wave propagation in glass fibers relying on total internal reflection at the core-cladding interface, where $n_{\mathrm{cladding}} < n_{\mathrm{core}}$. In hollow dielectric capillaries with diameters much larger than the wavelength, transverse circular

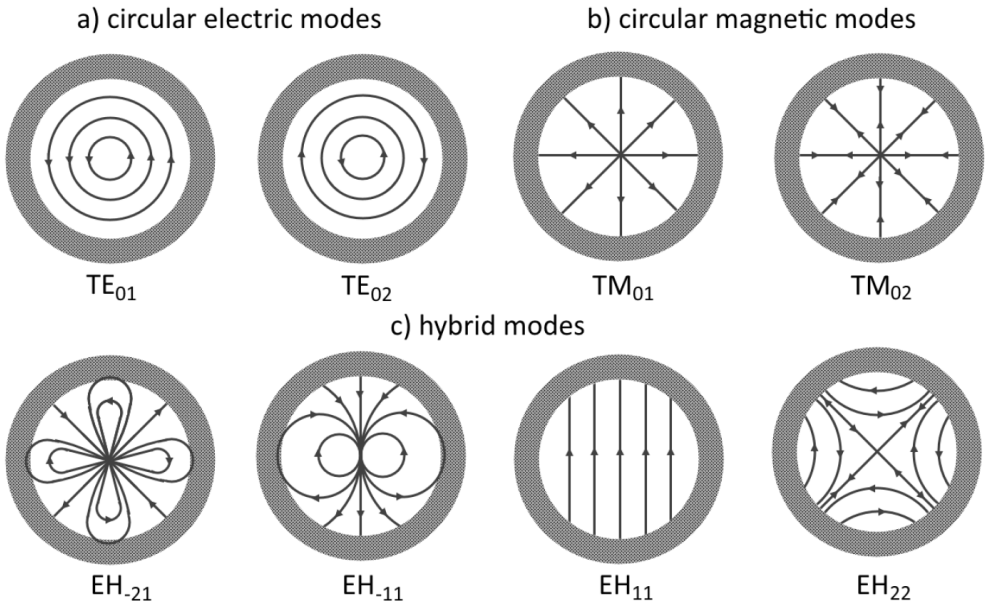

FIGURE 2.3: Most important modes for electromagnetic wave propagation in a hollow-core fiber. Adapted from references [106, 107].

electric (TE_{0m}), transverse circular magnetic (TM_{0m}) and hybrid modes EH_{pm} ($|p| \geq 1$) are supported [5, 106] (see also figure 2.3). For an increasing length of a fused silica HCF, the hybrid mode EH_{11} is more effectively transmitted and higher modes are suffering larger losses. Therefore, a long enough HCF ($L \geq 1$ m) also acts as a mode filter. A clean, radially symmetric intensity profile of the EH_{11} mode described by

$$I(r) = I_0 J_0 \left(2.405 \cdot \frac{r}{a} \right) \tag{2.29}$$

is obtained after the fiber, where I_0 is the peak intensity, J_0 is the zero-order Bessel function and a is the inner radius of the HCF [5]. According to Robinson *et al.* [108], the maximum efficiency of a Gaussian beam to couple into a hollow-core fiber is given at a beam radius w of

$$w = 0.65 \cdot a \, . \tag{2.30}$$

They also show, that the introduction of a gas gradient in a differentially pumped fiber, where a low pressure at the fiber ends is ensured, maximizes the transmission by avoiding defocusing through high ionization rates. This will be discussed further in section 3.3. Numerical calculations have been performed by Vozzi *et al.* [109] comparing unwished ionization effects with the Kerr effect. They maximize the intensity available for broadening, which can be reached for given pulse settings, and derive a minimum radius of an HCF for that case:

$$a_{\min} = A \cdot {\tau_0}^{-0.45} \cdot {E_0}^{0.51} \, . \tag{2.31}$$

Here, A is a parameter depending on the gas type ($A_{\mathrm{He}} = 2.62 \cdot 10^{-9} \mathrm{ms}^{0.45} \mathrm{J}^{-0.51}$ and $A_{\mathrm{Ne}} = 2.99 \cdot 10^{-9} \mathrm{ms}^{0.45} \mathrm{J}^{-0.51}$), τ_0 is the pulse duration and E_0 the pulse energy. According to equation 2.27, further optimization of the broadening is achieved by maximizing the

interaction length L and the nonlinearity n_2. However, the length is often restricted to laboratory conditions and also propagation losses are increasing with a longer fiber, especially when it is not aligned perfectly straight to the beam path. The maximum for n_2 can be reached by increasing the gas pressure up to a threshold given by the critical power P_{cr} for beam breakup, as defined above.

An efficient way for the dispersion compensation of the broadened, frequency-chirped pulses is achieved by a high-throughput chirped mirror array. In comparison to prisms or gratings, chirped mirrors offer a high reflectivity (> 99 % in some cases) and a broadband dispersion control also suitable for higher orders of chirp [92]. It has been shown, that this technique is capable of shortening broadened, high-energy pulses (70 µJ – 1.1 mJ) to the few-cycle regime with pulse durations below 5 fs [100, 110, 111]. From here on, these pulses are referred to as near-infrared (NIR) pulses, although its spectrum may contain ultraviolet, visible and near-infrared components.

High harmonic generation

Focused few-cycle, mJ pulses easily exceed peak intensities of $I_{\mathrm{thr}} \approx 10^{13} \frac{\mathrm{W}}{\mathrm{cm}^2}$, and the perturbative approach for the nonlinear response of dielectric materials, as described by the Taylor expansion in equation 2.11, is no longer sufficient. Above this threshold intensity, in the so-called strong-field regime, the enormous laser field strength gets close to or even surpasses the binding atomic Coulomb potential for the outer valence electrons. The probability for an electron to tunnel out of the atomic potential is growing with higher electric fields [7] and the freed electrons interact with the remaining ions and the electric field of the laser. The perturbative theory predicts an exponential decrease of the yield of higher optical harmonics up to the 11^{th} order, but first experiments with rare gases have revealed a flat intensity plateau in the spectrum for a wide range of harmonics up to the 33^{rd} order, before a so-called cutoff region with an exponentially dropping yield is reached [112–114] (see also figure 2.4 a)). Soon after the discovery, further increasing intensities of newly developed lasers have pushed the cutoff harmonics to the XUV (often also specified as soft X-ray) spectral regime with photon energies of 120 eV – 170 eV [14, 15, 115]. Further progress in high harmonic generation (HHG) has led to coherent radiation with photon energies in the water window (280 eV – 530 eV) [116] and even exceeding 1 keV [117].

The HHG process can be most intuitively understood by the semi-classical three-step model proposed first by Corkum [119]. It is illustrated in figure 2.4 b). In a first step, the atomic potential of a rare gas atom is asymmetrically distorted by the strong electric field within a laser pulse leading to a much weaker potential barrier for a valence electron. The tunneling rate increases and reaches a maximum around the local maxima of the oscillating light field. Then the freed electron first gets accelerated away from the ion by the electric field of the laser. Approximately a quarter optical cycle after the ionization event, the electric field inverts its direction and the electron begins to be decelerated until it comes to a stop and is then deflected back to the nucleus.

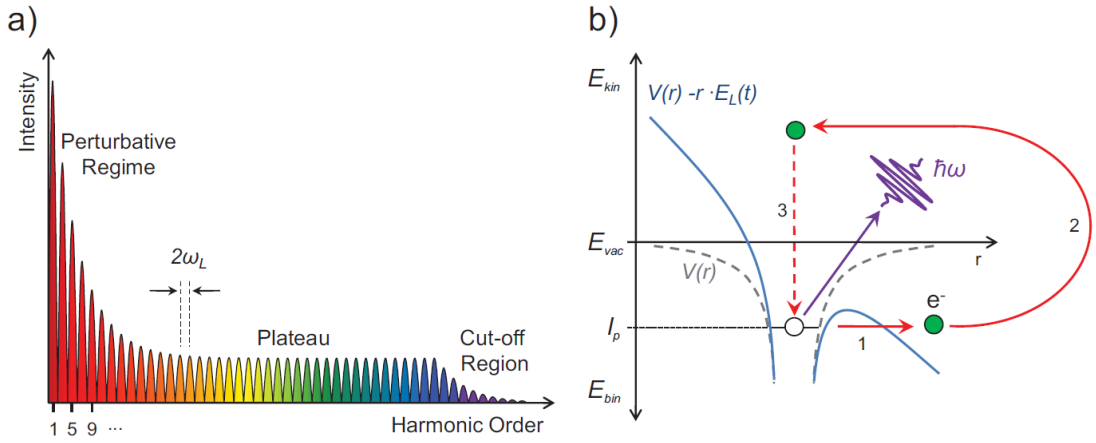

FIGURE 2.4: High harmonic generation with ultrashort laser pulses in rare gases: a) Spectrum of the harmonics with three characteristic regimes. b) Illustration of the three-step model of HHG. First, the atomic potential is deformed and a valence electron is tunneling through the potential barrier (1). The free electron is moving depending on the amplitude and direction of the laser field (2) and recombining (3) with the parent ion under emission of an XUV photon with energy $\hbar\omega$. Taken from [118].

With a small probability, the electron can recombine and an XUV photon with an energy of

$$E_{\mathrm{XUV}} = I_p + E_{\mathrm{kin}} \tag{2.32}$$

is emitted. Here, I_p is the ionization potential of the used HHG medium and E_{kin} is the accumulated energy resulting from the movement of the electron in the laser field. The cycle-averaged kinetic energy gained by an electron with mass m_e in the electric field with amplitude E_0 and angular frequency ω_0 is expressed by the ponderomotive potential [14]:

$$U_p = \frac{e^2 {E_0}^2}{4 m_e {\omega_0}^2} \,. \tag{2.33}$$

In general, the gained energy E_{kin} is strongly depending on the exact time of birth of the electron within the generating pulse. Derived from this semi-classical theory, the highest-energy photons are originating from the recollision of electrons generated by an ionization event at the phase of $\omega_0 t = 17°$ after the highest oscillation peak of the field [119]. Eventually, the maximum cutoff photon energy can be calculated by the phenomenological expression

$$E_{\mathrm{cutoff}} = I_p + 3.17 \cdot U_p \,. \tag{2.34}$$

Quantum-mechanical calculations by Lewenstein *et al.* [120] have yielded a similar result for E_{cutoff}, with an additional prefactor of 1.32 for the ionization energy in the expression above for the case where $I_p/U_p \leq 1$. For increasing ionization energies $I_p/U_p \gg 1$, this prefactor slowly decreases to 1 and we asymptotically obtain the phenomenological expression 2.34.

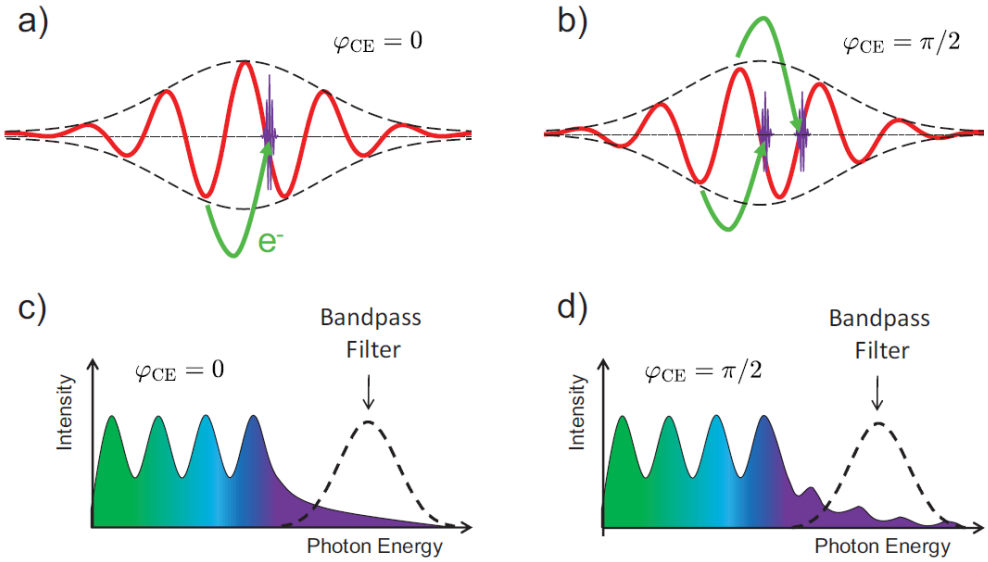

FIGURE 2.5: The influence of the CE-phase of a few-cycle laser pulse on the cutoff regime of the generated high harmonic spectra is illustrated. A cosine waveform as shown in panel a) gives rise to a flat spectrum around the cutoff energy in c), whereas clear modulations are observed in panel d) for sine waveforms (see panel b)). By spectral filtering, an isolated attosecond pulse (IAP) can be selected for $\varphi_{CE} = 0$. In the case of $\varphi_{CE} = \pi/2$, the spectral modulations in the filtered energy range lead to multiple pulses in the time domain. Adapted from [118].

For laser pulses consisting of many optical cycles T_0, the HHG process is repeated periodically in every half-cycle $T_0/2$. The observed plateau region is thus the consequence of the interference of all half-cycle events which gives rise to a similar photon energy. Due to the short wavelength of the emitted XUV radiation and the strong temporal confinement of the whole generation process to less than a half-cycle of the fundamental pulse, the bursts of high harmonics have a sub-fs duration. Hence, a train of attosecond pulses with a spacing of $T_0/2$ is obtained in the time domain, which corresponds to frequency spikes with a distance of $2\omega_0$ in the spectrum. Only odd harmonics are emitted for reasons of inversion symmetry in the gaseous medium [17, 121].

As already pointed out in section 2.1.1, the major difference of few-cycle and long laser pulses is the sensitivity of the peak electric field to the CE-phase. For few-cycle pulses, the contrast of the electric field between two half-cycles can be tuned strongly by a variation of the CE-phase between 0 and $\pi/2$ (see figure 2.1). As the energy of XUV photons is dependent on the amplitude of the field, a pronounced influence of the CE-phase on high harmonic spectra is found, when few-cycle pulses are used for driving the HHG process. For a cosine pulse ($\varphi_{CE} = 0$), the XUV photons with the highest energy are created only in the half-cycle with the maximum field amplitude (see figure 2.5 a)). Thus, only a single pulse within the attosecond train is emitted with the highest photon energy. This corresponds to a flat cutoff regime in the HHG spectrum (see figure 2.5 c)), whereas it is modulated for a sine pulse ($\varphi_{CE} = \pi/2$) as shown in figure 2.5 b) and d). This opens the

possibility to isolate attosecond pulses by a spectral bandpass filter in the cutoff regime while ensuring a stabilized CE-phase around $\varphi_{\mathrm{CE}} = 0$ [6, 16, 18, 21, 122, 123].

In general, the CEP is varying from shot to shot and thus has to be actively controlled for a reliable generation of isolated attosecond pulses (IAPs). The active CEP stabilization will be discussed in section 3.4.1. The bandpass filter can be realized by individually designed multilayer-coated mirrors. Using different, alternating material layers (i.e. Mo/Si or C/B_4C) with varying thickness, the central photon energy $E_{\mathrm{XUV}} = \hbar\omega_{\mathrm{XUV}}$ and the bandwidth ΔE_{XUV}, but also the spectral phase of the XUV attosecond pulses can be tuned over a wide range in the soft X-Ray regime [124–126].

The NIR and XUV pulses are collinearly propagating and both are inherently synchronized due to the HHG process. A spatial separation of the NIR and high harmonic beam can be accomplished by taking advantage of the decreasing divergence angle θ_n of the high harmonics with order n following the relation $\theta_n = \theta/\sqrt{n}$, where θ is the divergence angle of the NIR field [127]. A pump–probe spectroscopy scheme can be established by introducing a temporal delay between the spatially divided attosecond XUV and femtosecond NIR pulses [128]. Nevertheless, using IAPs for spectroscopy on the atomic level requires enough photon flux at a desired excitation energy. Pushing the HHG cutoff to higher energies requires either higher intensities or a smaller central frequency ω_0 of the driving laser pulses. On the other hand, higher central frequencies dramatically increase the efficiency of the HHG process [119, 120] with a proportionality of ${\omega_0}^5$ or even ${\omega_0}^6$ [129, 130]. Moreover, proper phase-matching of the XUV and the NIR pulses has to be ensured for constructive interference in the ensemble of atoms in the gas target to achieve sufficient high harmonic intensities [15].

By considering all the constraints elaborated above, the generation and use of IAPs shorter than 100 as has been accomplished in 2008 [6]. New records for the shortest pulses have been set in 2017 by Li *et al.* [131] with 53 as, and most recently Gaumnitz *et al.* [132] reported a pulse with a duration of only 43 as. The latter has been measured with the attosecond streaking technique, which will be presented in the following.

2.1.4 Photoelectron Streaking

Aiming on time-resolved spectroscopy with attosecond resolution, the knowledge of the temporal structure of the sub-fs XUV pulses is absolutely essential. For a temporal characterization on the attosecond timescale, a benchmarking quantity in the same order of magnitude is necessary, as demonstrated by the autocorrelation [88] or frequency-resolved optical gating [133] techniques in ultrafast optics, where a replica of the pulse is used to sample itself. However, this is not directly applicable to sub-fs pulses, because of missing beamsplitters or nonlinear crystals in the XUV spectral range [134]. To overcome these issues, the idea to use XUV-photoionized electrons dressed with the synchronized few-fs, NIR field for optical gating has come up [16, 18, 20, 22].

The so-called attosecond streak camera [22] shares its name and working principle with the microwave-driven streak camera, which has been applied to measure pulse shapes with sub-picosecond resolutions [135]. In this scheme, photoelectrons are generated in a photocathode following the temporal profile of the incident light pulse. On the way to a fluorescent screen, those electrons get deflected perpendicular to their movement by a time-varying electric field of known shape. In this way, the spatial distribution of the "streaked" electrons can be mapped to the instant of release and thus the temporal profile of the light pulse can be retrieved. However, the temporal resolution is not sufficient to measure sub-fs pulses, since it is limited mainly by the speed of the electronics driving the deflection field.

Therefore, the optical-field-driven attosecond streak camera uses the waveform-controlled, synchronized NIR field to deflect the XUV-ionized electrons of a suitable target. By varying the delay between both pulses, the first direct observation of the light field of a few-cycle pulse has been achieved in 2004 [136] with photoelectron streaking. It has been shown that this technique is not only able to provide the full characterization of the excitation and streaking pulses, but is furthermore capable of probing dynamic processes in atoms on the natural timescale of electronic motion by resolving characteristic shifts and distortions of photoelectron spectra [19, 23, 26].

By analogy with the HHG process, the basics of attosecond streaking can be understood fully with a classical treatment, although for revealing the full set of pulse properties a quantum-mechanical approach is necessary. Both of them are summarized in the following, mainly based on the work of Itatani *et al.* [22].

Classical Picture

An XUV pulse with energy $\hbar\omega_{\mathrm{XUV}}$ ionizes an atom and thereby a free electron with an initial momentum of $p_i = \sqrt{2m_e E_i} = \sqrt{2m_e(\hbar\omega_{\mathrm{XUV}} - I_p)}$ is ejected, if the energy of the XUV pulse is sufficient to excite a bound electron to a continuum state ($\hbar\omega_{\mathrm{XUV}} > I_p$). Treated classically as a charged particle, the electron is now exposed to the force field of the oscillating NIR laser. If $\hbar\omega_{\mathrm{XUV}} \gg I_p$, the Coulomb potential of the ion can be neglected, as the initial momentum is large enough for the electron to escape the atom quickly [128].

For a linear polarization of the NIR pulse along the z-coordinate, the equation of motion is now given by

$$m_e \ddot{z} = -eE_L(t) = -eE_0 \cos\left(\omega_0 t + \varphi_{\mathrm{CE}}\right) . \tag{2.35}$$

An integration over time — from the instant of ionization τ to a time, where both light fields are gone — is performed to calculate the momentum shift of the electron along the z-direction:

$$\Delta p_z(\tau) = m_e \dot{z} = -e \int_{\tau}^{\infty} E_L(t)\, dt = -eA_L(\tau) . \tag{2.36}$$

$A_L(\tau)$ is the vector potential of the electric field in the Coulomb gauge. Therefore, only electrons originating from an instant of excitation within the finite duration of the NIR

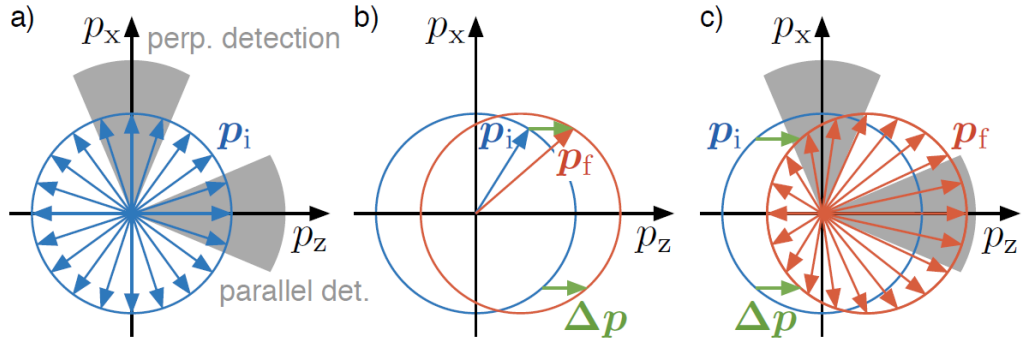

FIGURE 2.6: Angle-dependence of attosecond streaking: a) Unstreaked initial momentum distribution (blue). Parallel and perpendicular detectors (respective to the laser polarization) record similar photoelectron spectra in this case. b) The initial momentum distribution (blue) is shifted by Δp (green) along the z-direction following a non-zero vector potential component with polarization along z. The final momentum distribution is given by the red circle. c) In this case, an upshifted momentum distribution is detected for the parallel configuration. For the perpendicular detection, a down-shifted, asymmetrical broadening of the momentum distribution is recorded due to smaller projections of p_f along the x-direction. Taken from [137].

pulse will experience a net change of momentum, as the integral over the whole pulse vanishes:

$$\int_{-\infty}^{\infty} E_L(t)\, dt = 0\,. \tag{2.37}$$

The final momentum p_f of a streaked electron generally depends on the angle θ between laser polarization and detection (see figure 2.6). Assuming $U_p \ll E_i$, this results in the trigonometric relations

$$p_f{}^2 = p_i{}^2 + \Delta p_z{}^2 + 2\, p_i \Delta p_z \cos(\theta) \tag{2.38}$$

and

$$\begin{aligned} E_f(\tau) = \frac{p_f{}^2}{2m_e} &= E_i + 2\, U_p(\tau) \cos(2\theta) \sin^2(\omega_0 \tau + \varphi_{\mathrm{CE}}) \\ &+ \sqrt{8 E_i\, U_p(\tau)} \cos(\theta) \sin(\omega_0 \tau + \varphi_{\mathrm{CE}})\,. \end{aligned} \tag{2.39}$$

For a perpendicular detection at $\theta = 90°$, the third term vanishes. The final kinetic energy distribution is shifted to lower energies with a periodicity of $2\omega_0$. With a finite detection cone around $\theta = 90°$, the spectrum of the streaked electrons is found to be broadened compared to an unstreaked energy distribution [16, 18]. For a parallel detection scheme at $\theta = 0°$ and small values of U_p, the second term in equation 2.39 is negligible. The final kinetic energy is shifted periodically around E_i following the oscillation of the vector potential $A_L(\tau)$ for varying delays τ between the isolated XUV pulse and the CEP-stabilized NIR pulse [136]. In this way, the light field is sampled by adding the oscillating NIR-field induced momentum shift to the photoionized electrons.

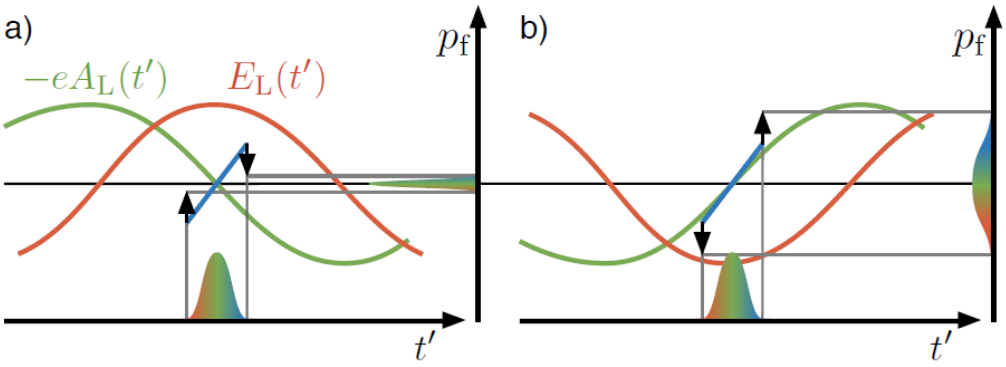

FIGURE 2.7: Influence of a positively chirped XUV pulse on streaked photoelectron spectra. The chirp-induced initial momentum distribution of the generated electrons is plotted in blue. The streaking shift is plotted with black arrows for the edges of the XUV pulse. a) The XUV pulse overlaps with a rising edge of the vector potential $A_L(t')$ ($-eA_L(t')$ is shown in green to directly visualize the proportionality to the streaking momentum shift Δp). The resulting streaked electron spectrum is compressed in this case, whereas it is stretched in panel b), where the falling edge of the vector potential overlaps with the XUV pulse. Taken from [137].

The influence of the ionizing XUV pulse with a certain duration and a possible chirp manifests in the streaked photoelectron distribution in the form of an additional time-dependent momentum component, as the initial kinetic energy of the ionized electrons is modified by the frequency sweep within the XUV pulse. For example, in parallel configuration, a linearly chirped XUV pulse with an instantaneous frequency $\omega_{\mathrm{XUV}}^{\mathrm{inst}}(t) = \omega_{\mathrm{XUV}} + \beta_{\mathrm{XUV}} \cdot t$ and a positive chirp coefficient β_{XUV} leads to a varying initial electron momentum given by

$$p_i(t') = \sqrt{2m_e(\hbar\omega_{\mathrm{XUV}}^{\mathrm{inst}}(t') - I_p)} \approx \bar{p_i} + \frac{\hbar m_e \beta_{\mathrm{XUV}}}{\bar{p_i}}\, t' \,. \tag{2.40}$$

With $\bar{p_i} = p_i(t = 0)$ and the momentum transfer given by the streaking vector potential Δp_z, the total momentum change is calculated to

$$p_f(t') = p_i(t') + \Delta p(t') = \bar{p_i} + \frac{\hbar m_e \beta_{\mathrm{XUV}}}{\bar{p_i}}\, t' - eA_L(t') \,. \tag{2.41}$$

At a zero crossing of the vector potential $A_L(t)$, it can be linearized and, depending on the sign of its slope, the additional term based on the XUV chirp can lead to compressed or stretched final momentum distributions, as visualized in figure 2.7 [137]. Following these simple considerations, not only the NIR pulse waveform, but also the properties of the XUV attosecond pulse are imprinted in an attosecond streaking spectrogram, which is composed of streaked photoelectron spectra for many XUV/NIR delay steps.

Quantum-Mechanical Picture

With the classical picture presented above, the main concepts of attosecond streaking can be understood qualitatively. A more thorough and general approach can be made by treating an electron as quantum-mechanical wave packet $|\psi(t)\rangle$ instead of as a classical particle. The time-dependent Schrödinger equation (TDSE)

$$i\frac{d}{dt}|\psi(t)\rangle = \hat{H}(t)\,|\psi(t)\rangle \tag{2.42}$$

in atomic units ($\hbar = e = m_e = 1$) is the starting point for the following derivations. The Hamiltonian in the dipole approximation is given by

$$\hat{H}(t) = \frac{1}{2}\left(\hat{p} + \vec{A}_L(t)\right)^2 + V_{\text{eff}}(\vec{r}) + \vec{E}_{\text{XUV}}(t)\cdot\vec{r}\ , \tag{2.43}$$

where $\hat{p} = -i\nabla$ is the canonical momentum operator, E_{XUV} is the XUV field and $V_{\text{eff}}(\vec{r})$ is the effective potential for a single electron moving in the vicinity of the remaining ionic atom (single active electron approximation). In the following, we assume a linear polarization of the XUV field and make even more suitable approximations to find a model for attosecond streaking that is more easily solvable than a full numerical simulation of the TDSE [138].

First, we look at the ionization process without NIR laser field ($A_L(t) = 0$). According to Quéré *et al.* [25], the release of a bound electron by an XUV pulse $E_{\text{XUV}}(t)$ is described by the transition amplitude

$$a_{\vec{p_f}} = \langle\vec{p_f}|\psi\rangle = -i\int_{-\infty}^{\infty} dt\; d_{\vec{p_f}}\vec{E}_{\text{XUV}}(t)\; e^{i({\vec{p_f}}^2/2\,+\,I_p)} \tag{2.44}$$

between the initial ground state to a final continuum state $|\vec{p_f}\rangle$. $d_{\vec{p_f}}$ is the dipole transition matrix element between the initial and final state. In the absence of resonances in the continuum and for a flat ionization cross section within the XUV bandwidth — i.e. $d_{\vec{p_f}}$ not depending strongly on $\vec{p_f}$ — the electron wave packet mimics the attosecond pulse directly in amplitude and phase. As long as the cross-section is well-known and resonant excitations are avoided, the full information of the XUV pulse can be calculated based on the photoelectron spectrum.

In the next step, we consider the interaction of the electron wave packet with the NIR streaking field with vector potential $A_L(t)$ being present during photoemission. Using the strong-field approximation (SFA) [120], the transition amplitude for a given delay τ between XUV and IR pulse is given by

$$a_{\vec{p_f}}(\tau) = -i\int_{-\infty}^{\infty} dt\; d_{\vec{p_f}+\vec{A}_L(t)}\vec{E}_{\text{XUV}}(t-\tau)\; e^{i\left(I_p t - \int_t^\infty dt'\left(\vec{p_f}+\vec{A}_L(t')\right)^2/\,2\right)}\ . \tag{2.45}$$

The influence of the NIR field is described with a field-dependent dipole matrix element $d_{\vec{p_f}+\vec{A_L}(t)}$ and an additional phase term. This gives rise to the definition of the Volkov phase

$$\Phi_V(t) = -\int_t^\infty dt' \left(\vec{p_f}\cdot\vec{A_L}(t') + \frac{1}{2}\vec{A_L}^2(t')\right) \tag{2.46}$$

and rewriting equation 2.45 to

$$a_{\vec{p_f}}(\tau) = -i\int_{-\infty}^{\infty} dt\; e^{i\Phi_V(t)}\; d_{\vec{p_f}+\vec{A_L}(t)}\vec{E}_{\mathrm{XUV}}(t-\tau)\; e^{i(\vec{p_f}^2/2\,+\,I_p)t}\;. \tag{2.47}$$

The angle-dependence of the streaked, final momentum is represented here by the dot product $\vec{p_f}\cdot\vec{A_L}$ in the Volkov phase and corresponds to equation 2.39 in the classical picture. The photoelectron spectrum $I(\vec{p}_f,\tau)$ for a given delay τ is given by the square modulus of equation 2.47:

$$I(\vec{p}_f,\tau) = \left|a_{\vec{p_f}}(\tau)\right|^2\;. \tag{2.48}$$

The master formula 2.47 is often used as a starting point for analyzing recorded streaking spectrograms $I(\vec{p}_f,\tau)$ and retrieving the pulse properties.

2.1.5 Pulse Retrieval and Delay Extraction

The comparison of two or more photoelectron lines with different energies in a streaking spectrogram might yield a characteristic phase shift in some cases. These shifts are attributed to attosecond photoemission delays $\Delta\tau$. The occurrence of a delayed photoemission has been predicted in 1955 by Wigner [139] and first been observed by Schultze *et al.* [26] with an attosecond streaking experiment on neon. Photoemission delays attributed to transport effects in solid samples have already been observed before by Cavalieri *et al.* [23] in 2007. The investigation of photoemission delays offers the possibility to gain insight into the mechanisms of electron dynamics in various samples with attosecond resolution. The measurement of a photoemission delay in liquid and gaseous water and the study of its origin are the main results of this thesis and will be discussed in detail in chapter 4.

For a statistically firm analysis, however, it is necessary to find a robust way to extract these attosecond delays from a large number of measured streaking spectrograms. Based on the quantum-mechanical approach derived before, two retrieval methods are presented briefly in this section. The first one is based on the FROG algorithm using the method of generalized projections [140] without assumptions on the involved pulses. It is referred to as least-squares generalized projection algorithm (LSGPA) in the following. The second method performs a least-squares fit of adequately predefined electron wave packets to a differentiated streaking spectrogram with a reduced number of free parameters, and is denoted as restricted TDSE fit throughout this thesis [26]. Both methods are suitable to extract the photoemission delay $\Delta\tau$ and also to completely characterize the XUV and NIR pulses, but with different accuracy and speed. Both routines and also the preprocessing of raw experimental data are implemented in an already existing software [137], which has been used for all reconstructions in this thesis.

Background Subtraction

Prior to any reconstruction routine, a proper background correction of the measured spectrograms has to be applied in order to achieve reliable results for the pulse retrievals and the photoemission delay extraction. The splitted-Shirley method [141] can be used to correct for the inelastic electron scattering background and proved to yield good results for streaking with solid samples [24]. In this thesis, it is used for preprocessing the spectrograms for the LSGPA algorithm.

A more sophisticated possibility of background subtraction is realized by differentiating a streaking spectrogram along the delay axis [26, 36, 137, 142]. With that, all constant background contributions to the spectrogram are removed. Due to the statistical nature of the scattering process, the inelastic electron scattering background is assumed to be constant for any XUV/NIR delay τ, as the streaking shift is not defined unambiguously for scattered electrons anymore. This routine is used for all photoemission delay retrievals based on the restricted TDSE algorithm, as presented in the following.

Least-squares generalized projection algorithm: LSGPA

A FROG spectrogram $S(\omega,\tau)$ is generally described with the expression

$$S(\omega,\tau) = \left| \int_{-\infty}^{\infty} E(t-\tau)G(t)e^{i\omega t}dt \right|^2 , \tag{2.49}$$

where $E(t)$ represents the pulse and $G(t)$ the gate function depending on their relative delay τ [25]. We recognize, that equation 2.47 has a similar form, and therefore a retrieval based on the FROG algorithm [133] can be applied for streaking spectrograms. This approach can be used only under the condition that the momentum dependence in the Volkov phase $\Phi_V(t)$ and in the matrix element $d_{\vec{p_f}} + \vec{A}_L(t)$ is removed. This is done by the substitution $p_f \to p_i$, of the final momentum with the initial, unstreaked momentum in these terms, and is called central momentum approximation (CMA) [140]. For further simplification, only the case of linear, parallel polarization of the NIR field and the XUV field is considered. The XUV field is given by

$$E_{\mathrm{XUV}}(t-\tau) = f(t-\tau)e^{i\omega_{\mathrm{XUV}}(t-\tau)} , \tag{2.50}$$

where $f(t-\tau)$ is the time-dependent amplitude. A suitable parametrization of both fields is described later in equations 2.53–2.55. The initial and final kinetic energies of the electrons are given by $E_i = \omega_{\mathrm{XUV}} - I_p$ and $E_f = {p_f}^2/2$. With these assumptions, we can rewrite the simplified expressions for a streaking spectrogram:

$$I(E_f,\tau) \approx \left| -i \int_{-\infty}^{\infty} dt\; e^{i\Phi_V(t)}\; d_{p_i}\; f(t-\tau)\; e^{i\left(E_f - E_i\right)t} \right|^2 \tag{2.51}$$

$$\Phi_V(t) = -\int_t^{\infty} dt' \left(p_i A_L(t') + \frac{1}{2}{A_L}^2(t') \right) . \tag{2.52}$$

In this way, the whole problem is reduced to a Fourier transformation given by equation 2.51. Applying alternating constraints between the time and frequency domain in the generalized projections algorithm, the complete XUV and NIR pulse properties can be retrieved iteratively, as described explicitly in [140]. The LSGPA algorithm is independent of intensity and phase shapes of the input pulses, and the restriction (in the classical picture) that the XUV pulse duration must be much shorter than that of the NIR pulse is lifted. In that way, any spectrogram, even with overlapping photoelectron lines can be analyzed and the photoemission delay can be calculated directly by the difference of the group delays of the individual electron wave packets. Thus, this FROG-type retrieval is a powerful tool for complete reconstruction of attosecond streaking traces, but it is time-consuming and can also lead to misinterpretation of noisy data [137].

Restricted TDSE algorithm with differential background subtraction

A straight-forward simplification of the pulse retrieval is to assume certain shapes for the electron wave packets and the streaking NIR field. As the fitting procedure is then reduced to just a few parameters, a Levenberg-Marquardt algorithm can be applied instead of the generalized projection routine used in LSGPA. Furthermore, possible ambiguities in the retrievals of noisy data are avoided, if the assumed pulse properties match the experimental conditions precisely. Following the elaborations in section 2.1.1, Gaussian pulse shapes with a linear chirp are used for parametrization of the XUV and NIR laser fields in expression 2.51. This is a good approximation for the experimental conditions in our case, as no higher-order chirps have been observed. In the time domain, we get

$$A_L(t) = \frac{1}{2} A_0 e^{-2\ln 2 \left(\frac{t-t_0}{\Delta t_L}\right)^2} e^{i\left(-\frac{1}{2}\beta_L (t-t_0)^2 - \omega_0 (t-t_0) + \varphi_{\mathrm{CE}}\right)} \tag{2.53}$$

$$f(t) = \frac{1}{2} f_0 e^{-2\ln 2 \left(\frac{t-t_0}{\Delta t_{\mathrm{XUV}}}\right)^2} e^{i\beta_{\mathrm{XUV}} (t-t_0)^2} \tag{2.54}$$

$$E_{\mathrm{XUV}}(t) = f(t) e^{i\omega_{\mathrm{XUV}} (t-t_0)} \tag{2.55}$$

Here, Δt_L and Δt_{XUV} are the FWHM durations of the respective pulses, A_0 and f_0 their amplitudes and β_L and β_{XUV} their linear chirp coefficients. t_0 is the respective group delay. Especially for $f(t)$, it is important to properly account for the fixed bandwidth $\Delta\omega_{\mathrm{XUV}}$ of the electron wave packets imprinted by the XUV pulse. A variation of β_{XUV} in the time domain leads to a different bandwidth and therefore, only a variation of the chirp in the spectral domain — referred to as b_{XUV} — is allowed. The correct conversion from the frequency to the time domain is given by the following expressions [142]:

$$\Delta t_{\mathrm{XUV}} = \sqrt{\left(b_{\mathrm{XUV}} \Delta\omega_{\mathrm{XUV}}\right)^2 + \left(\frac{4\ln 2}{\Delta\omega_{\mathrm{XUV}}}\right)^2} \tag{2.56}$$

$$\beta_{\mathrm{XUV}} = \frac{b_{\mathrm{XUV}} \Delta\omega_{\mathrm{XUV}}^4}{b_{\mathrm{XUV}}^2 \Delta\omega_{\mathrm{XUV}}^4 + (4\ln 2)^2} \,. \tag{2.57}$$

Having established the necessary expressions for the input waveforms, a first Gaussian fit of a single spectrum at one distinct delay step (out of the temporal overlap) is applied to get the initial values for the bandwidth $\Delta\omega_{\mathrm{XUV}}$ and amplitude of the electron wave packets in the frequency domain. The next step is a Center-of-Energy (COE) retrieval with Gaussian peak shapes, which performs a least-squares fit to determine the peak position for every delay step and delivers the waveform of the NIR field.

All these parameters are used as restrictions for a TDSE retrieval based on equation 2.51. As discussed above, the Levenberg-Marquardt optimization routine is performed on the derivative of the streaking spectrogram along the delay axis τ to get rid of constant background:

$$\frac{\partial}{\partial\tau} I(E_f,\tau) = \frac{\partial}{\partial\tau} \sum_l \left| -i \int_{-\infty}^{\infty} dt\; e^{i\Phi_V(t)}\; d_{p_i,l}\; f_l(t-\tau)\; e^{i(E_{f,l}-E_{i,l})t} \right|^2 . \tag{2.58}$$

Here, we write the streaking spectrogram explicitly as a sum of l electron wave packets originating from different bound states of a sample that are streaked by the same NIR field. In contrast to the LSGPA algorithm, the photoelectron lines must not interfere for a valid retrieval of the pulse properties and the photoemission delay. The latter is represented by a time-shift $\Delta\tau$ between two electron wave packets $f_l e^{i(E_{f,l}-E_{i,l})}$, that is allowed to get optimized in this routine. Stability is added by using the steady-state synchrotron spectra of the sample (if available) to fix the dipole matrix elements $d_{p_i,l}$ for each line. The application of the restricted TDSE retrieval with differential background subtraction thus allows the processing of a large number of data sets with similar constraints. This offers the possibility to accumulate large statistics in a reasonable amount of time and to obtain a reliable value of the photoemission delay $\Delta\tau$ between different electronic states of a sample.

2.2 Angular Streaking

All the elaborations above hold for a linearly polarized driving laser field in photoelectron streaking, where the angle-dependence is static and usually only one detection direction is applied [20]. The situation is different, when a circularly or elliptically polarized driving laser field is employed for translating the pulse properties to the detection angle [84]. For that, the photoemission spectra of the full 360° angle coverage within the detection plane perpendicular to the beam propagation direction have to be recorded simultaneously and evaluated appropriately. In the following, a brief theoretical description for the pulse retrieval of an angle-resolved streaking experiment is given following mainly the references [22, 86, 143].

The electric field of an elliptical laser field propagating along the z-axis is expressed by

$$\vec{E}_L(t) = \frac{E_0(t)}{\sqrt{1+\epsilon^2}} \left[\cos(\omega_L t + \varphi_{\mathrm{CE}})\; \vec{e}_x + \epsilon\; \sin(\omega_L t + \varphi_{\mathrm{CE}})\; \vec{e}_y \right] , \tag{2.59}$$

where $E_0(t)$ is the time-varying amplitude and ϵ the ellipticity of the polarization. For $\epsilon = \pm 1$, the field is circularly polarized and $\epsilon = 0$ describes the case of linear polarization along the x-axis. Similar to the deductions in section 2.1.4, the final kinetic energy of streaked photoelectrons in the case of using a circularly polarized driving field is calculated to

$$E_f(\theta) = E_i - U_p \cos\left(2(\varphi_L - \theta)\right) + \alpha_C \sqrt{4E_i\, U_p} \cos\left(\theta - \varphi_L\right) , \tag{2.60}$$

where $\varphi_L = \omega_L t + \varphi_{\mathrm{CE}}$ is the phase of the streaking field and θ is the observation angle in the plane perpendicular to the beam propagation direction. For $E_i \gg U_p$, the second term in this equation gets negligible and the prefactor of the third term α_C equals unity ($\alpha_C \approx 1$, see [22]). With the definition of the streaking kick amplitude $\sigma = \sqrt{4E_i\, U_p}$, the relation is then rewritten to

$$E_f(\theta) \approx E_i + \sigma \cdot \cos\left(\theta - \varphi_L\right) . \tag{2.61}$$

The offset phase φ_{CE} is subsumed into φ_L, as the driving laser pulses do not necessarily have to be in the few-cycle regime and be CE-phase stable for single-shot angular streaking pulse characterization measurements.

For electrons that are generated by an XUV/X-ray pulse at the instant of ionization t and streaked by the respective rotating vector potential of a circularly polarized driving pulse with wavelength λ_L, the angle-dependent final kinetic energy is thus derived to

$$E_f(\theta) \approx E_i + \sigma \cdot \cos\left(\theta - 2\pi \frac{ct}{\lambda_L}\right) . \tag{2.62}$$

The generalization of this expression for an elliptically polarized streaking field is accomplished by introducing an angle-dependent streaking kick amplitude

$$\sigma(\theta) = \bar{\sigma}(t) \sqrt{\sin(\theta - \theta_0)^2 + \epsilon^2 \cos(\theta - \theta_0)^2} , \tag{2.63}$$

where θ_0 is the angle of the major axis of the polarization ellipse in the detector frame [143]. $\bar{\sigma}(t)$ is proportional to the intensity-envelope of the streaking laser field $I_L(t)$ and time-dependent. Nevertheless, $\bar{\sigma}(t)$ can be assumed as constant for a single X-ray shot, if the average duration of the ionizing X-ray pulse is much shorter than the duration of the streaking pulse. This condition is fulfilled for FEL pulses with a FWHM duration of up to 25 fs and a streaking pulse duration of 340 fs that have been used in the experiments, as described in chapter 5 of this thesis.

Now, we consider a linearly polarized X-ray pulse used for the generation of photoelectrons originating from a spherically shaped atomic orbital (i.e. neon 1s). The angle-dependent photoelectron intensity distribution in absence of a streaking field is then given by

$$S(E, \theta) \propto \left[1 - \cos\left(2(\theta - \theta_x)\right)\right] \cdot e^{-\frac{(E - E_i)^2}{2\beta^2}} , \tag{2.64}$$

where θ_x defines the angle of the X-ray polarization with respect to the detector frame and β is the energy resolution of the respective detectors.

In the case of time-dependent angular streaking, it has to be considered that the photoelectron counts are directly proportional to the X-ray intensity profile $I_{\mathrm{X-ray}}(t)$ and that a possible chirp of the X-ray pulse influences the initial kinetic energy $E_i(t)$ depending on the instant of ionization. Merging all the findings above, the time-dependent photoelectron intensity distribution in an angular streaking experiment is given by

$$S(E,\theta,t) \;\propto\; I_{\mathrm{X-ray}}(t)\cdot\left[1-\cos\left(2(\theta-\theta_x)\right)\right]\cdot e^{-\frac{\left[E-E_i(t)-\sigma(\theta)\cos(\theta-\omega_L t)\right]^2}{2\beta^2}} \,. \tag{2.65}$$

The experimentally available spectrogram-like angular intensity distribution $S(E,\theta)$ is finally obtained by integrating the found expression along the time axis for each single shot:

$$S_{\mathrm{total}}(E,\theta) = \int dt\; S(E,\theta,t) \,. \tag{2.66}$$

Starting with these equations, a time–energy X-ray pulse reconstruction can be obtained using a complex, iterative optimization routine, that approximates the intensity distribution $S_{\mathrm{total}}(E,\theta)$ with a sum of many individually streaked photoelectron contributions [143]. In contrast to the full retrieval, an additional, speed-optimized algorithm to obtain the X-ray pulse shape has been developed in the course of this thesis. It is based on the simple integration of the signal in a well-defined area in the angle-dependent intensity distribution and will be comprehensively presented in chapter 5.

2.3 Free-electron Laser X-ray Pulses

In the following, the generation of femtosecond X-ray pulses based on the self-amplified spontaneous emission (SASE) process in high-gain free-electron lasers (FELs) is briefly described following the references [61, 63, 86, 144]. Compared to the well-defined and reproducible XUV laser pulses created within the HHG process, it will be pointed out in the following that ultrashort SASE X-ray pulses exhibit a stochastically varying pulse shape in contrast.

Undulator radiation

The operation principle of a free-electron laser is based on the generation of synchrotron radiation by electrons with relativistic energies in an undulator and the subsequent resonant interaction with the electron bunches, which leads to an enormous amplification of the generated radiation. The working principle of the undulator is schematically visualized in figure 2.8.

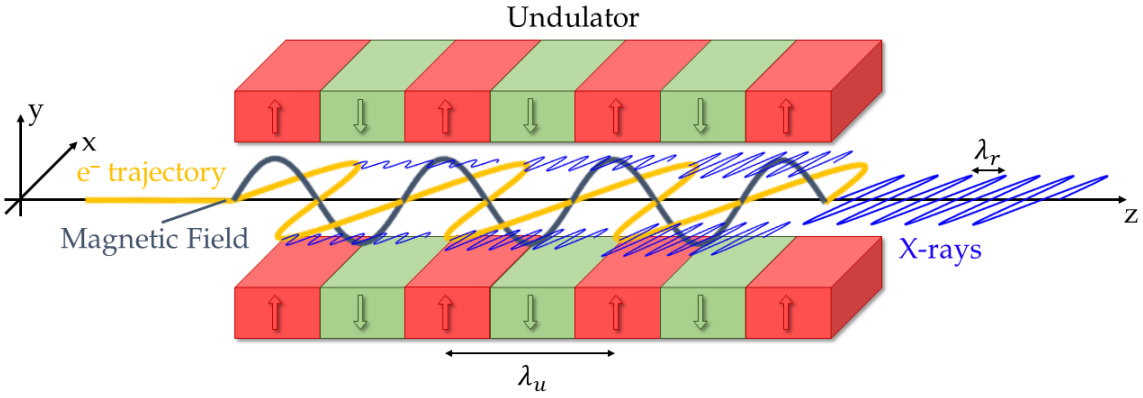

FIGURE 2.8: Alternating north and south poles form a planar undulator array with an undulator period λ_u. The magnetic field oscillates along the y-axis (black line) and due to the Lorentz force, the electron beam is forced to a sinusoidal path along the x-direction (orange line). Synchrotron radiation at the resonance wavelength λ_r is generated. With increasing propagation in the undulator, the intensity of the X-ray undulator radiation is amplified continuously. Taken from [86].

Compressed, highly energetic electron bunches — generated in a linear accelerator — propagate along the z-axis into a periodic array of alternately poled magnets that force a nearly sinusoidal movement of the electrons perpendicular to the magnetic field [61]. The undulator period λ_u, the peak magnetic field strength B_0 and the kinetic energy of the electrons $E_{\text{kin}} = \gamma m_e c^2$ define the dimensionless undulator strength parameter

$$K = \frac{eB_0\lambda_u}{2\pi m_e c} = 0.934 \cdot B_0[\text{T}] \cdot \lambda_u[\text{cm}] \tag{2.67}$$

and the resonant wavelength λ_r of the fundamental undulator radiation [144]

$$\lambda_r = \frac{\lambda_u}{2\gamma^2}\left(1 + \frac{K^2}{2}\right) . \tag{2.68}$$

With a variation of these parameters, the wavelength can thus be tuned over a wide range, as the photon emission of the free electrons is not restricted to any atomic transitions [145].

Self-amplified spontaneous emission in a high-gain FEL

For an exponential amplification of the generated undulator radiation in a so-called high-gain FEL, proper conditions for the self-amplified spontaneous emission (SASE) have to be ensured: Therefore, an interaction and thus an energy transfer from the co-propagating, but slower electron beam to the electromagnetic radiation has to occur resonantly. This requires sufficiently bright electron beams, sufficiently long undulators and an iterative adjustment of λ_r to the kinetic energy of the electrons, such that the electromagnetic radiation can overtake the electron beam by exactly one optical wavelength λ_r once per undulator period.

Furthermore, the resonant interaction leads to an energy change of the originally mono-energetic electron beam, since the radiation field induces either a gain or loss of electron

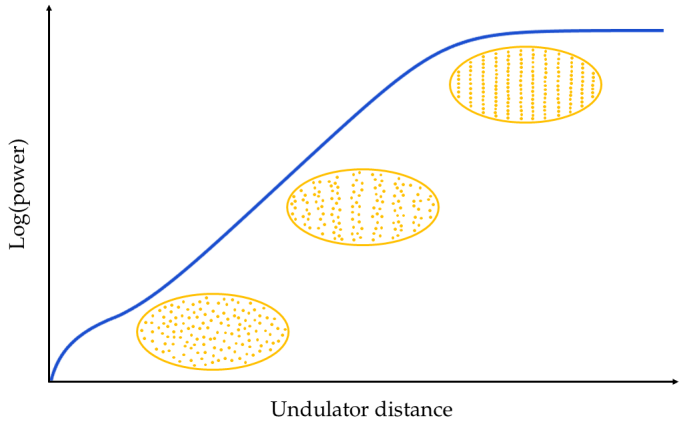

FIGURE 2.9: Exponential growth and saturation of the radiation power as a function of the undulator distance (blue). The increasing degree of microbunching of an electron bunch is illustrated in orange. Taken from [86].

kinetic energy, depending on their relative phase. In that way, electrons with larger kinetic energy can catch up to those with lower energy, which leads to the formation of electron microbunches. These can be seen as λ_r-periodic density modulations along the longitudinal direction of the electron bunch [61, 145].

The single microbunches act as coherent, high-charge radiation sources that increase the radiation field. This in turn enhances the microbunching effect and altogether, this leads to an exponential growth of the X-ray radiation power for an increasing undulator length, as shown in figure 2.9. A saturation of the radiation intensity and also the microbunching sets in at a certain undulator length, where the energy loss of the electron beam gets too large to preserve the resonance condition. No external seed signal or optical cavity is needed for the SASE process, as it starts up from shot noise. Thus, it is perfectly suited for generating highly intense, quasi-coherent X-ray pulses. In this wavelength regime, both, seed sources and reflecting optics are hard to obtain or highly inefficient and thus a laser based on an optical cavity is not feasible [144]. However, a successful operation of a high-gain FEL for generating X-ray pulses in the SASE mode requires a very precisely manufactured undulator and a highly brilliant electron beam with high peak current. This beam originates preferably from a linear accelerator, which is approximately 1000 times brighter than a storage ring source [61]. Thus, only a few of these large-scale facilities are operated worldwide.

For the characterization of the SASE pulses, first the dimensionless scaling parameter ρ for high-gain FELs is defined by

$$\rho = \left[\frac{1}{64\pi^2} \frac{I_p}{I_\mathrm{A}} \frac{K^2 [JJ]^2 \lambda_u^2}{\gamma^3 \sigma_x^2} \right]^{1/3} \tag{2.69}$$

and known as Fierce parameter [62]. Here, I_p is the electron peak current, $I_A \approx 17$ kA the Alvén current, σ_x the root-mean-square (rms) transverse size of the electron beam and $[JJ] = [J_0(\xi) - J_1(\xi)]$ the Bessel function factor with $\xi = K^2/(4 + 2K^2)$. The Fierce parameter ρ is a measure of the efficiency of an FEL concerning the electron beam power and is on the order of 10^{-3} for X-ray FELs (XFELs).

With increasing undulator length z, the power of the X-ray radiation P follows an exponentially growing behavior according to $P(z) \propto \exp\left(\frac{z}{L_G}\right)$, where

$$L_G = \frac{\lambda_u}{4\pi\sqrt{3}\rho} \tag{2.70}$$

is the power gain length [61]. It has been found, that the power is saturating after a distance of $L_{\mathrm{sat}} \approx 10\text{–}20 \cdot L_G$ [63] to a value of

$$P_{\mathrm{sat}} \approx \frac{\rho\gamma mc^2 I_p}{e} \,. \tag{2.71}$$

In saturation, the spectral rms bandwidth of a SASE pulse at central energy $\hbar\omega_r$ is limited to

$$\sigma_\omega \approx \rho\, \omega_r \,. \tag{2.72}$$

The coherence time t_{coh} is inversely proportional to the bandwidth and given by [146]

$$t_{\mathrm{coh}} = \frac{L_{\mathrm{coh}}}{c} \approx \frac{\sqrt{\pi}}{\sigma_\omega} = \frac{\lambda_r}{2c\sqrt{\pi}\rho} \,. \tag{2.73}$$

Thus, the coherence time is also limited and amounts to only a few hundred attoseconds in the hard X-ray regime. For a typical flattop SASE FEL pulse with a duration of $T \gg t_{\mathrm{coh}}$, statistically distributed energy fluctuations cause the temporal profile to be split up into a substructure consisting of an average number of $M = T/t_{\mathrm{coh}}$ coherent SASE spikes, that are approximately spaced by t_{coh}. The noisy start-up of the SASE process thus causes intensity fluctuations from shot to shot. In a nutshell, this results in a rather chaotic temporal mode of an X-Ray pulse that is different for every single shot and can only be described statistically in theory [144].

At the Linac Coherent Light Source (LCLS), the radiation of 1000 microbunches yields average, coherent SASE spikes of 0.3 fs – 3 fs duration. Few tens to hundreds of these SASE spikes, which have no fixed phase relationship to each other, form the temporal structure of a typical X-ray pulse of 10^{12} – 10^{13} photons [61]. The experimental, single-shot determination of the temporal structure of these pulses is of great interest and will be discussed in chapter 5 of this thesis.

Chapter 3

Setup of a Novel Attosecond Metrology Beamline

The experimental challenges for the measurement of physical processes on the attosecond timescale are enormous due to the requirements of few-cycle, phase-stable laser pulses, that have to be precisely and reliably guided mainly in a high-vacuum environment to avoid absorption losses or dispersive effects in air. Considering these aspects, the setup and commissioning of a completely new attosecond spectroscopy beamline at the chair of laser and X-ray physics have been realized in the course of this thesis in close collaboration with my colleagues Rupert Heider, Andreas Duensing, Michael Mittermair and Markus Wurzer. In this chapter, it is shown how the necessary infrastructure has been planned and realized within the existing construction conditions and how the so-called AS101 beamline has been built up in the specially renovated laboratories. After a description of the commercial laser amplifier system generating the fundamental ultrashort laser pulses, the in-house designed hollow-core fiber compressor, the high harmonic generation and characterization setups are presented. In a newly developed ultra-high vacuum (UHV) experimental end station containing a home-built double-mirror delay unit and time-of-flight detector, a gas-phase streaking experiment has been carried out for proof of operation and characterization of the compressed NIR and isolated attosecond XUV pulses. This chapter, as well as the results of the first attosecond spectroscopy experiments at the novel beamline presented in the next chapter, are also part of the PhD thesis of Rupert Heider [86], since both of us worked together on all these projects.

3.1 Laboratory Conditions and Beamline Roadmap

At the physics department of the Technical University of Munich, three inoperative laboratory rooms with an area of 45 m^2 each and next to each other turned out to be particularly suitable for establishing novel, state-of-the-art attosecond beamlines. For a start, these rooms had to be cleared out completely including the old, but intact laser tables and the defective air conditioning units. Several companies have been involved in planning and conducting the complex renovation process. The floor covering has been renewed, the electrical facilities have been extended and sufficient cooling water connections for the vacuum pumps and water-to-water heat exchangers have been installed. Especially the positioning of wall breakthroughs for laser beam transport, the dimensioning of the air

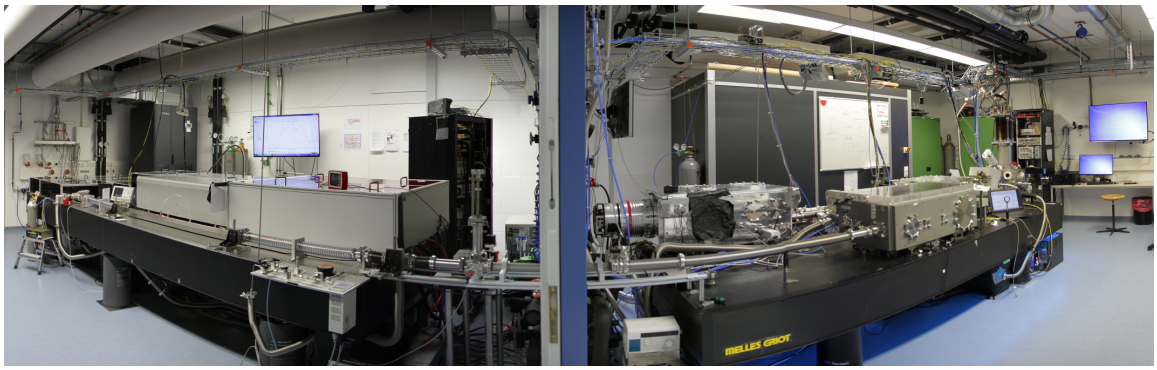

FIGURE 3.1: Panoramic view of the complete beamline (Photo taken in May 2017). In the room to the left, the frontend laser system and the pulse broadening setup (in the front) are situated. In the experimental laboratory in the right room, the vacuum chambers of the AS101 beamline are placed on a laser table and the experimental end station is located in the background, to the right of the dirt sluice.

conditioning system and the buildup of dirt sluices required thorough preparation. As all the rooms are accessible from the floor and also among each other, the idea of operating two experimental laboratories at the sides with one laser source in the middle room has been pursued. The permission of the direct entrance from the floor into the centered laser laboratory offers the major advantage of a separate and undisturbed operation of the highly sensitive laser source from the experiments, ensuring stability for long-term measurements. The high requirements on a clean, dust-free environment in the laser room are ensured by installing a dirt sluice in both experimental laboratories forcing the scientists to change shoes and wear cleanroom clothing. These measures and keeping the experimental rooms clean lead to the necessary cleanroom-like conditions in the laser laboratory. The separation of the rooms also allows a better design of the air conditioning system, as only the laser room requires a highly precise temperature stabilization to (22.0 ± 0.5) °C and a relative humidity below 40 %. The experimental rooms are only temperature-controlled to (22 ± 1) °C and don't need as much cooling power as the laser room.

After the renovation, a roadmap for the setup of the AS101 beamline has been developed, while the ordered laser amplifier system has been in the manufacturing process by the former company *Femtolaser Produktions GmbH*. The first tasks were to choose the best fitting laser tables of those in stock and arrange them adequately. After the installation of the laser system in September 2015, the priority was to complete one experimental laboratory (room 101 in the building) to perform first attosecond spectroscopy experiments as fast as possible. This goal has been achieved in August 2016, when the first streaking measurements on liquid water have been carried out successfully. This has been possible within only one year after installation, because the hollow-core fiber compressor and the XUV vacuum beamline (see figure A.4 in the appendix) have been planned, built up and tested prior to the laser installation (as far as possible) with the help of several bachelor and master students and colleagues from another attosecond laboratory of our chair.

Until June 2017, the second renovated experimental laboratory has been mainly used for steady-state and femtosecond spectroscopy. Then, the extension to the second attosecond spectroscopy experimental beamline with emphasis on solid-state samples started and still is in progress. After commissioning of this second experimental laboratory in early 2018, the sub-5 fs NIR pulses can be guided to end stations for gaseous, liquid and solid-state samples via a large vacuum beam transport system and therefore offers a great variety of feasible attosecond experiments. In the course of this thesis, the laser system and the first beamline (AS101) is described step by step, as this was the focus of my work. An overview the fully equipped laboratories is shown in figure 3.1.

3.2 Frontend Femtosecond Laser System

The commercial master oscillator power amplifier (MOPA) system consisting of a FEMTOSOURCE™ rainbow™ oscillator and a FEMTOPOWER™ HEHR CEP4 amplifier is the frontend of the novel attosecond beamlines. The most important output specifications are summarized in table 3.1.

Output power	P_0	10.0 W – 12.3 W
Pulse repetition rate	f_{rep}	4 kHz
Pulse energy	E_{pulse}	2.5 mJ – 3.1 mJ
Pulse duration	τ_0	23 fs
Central wavelength	λ_0	789 nm
Spectral width (FWHM)	$\Delta\lambda$	62 nm
Stability (pulse-to-pulse)	RMS	0.5%
CE-phase stability	$\Delta\varphi_{\mathrm{CE}}$	< 200 mrad

TABLE 3.1: Output specifications of the MOPA system.

Oscillator

Ultrashort sub-7 fs laser pulses are produced via passive Kerr-lens mode-locking [147] in a Ti:Sapphire (Ti:Sa) oscillator with a repetition rate of 75 MHz. The combination of a set of broadband dispersive mirrors and a thin titanium-doped sapphire (Al_2O_3) crystal in the resonator has proven to deliver ultra-broadband, nearly bandwidth-limited pulses with excellent stability and reproducibility [148]. A detailed description of the oscillator together with the CE-phase stabilization unit CEP4™ SEED is given in the appendix A.1.2, whereas the key parameters of both systems are summarized in the following.

A frequency-doubled, diode-pumped Nd:YVO_4 laser at λ = 532 nm — operated at an output power of 3.5 W — serves as a pump source for the oscillator. In mode-locked operation, the oscillator emits a NIR laser beam with a central wavelength of 790 nm, a spectral width of more than 300 nm and a power of ~ 300 mW. In the CEP4™ unit, the difference frequency of the NIR beam is generated and the frequency combs of the fundamental and

the difference frequency are mixed in a 0-to-f self-referencing scheme [149–151] in order to stabilize the CE-phase of the ultrashort laser pulses. The main portion of the NIR beam is focused into an acousto-optic frequency shifter (AOFS), which enables to modify the dispersion properties of a birefringent crystal with acoustic waves [152]. Following the feed-forward method [153], the detected carrier-envelope offset frequency is then subtracted from the frequency comb of the NIR beam in the AOFS. This is the so-called fast loop CE-phase stabilization, as it offers the compensation of short-term variations. The fast loop is working only in a small frequency range and therefore, further stabilization mechanisms have to be implemented. These will be discussed in section 3.4.1. Due to substantial losses in the CEP4™ unit, the remaining beam power is reduced to approximately 100 mW corresponding to a pulse energy of E_{pulse} =1.4 nJ.

Chirped Pulse Amplifier

As the output power of the oscillator is far too weak to reach the intensities necessary for high harmonic generation, the generated pulses are used as a seed for a multi-pass chirped pulse amplification (CPA) system [154, 155]. In this scheme, the input pulse is stretched temporally by introducing a large amount of positive chirp in order to avoid intensities above the damage threshold of the gain media that are used for the amplification. The recompression of the high-power pulses lifts the peak power to the terawatt regime. An overview of the two-stage amplifier system (without recompression setup) is shown in figure 3.2.

The seed beam is guided into the amplifier housing with a periscope and then through a Faraday isolator, which prevents possible back reflections to the oscillator. The beam path is stabilized using two quadrant photodiodes (QD) and two motorized mirror mounts to compensate for possible drifts in the oscillator and the CEP4 unit. Afterwards, the pulses are stretched from 7 fs to 20 ps – 30 ps resulting from the accumulated dispersion from two passages of three SF53 glass blocks (DS) and a pair of prisms (MW). By moving one of the prisms with a piezo stage, the beam path through the prisms can be changed slightly, which allows shifting and stabilizing the CE-phase without remarkably influencing the pulse duration. The beam is then guided into a nine-pass amplifier system mounted on a temperature-controlled baseplate. The gain medium (amplifier crystal AC) is a cooled Ti:Sa crystal placed in a small vacuum chamber (0.1 mbar) with beam entrance windows Brewster angle geometry. It is pumped with a frequency-doubled, Q-switched Nd:YLF laser (*Photonics Industries Inc. DM-30-527*) generating pulses with an energy of 10 mJ at a repetition rate of 4 kHz. In thermal equilibrium, the crystal is operated at a temperature of 180 K and passed by the seed beam nine times in a confocal geometry [156].

The repetition rate of 75 MHz is reduced to 4 kHz after the first four passes with an array of two crossed polarizers and a Pockels cell (PC), which is synchronized to the pump source and the oscillator in an external timing and trigger unit. Therefore, a higher population inversion is available due to less rivaling seed pulses and a higher gain can be achieved

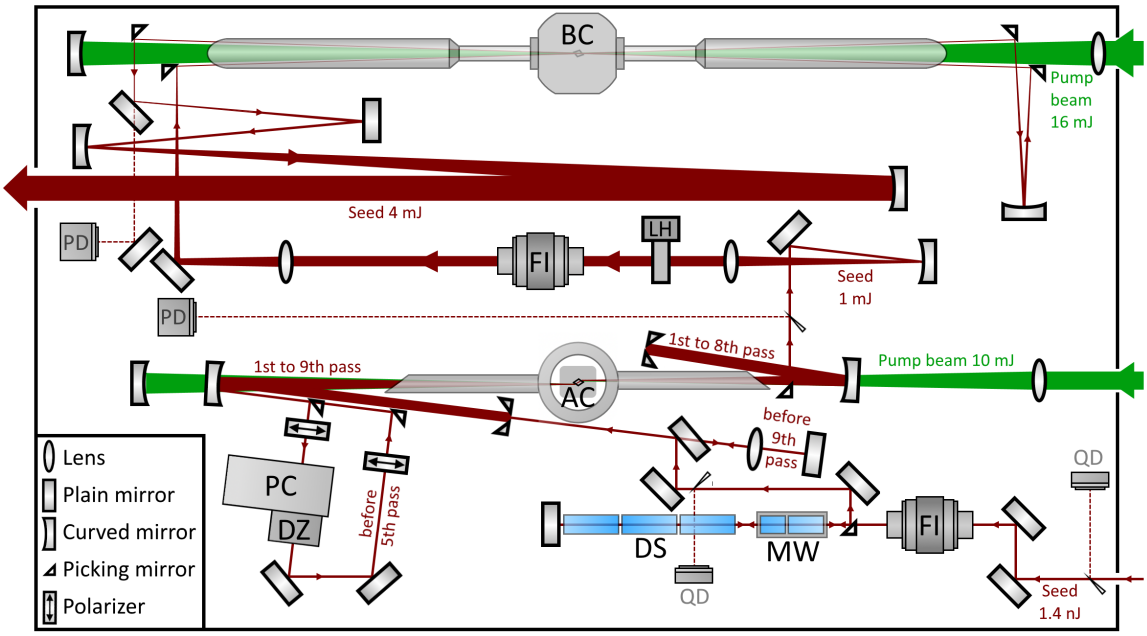

FIGURE 3.2: Beam path of the FEMTOPOWER™ HEHR CEP4 amplifier. The abbreviations and the functionality of the amplifier system are explained in the main text. Adapted from [107, 156].

for the residual pulses. In this way, the pulse energy is increased to approximately 1 mJ after another five passes through the gain medium. An acousto-optic programmable dispersive filter (*Fastlite DAZZLER*) after the Pockels cell allows to precompensate higher-order dispersion up to the fourth order and to shape the spectral amplitude for a reduction of the gain narrowing effect [93, 94].

After the pre-amplifier, the mode area of the beam is enlarged with a telescope preventing a damage of the following optics, which are a half-wave plate (LH) for power adjustment and another Faraday isolator (FI). Afterwards, the pulses undergo a further amplification in a power amplifier stage (booster), where they pass another Ti:Sa crystal (BC) twice. Due to the increased pulse energy, the focus of the NIR beam is chosen far enough away from the gain medium to avoid damages in the crystal. For this reason, it is also cryo-cooled and operated at a temperature of 110 K, when the 4 kHz pump laser (*Photonics Industries Inc. DM-60-527*) with a pulse energy of 16 mJ is focused into the crystal. After the booster, the picosecond seed pulses have an energy of 4 mJ and are now guided to a transmission grating compressor for a recompression to the femtosecond regime (see references [107, 156] for a detailed description). In order to avoid damages in these gratings and further optics in the setup, the spot size is enlarged with a mirror telescope before leaving the amplifier housing. We have to deal with nearly 25 % power loss and non-negligible higher-order dispersion in the grating compressor. Thus, the *DAZZLER* is used for precompensation of all dispersive elements in the setup in order to get transform-limited pulses at the entrance of the hollow-core fiber, where we wish to maximize the intensity for spectral broadening.

3.3 Hollow-core Fiber Compressor

For the setup of a hollow-core fiber pulse broadening system, the inner radius and the length of the wave-guiding fiber, as well as the gas type and pressure are the crucial parameters (see 2.1.3), that have to be optimized within the constraints of given laser output parameters, minimum costs for gas consumption and the limited space available in the laboratory. With the pulse parameters given in table 3.1, the minimum inner core diameter of the fiber is calculated for the different nonlinear media neon and helium using equation 2.31:

$$d_{\mathrm{He}} = 378\ \mu\mathrm{m} \quad , \quad d_{\mathrm{Ne}} = 431\ \mu\mathrm{m}\ . \tag{3.1}$$

A larger core diameter of 500 µm has been chosen to account for the deviations of the real transversal laser mode from a perfect TEM_{00}-mode (beam quality factor $\mathrm{M}^2 > 1$) and for reasons of commercial availability. If the beam is then properly focused to a beam diameter of $2w = 0.65 \cdot 500$ µm = 325 µm (see equation 2.30), plasma generation and beam breakdown for both gases are safely excluded and optimum fiber incoupling is ensured. However, the large beam diameter requires optics with a large focal length of more than two meters.

For a statically filled [5, 104], as well as for a differentially pumped HCF system [157], the inner core of the fiber has to be free of impurities and has to be evacuated before the nonlinear gas is employed. Therefore, thin vacuum entrance windows have to be used for laser transmission to the fiber entrance. Due to the large focal length, these windows have to be placed far enough away from the fiber entrance to avoid SPM and damages that may be caused by too high intensities in the focused beam. This has to be taken into account for the determination of the maximum length of the fiber, which is ultimately limited by the length of the laser table (4.8 m), where the laser system and also the fiber are fixed to. In our case, this resulted in a total fiber length of $L \cong 3$ m, split into two separate glass capillaries with a length of $l \cong 1.5$ m, a core diameter of $d = 500$ µm and an outer diameter of 2 mm.

In case of a statically filled HCF setup, the capillary is incorporated into a pipe with entrance and exit windows for the laser beam. The whole system is filled with the nonlinear gas at constant pressure and not exchanged during experiments. The highly-intense, focused laser beam experiences nonlinear propagation effects between the fiber ends and the windows, which lead to a degradation of the spatial and temporal beam profile and also to unwished plasma generation at the fiber ends.

A solution of these problems has been proposed by Nurhuda *et al.* using a differential gas pressure [158] or a conjugate-gradient pressure method [159] for spectral broadening in HCFs. In the latter, the gas is supplied in the middle of two fibers (total length L) with a pressure p_{max}, streaming through the inner core and being continuously removed at the fiber ends with an attached vacuum pump. This leads to a very low pressure p_{min} between the fiber ends and the windows reducing the aforementioned degrading effects.

The pressure within the capillary is approximated [159, 160] by equation

$$p(z) = \sqrt{p_{\min}^2 + \frac{L - 2\left|z - \frac{L}{2}\right|}{L}(p_{\max}^2 - p_{\min}^2)} \ , \qquad 0 < z < L \ . \tag{3.2}$$

With this symmetrically decreasing pressure gradient around $L/2$, the pressure at the gas inlet $p_{\max}$ in the middle of the fibers has to be higher than in the static case for achieving the same broadening effect. An integration over the pressure gradient $p(z)$ along the whole fiber setup length L reveals that the needed pressure $p_{\max}$ has to be approximately 15 % higher than in a statically filled fiber [107].

A conjugate-gradient setup supplied with helium and neon has been successfully built up and used at an attosecond beamline of the Max-Planck-Institute of Quantum Optics [157]. The setup has been adapted and improved for the operation at the novel AS101 attosecond beamline. The major novelty of the HCF compressor system presented in the following is the full implementation of the differentially pumped HCF into the subsequent high-vacuum beamline. A beam output window to guide the beam into the pulse compressor is not necessary anymore, when the chirped mirrors are also put into a high-vacuum chamber and the gas flow from the fiber can be reduced sufficiently.

3.3.1 Beam Focusing and Stabilization

For an optimum fiber incoupling, broadening and transmission, the focus of the incoming beam has to be adjusted to a diameter of approximately 325 µm in our case and its position has to be actively stabilized to avoid throughput changes or damages of the fiber entrance. These two requirements determine the beam path between the grating compressor and the fiber entrance.

Originally, a Galilean lens telescope consisting of a convex and a concave lens has been designed and built up due to the advantage of easily adjusting the focal length and beam width without altering the beam path dramatically. Despite efforts to precompensate dispersion effects in air and the lenses, it has not been possible to cope with unwished SPM effects present at high intensities. Therefore, a focusing setup with a single, concave mirror has been chosen. After testing some mirrors with a different radius of curvature R in an imaging setup, the best matching focus diameter of d = 335 µm has been found for R = 5 m. In order to avoid astigmatism, the angle between incoming and outgoing beam at the curved mirror is kept as small as possible.

For precisely tuning the focal length, the mirror can be moved along the beam propagation axis with a linear stage. This movement leads to a beam displacement and is a disadvantage of the reflective beam focusing setup. Nevertheless, this issue can be circumvented with a beam stabilization system that is able to compensate for this movement, as well as for drifts caused by other fluctuations along the beam path, which has a total length of more than

20 meters after the first beam stabilization unit. Air turbulences and thermal fluctuations are minimized by a protective housing of the beam path on the laser table and a precision air conditioning system, but remaining perturbations have to be ruled out for a stable operation of the HCF setup. This is accomplished by the advanced 4D beam stabilization system *Aligna*® manufactured by *TEM Messtechnik GmbH*, which is able to handle up to four motorized mirrors and position-sensitive detectors (PSD) that record the pointing of the main beam via reflections or mirror leakages.

For the stabilization of the beam being focused into the fiber, two motorized mirrors are used to regulate the beam position at the PSDs, one placed in the nearly collimated beam far away from the focus and one measuring the focus position. Using these beam positions and a software-implemented learning procedure, the *Aligna*® system is able to separately compensate for an angular or spatial displacement of the beam (see [161]). For this, the best motor movements are calculated and performed by using the axes of both mirrors simultaneously. The mirror mounts feature servo motors for large displacements and additional piezo actuators for a fast and even more precise stabilization of the beam pointing.

3.3.2 Vacuum Setup, Fiber Mounting and Gas Supply

As discussed above, the focused beam has to pass a 0.5 mm thick fused silica window, which is mounted in Brewster's angle to minimize reflection losses. Despite the maximum possible distance of the window to the fiber entrance ($\approx$ 1.4 m), the beam diameter is already reduced to a few millimeters at this point. The increased intensities have formed dark spots on the window after only a few days of operation leading to a dramatic decrease in the performance of the HCF system (see [107] for more details). Assuming that carbon atoms are the source of the problem, an oxygen plasma cleaning procedure has been tested successfully. Based on this finding, the idea has come up to supply a small amount of pure oxygen through a port close to the vacuum side of the entrance window. After pumping down the whole HCF system, an oxygen partial pressure of $\approx 10^{-1}$ mbar is applied using a gas flow controller. Thus, oxygen molecules for the reaction with the carbon atoms are continuously supplied and the gaseous carbon oxide reaction products can then be removed by the vacuum pump. Since this modification has been implemented, there is no need to exchange the entrance window anymore, which ensures a stable operation of the HCF setup.

The vacuum tube with the attached Brewster window is connected with a KF40 four-way cross, where also a pressure gauge and the vibration-decoupled front connection to the vacuum pump (*A 100 L ES* from *Pfeiffer Vacuum GmbH*) are located. All these components are fixed to the laser table. A T-piece with a viewport on top and a flexible vacuum hose connect these static parts to the first of two fiber support mounts that can be precisely positioned along the axes perpendicular to the beam direction with two translation stages. The support mounts carry a straight, stress-relieved steel bar with the dimensions of 3000 mm x 30 mm x 15 mm (length x height x width) at its so-called Bessel points, which

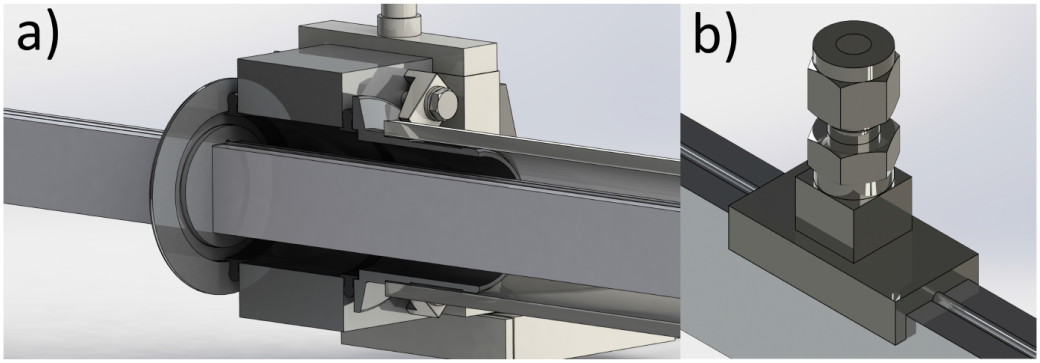

FIGURE 3.3: a) Detailed view of a hollow-core fiber support mount, where a special flange carries the steel rod with the fiber on top. b) Gas inlet part on top of the fiber with a gas connector on top. Taken from [161].

are located approximately 800 mm away from the center. In this case, the bending due to gravity is minimum according to the Euler-Bernoulli bar theory [107, 157]. A V-shaped groove is milled on top of the steel bar for placing and guiding the two hollow-core fused silica fibers, which are manufactured by *LEONI AG* with high precision and cut to a length of approximately 1.55 m each. These components serve for avoiding a curvature of the HCF system, which is crucial for optimum transmission.

The construction of the support mounts is shown in more detail in figure 3.3 a). The steel bar is supported only at the points, where it is guided through specially cut-out flanges, that are fixed to the support mounts. To preserve the vacuum conditions, the bar and the fiber in the V-groove have to be glued to these flanges. Therefore, the part of the fibers and the steel bar in between the two support mounts are freely accessible in air and the gas inlet can be placed anywhere within this range. In our case, the conjugated pressure gradient is symmetric and the fiber junction is in the middle of the bar with a gap of less than 0.5 mm between the two fibers. The gas inlet (see figure 3.3 b)) base is shaped like a slide fitting to the steel bar and its top is equipped with a 6 mm Swagelok™ gas connector. Taking care of not blocking the fiber junctions, the slide is then glued onto the steel rod and the fibers to ensure vacuum tightness. Pressure reducers, a series of pipes, valves and a pressure sensor offer the possibility to evacuate, vent or flush the setup, as well as to apply a constant pressure to the HCF system for the continuous operation. A photo of the HCF setup during operation is shown in figure 3.4.

The second support mount in the rear part of the system is again connected with a flexible vacuum hose to a T-piece with the rear port for the vacuum pump. After that, a self-designed skimmer, which is basically a closed KF40 centering ring with a small aperture for the beam ($d \approx 4$ mm), is attached. It can be adjusted for optimum beam transmission and acts as a pressure barrier for the noble gas flowing out of the fiber. Only with this simple device, the high-vacuum conditions in the following part of the attosecond beamline can be preserved. The next piece is a six-way KF40 vacuum cross equipped with a window at the side and a manipulator at the top. This enables to guide the broadened beam out

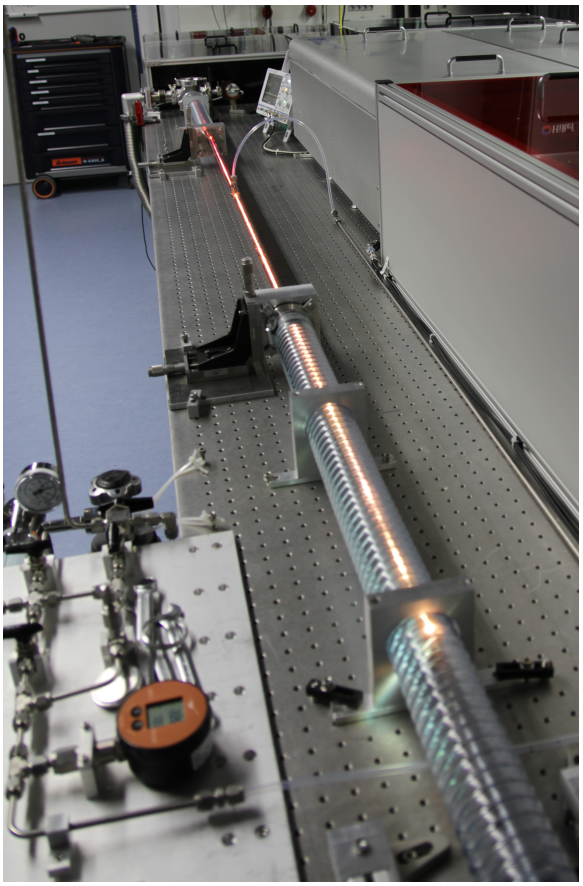

FIGURE 3.4: Differentially pumped hollow-core fiber during operation: The spectral broadening is directly visible, as the color of the strayed light turns from red at the fiber entrance in the background to a bright orange (nearly white) at the end of the second fiber. The gas supply setup shown in the bottom, left corner is connected to the gas inlet in the middle of the fiber via flexible and metallic gas pipes. Also the two support mounts for adjusting the fiber position can be seen nicely in this photo.

of the vacuum in order to optimize its spectrum, power and mode shape on a daily basis. The broadened, divergent beam is then propagating to the experimental lab, where a gate valve allows the separation of the HCF system from the rest of the high-vacuum beamline.

3.3.3 Fiber Operation and Output Characterization

The first start-up procedure and establishment of an alignment procedure of the 3-m long fiber system has been quite time consuming. First, the desired laser pointing is adjusted thoroughly without the HCF in the beam path. After that, the fibers are loosely lying on the steel bar and the strongly attenuated NIR laser is coupled in. At this point, it is crucial to assure that the incoupling, as well as the transmission between the two fiber parts in the middle are optimized regarding the beam profile and power, before the fibers are glued to the gas inlet and the flanges of the support mounts. Once fixed, the glass capillaries can hardly be removed without any damage. If the whole vacuum system is leakage-free, a pressure in the range of 10^{-3} mbar can be achieved. The noble gas is supplied and

differentially pumped, before the intensity is increased stepwise and the throughput and broadening are optimized iteratively. As the beam pointing and the focus position before the fiber is stabilized, it turned out to be most efficient to vary the gas pressure, the focal length and the fiber itself with the translation stages at its support mounts. For a fine tuning of the spectral shape, also the third-order dispersion of the input pulses is varied slightly using the *DAZZLER* in the amplifier system.

After a successful first start-up and some time to burn an optimized incoupling channel into the fiber tip by the laser with full power, the daily alignment of the HCF system is done within minutes, as long as the beam output of the amplifier system has not changed significantly. After a period of some months, it is necessary to renew the fiber entrance by cutting a few millimeters off using a ruby crystal knife. As the fibers are a few centimeters longer than the rod, this cleaving procedure can be repeated many times. For that, it has not been necessary to replace the fiber pair so far.

The output of the fiber setup has been extensively characterized within the bachelor and master theses carried out in our laboratories [107, 161, 162]. In figure 3.5, the spectral broadening is shown for the different gas types in dependence of the pressure at the gas inlet. The input power has been kept constant at P= 11 W for these measurements. The maximum broadening effect for helium is found at 2.3 bar – 2.7 bar, depending on the daily alignment and the input power, whereas the ideal pressure for neon is substantially lower at roughly 0.9 bar – 1.2 bar. In the bottom panel of figure 3.5, the broadest spectra are depicted and compared to that of the fundamental input pulse. Here, it becomes obvious that parts of the input spectrum are still contained in the blue-shifted, broadened spectra that are situated around a new central wavelength of about 650 nm. The shift to lower wavelengths is more pronounced in helium, whereas the broadening in neon is more uniform [162].

However, the broadest, nearly Gaussian-shaped spectra are found in helium at pressures around 2.35 bar. Not only the spectral broadening is optimum for these settings, but also the power transmission of 55 % – 60 % is better than in neon, where only 50 % – 55 % transmission is achieved [162]. Since helium is much cheaper than neon, the higher gas consumption is leveled out in the daily operation costs. It shall be noted, that also argon has been used for the characterization of the fiber, but plasma filamentation and beam breakdown effects occurred already at very low pressures of 0.2 bar [162]. In conclusion, helium is the cheapest and most effective broadening medium. Despite a similar power throughput in comparison to shorter, conventional fiber setups [107, 157], the spectral broadening effect, as well as the shape of the output spectrum of our differential HCF assembly is remarkably better. Using an inverse Fourier transformation, the theoretical minimum pulse duration of the optimum spectrum of helium at 2.35 bar (see figure 3.5) is calculated to 2.74 fs [162], which is only 25 % longer than one single cycle at a central wavelength of λ = 650 nm. To achieve such short pulse durations, a proper temporal compression setup of the broadened spectra — as explained in the following — is indispensable.

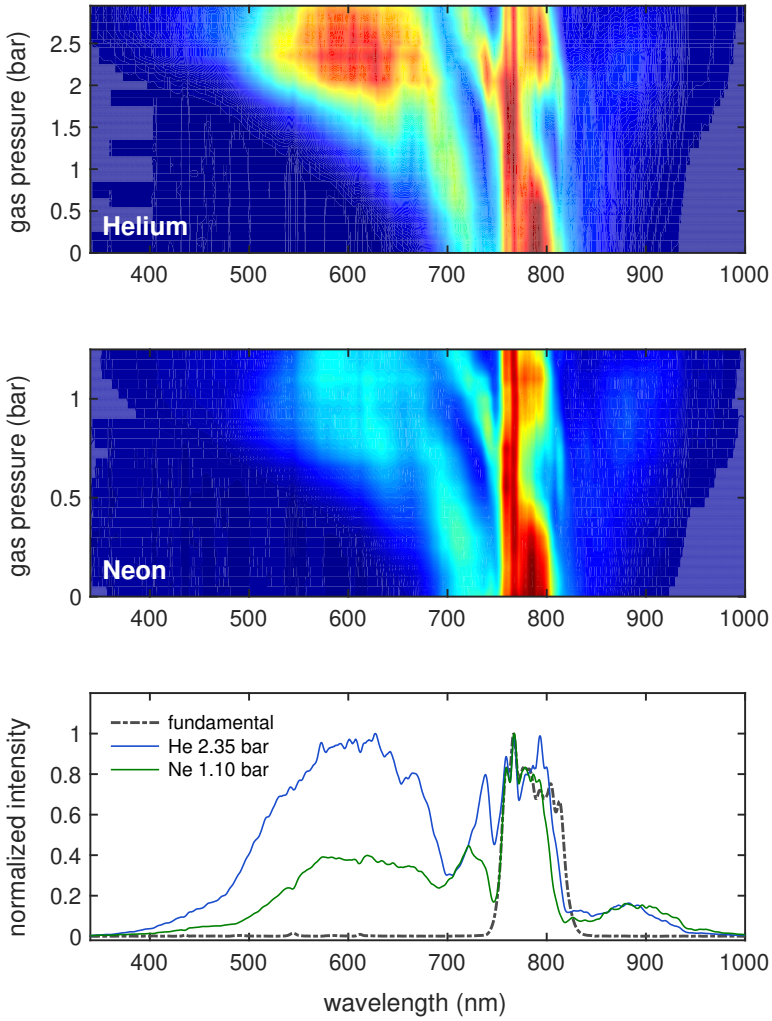

FIGURE 3.5: Output characterization of the HCF setup. The top panel shows the spectral broadening for different helium gas pressures varying from 0 bar to 2.9 bar. In the middle, the spectra of neon with pressures of up to 1.25 bar are shown for comparison. The bottom panel shows the spectrum of the fundamental input pulse (gray, dashed line) and the lineouts of the contour plots above for helium (blue) and neon (green), where maximum spectral broadening is obtained. Note, that all the spectra have been smoothed with a moving-average routine.

3.3.4 Pulse Compression Setup

Propagating through a long, flexible vacuum bellow, the generated supercontinuum enters the pulse compression high-vacuum chamber in the experimental lab, that is pumped by a *Leybold Turbovac 450 i* turbomolecular pump (TMP) with another *Pfeiffer Vacuum A 100 L ES* as backing pump. Without gas load, pressures of up to 10^{-7} mbar can be reached. Thanks to the skimmer aperture, the pressure increases to only 10^{-4} mbar during operation of the differentially pumped fiber. The compression chamber is built out of a massive, rectangular steel frame with removable side plates and a plexiglass cover that can be easily opened and closed with supporting pneumatic springs. The breadboard in the chamber is decoupled from the frame and the laser table to avoid transfer of vibrations from the TMP.

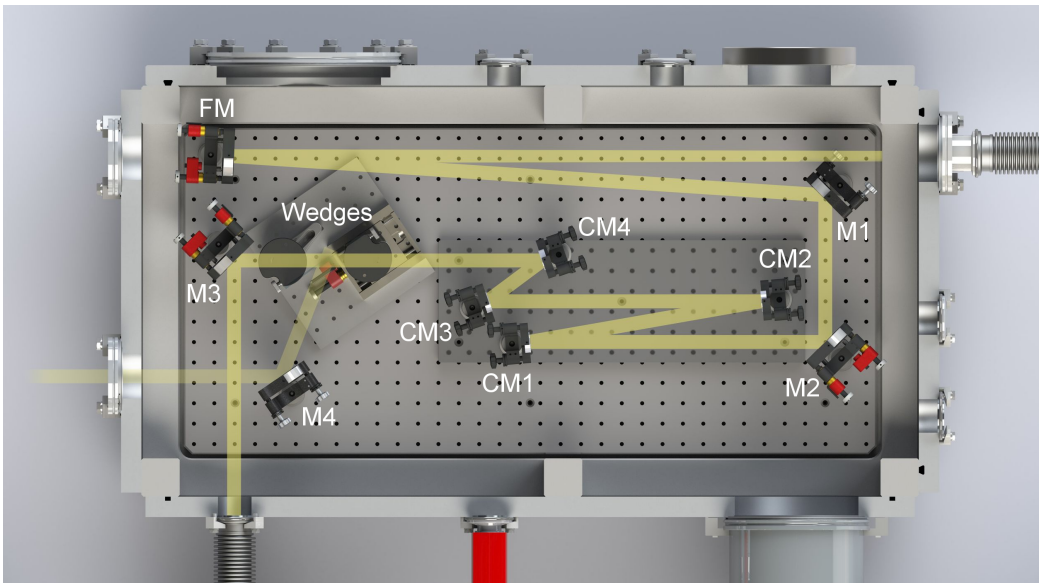

FIGURE 3.6: Beam path in the pulse compression chamber. The supercontinuum beam (drawn in yellow) enters the chamber through a port at the top, right corner in this illustration, passes a focusing mirror (FM), folding mirrors (M1–M3), chirped mirrors (CM1–CM4) and two glass wedges. Mirrors with red piezo adjustment knobs are motorized. The mirror M4 couples out a small, reflected portion of the beam for monitoring or CEP stabilization purposes. Credits: Andreas Duensing, Chair for Laser and X-ray Physics, Technical University of Munich.

The beam path in the compressor chamber can be seen in figure 3.6. Before reaching the actual pulse compressor, the supercontinuum hits a curved silver mirror (FM, $R = 6.5$ m) for a recollimation of the divergent beam exiting the HCF as well as two more folding mirrors (M1, M2). As already mentioned in the theory part, the pulse experiences besides spectral broadening also a temporal prolongation due to dispersion upon propagation through the gas gradient in the fiber. Therefore, a set of negatively chirped mirrors (CM1–CM4) and a pair of fused silica wedges are needed to temporally compress the broadened pulse as close as possible to its Fourier limit, as discussed in the previous section. For that, we use up to two pairs of negatively chirped PC306 mirrors in double-angle design that are produced in-house within the Munich Advanced Photonics cluster. Details on the design of these mirrors are given in [157].

After the chirped mirrors, the beam is transmitted through a pair of thin fused silica wedges mounted in Brewster angle geometry. With a remote-controlled movement of one of the wedges, the accumulated amount of positive chirp can be precisely adjusted and thus, the compression can be effectively fine-tuned. One of the reflections of the first wedge is picked with a folding mirror (M4) and guided through a small window out of the vacuum chamber to the *Femtolasers CEPset*™ CE-phase stabilization unit or to a transient grating frequency-resolved optical gating setup (TG-FROG) [107, 163] for the purpose of pulse characterization. The broadband pulses are propagating almost dispersion-free in high vacuum. Therefore, only one pair of chirped mirrors is necessary to obtain Fourier-limited pulses, if very thin fused silica wedges are used and two of the chirped mirrors can be left out.

In that case, they are replaced with silver mirrors to leave room for the compensation of additional positive chirp that may come up in the further beam path.

The output of the HCF compressor has been first measured with the TG-FROG setup yielding a shortening from over 60 fs after the fiber to approximately 4.5 fs after the compressor. Nevertheless, the measurement in air, as well as the capability of the FROG retrieval for broad input spectra, give rise to ambiguities. Therefore, the compressed NIR pulse is best characterized with a reconstruction of a streaking spectrogram [140], which is shown and discussed at the end of this chapter.

The compression chamber is the first part of the beamline, where the motorization of optical mounts is getting indispensable to align the beam without breaking the vacuum. For that, several piezo actuators can be steered with a standard, wireless PC keyboard thanks to an advanced Labview™ environment developed by our former bachelor student Christian Schröder and my colleague Michael Mittermair. It facilitates an easy control of nearly all motorized parts of the beamline. Additionally, the curved mirror (FM) and the outcoupling silver mirror (M3) in this chamber are placed on *Aligna*® motorized mirror mounts for stabilizing the position of the focus in the HHG chamber. This is crucial to compensate for relative drifts between the laser tables in the two different laboratories and ensure constant conditions for the subsequent attosecond pulse generation.

3.4 Generation of Attosecond Pulses

The peak intensity of the Fourier-limited, few-femtosecond pulse after the HCF compressor is high enough to efficiently generate photons with energies in the extreme ultraviolet regime via high harmonic generation. As a first step, it is briefly shown how the CE-phase of the compressed pulse is stabilized, as it is a crucial parameter for the shape of the XUV spectrum. The vacuum setup for the generation and characterization of the high harmonic radiation is presented afterwards.

3.4.1 CEP Stabilization

Besides the f-to-0 CEP stabilization unit (see section 3.2) that delivers a train of pulses with constant CE-phase ϕ_{CE}, another CEP stabilization system is necessary to compensate for long-term drifts occurring in the amplifier and the HCF compressor. For this, the so-called slow loop is implemented using a f-to-2f scheme, where the frequency combs of the NIR pulse and its second harmonic are overlapped [150]. As the pulses after the HCF compressor are spectrally broad enough for a direct implementation of this scheme, we use a small portion of the NIR beam after the chirped-mirror compressor and guide it to the *Femtolasers CEPset*™, as already mentioned above.

The second harmonic is created in a BBO crystal and overlaps with the fundamental NIR pulse, which leads to fringes in the overlapping spectral region around 450 nm – 500 nm.

The CE-phase is calculated with a fast Fourier transformation of these interferences. Thus, the offset respective to a reference value of the CE-phase is measured and can be actively corrected using a feedback loop to a control unit of the amplifier system. A piezo in the dispersive stretcher changes the amount of glass in the beam path and the CE-phase is shifted accordingly. Assuming constant changes of the CEP after the wedges in the pulse compressor, all CEP fluctuations in the beamline can be accounted for. The actual value of the CEP can be directly changed in a software, which allows precise fine tuning for optimizing the HHG output. The combination of all the mentioned stabilization mechanisms leads to a CEP jitter of less than 200 mrad.

3.4.2 High Harmonic Generation

After the pulse compression chamber, the beam is guided via a small vacuum cube, which contains a single, motorized deflection mirror, to the HHG vacuum chamber. It is designed similarly to the pulse compression chamber despite of its larger volume and the aluminum cover with glass viewports. The chamber and the beam path are illustrated in figure 3.7. First, the beam passes a thin window (W1, thickness: 100 µm) for obtaining a reflection that is focused and used as a position reference for the second beam stabilization system in the experimental laboratory. Afterwards, an iris is used to align the beam and remove outer parts of the NIR beam symmetrically. This results in a cleaner beam shape and helps to adjust the intensity for the focus in the HHG target. After the iris, a remote-controlled reflective filter (not shown in figure 3.7) can be moved into the full beam to weaken it for alignment purposes. Thanks to the height of the chamber and lots of free space on the breadboard, it is optionally possible to switch to s-polarization of the compressed beam by inserting two beam height changing periscopes, one of them assembled in a way that the linear polarization is rotated by 90°. Depending on the detection scheme of the experiment to be carried out, either an s- or p-polarized beam is used for the HHG process.

The next part of the beam path is also varying depending on the focal length of the curved mirror (FM in figure 3.7), which is chosen according to the desired photon energy for the planned streaking experiment. Higher intensities in the focal area are obtained for shorter focal lengths. The standard configuration for moderate XUV photon energies around 100 eV consists of two folding mirrors (M1, M2) guiding the beam to a curved mirror (R = 3 m) ensuring a small angle of incidence (AOI). Afterwards, the focused beam hits another motorized folding mirror as the focal length exceeds the length of the vacuum chamber. The focal position can be determined by generating a filament in a noble gas atmosphere with very low partial pressure (≈ 1 mbar).

The actual HHG process takes place in a noble gas, supplied to a ceramic tube with an aperture of 250 µm for the NIR beam and the generated XUV radiation. It is mounted to a stack of motorized translation stages allowing a precise 3D alignment of the target. The gas can only stream out through the small aperture and its backing pressure is controlled externally with a precision gas dosing valve. With this target, attosecond pulse bursts with

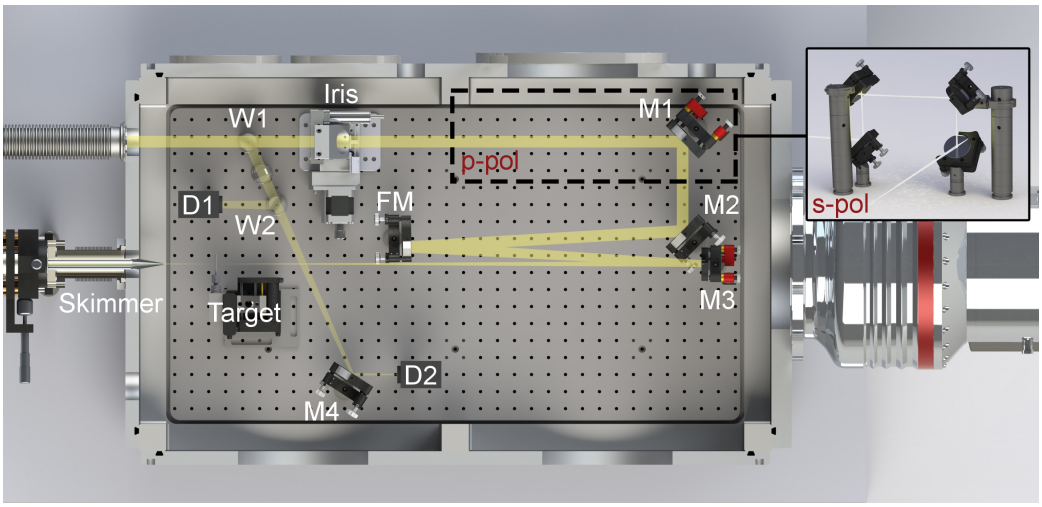

FIGURE 3.7: Beam path in the HHG chamber. In this illustration, the beam enters the chamber via a vacuum port in the top, left corner, and passes a thin window (W1) and the iris. In the case of p-polarized operation, three folding mirrors (M1–M3) and a curved mirror (FM) are used to guide and focus the beam into the target. For s-polarized operation, M1 is removed and two periscopes in polarization changing arrangement (see inset) are mounted instead. The windows W1 and W2 reflect small portions of the beam, which are guided directly or with an additional mirror M4 to the position-sensitive diode detectors D1 and D2. After the target, the NIR and the XUV beam pass the conically-shaped skimmer. Credits: Andreas Duensing.

different energies in the XUV regime are created under controlled conditions following the three-step model as discussed in section 2.1.3. With the measured pulse energy of $E_{\text{pulse}} \simeq 1$ mJ, the estimated pulse duration of $\tau_0 = 3$ fs and a focus diameter of $2w = 100$ µm, the peak intensity I_p at the target is calculated to

$$I_p = \frac{E_{\text{pulse}}}{\tau_0 \cdot \frac{\pi w^2}{2}} \approx 8.5 \cdot 10^{15}\ \text{W cm}^{-2}, \tag{3.3}$$

which is a lot more than the threshold for high harmonic generation of $I_p > 10^{13}$ W cm^{-2}.

In order to maintain high-vacuum conditions with a constant gas load in the chamber and prevent reabsorption of the generated XUV photons, a large TMP with a pumping speed of 1250 l/s (*HiPace® 1200* from *Pfeiffer Vacuum GmbH*) is operated there and connected to the same rough vacuum system as that of the pulse compression chamber. As the pressures in the HHG chamber may increase to up to $1 \cdot 10^{-3}$ mbar during operation, it is crucial to efficiently prevent gas flow to the subsequent parts of the vacuum beamline. Therefore, a conically-shaped tube with a minimum aperture of 1.5 mm can be placed close to the target and moved perpendicular to the beam propagation. This skimmer design is able to decrease the pressures between the HHG chamber and the following diagnostics chamber by up to four orders of magnitude [164]. The HHG chamber can be separated from the rest of the beamline with two gate valves with built-in windows. In this way, rough alignment procedures can be also performed by hand under atmospheric conditions.

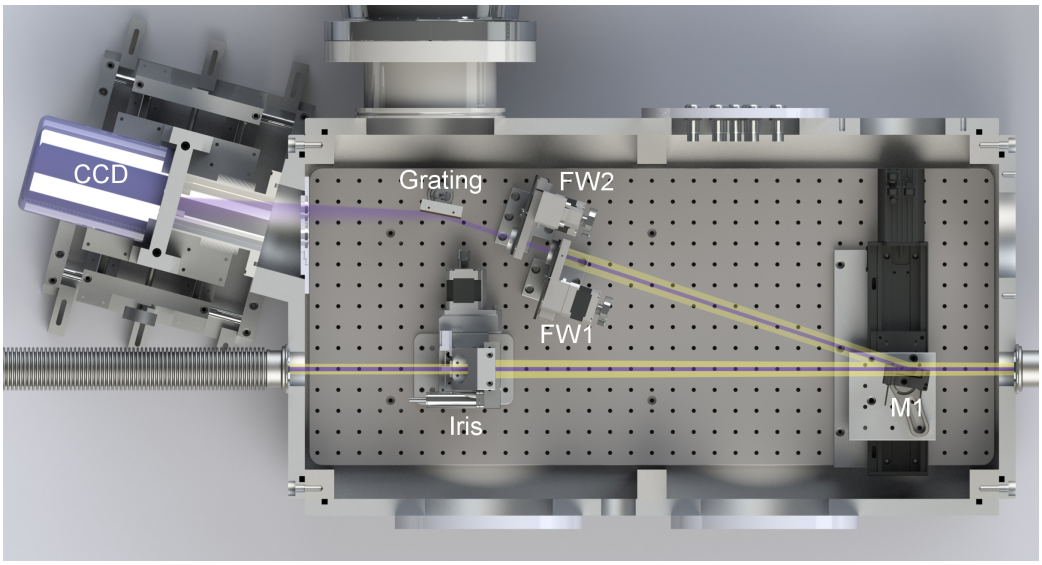

FIGURE 3.8: Beam path in the HHG diagnostics chamber. The collinearly propagating beams enter the chamber from the right and pass only the iris, before they are guided to the experimental end station. If mirror M1 is moved into the beam path, the beams are guided to the spectrometer setup, which consists of two filter wheels (FW1, FW2), an XUV grating and a CCD camera. Credits: Andreas Duensing.

3.4.3 HHG Diagnostics

The spectrum of the high harmonics can be recorded in a self-built XUV spectrometer embedded in the HHG diagnostics chamber. It is dimensioned considerably smaller, but follows the design of the HHG chamber. It is pumped by a *Leybold Mag W 1300 iP* TMP with a separate *Pfeiffer Adixen ACP 40* as backing pump. The beam path inside the chamber is illustrated in figure 3.8.

After the HHG process, the NIR and XUV beams propagate collinearly. With a first translation stage, a gold mirror (M1) can be driven into the beam path in grazing incidence geometry for obtaining maximum XUV reflectance towards the spectrometer. The beams are guided to a blazed, aberration-corrected concave grating that spatially separates the different wavelengths and simultaneously focuses the spectral components onto a back-illuminated, Peltier-cooled CCD camera (*Princeton Instruments PIXIS-XO:400B*). In order to avoid damage of this CCD, the NIR beam has to be filtered out using various thin zirconium (300 nm or 500 nm) or molybdenum (300 nm) highpass filters. These are mounted in two separate, remote-controlled filter wheels (FW1, FW2) together with thin aluminum and silicon foils, which are used for an energy calibration of the XUV spectrometer. These materials exhibit large absorption edges at 72 eV (Al) and 100 eV (Si) that are accessible within the XUV photon energy range of our system.

For higher energies, it is necessary to extrapolate the energy axis. The respective filter transmissions and the influence of the absorption of silicon in the CCD chip have to

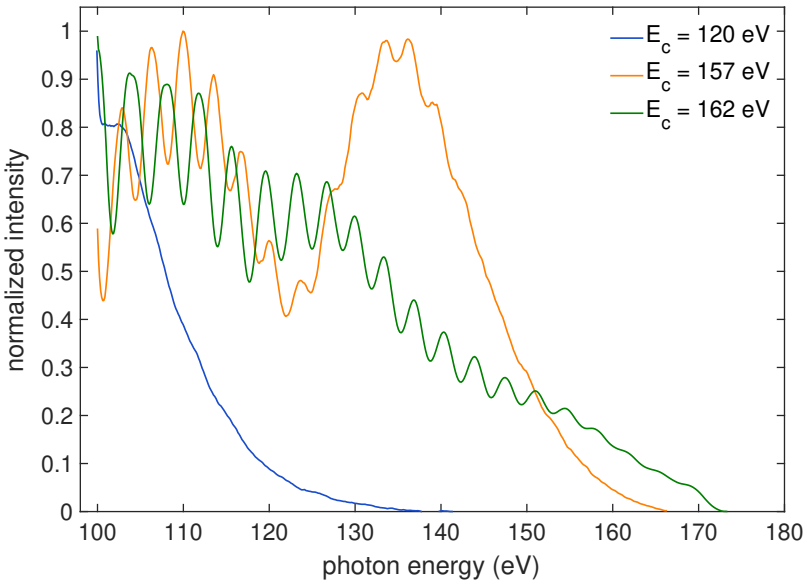

FIGURE 3.9: Zoom into the high-energy range of calibrated high harmonic spectra recorded with the XUV spectrometer in the diagnostics chamber. The HHG process has been optimized to obtain a moderate cutoff energy of E_c = 120 eV (blue) or very high cutoff energies of E_c = 157 eV (orange) and E_c = 162 eV (green).

be accounted for in the analysis of the recorded spectra. In figure 3.9, three exemplary HHG spectra are shown that have been optimized to a distinct cutoff photon energy E_c. The modulated part of the spectrum and the almost flat cutoff regime can be distinguished nicely, especially for E_c = 157 eV.

With the first translation stage mentioned above, also an XUV highpass filter combination (Zr and Mo) can be moved into the direct, unreflected beam path to block the NIR beam for the optimization of the XUV beam profile and flux using a multi-channel plate detector (MCP). There, electron cascades — induced by XUV photons and amplified by a strong electric field of 3 kV — are detected on a phosphor screen. The MCP assembly can be attached directly to the exit port of the diagnostics chamber, which has been done for the first alignment of the HHG beamline. At the complete attosecond spectroscopy beamline with experimental end station attached to the exit port, the MCP has to be mounted to a suitable flange there (see section 3.5.2).

For adjusting the intensity of the NIR beam in the subsequent experimental chamber, a remote-controlled iris is also situated in the diagnostics chamber. It is motorized in the vertical and horizontal axis to center it perfectly to the beam. For the spatial separation of the XUV and NIR beams, wire grids are assembled consisting of a small Zr filter ($d \approx 3$ mm) glued onto a washer, which is centered in a hollow aluminum ring ($d \approx 30$ mm) using two very thin tungsten wires forming the grid. Originally, another motorized panel for the insertion of large Zr filters and wire grids had been planned to be placed directly after the iris, but it turned out that the intensity of the NIR beam at this position is too high and destroys the thin metal filters in the wire grids too fast. Therefore, a separate wire grid

vacuum cube is attached to the diagnostics chamber via another spring bellow and a gate valve, as visualized in the CAD model of the AS101 beamline in figure A.4 in the appendix. It is placed at the end of the laser table, such that the distance to the NIR focus in the HHG chamber is maximized and the larger beam divergence avoids filter damage. The whole cube can be translated horizontally and the height of the wire grid can be adjusted with a vacuum manipulator. The wire grid can be quickly exchanged, since the cube can be vented and pumped individually from the neighboring chambers. The wire grid cube is then connected to the experimental chamber, which is described in the next section.

Alternatively to our experimental end station, a vacuum assembly specially designed for attosecond spectroscopy on liquid targets (see chapter 4) can be attached to the exit port of the diagnostics chamber. At this point, it should also be noted that the alignment and optimization procedure for obtaining high XUV flux, a good NIR/XUV overlap and thus proper streaking spectrograms is described thoroughly later in section 4.3.

3.5 Ultra-high Vacuum Setup for Attosecond Spectroscopy

The experimental ultra-high vacuum (UHV) end station of the attosecond beamline consists of a large, cylindrical vacuum vessel with various CF connection flanges for large-scale detectors, a sample manipulator, TMPs and the double-mirror delay unit. Originally designed for gas-phase streaking experiments in iodine compounds [37, 142, 164], the assembly has proven to be also usable for attosecond spectroscopy measurements on amorphous solid samples. In addition, the combination of time-dependent ion and transient absorption spectroscopy in krypton has been successfully realized using this assembly and the results have been recently published [165]. The delay unit and the experimental chamber that are presented in the following have been designed in the course of the master thesis of Alexander Späh [164]. Photos and a schematic overview of the whole experimental laboratory of the AS101 beamline can be found in the appendix A.1.1.

3.5.1 Double-Mirror Delay Unit

The centerpiece of the experimental end station is a common-path interferometer, which is necessary for a temporal delay of the spatially separated and copropagating XUV and NIR pulses. Therefore, a double mirror consisting of an inner multilayer XUV mirror (d = 3 mm) and an outer, annularly shaped metal mirror (d = 25.4 mm) is used to focus both beams to the target with a focal length of f = 125 mm. The bandpass-like reflection curve (see section 4.3 for more details) of the inner XUV mirror determines the central energy of the attosecond pulse and also its duration and temporal shape. The XUV mirror can be shifted with respect to the outer NIR mirror along the beam propagation direction using a closed-loop piezo nano-positioning system *PI Hera P-622.1 UD*. In this way, the delay between the XUV and the NIR pulse can be accurately adjusted and scanned with a minimum delay step size of 2.6 as.

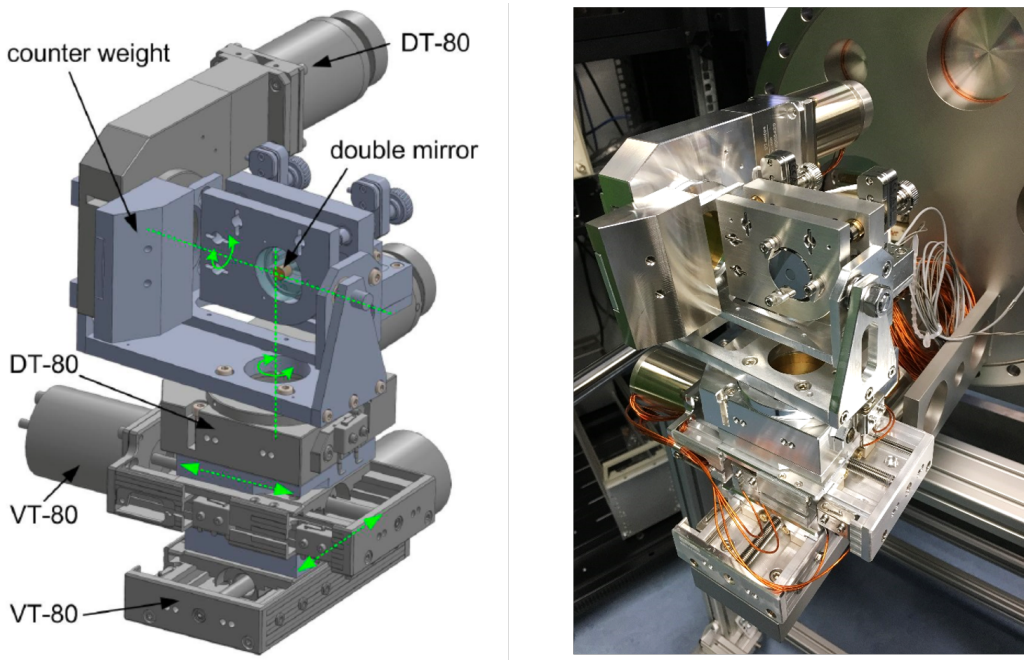

FIGURE 3.10: Left panel: Technical drawing of the double-mirror mount (taken from [164]). Two linear stages VT-80 and two rotation stages DT-80 are assembled to move the double mirror along the axes marked in green. A counterweight had to be placed to minimize the torque on the uppermost rotation stage. Right: Photo of the final UHV double-mirror assembly mounted to its supporting flange.

For adjusting the spatial positions of both beams individually, the outer mirror is mounted in a specially designed UHV mirror mount and can be moved with three piezo actuators without altering the inner mirror. The pointing of the XUV mirror can be changed using a stack of translation and rotation stages that is shown in figure 3.10. For a linear movement along the horizontal beam axes, two UHV-capable, linear stages (*PImicos VT-80*) are used. This allows for absolute positioning of the double mirror with a precision of 0.2 µm in a travel range of ± 25 mm. The tilt of the XUV mirror along the vertical and horizontal axis can be adjusted with two rotation stages (*PImicos DT-80*) mounted on gimbals. Absolute values for the angular displacement can be set with an accuracy of 0.004° and a maximum accessible range of ±15°. This range is restricted due to the dimensions of the whole positioning platform. With the gimbal mounting of the rotation stages, it can be ensured, that the inner mirror is centered to the Pivot point of the assembly. Due to its height of 210 mm, the whole stack has to be connected to a large CF300 flange, which also includes all necessary electrical vacuum feedthroughs. For the replacement and rough alignment of an XUV mirror, the flange can be attached to and removed from the experimental chamber quickly and easily.

3.5.2 Experimental Chamber

The body of the chamber is a stainless steel cylinder with a length of ≈ 400 mm and an inner diameter of d = 500 mm with totally 24 CF flange ports of different sizes. UHV conditions down to 10^{-9} mbar can be reached with a *Pfeiffer Vacuum GmbH ATP 2300 M* TMP with

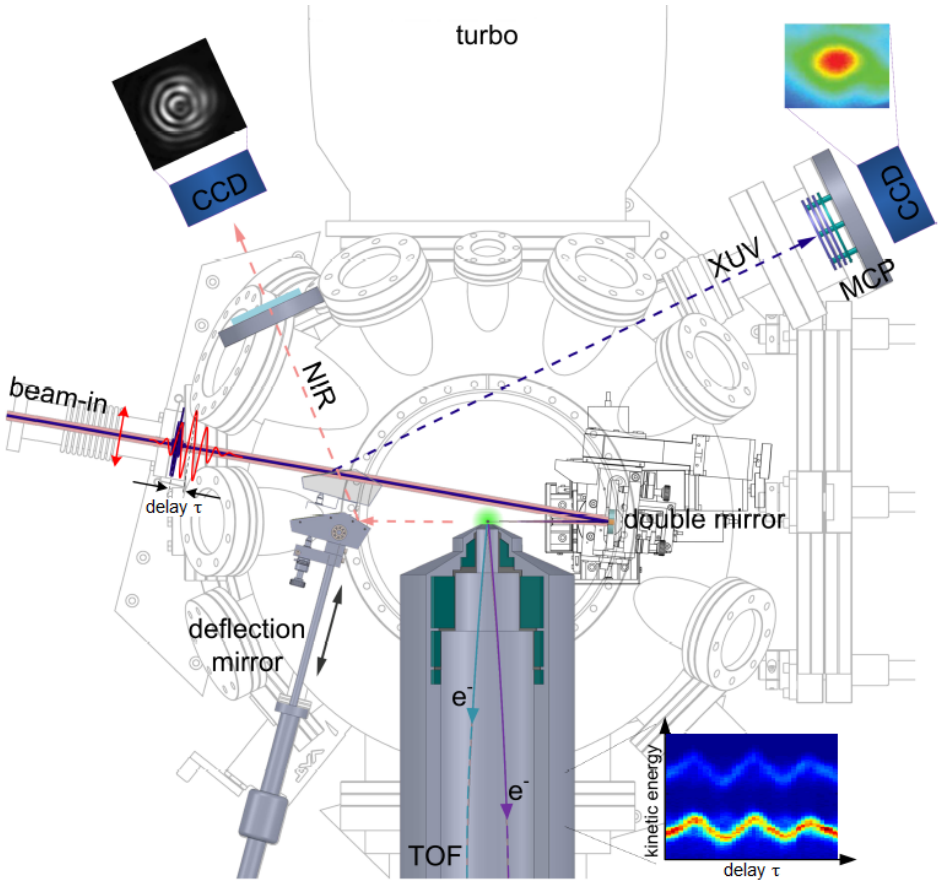

FIGURE 3.11: Top view of the experimental chamber and schematic illustration of the beam path and measurement principle with parallel polarized NIR (red) and XUV (blue) beams. Both pulses enter the chamber from the left through a CF40 port and hit the respective inner or outer mirror placed on the double-mirror mount at an AOI of 5 °. They are focused to the gas sample (green) in the interaction region in front of the TOF detector. The nozzle for the gas injection cannot be seen in this view. By scanning the XUV/NIR delay τ, a streaking spectrogram is recorded (inset in the bottom, right corner). With a deflection mirror on a manipulator, the XUV beam can be guided to the MCP detector (dashed, blue line). The NIR beam can be guided through a viewport to a CCD beam profiler with another mirror on the same manipulator (dashed red line) for adjusting the spatial and temporal overlap of the double mirror. Adapted from [164].

another *Pfeiffer Adixen ACP 40* as backing pump. The geometry of the setup is schematically shown in figure 3.11 for a streaking experiment with a parallel polarization of the beams. In this case, the TOF detector and the TMP are mounted horizontally, while the manipulator for 3D translation of the gas nozzle is placed on the top flange. The arrangement of these devices can be flexibly changed, as the respective flanges have the same size (CF 250). For streaking experiments with s-polarized beams, the TMP is mounted to the bottom, the TOF detector at the top and the manipulator to one of the side flanges (see figure A.3 in the appendix). The whole chamber is mounted on a triangle-shaped aluminum rack with the possibility to adjust the chamber height. This is important for the vertical alignment of the double-mirror assembly to the incoming beams. Ten additional viewports allow a good sight of the double mirror assembly and the interaction zone, which is crucial for alignment

and signal optimization. The double-mirror assembly flange is attached to the chamber via a CF300 port, which is situated at the opposite of the beam entrance flange. After the reflection at the double mirror and passing the interaction zone, the beams are guided to a beam exit flange, where they may be used for monitoring or for a subsequent experiment, i.e. transient absorption measurements [165].

The electron detection setup used in this chamber is a large-angle, anode-segmented TOF detector that has been designed and built up by Andreas Kim [166]. It offers a flat, almost energy-independent transmission in a broad electron kinetic energy range from 40 eV to 150 eV. The energy resolution is determined to 0.7 eV for 150 eV electrons, but is even better for lower kinetic energies. Three seperated anode plates, each divided into five individual segments, can be used for angle-resolved experiments with an angular resolution of roughly 10°. An array of electrostatic lenses allows a maximum electron collection AOI of up to ± 50° and a tunable angular resolution. For the first gas-phase streaking experiments in iodine-helium mixtures, the angular resolution has not been of interest. However, it is favorable for attosecond spectroscopy on solid-state samples.

3.6 Streaking in Neon for Pulse Characterization

With the experimental end station described above, we performed also gas-phase streaking scans in neon for a characterization of the XUV and NIR pulses created in the AS101 beamline. In figure 3.12, the attosecond pulse reconstruction based on the LSGPA algorithm (see section 2.1.5) is used to retrieve the pulse properties with an exemplary streaking scan with a fine resolution in the delay step size. Of course, the XUV pulse properties are depending on the alignment and the XUV mirror properties. Here, we excite the neon 2p line with a central photon energy of E_{XUV} = 125 eV and a bandwidth of ΔE = 5 eV, which results in a kinetic energy of the generated photoelectrons of roughly 103 eV.

In contrast to the restricted TDSE retrieval, the LSGPA algorithm does not use initial guesses and predefined boundaries. In the presented reconstruction, the spectral bandwidth appears to be overestimated by the retrieval. The duration of the attosecond pulse is determined to 230 as, which is smaller than the expected bandwidth limit given by the XUV mirror reflectivity (360 as). This can be explained as an effect of the overestimated bandwidth. However, the electric field of the few-cycle NIR pulse is nicely reproduced and its intensity profile indicates a FWHM pulse duration of 2.9 fs, which is only slightly larger than the Fourier limit of 2.74 fs for the broadened spectra out of the HCF system, as discussed in section 3.3.3. This measurement is presented as a benchmark test for the chirped-mirror compressor and to show that isolated attosecond pulses can be generated with the AS101 beamline. These pulses have been successfully used for gas-phase streaking measurements in iodine-helium mixtures (presented in [142]) as well as for investigating the electron dynamics in liquid and gaseous water, which is the main part of this thesis and described in the next chapter.

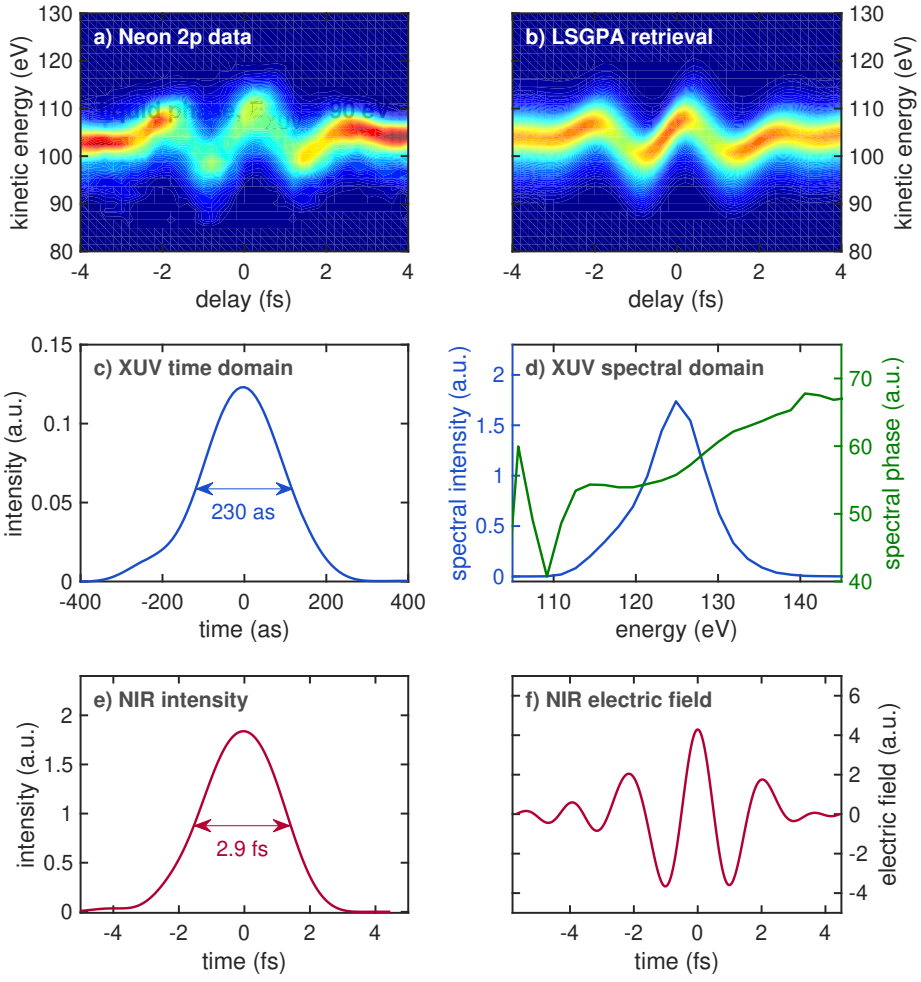

FIGURE 3.12: Streaking of the neon 2p line with an excitation energy of 125 eV. The background-subtracted data (a) are shown in comparison to the LSGPA retrieval (b). The retrieved XUV pulse properties are shown in panel c) for the time domain and d) for the spectral domain. The FWHM of the XUV pulse is determined to 230 as. The shape of the spectral phase indicates a positively chirped XUV pulse. The intensity envelope and the underlying electric field of the NIR pulse are shown in the panels e) and f) and yield a FWHM duration of the NIR pulse of 2.9 fs.

Chapter 4

Attosecond Streaking Spectroscopy in Liquid and Gaseous Water

After the assembly of the novel AS101 beamline and the characterization of the high harmonic generation, the first experiments have been conducted in cooperation with the group of Prof. Wörner at the ETH Zurich. The aim is to extend the measurement scheme of attosecond streaking to the liquid phase, which has not yet been reported and offers the potential for a great variety of new samples for attosecond spectroscopy. For this, an experimental end station specially designed for liquid sample delivery in a high-vacuum surrounding [44, 45] has been shipped from Zurich and adapted to fit to our vacuum beamline. The capability of our new setup to reliably produce isolated attosecond pulses together with the expertise of the Zurich group in handling the liquid sample and optimizing the photoelectron (PE) detection has resulted in evaluable streaking spectrograms of liquid water after only one week of alignment.

In the following chapter, first a brief introduction on steady-state photoelectron spectroscopy (PES) in water is given. After that, the experimental apparatus for attosecond spectroscopy in liquid and gaseous water is presented following the original publication and the doctoral thesis of Inga Jordan [45, 46]. The experimental methods for the time-resolved measurements are discussed in detail and exemplary data are shown. Attosecond delays between two electronic states of the water molecule have been determined by a statistical analysis of an extensive set of fitted streaking spectrograms. As these unprecedented findings constitute the main achievement of this thesis, the different physical effects contributing to a delayed photoemission in a liquid surrounding are presented in summary.

4.1 Photoemission from Liquid and Gaseous Water

The geometric and electronic properties of the water molecule are of great interest for the understanding of the structure of its condensed, liquid phase, and for the interactions with solvated species [40]. With X-ray absorption and emission spectroscopy techniques, the local electronic structure of liquid water has been studied experimentally and powerful theoretical calculations have been performed for this purpose [40–42, 167, 168]. As high-vacuum environments are required for electron detection, the use of liquid targets with high vapor pressures of typically 1 mbar – 30 mbar poses difficulties. PES on liquid samples

has become available using the liquid microjet technique [39], which is briefly presented in the following. With this approach, the valence and inner-shell electronic properties of liquid water have become accessible using XUV synchrotron radiation as excitation source [43]. These results are presented and the electronic structure of water is explained in this context. Finally, some basic concepts of electron transport in dense media are summarized for a deeper understanding of the measured steady-state and time-resolved PE spectra, as well as the retrieved electron dynamics.

4.1.1 Liquid Microjet Technique

The range of possible liquid targets in PES has been restricted to either low-vapor pressure liquids like formamide and glycol or high vapor pressure liquids, like ethanol or brine water, cooled down close to their freezing points [40]. These constraints have been lifted with the invention of the liquid microjet technique in 1997 [39]. From then on, pure liquid water and also aqueous solutions could be used without cooling in high-vacuum surroundings down to 10^{-5} mbar.

The idea of the liquid microjet technique is to create a thin filament of a fast flowing liquid in a vacuum environment. A stationary surface in cylindrical geometry with a very small surface area cross section can be obtained in that way. For very small jet diameters D_0 approaching the Knudsen limit, the electron mean free path at the equilibrium vapor pressure p_{vap} of the surface gets larger than D_0 [40]. In this regime of laminar flow, the effective electron path length in cylindrical geometry

$$l_{\mathrm{eff}}(r) = \ln\left(\frac{2}{D_0}\right) - \ln\left(\frac{1}{r}\right) \tag{4.1}$$

is significantly increased [40]. Due to the vapor distribution surrounding the liquid filament, the path length also depends on the distance r to the center of the jet. Typically, the diameter of the filament is 5 µm – 50 µm, depending on the size of the injection nozzle. An advantage of using flowing jets with velocities of up to 140 m s^{-1} is the fast and ongoing replacement of the liquid, which efficiently reduces the effects of evaporative cooling and electrostatic charging of the sample [40]. Outside the region of laminar flow, the jet breaks into water droplets and the freezing process begins (see inset in figure 4.6) [169]. The experimental realization of the liquid microjet technique in a vacuum end station for attosecond streaking is presented explicitly in section 4.2.

4.1.2 Electronic Structure and Synchrotron Spectra

Using the MBI-BESSY undulator beamline, photoemission spectra of liquid water at excitation photon energies between 60 eV and 120 eV could be acquired with high energy resolution of about 100 meV [43]. In general, the signals of the liquid phase always contain gas-phase contributions due to the continuous evaporation of molecules from the liquid surface in the high-vacuum surrounding. In figure 4.1, the combined spectrum is shown

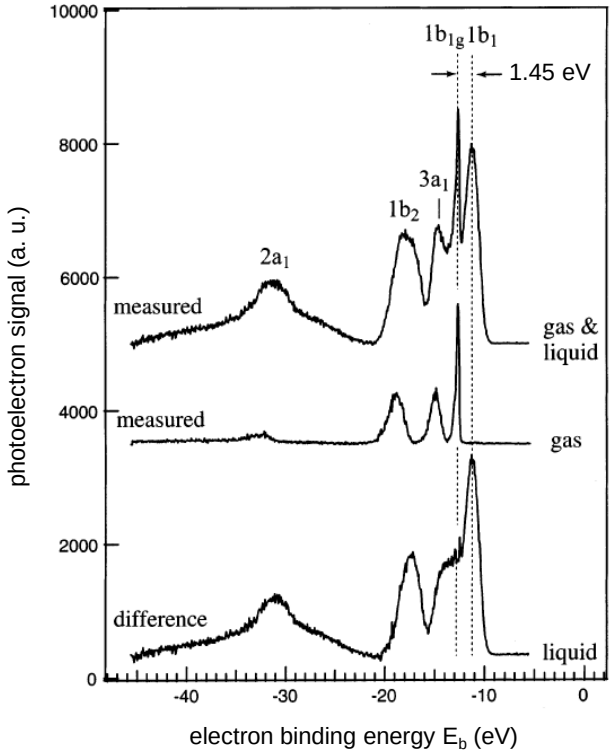

FIGURE 4.1: Measured PE spectra of liquid (top) and gaseous (middle) H_2O and the calculated difference spectrum (bottom), which represents the pure liquid-phase contribution in a liquid microjet experiment. The spectra are recorded with an excitation energy of 60 eV. The $1b_{1g}$ peak is taken as an energy reference due to the similarity of their spectral positions in both measured spectra at the top. The shift of 1.45 eV between the $1b_1$ peak in the liquid and the gaseous phase is highlighted in the figure. Adapted from [40].

at the top, the measured spectrum for purely gaseous water in the center and the resulting difference spectrum at the bottom, calculated to extract the pure liquid contribution. The binding energies have been found to be independent of the excitation energy within the experimental errors.

The peaks are labeled according to the assignment to the underlying molecular orbitals of the electrons, which are shown in figure 4.2 and explained briefly in the figure caption. In the combined and gaseous spectra, the sharpest peak at -12.6 eV refers to the well-known $1b_{1g}$ valence molecular orbital of gaseous H_2O and is used as a relative reference for obtaining the binding energies of the different peaks [170]. The other features are corresponding to the four valence molecular orbitals $1b_1$, $3a_1$, $1b_2$ and $2a_1$ of liquid H_2O. The extremely broadened $2a_1$ peak shape can be explained by two electron-loss features in close proximity to the peak, which originate from high-kinetic energy, primary photoelectrons that can excite molecular transitions in the water molecule similarly to photons [40]. These absorption features have been accounted for in the analysis of the synchrotron spectra. The retrieved binding energies in liquid and gas-phase water are listed in table 4.1.

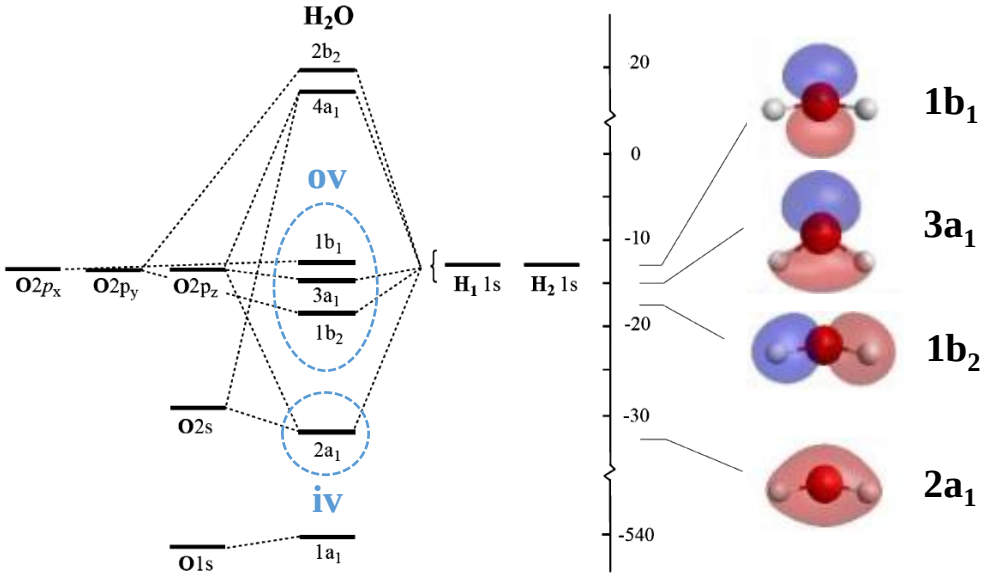

FIGURE 4.2: Left: Energy level diagram of the water molecule and its constituents oxygen and hydrogen. The black dashed lines mark the contributions of the oxygen and hydrogen atomic orbitals to a respective H_2O molecular orbital (MO). They are divided into inner valence (iv) and outer valence (ov) bands and shown in more detail at the right. The red and blue colored regions indicate a different sign of the electron wave function. The $1b_1$ orbital is non-bonding and consists mainly of the oxygen $2p_x$ lone pair. The $3a_1$ and $1b_2$ MOs are a mixture of the O $2p_y$/ $2p_z$ with the H $1s$ orbitals. They are oriented in the molecular plane and therefore form the OH bonding orbitals. The $2a_1$ MO has a strong O $2s$ character and is O $2s$ - H $1s$-bonding. Adapted from [40].

A weaker binding of the valence electrons in the liquid is observed in form of a pronounced shift of 1.4 eV – 1.7 eV with respect to the gas phase. This shift is mainly attributed to screening caused by the electronic polarization of the local environment in the liquid and can be calculated in a macroscopic model to 1.4 eV, which is in good accordance with the experimental values. The deviations from this value within the different valence orbitals are supposed to originate from the change of the orbital structure due to hydrogen bonding in the liquid, but a theoretical confirmation of these effects in a microscopic picture is still a challenge. The observed peak broadening in the liquid phase can also be explained by the statistical distribution of different configurations of the H-bonding network [40].

4.1.3 Electron Dynamics in Liquids

For an interpretation of photoelectron streaking spectra and the extracted dynamics, it is helpful to describe the photoemission process in condensed media with a three-step model [118, 171]. Afterwards, the underlying electron transport processes in the liquid phase are presented in more detail.

Molecular Orbital	E_b liquid (eV)	E_b gaseous (eV)
$1b_1$	-11.16	-12.60
$3a_1$	-13.50	-14.84
$1b_2$	-17.34	-18.78
$2a_1$	-30.90	-32.62

TABLE 4.1: Experimental electron binding energies E_b of liquid and gas-phase water for the respective valence molecular orbitals. Taken from [43].

Condensed Matter Photoemission Model

The first step of photoemission in condensed matter is the molecular photoionization following the absorption of an XUV photon occurring on the attosecond timescale [40]. Analogous to the situation in isolated atoms (see 2.1.3), the generated photoelectron is ejected with an initial momentum depending on the excitation energy, as well as the binding energy and symmetry of its molecular orbital. However, due to the high density in condensed matter the electron is undergoing interactions with the surrounding molecules upon its propagation to the surface (step 2). In X-ray diffraction experiments, the distance between adjacent water molecules in the liquid phase has been determined to be only 0.28 nm by measuring the oxygen–oxygen pair correlation function [172]. The propagation of an electron in the medium is therefore strongly altered by elastic and inelastic collisions with the neighboring molecules leading to changes of the momentum and kinetic energy. If the electron is not absorbed and has enough kinetic energy, it may pass the liquid–vacuum interface (step 3), where it is influenced by the so-called surface dipole, which is related to the work function in solid samples. This rather small surface potential originates from a substantial amount of free OH bonds (non-hydrogen bonded) pointing out and the respective hydrogen-bonded OH bonds pointing into the liquid [40, 173, 174]. The electrons, which are reaching the detector, add up to a characteristic liquid-phase photoelectron spectrum as discussed in the previous section.

An overview of photoelectron emission near a water–vacuum surface is shown in figure 4.3. The XUV radiation is penetrating into the water jet and getting damped due to a large absorption cross section in this spectral regime. Two-dimensional Mie calculations have revealed a total attenuation of XUV photons within 100 nm for energies of 20 eV – 23 eV [46]. For higher excitation energies, the absorption length is increasing, but still much smaller than the liquid jet diameter with a thickness of 5 µm – 50 µm. Photoelectrons are created within the penetration depth of the XUV radiation, but as they suffer energy loss on their way to the surface due to inelastic scattering, their escape depth is limited. For an electron kinetic energy in the range of 10 eV – 100 eV, the escape depth is only 1 nm –10 nm, as found by Suzuki *et al.* [175]. Therefore, it can be concluded that the XUV penetration depth plays a minor role. The basic quantities for the description of electron scattering are derived briefly in the following.

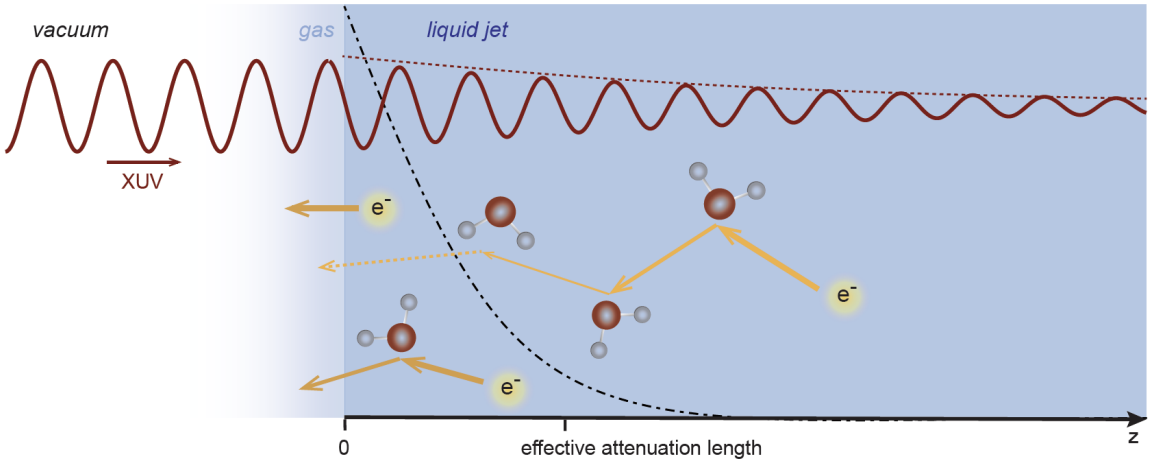

FIGURE 4.3: XUV-induced photoelectrons (yellow clouds) are generated in liquid water and propagate towards the surface. The number of scattering events with water molecules is increasing with larger distances of their origin to the surface (probing depth z). The probability of an electron to be detected with no energy loss and therefore contribute to the structured part of a PE spectrum is given by the black dash-dotted line. The XUV attenuation length is much longer than the effective attenuation length (EAL) of the electrons (see also figure 4.4). Electrons generated at probing depths larger than the EAL suffer energy loss or are absorbed in the liquid with high probability. Taken from [46].

Electron Scattering Theory

The easiest form of interaction of an electron with a scattering target is elastic scattering, where the kinetic energy of the electron is preserved within the experimental resolution and only the direction of the propagation is modified. Inelastic scattering of an electron additionally leads to substantial loss of kinetic energy and changes the vibrational or electronic quantum state of the scattering target. In both cases and for a randomly orientated sample, the scattering probability can be described with an energy and angle-dependent differential scattering cross section (DCS)

$$\frac{d\sigma}{d\Omega} = |f(\theta, E)|^2, \tag{4.2}$$

where $f(\theta, E)$ is the scattering amplitude, σ is the total cross section, Ω the solid angle of detection, θ the polar angle between in- and outgoing wave vector and E the kinetic energy of the electron. The scattering amplitude is defined in the expression for the outgoing scattering wave function

$$\phi(\vec{r}) = e^{ikz} + f(\theta, E)\frac{e^{ikr}}{r} \tag{4.3}$$

in the asymptotic limit far away from the target ($r \to \infty$), where z is the direction of the incoming electron wave function [168, 176, 177].

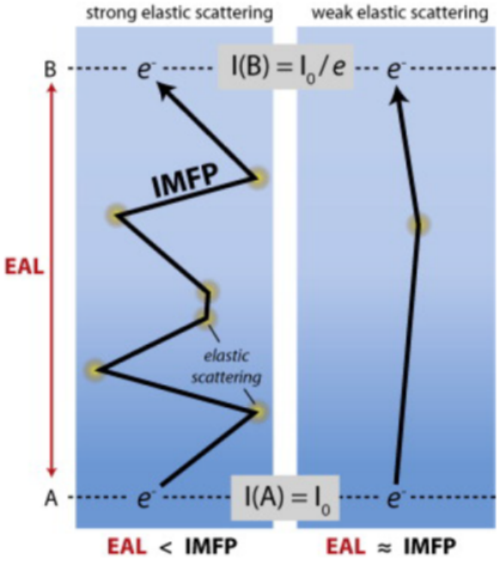

FIGURE 4.4: Comparison of the effective attenuation length (EAL, red line) and the IMFP (black line) in a medium. In the case of strong elastic scattering (left), the EMFP is short and many scattering events without energy loss take place before the signal is attenuated from I_0 to I_0/e. The pathway of the electron in the liquid is prolonged with more elastic scattering events. Hence, the IMFP can be much larger than the EAL. In the case of weak elastic scattering, the values for the IMFP and EAL are comparable. Taken from [169].

The elastic/inelastic mean free path (EMFP/IMFP) of a particle in an environment with number density ρ is a measure for the average trajectory length before an elastic/inelastic scattering incident happens and defined by the expressions [177]

$$\text{EMFP} = \frac{1}{\rho\sigma_{\text{el}}} \quad , \quad \text{IMFP} = \frac{1}{\rho\sigma_{\text{inel}}}. \tag{4.4}$$

Here, σ_{el} and σ_{inel} are the elastic and the inelastic cross sections, respectively. These mean free paths are important quantities for the description of electron transport in a material. As a next step, their contributions to the recorded liquid water PE spectra will be derived.

Influence of Scattering in PES

As already mentioned above, the probing depth in condensed matter PES is proportional to the IMFP. The sharp features in a PE spectrum result only from non-inelastically scattered electrons generated near the surface or electrons with a total path length in the medium shorter than the IMFP. Inelastically scattered electrons are either trapped in the medium or contribute only to a non-structured low-energy background (see measured raw PE spectra in section 4.4.1). However, the IMFP is not easily experimentally accessible, as there may be a large discrepancy between the probing depth and the IMFP depending on the strength of elastic scattering [169, 178]. This situation is illustrated in figure 4.4, where the relation between the IMFP and the EAL is shown for two different cases with varying EMFPs. In good approximation, the EAL is inversely proportional to the integrated particle density in a sample and thus experimentally more easily available in comparison to the mean free paths.

An EAL in liquid water of ≈ 1.5 nm at an electron kinetic energy of 80 eV decreasing to ≈ 1.2 nm at 110 eV is reported by measuring and comparing photoelectron signals of pure water and NaI solutions. These values are in good agreement with EAL data for ice [169].

Another method of EAL extraction is to perform angle-resolved PES with linearly polarized light and compare the anisotropy parameter β from liquid and gaseous water at various electron kinetic energies. For decreasing kinetic energies, the PE emission anisotropy is expected to be smeared out for the liquid phase due to increasing elastic scattering, which leads to a higher degree of randomly distributed momentum directions of the scattered photoelectrons. Thus the angle distribution gets more isotropic and the anisotropy parameter β is reduced. In comparison to the values reported by Ottosson *et al.* [169], slightly smaller, but similar values of the EALs in liquid water of 0.7 nm increasing to 1.5 nm in the kinetic energy range of 50 eV to 110 eV have been found.

The experimental access to the EAL for liquid water is complex, which leads to significant deviations between the extracted values reported above and a newer experimental publication by Suzuki *et al.* [175]. Their results show also a rather flat kinetic energy dependence of the EAL between 10 eV and 100 eV, but it is overall larger with a value of ≈ 2 nm. Concerning measurements of the IMFP, it has been concluded that at lower kinetic energies (< 70 eV) it appears to be smaller than the values predicted from simulations explicitly conducted for liquid water [178, 179]. In summary, a rather flat energy dependence of the IMFP in liquid water between 10 eV and 100 eV is found [180]. In stark contrast, all experimental values of the IMFP and EAL are higher than expected from the so-called universal curve for the IMFP, which holds for many solids (see references [46, 118, 171, 181] for more details). Here the IMFP is significantly smaller than 1 nm for most of the materials in the energy range of 20 eV – 200 eV.

As can be seen in figure 4.4, the EAL is only a lower boundary for the IMFP, which increases significantly for stronger elastic scattering. The propagation time of an electron with given kinetic energy in a medium is therefore sensitive to the IMFP-EMFP-ratio, which is equivalent to the elastic-to-inelastic scattering ratio of the DCS [180], and given by:

$$\eta(E) = \frac{\sigma_{\mathrm{el}}(E)}{\sigma_{\mathrm{inel}}(E)} = \frac{\mathrm{IMFP}(E)}{\mathrm{EMFP}(E)}. \tag{4.5}$$

However, all these quantities are hard to extract from experiments and measurements differ from each other as discussed above. Therefore, as a complementary method, also Monte Carlo simulations are used to model the electron transport in water [168, 178, 179]. In these simulations, a statistical analysis of a large number of electron trajectories is carried out to model the electron transport using energy- and angle-dependent elastic and inelastic scattering cross sections. Especially for the discussion of electron dynamics in section 4.5, the results of this modeling will be very important, as the scattering phase shift of electron wave packets in a liquid has a major contribution to the measured attosecond delays.

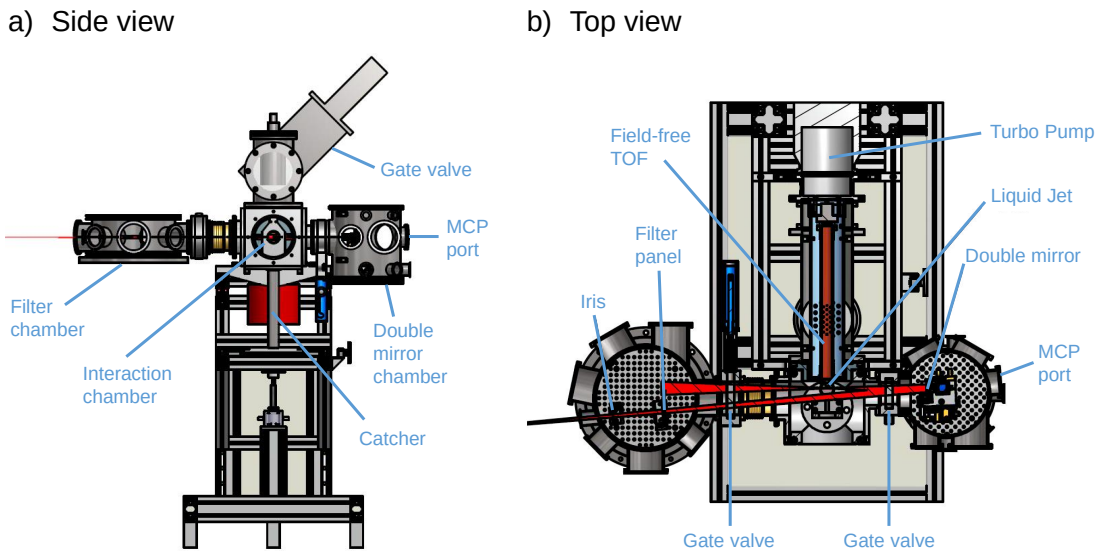

FIGURE 4.5: Technical drawings of the complete experimental vacuum end station for PES in the liquid phase. The beam enters the setup from the left in both, the side view in panel a) and the top view in panel b). The setup is mounted onto a height-adjustable aluminum rack and divided into three separable units: filter chamber, interaction chamber and double-mirror chamber. Credits: Arohi Jain, Laboratory for Physical Chemistry, ETH Zurich

4.2 Experimental Setup for Attosecond Spectroscopy on Liquid Samples

For the efficient detection of photoelectrons and also for avoiding strong attenuation of the XUV radiation, high-vacuum conditions are a prerequisite for attosecond streaking measurements. An overview of the whole vacuum setup, that was designed in Zurich and shipped to Garching for attosecond streaking measurements in the liquid phase, can be seen in figure 4.5. It consists of three separable vacuum units, which are the filter chamber, the interaction chamber with the liquid microjet assembly and the double-mirror chamber. As it is the centerpiece of the setup, the experimental realization of the liquid microjet and the implementation in a photoelectron spectrometer is described first.

4.2.1 Liquid Microjet and Interaction Chamber

The experimental realization of a liquid microjet requires mainly a thin quartz capillary with typical inner diameters of 5 µm – 50 µm, a high-pressure liquid chromatography (HPLC) pump and liquid nitrogen (LN_2) cooling traps. A schematic overview of an experimental vacuum chamber very similar to the one used for the measurements in this thesis is shown in figure 4.6, where the components associated with the liquid jet are highlighted in blue.

For the measurements in this thesis, the whole jet assembly is mounted on an ISO-K DN 160 flange and can be connected to the bottom port of a vacuum cube, which is the centerpiece interaction chamber of the spectrometer (see figure 4.5). Via a vacuum feedthrough and

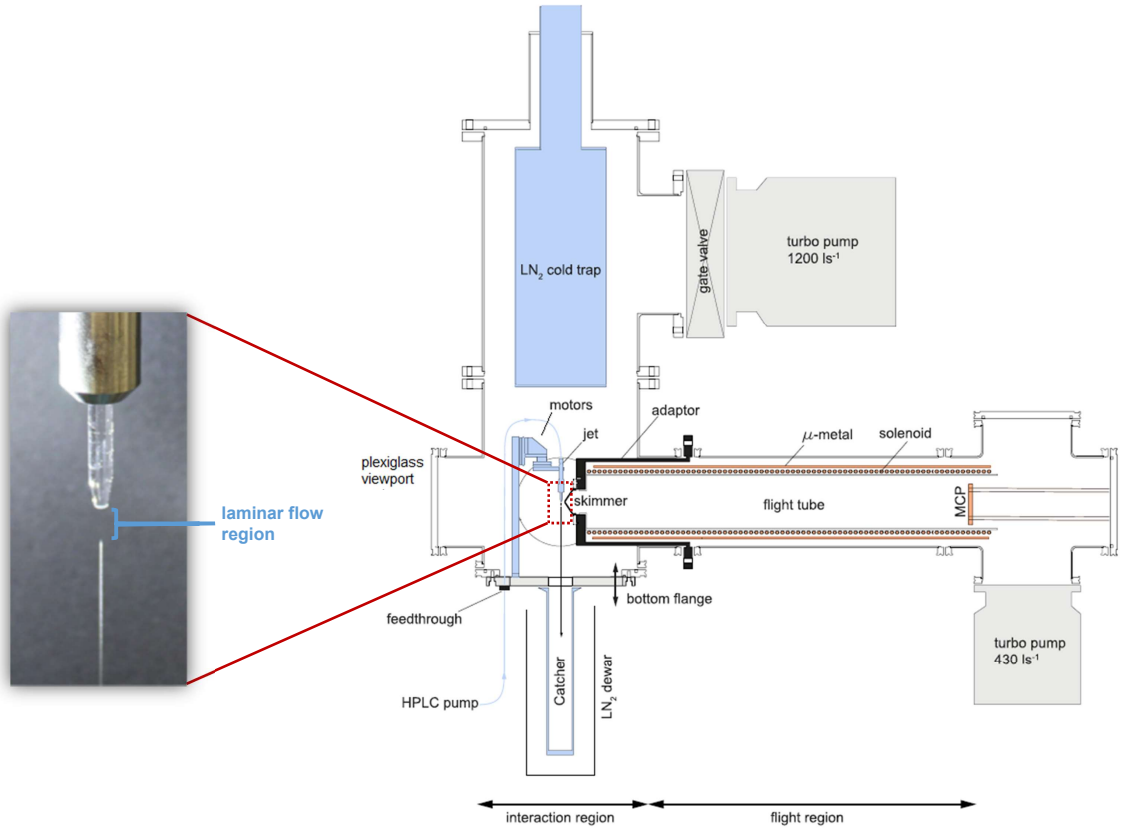

FIGURE 4.6: Schematic overview of the interaction chamber containing the liquid water microjet parts (blue) and the photoelectron detector. The inset shows a zoom to the laminar flow region of the liquid filament created by the quartz nozzle. The catcher and the liquid nitrogen cold traps freeze the generated water vapor and together with the turbo pumps, a high-vacuum environment for photoelectron streaking measurements can be preserved. Adapted from [45].

PEEK (polyether ether ketone) piping the quartz nozzle is supplied with the liquid sample to be studied. The quartz nozzle can be moved with 1 µm precision piezo motors in each direction. The sample streams from the top into a LN_2-cooled, removable catcher mounted at the bottom flange. It is also possible to switch to gaseous samples by simply replacing the quartz nozzle and using a gas feedthrough. At the top of the interaction chamber, a pipe with a large LN_2 cool trap and a 1200 l/s turbo molecular pump is attached for obtaining pressures below $1 \cdot 10^{-3}$ mbar [45].

Additional to the components in figure 4.6, the liquid jet has been equipped with an ice breaker, which cuts the growing ice from the bottom periodically to avoid freezing of the filament in the laminar flow region. Another modification of the setup is the possibility to apply a constant potential to the liquid filament via an electric contact with the jet assembly. The charging of the liquid has been verified by measuring a finite resistance between the liquid filament and the jet assembly [46]. The influence of this potential on the measured spectra is discussed in section 4.4.1.

In figure 4.6, a magnetic-bottle detector is shown. However, for the streaking measurements discussed in this thesis, a similar field-free TOF detector has been used instead (see figure 4.5). The plexiglass viewport is important for the rough alignment of the water jet to the skimmer of the TOF detector and the focused laser beam. The skimmer has an aperture of 1 mm and acts as a differential pumping stage, as the flight tube of the TOF spectrometer is pumped separately. There, a lower pressure ($\approx 10^{-7}$ mbar) than in the interaction chamber has to be maintained for efficient electron detection and to avoid damaging the MCP.

For daily operation of the jet, it is highly favorable to be able to pump and vent the interaction chamber fast, because after some hours of operation the catcher and the surface of the cold trap are full of ice and have to be emptied and cleaned. For this aim, the skimmer aperture to the TOF detector can be closed tightly to maintain low pressure in the flight tube. Further, large gate valves are built in to be able to separate the neighboring vacuum chambers and the continuously running TMP. To start a measurement, the liquid jet has to be started under atmospheric pressure and is then pumped down with a scroll pump until a pre-vacuum pressure of about 0.1 mbar is reached. Then the cooling traps are filled with liquid nitrogen and the gate valve to the running TMP is opened, while the valve to the scroll pump is closed simultaneously. When the pressure in the interaction chamber is good enough, the skimmer and the gate valves to the adjacent filter and double-mirror chambers can be opened [45].

4.2.2 Filter and Double Mirror Chamber

The filter chamber is a cylinder with an inner diameter of 318 mm according to the ISO DN 320 standard. Optics can be mounted flexibly on the breadboard baseplate mounted to the bottom of the chamber. For laser alignment purposes, the top flange is a plexiglass viewport. Various vacuum ports are attached at the side of the cylinder for electrical feedthroughs, a beam outcoupling viewport and for the connection to the adjacent vacuum chambers of the beamline. The whole assembly is mounted on the laser table with suitable aluminum posts to match with the fixed beam height of the attosecond beamline. It is connected to the HHG diagnostics unit via a flexible KF40 spring bellow and a gate valve. Due to a separate pre-vacuum connection, the chamber can be pumped and vented independently from the rest of the beamline.

The collinear XUV and NIR beams are guided through a motorized iris and a motorized panel allowing to choose different filters, the full beam or a Zr wire grid for the time-resolved measurements. With large, but very thin (200 nm – 300 nm) Zr high pass filters, steady-state photoelectron spectra can be recorded. The insertion of a Zr wire grid blocks the NIR just for the inner mirror and the outer parts of the beam can hit the outer mirror for time-resolved streaking measurements (similar setup as described in section 3.4.3). The iris is important for alignment of the beam from the HHG source to the experiment and also serves for adjusting the intensity for the streaking measurements by cutting outer parts of the NIR beam.

After these components, the beams leave the filter chamber, pass a large gate valve, traverse the whole interaction chamber (with enough distance to the water filament) and another gate valve, before they enter the double-mirror chamber. There, both beams are back-focused by the double mirror (focal length f = 250 mm) to the water jet in the interaction region in front of the TOF detector. Afterwards, the transmitted, divergent NIR beam enters the filter chamber again and hits a motorized silver mirror that couples out the beam of the filter chamber through a fused silica viewport. Outside the chamber, the beam is refocused by a lens to either a power meter for measuring the NIR intensity or a beam profiler for a proper adjustment of the spatial and temporal overlap of the foci of the inner and outer mirror.

For this purpose, the inner and the outer mirror must be movable separately. Similar to the double-mirror setup constructed for our beamline (see chapter 3.5.1), an assembly of vacuum positioning stages, a motorized mirror mount and a piezo stage for adjusting the temporal delay has been constructed to fit to the liquid water jet interaction chamber. The operation principles are comparable, but here, the vertical and horizontal rotation axis (tip/tilt) of the inner mirror are missing. Further, piezo actuators are used instead of closed-loop translation stages. These measures reduce the size and the costs of the double-mirror delay unit, but also lead to less reproducible beam positions and cause more inconvenience when searching the optimum signal.

Nevertheless, the double-mirror stack is compact and stable. It has been placed in a separate double-mirror chamber, which is also a cylinder with an inner diameter of 261 mm (ISO DN250). Besides various ports for electric feedthroughs and the separate pre-vacuum connection, an additional MCP assembly can be mounted to the vacuum vessel behind the double-mirror stack to optimize the beam profile and flux of the high harmonics. For this, the double mirror has to be moved out of the beam path with a manipulator.

4.2.3 Additional Equipment

Besides the large-scale vacuum assembly, also the necessary periphery has been transported from Zurich to Garching for the measurement periods. The required data acquisition equipment is installed in a 19" rack together with the power supplies and electronics for the TOF detector, the turbo pumps and the vacuum motorization. The pre-amplified signals of the time-of-flight detector are digitized with a time-to-digital converter (TDC) using the trigger signal of the laser system and then read out by a LABVIEW™ environment that also saves the data in a well-defined, structured form. Several other LABVIEW™ programs have been used on a separate PC for monitoring the pressures and steering the iris, the filter panel and the double-mirror motorization.

4.3 Experimental Methods

The combination of a new attosecond beamline and the described liquid microjet vacuum setup required thorough planning in both groups prior to the appointed beamtimes. As the experimental apparatus is continuously used in the laboratories in Zurich, the streaking measurements had to follow a tough schedule of only five weeks in a first and three weeks in a second beamtime. In the following, our experimental procedure to obtain best possible data sets for a reliable analysis of attosecond dynamics in water is described.

4.3.1 Calibration Measurements

After assembling and evacuating the setup to a pressure below 10^{-5} mbar, the beams are aligned to the double mirror and the MCP is used to optimize the high harmonic flux. In order to find a first XUV-induced photoelectron signal and to calibrate the spectrometer, a gas nozzle is used instead of the liquid microjet. With a large Zr filter, the NIR beam is blocked and neon is used to optimize the XUV signal due to its large cross section at photon energies around 90 eV. After that, steady-state PE spectra of xenon have been acquired for the time-to-energy conversion of the TOF detector. For that, photoelectron and Auger electron peaks in time-of-flight signals integrated over several ten minutes are assigned to their literature kinetic energies [45, 182] and a hyperbolic fit according to the expression

$$E_{\mathrm{kin}} = \frac{m}{2}\left(\frac{s}{(t-t_0)}\right)^2 + E_0 \tag{4.6}$$

is performed. The fit optimizes the free parameters to $s = 0.49$ m, $t_0 = 93.26$ ns and $E_0 = 0.52$ eV. Due to the nonlinear conversion formula, the integral of the signal between two distinct time-of-flight values in the time domain has to be preserved upon transformation to the corresponding interval in the energy domain. Therefore, the Jacobian is multiplied with the spectral intensity after the energy conversion for a proper correction.

First streaking traces in neon have been recorded for the optimization of the overlap of the NIR focus with the interaction region. These scans also demonstrated for the first time, that the new experimental attosecond beamline delivers few-cycle NIR and isolated attosecond pulses. Having accomplished these calibration steps, we could switch to the liquid microjet target for the rest of the measurement campaigns. The first streaking in a liquid sample has been achieved within a few days after installation of the experimental setup and we could go over to a daily operation measurement scheme.

4.3.2 Measurement Parameters

In the first beamtime, the aim was to demonstrate streaking in liquid and gaseous water and to obtain a large data set of time-resolved scans under similar conditions with the same excitation energy of $E_{\mathrm{XUV}} = 90$ eV. In the second beamtime, the measurements have been extended to the additional photon energies $E_{\mathrm{XUV}} = 80$ eV and $E_{\mathrm{XUV}} = 105$ eV in order to

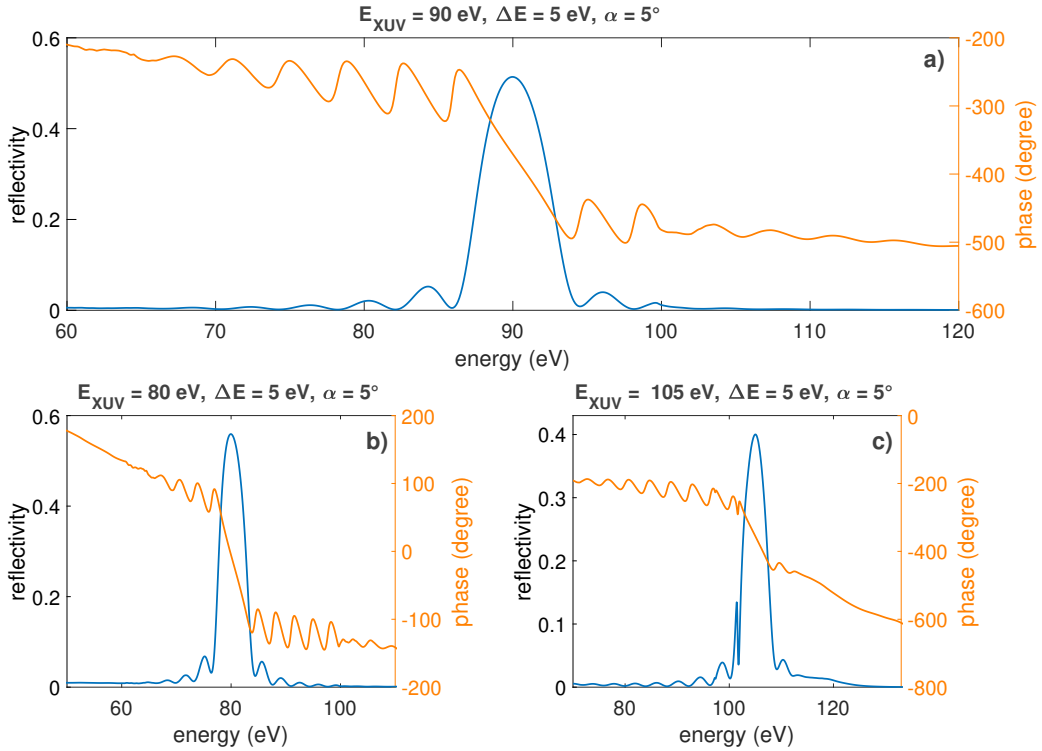

FIGURE 4.7: Reflectivity (blue) and phase (orange) properties of XUV multilayer mirrors used for the streaking experiments. The central energy E_{XUV} is 90 eV in panel a), 80 eV in b) and 105 eV in c) and the spectral width of the reflectivity is 5 eV for all mirrors. The most streaking scans have been acquired with E_{XUV} = 90 eV. The phase dependence is linear within the main peak and no higher-order chirp is induced therefore.

extract a possible energy-dependence of the measured attosecond delays. For that, the inner multilayer XUV mirror, which acts as a bandpass filter and defines the central energy of the XUV excitation pulse (see 2.1.3), has been exchanged several times. These mirrors have been specially designed and manufactured by Alexander Guggenmos [126] for these experiments. Their reflection properties are shown in figure 4.7.

Within the measurements at a specific photon energy, all other experimental parameters have been kept constant as far as possible. The sample is prepared on a daily basis by adding a small amount of sodium chloride to purified, highly demineralized water to get a concentration of 0.05 mol $\cdot$ l^{-1}. This is done to ensure enough conductivity in the filament to avoid electro-kinetic charging of the sample [45]. The diameter of the water filament was 25 µm at a constant flow rate for all the measurements. In the second beamtime, additional liquid-phase scans with an electrostatic potential of 20 V applied to the liquid jet have been conducted for all photon energies (see section 4.4.1).

The laser parameters at the interaction zone are dependent on the alignment of the beamline. The pulse energy after the HCF compressor varies only slightly around the optimum of 1.2 mJ, but the alignment for HHG has to be optimized on a daily basis. For this, the spectral intensity of the high harmonics at the desired XUV excitation energy has to be optimized

using the XUV spectrometer in the HHG diagnostics unit (see section 3.4.3). This is done by changing the dispersion of the NIR pulse, its focus and also the pressure of the HHG target, which influences the flux and chirp of the generated attosecond pulses.

However, these differences can be accounted for statistically by recording a large set of streaking scans on different days. The intensity of the NIR beam at the liquid target has been chosen such, that the amplitude of the streaking shift of the photoelectron lines in a recorded spectrogram is large enough and clearly visible, but the NIR-induced low-energy ATI (above threshold ionization) background is not smearing out the region of interest. In order to exclude effects due to different NIR intensities, the power after the interaction zone has been logged and systematic intensity scans have been performed on one day of each beamtime.

4.4 Measurements and Results

In the following, the results of the first attosecond streaking measurements in the liquid and gaseous phase of H_2O are summarized and exemplary steady-state and time-resolved spectra are shown. Eventually, the statistical analysis of a large number of fitted spectrograms reveals the intra-species photoemission delay between the inner and outer valence band of water.

4.4.1 Steady-state Photoelectron Spectra

As already shown in figure 4.7, we use XUV-multilayer mirrors with a bandwidth of 5 eV to generate isolated attosecond pulses with a minimum duration of approximately 360 as for excitation of the water target. Of course, this bandwidth also limits the energy resolution of all the photoelectron spectra, which have been recorded with our experimental apparatus. Looking at the spacing of the different binding energies within the outer valence (ov) molecular orbitals $1b_1$, $3a_1$ and $1b_2$ in table 4.1, it becomes obvious, that the single lines cannot be resolved. Taking this into account, the high-resolution PE spectrum shown in figure 4.1 has to be convolved with the mirror reflectivity.

In figure 4.8 a), we can see a good accordance between the convoluted synchrotron spectrum (orange) and a measured PE spectrum of liquid water using isolated attosecond pulses at 90 eV (blue) for excitation and a 200 nm Zr filter for blocking the NIR beam. The measured spectrum is not as broad as the convolution, but this might be also a side effect of the applied Shirley-type background subtraction. In panel b) of figure 4.8, the energy-calibrated and Jacobi-corrected raw spectrum is shown in dark red, together with the respective background-corrected spectrum. Here, the unstructured low-energy background from secondary inelastically scattered electrons, as discussed in 4.1.3, is clearly observed for electron kinetic energies < 30 eV. This broad background has been subtracted and additionally discarded by cutting the spectrograms at suitable positions.

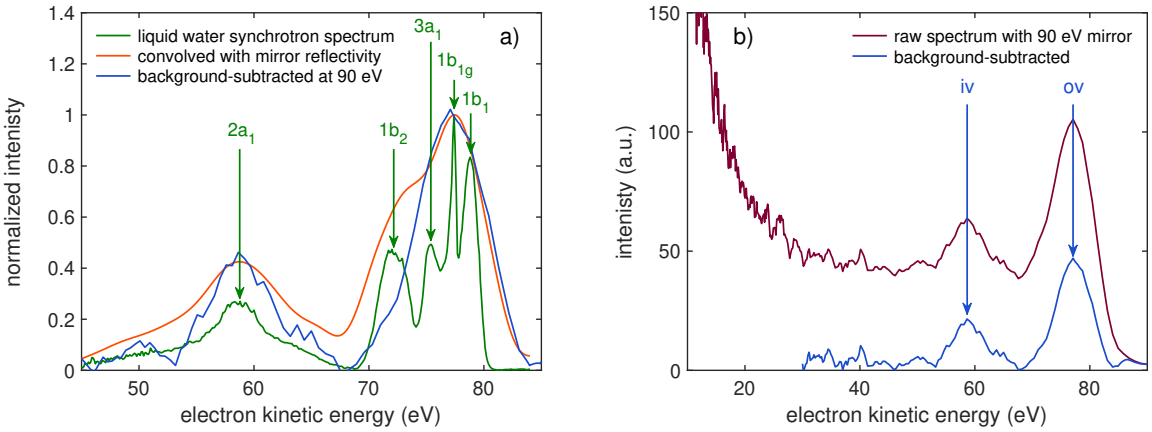

FIGURE 4.8: a) High-resolution synchrotron spectrum of liquid H_2O (green, data extracted from [43]), its convolution with the mirror reflectivity of the 90 eV XUV inner mirror (orange) and measured, background-corrected PE spectrum with 90 eV IAP excitation (blue). The peak positions of the different molecular orbitals (see figure 4.1) are marked with green arrows. b) Energy-calibrated PE spectrum (dark red) shown for a larger kinetic energy range including secondary electron background and again the corresponding Shirley-type background-subtracted spectrum (blue). The inner (iv) and outer valence (ov) peaks are marked with blue arrows.

In figure 4.9, raw PE spectra of liquid and gaseous water are compared. The shift in energy between the two aggregate states amounts to roughly 4 eV, which is substantially larger than expected from the synchrotron data (1.45 eV). It can be attributed to small potentials on the jet due to charging effects and the surface dipole of the liquid microjet surface. Thus, the gas-phase measurements are influenced due to the proximity of the liquid filament. The consequence is a non-vanishing liquid-phase contribution in the gas-phase measurements, which is dependent on the jet position. This influence manifests itself in the relative peak ratio of the ov and iv lines in the gas-phase spectra, which is too large in comparison to the synchrotron measurements. In the gas phase, the broad, low-energetic background is an order of magnitude smaller, as electron scattering is suppressed in the gas phase due to the lower density of water molecules near the liquid–vacuum interface. In that case, it is ensured that the gas phase is dominating. Thus, the jet has been positioned according to this criterion for obtaining gas-phase streaking measurements.

As shown by the steady-state XUV spectra in figure 4.8, it is only possible to distinguish between one main feature of iv and ov photoelectrons in streaking experiments with isolated attosecond pulses. Therefore, we always have to consider in the further analysis that the outer valence line in a liquid spectrogram is composed of different energy states and contains also gas-phase contributions. To get rid of these gas-phase effects in the liquid measurements, the influence of an additional, static electric potential — applied to the liquid filament — on the liquid water PE spectra has been investigated thoroughly following the idea of Lundholm *et al.* [183]. For that purpose, measurements at a monochromator beamline in Zurich have been performed. A negative voltage leads to an acceleration

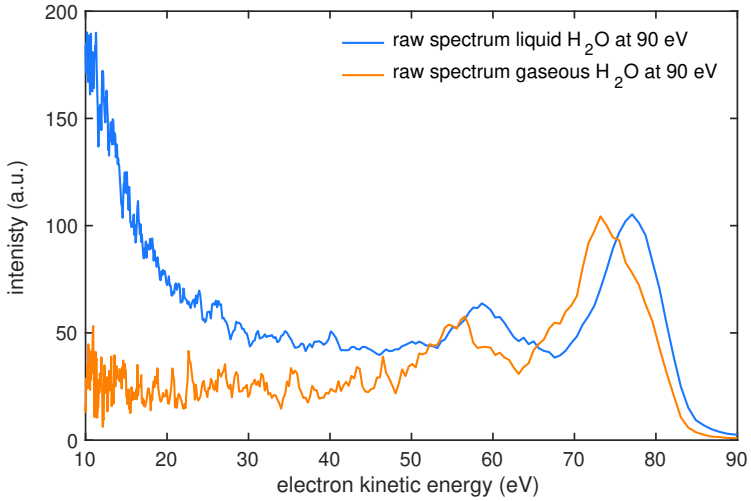

FIGURE 4.9: Energy-calibrated PE spectra of liquid (blue) and gaseous (orange) water recorded with IAP excitation at 90 eV.

of the electrons and a shift of the spectrum to higher kinetic energies, a positive voltage analogously to a retardation. It has been found that the gas-phase $1b_1$ peak in the spectrum is extremely broadened and reduced in peak amplitude for potentials < -5 V and > 7 V. Hence, the gas-phase contribution can be suppressed very efficiently with the application of sufficiently large potentials and it is possible to carry out essentially vapor-free measurements with the liquid microjet for extracting liquid-phase only effects (see reference [46] for a more detailed discussion).

4.4.2 Time-resolved Streaking Scans

For obtaining time-resolved streaking spectra, only the inner part of the collinearly propagating XUV and NIR beams is filtered with a thin foil of Zr or Mb and hits the inner XUV mirror, which is moved by the piezo in small steps of typically 15 nm respective to the outer mirror. This corresponds to a delay step size of 0.1 fs for the high-resolution spectrograms that have been used for the analysis. In all beamtimes, the direction of this movement has been chosen following the standard sign convention in the attosecond community [46]: The NIR pulse arrives first in the case of negative XUV/NIR delay values, whereas it is late for positive delays.

To capture the full range of XUV/NIR delays, where the NIR pulse with a FWHM duration of approximately 4.5 fs modulates the kinetic energy of the photoelectrons, the width of the scanned delay windows has been chosen to span at least 8 fs. Of course, this scan range has to be kept as small as possible to minimize the total duration of a single measurement, since a large number of spectrograms is needed for a statistically significant analysis and for reasons of stability. Therefore, also the integration time per delay step is an important parameter and has been set such that a good signal-to-noise ratio (SNR) and a good separability of the two photolines is ensured. For the liquid-phase measurements, the integration times are 5 s – 10 s per delay step depending on the daily alignment and XUV photon flux.

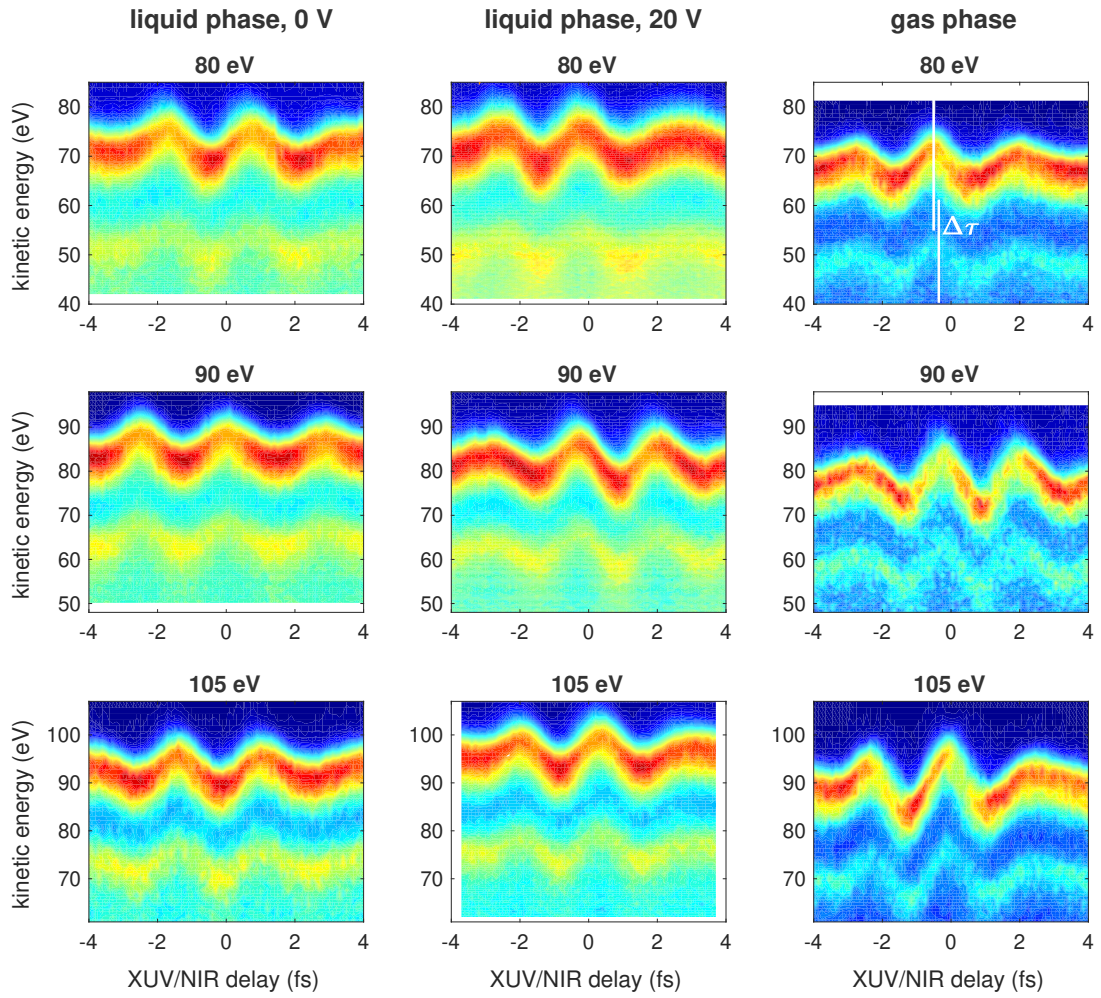

FIGURE 4.10: Measured and energy-calibrated streaking spectrograms of liquid and gaseous H_2O for all different XUV excitation energies 80 eV (top row), 90 eV (middle row) and 105 eV (bottom row). Liquid phase scans at 0 V potential are shown in the left column, those at 20 V in the middle column and the gas-phase measurements are displayed in the right column. Large chirps of the XUV pulses (see spectrogram at 105 eV, gas phase) result in narrower or more broadened photolines depending on the XUV/NIR delay. The small shift between the inner and outer valence photoline along the delay axis — i.e. the photoemission delay $\Delta\tau$ — is highlighted in the gas-phase scan at E_{XUV} = 80 eV, since the shift is largest in this spectrogram.

This corresponds to a total scan time of 8 min – 17 min per streaking trace. The measurements with 20 V potential on the jet usually required longer integration times of 8 s – 13 s per step (total time of 13 min – 22 min). For the scans in the gas phase, significantly higher integration times of up to 15 s – 22 s per step (total duration of 22 min – 37 min) have been necessary to record well evaluable spectrograms.

In figure 4.10, exemplary streaking traces are shown for each excitation energy and measurement scheme. The change of the central kinetic energy of the photolines for the different excitation energies, as well as the shift between liquid and gas phase can be observed clearly besides the modulations caused by the NIR field. Note that the shift due to the

20 V retardation potential has been accounted for during the energy calibration. In these raw spectrograms, the shift between the streaking traces stemming from inner and outer valence states along the abscissa can hardly be recognized by eye in most cases, which already suggests rather small values for the relative photoemission delay $\Delta\tau_{\mathrm{ov-iv}}$.

For a reliable extraction of these small delays, the raw spectra have been post-processed with the restricted TDSE retrieval with differential background subtraction described in section 2.1.5. There, also a normalization of the recorded intensity to the total number of detected photoelectrons at a given delay step is performed. For visualization, the raw spectrograms of a liquid and a gas-phase scan are shown in figure 4.11 together with their corresponding TDSE retrieval and the remaining difference. The difference spectrogram consists mainly of the detected background signal, but also contains small parts of the streaking signal, that could not be perfectly retrieved. Nevertheless, only weak modulations are observed in the difference spectra in most cases, speaking for a good agreement of the retrieval with the underlying data.

4.4.3 Results and Statistics

The results of the restricted TDSE fitting procedure applied to the full data set are presented and discussed in the following. To obtain a high quality of the results, some measurements have been excluded from the evaluation. Besides XUV/NIR overlap scans with low integration times and spectrograms with suddenly dropping photoelectron counts, also some scans with well-separable PE lines, enough integration time and apparently sufficient SNR are discarded if the retrieval has not converged or the merit has been too large. Nevertheless, a large number of spectrograms is taken into account for a statistically significant analysis of the photoemission delay $\Delta\tau_{\mathrm{ov-iv}}$ for the different measurement configurations, as summarized in table 4.2. Particularly for E_{XUV} = 90 eV in the liquid (0 V) and gas phase, a large number of spectrograms have been processed, as solely this configuration has been used both in the first and second beamtime. Unfortunately, only a small number of streaking scans at 20 V potential could be evaluated for 90 eV XUV excitation.

	E_{XUV} = 80 eV	E_{XUV} = 90 eV	E_{XUV} = 105 eV
H_2O liquid 0 V	35	60	42
H_2O liquid 20 V	20	16	30
H_2O gaseous	28	49	22

TABLE 4.2: Number of streaking scans taken into account for the statistical analysis for the respective target and XUV photon energy.

For a quantitative assessment, we look at the distributions of the retrieved attosecond delays $\Delta\tau_{\mathrm{ov-iv}}$ and calculate the arithmetic mean and the standard deviation for each XUV photon energy setting. The results for liquid H_2O are shown in figure 4.12 for all measurement schemes carried out within both beamtimes. Despite the large standard deviations

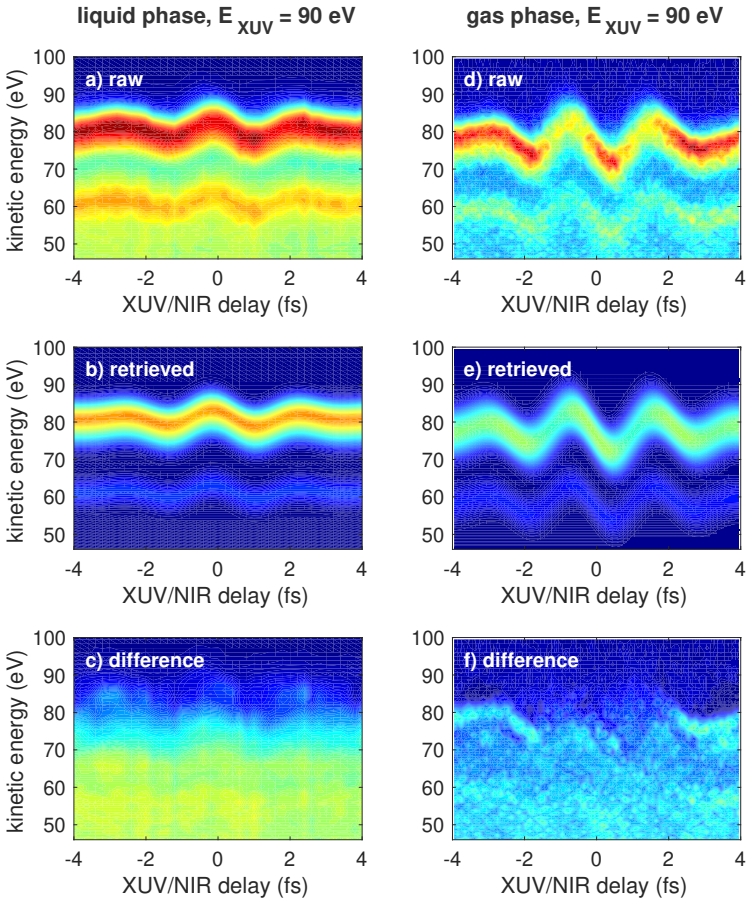

FIGURE 4.11: Comparison of liquid-phase (a – c) and gas-phase (d – f) measurements and retrievals at an XUV photon energy of E_{XUV} = 90 eV. Raw, energy-calibrated streaking scans are shown in panel a) and d) in comparison with their corresponding TDSE fits in b) and e). The difference spectra in c) and f) show a mainly time-independent background signal and also weak, modulated parts that could not be retrieved with the fit. For the liquid phase, more background signal at lower kinetic energies due to scattered electrons has to be subtracted for a proper retrieval.

particularly at E_{XUV} = 80 eV, the distributions reveal a positive value of $\Delta\tau_{\mathrm{ov-iv}}$ which implies a delayed arrival of the outer valence photoelectrons with respect to the inner valence photoelectrons. Further, a slightly decreasing trend of the delay with increasing excitation energy is observed independently of the applied potential, as visualized best in figure 4.13.

For all excitation energies, the mean delay of the measurements at 20 V retardation potential is reduced by 3 as – 5 as with respect to those at 0 V. The additional delay in the case of zero potential could be due to the non-vanishing gas-phase contribution or only an uncertainty resulting from the width of the distributions, as the mean values also match within the confidence intervals (see table 4.3). Due to the small deviations between the 0 V and 20 V data sets, we decided to merge both distributions for the respective photon energy in order to obtain a broader data basis for the liquid phase.

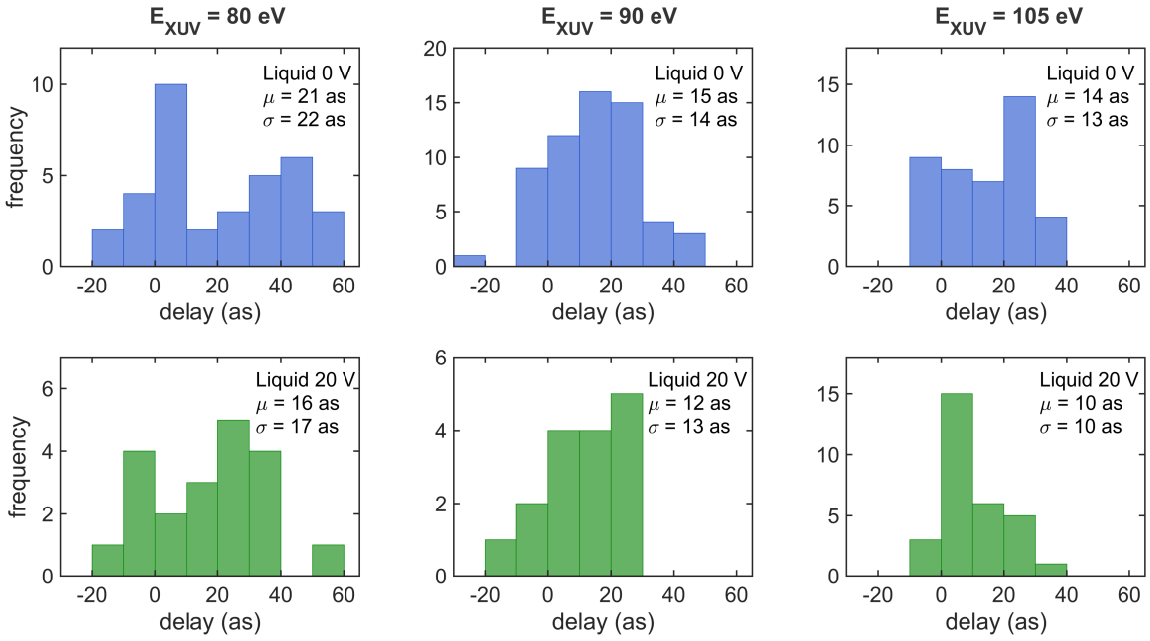

FIGURE 4.12: Distributions of retrieved attosecond delays $\Delta\tau_{\mathrm{ov-iv}}$ in the liquid phase. In the three columns, the results for 80 eV (left), 90 eV (middle) and 105 eV central photon energy of the XUV pulse are shown. The first row displays data sets without voltage applied to the jet, the second row with 20 V. The mean μ and standard deviation σ of the respective distribution are given additionally.

	E_{XUV} = 80 eV	E_{XUV} = 90 eV	E_{XUV} = 90 eV
liquid 0 V	21 (13 , 28) as	15 (11 , 19) as	14 (10 , 18) as
liquid 20 V	16 (8 , 24) as	12 (5 , 18) as	10 (6 , 14) as
liquid combined	19 (14 , 24) as	14 (11 , 18) as	12 (10 , 15) as
gaseous	31 (25 , 38) as	-1 (-6 , 4) as	9 (-2 , 19) as

TABLE 4.3: Retrieved relative photoemission delays $\Delta\tau_{\mathrm{ov-iv}}$ between outer and inner valence photoelectrons of water in the liquid and gaseous phase for all used XUV excitation energies E_{XUV}. The mean values are given together with the 95 % confidence interval in brackets.

The distributions of the combined liquid-phase photoemission delays are shown in the top panels of figure 4.14. Especially for the XUV excitation energies of 80 eV and 105 eV, the combined distributions now look more trustworthy and converge towards a normal distribution. From these, we determine the final mean values and 95% confidence intervals — given in brackets behind the mean value — for liquid H_2O of $\Delta\tau_{\mathrm{ov-iv}}$ = 19 (14 , 24) as for E_{XUV} = 80 eV, $\Delta\tau_{\mathrm{ov-iv}}$ = 14 (11 , 18) as for E_{XUV} = 90 eV and $\Delta\tau_{\mathrm{ov-iv}}$ = 12 (10 , 15) as for E_{XUV} = 105 eV.

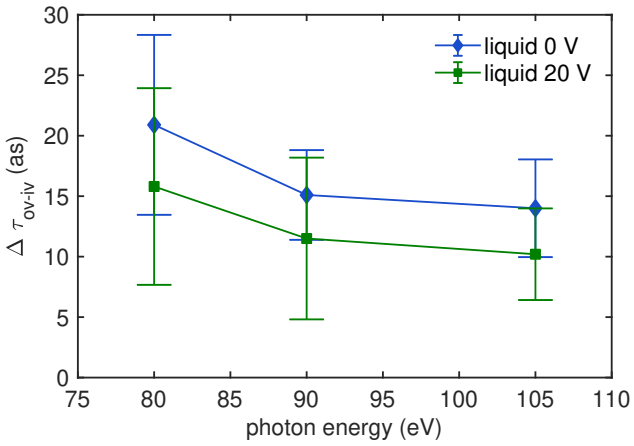

FIGURE 4.13: Mean values of the retrieved attosecond delay $\Delta\tau_{\mathrm{ov-iv}}$ versus central photon energy E_{XUV} of the excitation pulse for liquid-phase measurements with 0 V (blue diamonds) and 20 V (green rectangles) potential. The lines in between are a guide for the eyes and the error bars indicate the 95 % confidence intervals (see table 4.3).

As already discussed in the theory part of this thesis (see 2.1.5), the TDSE algorithm also retrieves the chirp of the electron wave packets, which is a consequence of the chirp of the attosecond XUV pulse. Large values for the chirp could alter the proper retrieval of the delay between the photolines. However, the retrieved chirps are quite small and do not differ significantly between the inner and outer valence band electron wave packets. Therefore, only the chirp of the ov electrons is considered to simplify the discussion. The dependence of the retrieved photoemission delays on the chirp is displayed in the bottom panels of figure 4.14. The linear trend suggests an increasing delay for a growing chirp of the ov electron wave packets. The slope of this regression is most pronounced in the case of E_{XUV} = 80 eV and decreasing for the XUV photon energies where more single measurements N have been evaluated, which implies that this dependence might originate only in a lack of more statistics. However, if we look at the intercept of the linear delay regression at zero chirp, this value is in good agreement with the mean value obtained from the whole distribution within the confidence intervals.

In a similar way as described above, the gas-phase measurements are visualized in figure 4.15. In the case of 80 eV excitation, the largest delay within all measurement settings is obtained with a value of $\Delta\tau_{\mathrm{ov-iv}}$ = 31 (25 , 38) as. In contrast, the only negative delay of $\Delta\tau_{\mathrm{ov-iv}}$ = -1 (-6 , 4) as is found at E_{XUV} = 90 eV for the gas phase. In these two cases, the delay distributions exhibit a regular Gaussian shape and the chirp dependence is negligible there. However, at E_{XUV} = 105 eV, the situation is more complicated, as the delay distribution is too structured to assume a Gaussian shape and the slope of the fitted chirp–delay correlation is quite large. Accordingly, the standard deviation of 24 as is the largest of all data sets, which might be attributed to data taken with strongly positively chirped XUV pulses (> 30 as/eV). The mean value of the photoemission delay is calculated to $\Delta\tau_{\mathrm{ov-iv}}$ = 9 (-2 , 19) as, but appears to be too large when looking at the left wing of the

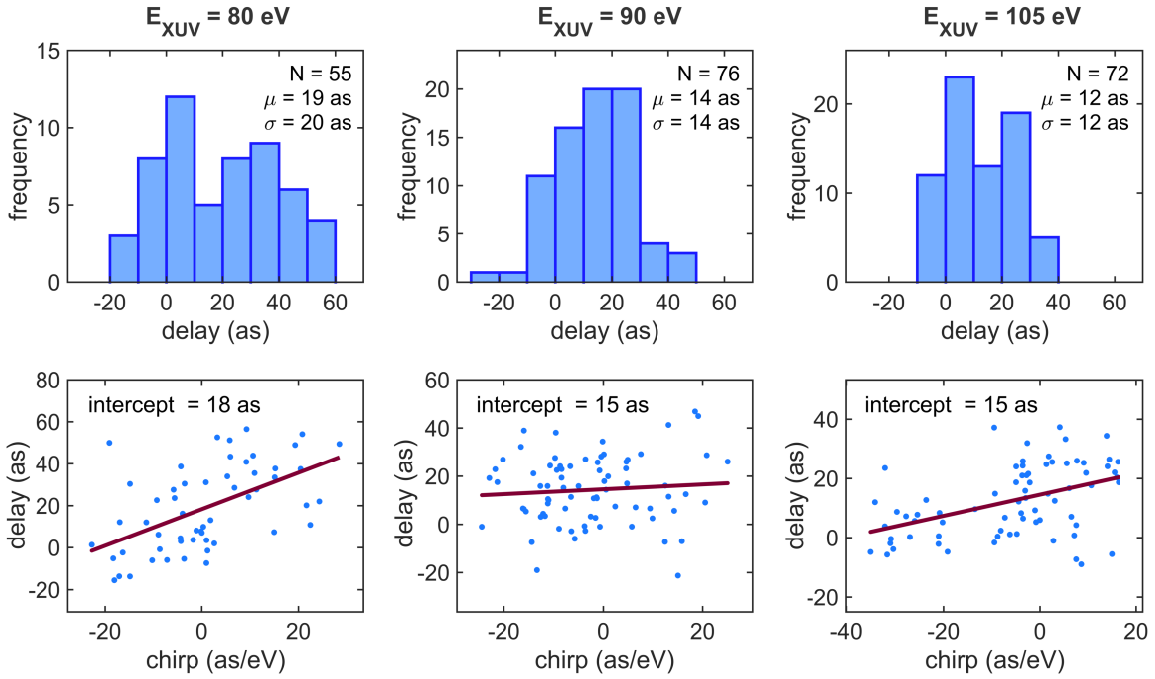

FIGURE 4.14: Top row: Distributions of retrieved delays $\Delta\tau_{\mathrm{ov-iv}}$ for the liquid phase based on the combination of 0 V and 20 V potential data sets at 80 eV (left), 90 eV (middle) and 105 eV (right) excitation energy. The total number of streaking scans N forming the respective distribution, as well as its mean μ and standard deviation σ are given in the panels. Bottom row: The retrieved delay $\Delta\tau_{\mathrm{ov-iv}}$ is plotted versus the retrieved chirp of the outer valence band for each streaking scan (blue dots). The linear regression is shown as a red, solid line and the ordinate-axis intercept of zero chirp is explicitly given in each panel. This intercept is in good agreement with the mean of the delay distributions.

distribution and the intercept of zero chirp of 5 as given by the chirp–delay linear regression. However, more data points are necessary at this excitation energy to rule out these ambiguities and get a reliable value for the photoemission delay.

In figure 4.16, the retrieved delays $\Delta\tau_{\mathrm{ov-iv}}$ of liquid and gaseous water are plotted versus the XUV excitation energy (values in table 4.3). In summary, the retrieved photoemission delays $\Delta\tau_{\mathrm{ov-iv}}$ in the liquid phase of water are very small, but definitely positive within the confidence intervals. They show a decreasing trend from 19 as to 12 as with increasing XUV excitation energy. For the gaseous phase, the energy-dependence of the delay is not simply monotonically decreasing as in the liquid phase. The delay appears to drop from a large positive value of 31 as at 80 eV excitation energy to a slightly negative value close to zero at E_{XUV} = 90 eV, and then returns to small positive values at E_{XUV} = 105 eV. This behavior is complex to describe as it relies on many energy- and angle-dependent mechanisms in the photoemission process of gaseous H_2O, giving rise to the experimentally available relative delay $\Delta\tau_{\mathrm{ov-iv}}$. In the following, a brief overview of the theoretical framework for the photoemission delay contributions in the gaseous and liquid phase is given for a discussion of the presented, novel time-resolved results on the attosecond timescale.

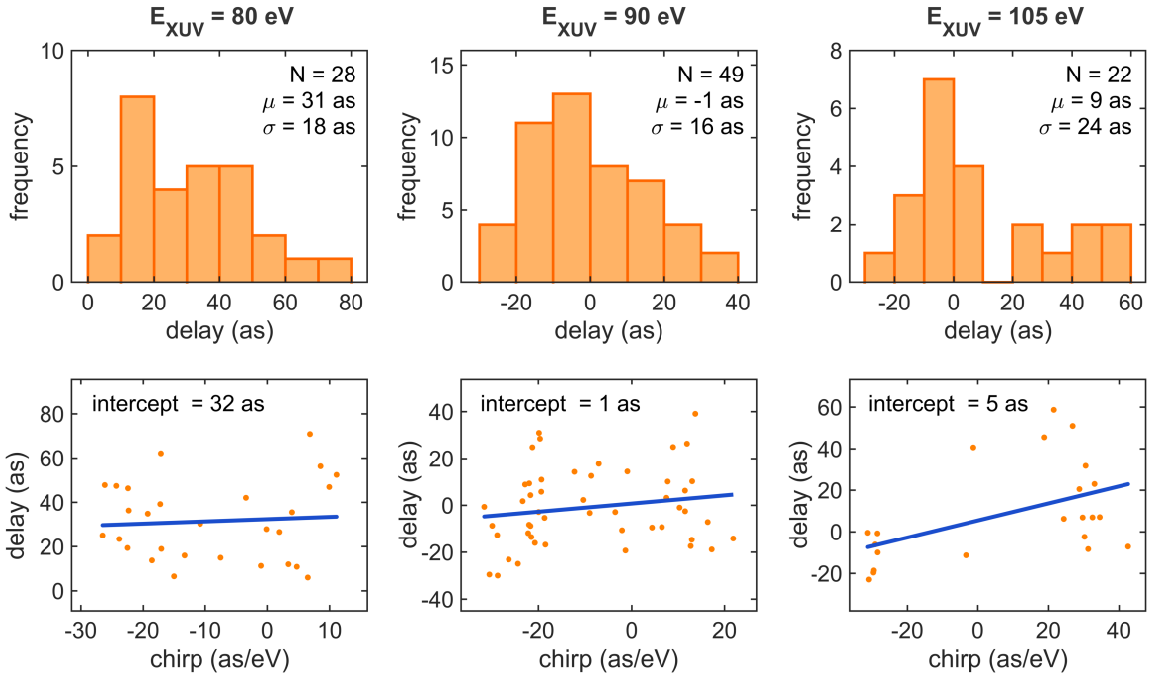

FIGURE 4.15: Top row: Distributions of retrieved delays $\Delta\tau_{\mathrm{ov-iv}}$ for gaseous water at 80 eV (left), 90 eV (middle) and 105 eV (right) XUV excitation energy. The total number of streaking scans N forming the respective distribution, as well as its mean μ and standard deviation σ are given in the panels. Bottom row: The retrieved delay $\Delta\tau_{\mathrm{ov-iv}}$ is plotted versus the retrieved chirp of the outer valence band for each streaking scan (blue dots). The linear regression is shown as a red, solid line and the ordinate-axis intercept of zero chirp is explicitly given in each panel. This intercept is in good agreement with the mean of the delay distributions.

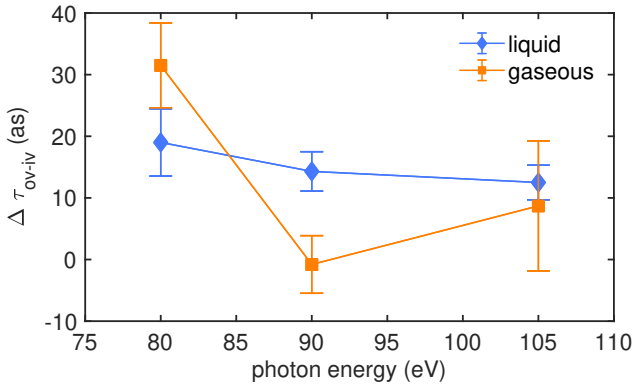

FIGURE 4.16: Mean values of the retrieved attosecond delay $\Delta\tau_{\mathrm{ov-iv}}$ versus central photon energy of the excitation pulse for the combined liquid-phase measurements (blue diamonds) and gas-phase measurements (orange dots). The lines in between are a guide for the eyes and the error bars indicate the 95 % confidence intervals.

4.5 Delay Contributions

For the interpretation of attosecond photoemission delays in the condensed phase, the local environment of the ionized molecule plays a crucial role, since the propagation of the electron is additionally strongly influenced by elastic and inelastic scattering processes [28], as well as the streaking laser field penetrating into transparent media [33, 46, 184]. As already mentioned in section 4.1.3, each elastic collision leads to a scattering delay between electrons of different kinetic energy and contributes to the total photoemission delay extracted from a streaking spectrogram, if no inelastic collision with significant kinetic energy loss occurs. In the gaseous phase, the situation is much easier, as the electron transport effects are negligible due to orders of magnitude larger mean free paths for low-density sample pressures being present in a gas-phase streaking experiment. In the following, first the molecular photoionization delays from isolated water molecules in the gaseous phase are briefly discussed, before a comprehensive overview of the additional electron transport effects in the liquid phase is given. It will be shown, that attosecond metrology in combination with Monte Carlo simulations becomes a powerful tool to shed light onto the dynamics of electron transport in water.

4.5.1 Molecular Photoionization Delays

The theoretical investigation of intra-species photoemission delays of atoms resulting from self-referenced attosecond streaking experiments has been conducted for various samples like neon [26, 185, 186] or helium [36]. Following the concept of Eisenbud, Wigner and Smith (EWS) [139], the photoionization process is treated quantum-mechanically as half-scattering event with the attractive electrostatic potential of the ionized atom. In other words, an energy-dependent phase-shift of the scattered, outgoing electron wave packets is accumulated and leads to a delayed emission of electrons with respect to the unscattered case. Additional to this EWS-delay, the effects of the streaking laser field dressing the long-range ionic Coulomb potential result in another component in the delay, known as Coulomb-laser coupling or geometric delay [36, 46]. Further contributions to the total atomic photoemission delay can occur due to electron–electron correlation effects at certain kinetic energies [36, 142].

In the case of molecular photoionization, the situation is even more complicated, as the asymmetric molecular structure leads to a strong dependence of the photoionization delay on the light polarization and the electron emission angle, as well as on molecular shape resonances resulting from quasi-bound states in the molecular potential [47, 187]. The polar linear molecule N_2O, as well as the non-linear, isolated H_2O molecule have been already studied with attosecond interferometry at low photon excitation energies (< 40 eV) to reveal the intra-species delays of different molecular states [47]. For the analysis, a rich theoretical framework has been developed by D. Baykusheva and H. J. Wörner [187] relying on comprehensive, state-of-the-art molecular scattering simulations. Whereas large delays of more than 100 as have been found in N_2O and attributed to shape resonances, the unstructured

continua of H_2O resulted in delays of comparatively small magnitude decreasing for higher photon energies. Hence, the retrieved delays from our attosecond streaking experiments also support this decreasing trend to almost zero at very high XUV excitation energies around 100 eV. A more detailed comparison of the measured delay in the gaseous phase cannot be provided yet, as the specific calculations at the Zurich group are still in progress.

4.5.2 Electron Propagation Delays in the Liquid Phase

The theoretical investigations in the relatively new field of attosecond spectroscopy in liquids have recently revealed the existence of a new mechanism in attosecond interferometry that is expected to be general to all transparent media and is mediated by the enhanced interaction of the photoelectron with the assisting NIR field inside the medium. A similar effect is also found in attosecond streaking experiments on NIR-transmitting dielectric SiO_2 nanoparticles [33], which is not present in the non-transparent samples like metals or adlayer-covered systems studied so far [23, 24, 27–29], where the photoelectrons are streaked only at the surface. These findings have shown, that the non-local interaction of generated photoelectrons with the NIR field inside the medium makes the observed, relative photoemission delays in liquid water sensitive to both, the elastic and inelastic mean free path of the electrons of different kinetic energy (see section 4.1.3).

The relevant delay contributions arising from electron propagation inside a liquid are visualized in figure 4.17. A photoemission delay contribution $\Delta\tau_{\mathrm{transport}}$ due to the different transport times of electrons of different kinetic energy has to be considered in condensed, transparent media. The transport time of photoelectrons to an elastic scattering site depends not only on the kinetic energy, but also on the distance between neighboring molecules, which is given by the EMFP or in good approximation by the next-neighbor distance in the pair correlation function $h_{\mathrm{OO}}(r)$. It reflects the mean distance of the oxygen atoms in water and is accessible with different measurement and calculation methods, but the reported values differ significantly depending on the applied technique [40]. However, these transport delays are only relevant as long as the electron is not inelastically scattered or trapped in the medium. Thus, as already implied in section 4.1.3, the transport delay is depending on the energy-dependent IMFP-EMFP-ratio $\eta(E)$, as defined in equation 4.5. Not only the electron transport between the scattering sites induces a relative photoemission delay, but also the EWS-like phase shift resulting from elastic scattering at the electrostatic potentials of neighboring water molecules. The so-called scattering delay $\Delta\tau_{\mathrm{scatter}}$ is thus also depending on the number of elastic collisions given by the ratio $\eta(E)$. However, it is still unclear, if these electron propagation delay contributions and the molecular photoionization delay can be simply added up for a comparison with the total, measured delay.

For a thorough analysis of the underlying electron dynamics, the complex, non-rigid structure of liquid water due to the highly-dynamic hydrogen bonding network is a problem. The theoretical modelling of the structure is still tedious and requires the approximation of different water clusters in the form of water polymers in different sizes [167].

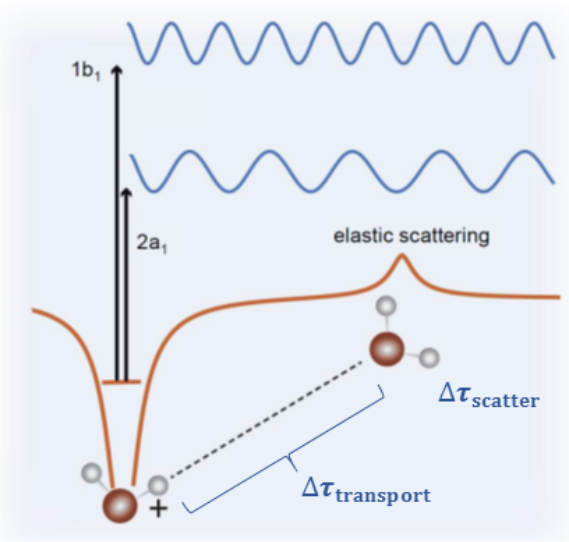

FIGURE 4.17: Relative photoemission delay contributions caused by electron propagation effects in liquids are illustrated. The transport delay $\Delta\tau_{\mathrm{transport}}$ is induced by different travel times of $2a_1$ (iv) and $1b_1$ (ov) electrons from the ionized water cation to a neighboring water molecule, where they are elastically scattered. The perturbing scattering potential induces another delay $\Delta\tau_{\mathrm{scatter}}$ in photoemission, equivalent to an EWS delay. Adapted from [46].

These are needed for carrying out time-dependent scattering calculations with reasonable computation times. It has been found, that these calculations fit best for an ideal cluster size of 6–8 water molecules [168]. The resulting, simulated differential scattering cross sections allow to calculate the according electron scattering delays. Subsequently, these results are used as an input for the sophisticated modelling of electron photoemission and propagation in the liquid using a complete 3D Monte Carlo simulation. Finally, the desired intra-species attosecond delays between the inner and outer valence molecular orbital can be calculated within these simulations. Preliminary results show a good agreement with the measured photoemission delays in the liquid phase and confirm the dependence of the delays on the IMFP and EMFP.

As soon as the Monte Carlo simulations are finalized, a thorough comparison to the measured, energy-dependent results, as summarized in figure 4.16, will be conducted. The novel application of attosecond metrology on transparent, liquid-phase samples has thus the potential to reveal accurate experimental values of the electron mean free paths in a wide range of accessible electron kinetic energies. As already stated in section 4.1.3, the currently available values of liquid water MFPs in the range of 10 eV – 100 eV differ by up to an order of magnitude [175, 180]. The results presented in this thesis will help to rule out these ambiguities and provide well-defined electron mean free path values for validating theories and models that are of greatest importance for the study of radiation damage or many other processes occurring in aqueous solution.

Chapter 5

Characterization of Femtosecond X-ray Pulses at the LCLS

Since the timescale of state-of-the-art time-resolved pump–probe experiments at X-ray free-electron laser (XFEL) facilities, such as the Linac Coherent Light Source (LCLS) at the Stanford National Accelerator Center (SLAC), already approaches the few-femtosecond regime [74, 75], it is crucial to know the time resolution that is mainly given by the duration of the involved laser pulses. As discussed in section 2.3, the temporal structure of a SASE FEL pulse varies on a single-shot basis. Thus a reliable and non-invasive technique for directly measuring the pulse shape of these ultrashort X-ray pulses with a few- or even sub-femtosecond resolution is desirable [64]. Besides X-ray pump–probe spectroscopy, it is also typical that FEL pulses are used to excite the sample and a synchronized optical laser pulse serves for probing the relaxation dynamics or vice versa. However, the synchronization of these pulses is limited by an inherent arrival time jitter resulting from shot-to-shot variations of the energy and thus the flight time of the electrons in the linear accelerator (linac) prior to the undulator [76]. As this X-ray/optical jitter is in the order of 50 fs or larger, it also influences the time resolution of experiments and complicates most direct FEL pulse characterization methods.

Despite existing, separate methods to determine the arrival time jitter [78, 79], it is desirable to simultaneously measure both, the temporal pulse shape, as well as the relative arrival time on a single-shot basis for a real-time characterization of SASE X-ray pulses in ongoing experiments. In this chapter, a method capable of reaching this goal is presented: two-color angular streaking. In a first step, the working principle of this method is summarized. To demonstrate the applicability in a state-of-the-art XFEL facility, measurements have been performed at the atomic, molecular and optical science (AMO) end station of the LCLS in 2015. With the description of the experimental setup and the different measurement schemes, an overview of the performed experiment shall be given. The subsequent data processing and evaluation in order to accomplish an online, single-shot retrieval of the FEL pulse structure is summarized. The necessary algorithm has been developed in collaboration with Rupert Heider and Dr. Wolfram Helml and a manuscript is planned to be published soon. As every single step of this algorithm and a detailed discussion of the results is conducted within the main part of the dissertation of Rupert Heider [86], only a brief summary will be given in this work.

5.1 Angular Streaking for FEL Pulse Characterization

After a brief discussion on previous works in the field of FEL pulse characterization, the fundamental idea of angular streaking is introduced in this context based on the theoretical considerations in section 2.2.

5.1.1 Previous Work

Indirect measurements of the electron bunch [188] or analyzing the spectral correlation function of the FEL pulse itself [189] have been used to determine the X-ray pulse duration, but significant deviations from the actual values have been revealed later by a two-color X-ray/optical cross correlation technique [81]. The most reliable indirect technique is the X-band radiofrequency transverse cavity (XTCAV) [190], that deflects the electron bunch time-dependently after the undulator at a zero crossing of the radiofrequency similar to a classical streak camera. An additional magnetic deflection makes it possible to record the time–energy intensity distribution of the electron bunch after the lasing process in the undulator. Energy-loss features resulting from the lasing process in the undulator are visible in these distributions and can be used to predict the time structure of the corresponding X-ray pulse, but only if a calibration run without lasing is performed in advance [143]. With a time resolution of 4 fs (rms) [191], it is however not suitable for measuring the SASE substructure of X-ray pulses or single, sub-fs X-ray pulses. The XTCAV is in user operation at the LCLS and has been used as a benchmark for the angular streaking results in [143] and [86].

The direct measurement of X-ray pulses with autocorrelation or FROG fails due to missing optics or too small cross-sections at short wavelengths. For few-femtosecond X-ray pulses, the comparatively long inherent relaxation times in condensed matter are the limiting factor in X-ray/optical cross-correlation experiments [192, 193]. Therefore, the principle of the attosecond streak camera has been applied for FEL pulse characterization using linearly polarized terahertz [80, 82] or infrared optical laser fields [81, 83] that translate the temporal properties to a shift of photoelectron distributions originating from an ionized neon gas target. This two-color streaking approach is a non-invasive measurement scheme and demonstrated retrievals of the X-ray pulse substructures with pulse durations as short as 6 fs (rms) [82] or single-spike FEL pulses with sub-fs duration [83]. However, the precise and stable time overlap of the inherently jittering X-ray pulses with the maximum slope of the linearly polarized streaking field cannot be ensured in these measurements, which leads to ambiguities in the subsequent data evaluation and a worse time resolution for many shots. In the following, it is shown, how these problems can be accounted for with a circularly polarized streaking field of suitable wavelength.

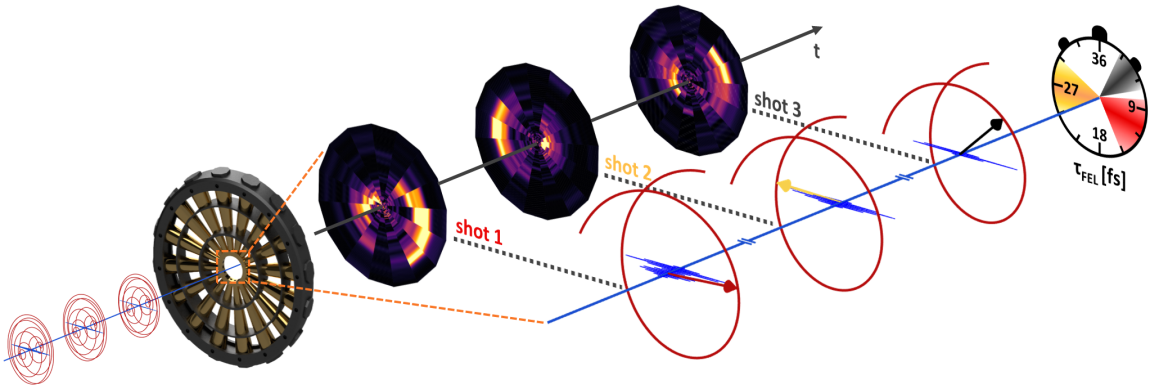

FIGURE 5.1: Schematic illustration of the angular streaking technique: X-ray pulses ionize the target gas in the center of the detector. The concomitant rotating IR laser field modifies the kinetic energy of the photoelectrons depending on their ionization time. Three individual X-ray pulses, denominated as shots 1, 2 and 3, overlap in the detection area (dashed orange rectangle, magnified picture on the right) with three IR pulses at different phases of their circularly polarized field and generate clearly distinguishable photoelectron time–energy distributions, shown as false color polar plots of experimental data. In these plots, the intensity is proportional to the number of photoelectrons, the distance from the center represents the kinetic energy of the photoelectrons, and the angle along the circle corresponds to the IR phase during photoionization by the X-ray pulse. The intensity structure and pulse duration (τ_{FEL}) of each X-ray pulse can be read from these distributions, similar to reading from a clock face. Figure and caption taken from [143].

5.1.2 The Angular Streaking Technique

As already mentioned in section 2.2, the use of a circularly polarized streaking field maps the temporal structure of an XUV or X-ray pulse into the angular spatial direction [22, 84, 85]. The continuously rotating vector potential acts like the hand of an analog clock, which exhibits a duration of one full cycle defined by the wavelength λ of the streaking field:

$$t_{\mathrm{rot}} = \frac{\varphi}{2\pi} \cdot \frac{\lambda}{c_0} \,. \tag{5.1}$$

In the two-color angular streaking experiment at the LCLS, a linearly polarized X-ray pulse ionizes the atoms of a gas target and the momentum distribution of the released electrons is shifted to the angular direction, where the vector potential of the streaking IR field points to at that distinct moment. The final kinetic energy distribution of the streaked photoelectrons is recorded simultaneously for a single X-ray shot with an array of 16 individual time-of-flight detectors in the full $360°$ angular plane perpendicular to the beam propagation. The temporal structure of the X-ray pulse is encoded in this distribution, since a phase shift within the X-ray pulse leads to a different streaking direction [84, 86]. This principle is illustrated in figure 5.1. If the streaking laser wavelength is chosen such that the time t_{rot} for one full revolution of the vector potential is slightly longer, but in the same order of magnitude as the X-ray pulse duration τ_{FEL}, the temporal structure of the FEL pulse can be retrieved on a single-shot basis (see section 2.2).

The resolution of the angular streaking technique can easily be adapted by using a different, suitable wavelength of the circularly polarized streaking field. Multiple revolutions of the streaking vector potential during the presence of a single FEL pulse should be avoided to rule out ambiguities in the data evaluation. A reconstruction of the bandwidth and chirp of the X-ray pulse is also feasible with a precision limited by the energy resolution of the spectrometer. Furthermore, also the single-shot, relative arrival time can be measured simultaneously thanks to the 2π-periodicity of the vector potential and a sufficiently long duration of the streaking IR pulse. Eventually, the angular streaking technique is able to cope with the issues mentioned in the previous section and thus is a viable tool for a non-invasive, single-shot characterization of FEL pulse properties. The resolution can be pushed to the attosecond regime and thus, also the SASE substructure becomes accessible [143].

5.2 Experimental Setup

With the proposal of angular streaking as an FEL pulse characterization technique, five 12-hour measurement periods at the LCLS free-electron laser facility at SLAC in Menlo Park, California, have been scheduled in March 2015. The experiments have been conducted within an international collaboration with roughly 25 scientists involved. After some weeks of preparation, the local infrastructure of the AMO end station has been adapted for the beamtime and the angle-resolved time-of-flight spectrometer vacuum setup, which has been shipped from the DESY (Deutsches Elektronen-Synchrotron) in Hamburg, has been assembled and aligned. After a brief summary of the specification of the LCLS, the vacuum and laser setups for the two-color angular streaking measurements are presented in this section following the detailed description in [86, 143]. The properties of the FEL and the optical lasers are given for the different measurement schemes applied.

5.2.1 The Linac Coherent Light Source

For the operation of the LCLS, one kilometer of the SLAC linac is used to accelerate electron bunches, which are created by UV laser pulses hitting a copper cathode, to energies of up to 15 GeV [60]. The electron bunches are compressed and modified along the acceleration line, before they enter a 132-m long undulator, where FEL pulses in the soft and hard X-ray regime can be generated (see section 2.3). After the undulator, the electrons are deflected and dumped, whereas the X-ray beam is guided within a large scale vacuum beamline to two different experimental halls. In total seven so-called experimental hutches with different scientific instruments are located there. An overview of the SLAC area is shown in figure 5.2, where the LCLS beamline — situated below the ground level — is highlighted. In the following, the most important parameters of the LCLS are quantified.

Compressed electron bunches with peak currents of up to 3.5 kA are guided to the undulator consisting of 33 permanent magnet segments with a length of 3.4 m and a period of $\lambda_u = 3$ cm. The created X-rays can be tuned within a photon energy range of 0.28 keV – 12.8 keV. For a typical operation mode in the soft X-ray regime (270 eV – 2 keV),

FIGURE 5.2: The aerial view of the SLAC area shows the major parts of the LCLS facility highlighted in blue. Taken from [194].

X-ray pulses with an energy of up to 4 mJ and a repetition rate of 120 Hz can be generated [60, 61]. The peak brightness (see reference [63] for definition) is approximately ten orders of magnitude larger than that of conventional synchrotrons. The SASE process and fluctuations of the electron peak current lead to an intensity jitter of 3 % – 10 % rms. The FWHM pulse duration varies between 50 fs and 500 fs, the FWHM bandwidth between 0.1 % and 0.8 % of the photon energy [61]. The full set of parameters, provided also for the hard X-ray regime, can be found in [60, 61, 86].

Since the demonstration of first lasing at the LCLS in 2009, the source has been further improved and several new operation modes have been established to meet the user requests. For this work, especially the methods for further shortening the X-ray pulses to the few-femtosecond or even attosecond regime are of high relevance. For this aim, the first of two common techniques is based on reducing the charge of the electron bunch to 20 pC, which allows for a better bunch compression, as the transverse emittance is improved and collective effects in the accelerator are weakened [61]. In this so-called low-charge operation mode, the pulse duration is shorter than 5 fs and usually consists only of one or two coherent spikes with a photon energy in the soft X-ray energy. However, one has to deal with reduced pulse energies (0.1 mJ – 0.2 mJ) in this mode [61, 188].

The second method proposed by Emma *et al.* in 2004 [195] is to insert a so-called emittance-spoiling slotted foil (see figure 5.3) into the dispersed electron bunch in the beam path of an electron bunch compressor. The parts of the electron beam hitting the aluminum foil undergo Coulomb scattering and are thus suppressed from lasing in the undulator due to the spoiled emittance. Consequently, the unspoiled time slices of the electron bunch passing the single- or double-slots in the foil lead to single or double femtosecond X-ray pulses after the undulator. Due to the V-shaped profile of the single-slot, as schematically shown

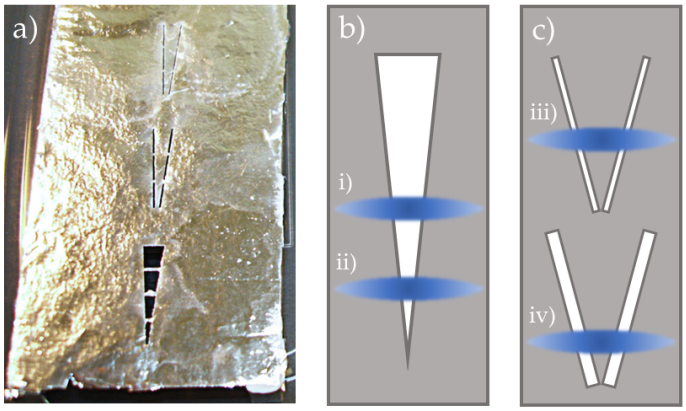

FIGURE 5.3: The emittance spoiling aluminum foil used at LCLS is shown in panel a). It is 3 µm thick and divided into three vertical divisions. The bottom part is illustrated in panel b) and the top divisions in panel c). The electron bunch hits the foil depending on the vertical insertion depth. For position i) in panel b), a single X-ray pulse of longer duration than in position ii) is obtained. For a double-pulse operation mode, the foil is adjusted to position iii) or iv) as marked in panel c). With a variation of the distance and the width of the slots, the separation and duration of the resulting X-ray double pulses can be adjusted. Taken from [86].

in figure 5.3 b), the width of the slot and thus the average pulse duration can be varied with the insertion depth of the foil from 50 fs down to 6 fs [61]. Of course, this also leads to a decrease in pulse energy of up to two orders of magnitude. Even shorter, sub-fs pulses have been observed in this configuration with the linear streaking pulse characterization technique [83]. By using the double-slotted parts of the foil (see panel c) in figure 5.3), two X-ray pulses of similar duration, but variable temporal separation between 10 fs and 80 fs can be obtained [196, 197]. With a variation of the distance of the slots, the relative delay between two X-ray pulses in pump–probe experiments can be scanned, while the resolution is determined by the width [197].

5.2.2 Vacuum and Laser Setup for Angular Streaking

As the angular streaking experiment is conducted with short pulses in the soft X-ray regime (SXR), it is performed at the AMO instrument, which is located in the first of three hutches in the Near Experimental Hall (see figure 5.2). It has been specially designed for electron and ion spectroscopy with tightly focused (as small as 1.5 μm^2) X-ray beams and high photon flux, which is a great advantage when working with X-ray pulses of low pulse energy [61, 198]. The focusing is achieved by two special, dynamically bendable SXR mirrors that allow to adjust a variable X-ray focal length and size to match the respective experimental requirements [198]. Three experimental vacuum end stations are available at this infrastructure, one of them exclusively made for X-ray/optical pump–probe experiments [61]. Nevertheless, for our experiments, a specially designed end station for angle-resolved photoelectron spectroscopy has been mounted to the existing UHV vacuum setup in the AMO hutch. This spectrometer is described in more detail in the following.

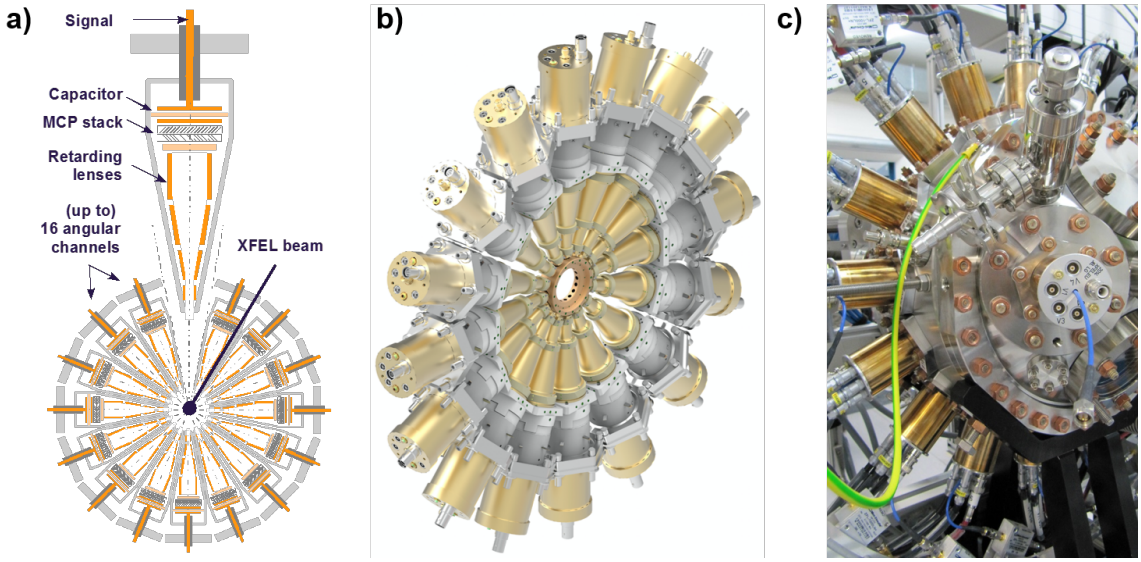

FIGURE 5.4: The spectrometer array for angle-resolved photoelectron detection is shown as a schematic illustration in panel a), as a rendered 3D drawing in panel b) and fully assembled within the UHV chamber on a photo in panel c). The evenly symmetrical arrangement around the interaction center, as well as the setup of a single TOF detector are depicted in these graphics. Adapted from [86].

Vacuum Setup for Angle-resolved Electron Detection

The custom-built spectrometer consists of 16 identical, but individually working TOF detectors that are symmetrically mounted to a UHV vacuum vessel in steps of 22.5° perpendicular to the FEL beam propagation axis. It has been designed at the DESY and European XFEL in Hamburg and is shown in figure 5.4. It has already been used for measuring the electron distributions originating from different atomic shells for determining the degree of linear polarization of an FEL beam [199]. The geometry of this spectrometer requires a compact design of the electron flight tubes, which are circularly arranged around a defined interaction center. In our experiments, the X-ray beam is focused to this interaction center with a spot size of approximately 50 µm diameter ($1/e^2$) and ionizes a dilute gas target at an ambient pressure of $4.4 \cdot 10^{-6}$ mbar [143]. There, it is additionally overlapped with the focused, circularly polarized IR laser for angular streaking, so that it is ensured that the position of both beams matches the common acceptance volume of the spectrometer array. In this way, the interaction region of the experiment is centered and an equal distance to each flight tube is achieved, which allows a simultaneous measurement of 16 angle-dependent photoemission spectra. Details on the specifications of the TOF detectors are described in the following excerpts of the methods part of our first publication concerning the angular streaking measurements [143]:

"The angular acceptance of each flight tube depends on its configurable deceleration voltage of a few to thousands of volts and has an upper limit of $3.8 \cdot 10^{-2}$ sr (corresponding to a full opening angle of 12.6° from the beam position), determined by the diameter of its entrance aperture. The detector unit uses a stack of three multi-channel plate (MCP) amplifiers with

capacitive outcoupling of the area-integrated signal. (...) Since the time of flight of each incoming electron is strictly related to its kinetic energy, the energy resolution of the method (...) depends on the actual time of flight of the recorded electrons — and is worse for shorter flight times and thus for high-energy electrons. The experimentally determined resolution amounts to better than 0.75 eV to 1 eV for the highest-energy electrons under the applied measurement conditions." [143]

Angular Streaking Laser Setup

The optical laser pulses necessary for the angular streaking experiments are provided by a Ti:Sa amplifier system and a commercial Optical Parametric Amplification (OPA) system. In the central laser facility of the Near Experimental Hall, a *Coherent Vitara*™ Ti:Sa oscillator creates laser pulses with a central wavelength of 800 nm, which are synchronized to the FEL. After a two-stage amplifier system, the pulses have an energy of 30 mJ, a duration of 100 fs and the repetition rate is reduced to 120 Hz. The 800-nm beam is guided to the AMO hutch, where it is used as input for an OPA that allows a conversion to a wavelength in the range of 4 µm – 20 µm [198]. A detailed description of the laser infrastructure can be found in references [200] and [86]. The detailed optical laser settings for our experiments are described as summarized in [143]:

"The 800-nm input is converted to 10.6 µm via difference frequency generation of signal and idler in the commercial OPA system, generating 340 fs FWHM pulses with an average pulse energy of 38 µJ. (...) A reflective phase retarder commonly used for CO_2 lasers converts the linear polarization of the OPA output to close-to-circular polarization with an ellipticity $\epsilon = 0.73 \pm 0.03$, measured as the ratio of the two half-axes of the polarization ellipse, with a tilt of $22.5° \pm 5°$ of the major half-axis with respect to the vertical detector orientation. Since the stability of the ellipticity is directly related to the inherently stable original linear polarization of the OPA and the set-up for conversion from linear to elliptical polarization was relying only on one fixed reflective optic, the ellipticity is stable within the measurement error during the experiment. A ZnSe lens of 150 mm focal length, positioned directly in front of the KBr incoupling window, focused the mid-infrared beam to a spot size of 500 µm ($1/e^2$ diameter) in the interaction region." [143]

The close-to-circularly polarized pulses have a rotation period of t_{rot} = 35.3 fs and are used to shift the angular electron distributions of a neon gas target, which is ionized by 1180-eV X-ray pulses of various average durations. The settings of the FEL for the different experimental runs and the corresponding schedule is summarized in the next section.

5.2.3 Experimental Parameters

Prior to the beamtime, the preparation of the vacuum setup and especially, the alignment of the circular polarization and the wavelength of the IR laser has been conducted. As soon as the X-ray beam was available, it was necessary to align the FEL beam to various diagnostic

systems and to find and optimize the spatial and temporal overlap of the X-ray and IR pulses using a pinhole, a knife edge and an oscilloscope with large bandwidth. Furthermore, some experimental runs with varying FEL photon energies for the accurate energy calibration of the detectors have been performed before the time-resolved measurements. The angular streaking experiments have been conducted within the last two days of the beamtime. Besides using different X-ray pulse settings, it was also intended to use electrons of different origin and kinetic energy, namely photoelectrons from the Ne 1s orbital and Ne K-LL Auger electrons. The FEL, as well as the detection parameters and the according experimental schedule are described in the following.

FEL Parameters

The FEL was run at 120 Hz, with a mean bunch charge of 150 pC, an average electron beam energy of 5087 MeV and a mean peak current of 1500 A. The electron bunch length was about 85 fs, but the effective lasing part is considerably shorter because of the emittance spoiler [143], as discussed in the beginning of this chapter. The average pulse energy of the generated X-ray pulses is only 60 µJ at a photon energy of 1180 eV. The mean X-ray pulse durations (rms) provided by the LCLS XTVAC system (see section 5.1.1) have been set to 3.5 fs, 6.5 fs and 10.5 fs by varying the vertical insertion depth of the slotted foil. In a similar way, X-ray double pulses with average separations of 20 fs and 25 fs and a single pulse duration of 3.5 fs (rms) are obtained by using the double slots in the emittance spoiling foil. For the energy calibration runs, the electron bunch charge (150 pC) and the peak current (1460 A) are slightly reduced, the IR laser is blocked and the X-ray photon energy is set to four distinct values: 1166 eV, 1180 eV, 1193 eV and 1214 eV [86].

Detection Parameters

The aim of the angular streaking technique is to determine the X-ray pulse shape for a wide range of available photon energy range at an XFEL. Thus, the measurements have not only been performed using photoelectrons, but also with secondary Auger electrons, which are emitted after a characteristic lifetime at a higher kinetic energy than the photoelectrons [40]. The non-resonant excitation of neon atoms with a photon energy of 1180 eV causes an emission of various photoelectrons from the core and also the valence shells, as well as Auger electrons with a kinetic energy independent from the X-ray excitation energy. However, the detection range of the detectors has to be adapted by changing the retardation voltage in order to preserve a proper resolution in the desired kinetic energy range.

In our case, the photoemission from the Ne 1s core orbital with a binding energy of E_b = 870.2 eV has been studied. The mean kinetic energy of these photoelectrons is given by E_{kin} = 1180 eV - 870.2 eV ~ 310 eV, but varies with the fluctuations of the photon energy in the FEL. The retardation voltage for all TOF detectors has been set to 270 V for all the Ne 1s runs accordingly. The angular distribution of the detected Ne 1s electron counts is dumbbell-shaped with minima at 0° and 180° and maxima at 90° and 270°.

This $\beta = 2$ emission anisotropy (see also 4.1.3 and [40, 169, 180]) results from the horizontal, linear polarization of the FEL beam and the spherical symmetry of the atomic 1s orbital.

For Auger K-LL electrons, the kinetic energy of the main peak is fixed to $E_{\mathrm{kin}} \approx 803.5$ eV and given by a weighted convolution of two small-linewidth Auger lines [201], since the single lines cannot be resolved with the used spectrometer array. For the Auger runs, the retardation voltage has been set to 770 V, respectively. The emission characteristics is isotropic in this case, as the Auger process results from secondary electrons and is thus independent of the polarization of the X-ray pulse.

Both detection schemes (Ne 1s or Auger) have been applied to each FEL single pulse duration setting, as well as to different FEL double-pulse settings. For all these combinations, an average of ≈ 50000 X-ray shots has been recorded per run, which corresponds to roughly 7 min per measurement. Together with the calibration runs, a number of approximately 20 runs has been evaluated within the data analysis that is summarized in the following and comprehensively presented in [86].

5.3 The FEL Pulse Retrieval Algorithm

Based on the idea of angular streaking, new data analysis procedures had to be established in order to interpret the experimental outcome. Besides a more general treatment of angle-resolved streaking in 2010 [202], also a detailed theoretical description and more sophisticated simulations have been reported after the experiments by Kazansky *et al.* in 2016 [203] and 2017 [204]. The objectives of the analysis have been to extract the temporal and spectral properties of the SASE pulses with maximum resolution, but also to develop a routine, which determines the X-ray pulse shape and duration fast enough to be used as an online diagnostic tool at high-repetition rate XFELs.

The detailed time–energy reconstruction, mentioned already in the previous parts of this thesis, has been mainly developed by Dr. Nick Hartmann and Dr. Gregor Hartmann within our collaboration. It is based on a complex projection algorithm, which delivers the temporal substructure with a precision in the attosecond timescale, as well as the spectrum and chirp of the SASE pulses. The results have been verified with a comparison to the XTCAV pulse diagnostics tool and have recently been published [143]. However, this method requires higher demands on computation time and power due to its complexity. Therefore, an alternative, simpler approach for a rougher, but much faster pulse retrieval has been pursued in our group. It is based on the angle-dependent integration of electron counts within a defined spectral range at high kinetic energies, defined by the maximum streaking-induced energy shift for one particular X-ray shot. The integrated intensity versus detection angle then mimics the X-ray pulse shape according to the angular streaking principle. In the following, the fundamental steps of data preparation and the functionality of the algorithm are presented briefly.

5.3.1 Data Processing

The raw data of the experiments are stored in large file containers consisting of the single-shot time-of-flight signals of each detector, the IR pulse energy and a variety of electron and X-ray beam parameters that are logged during the operation of the FEL. In a first usability check of the raw data of the different runs within the experimental schedule, issues regarding the signal strength and noise level of two distinct flight tubes at the detection angles 22.5° and 45° have been recognized. For the analysis of the Auger data sets, these two detectors have to be discarded. For the Ne 1s data recorded with a smaller retardation voltage, however, these two detectors could be taken into account. In contrast, two different flight tubes mounted perpendicular to the X-ray polarization (0° and 180°, vertical TOF detectors) are in the minimum of the angle-dependent, dumbbell-shaped Ne 1s photoemission pattern (see figure 5.5) and have to be left out for the according runs due to almost zero photoelectron counts at these positions. Therefore, only 14 of the 16 detectors can be considered for the further analysis of the data for both electron detection schemes.

In a first step of the analysis, a standard Wiener noise filter routine is applied to remove high-frequency electronic noise in the raw, time-of-flight signals recorded by the detectors [86]. As the fast pulse retrieval algorithm is based on integration of photoelectron counts, the normalization of the single detectors with respect to each other is a next, crucial step to obtain a similar signal level. For this, the integrated electron counts within the main peaks have been determined for each detection scheme and each flight tube using unstreaked calibration runs. These normalization values have been determined only once and are used to scale all the subsequent runs with similar detection settings assuming a constant alignment of the interaction zone during the experiments. For the Auger electrons, only small deviations from the optimum, isotropic distribution have been determined, as expected. For Ne 1s data, the obtained values are shown in figure 5.5 together with a fit of an expected, ideal photoelectron distribution ($\beta = 2$) [143] according to formula

$$\beta(\varphi) = \frac{A}{2} \cdot [1 - \cos(2 \cdot (\varphi - B))] + C, \tag{5.2}$$

where φ is the detection angle, $A = 883.7$ is the fitted amplitude, $B = 3.2°$ is the offset angle and $C = 41.9$ is a small directional emission offset [86]. The good accordance of the fit with the integrated values indicates a well-centered alignment of the spectrometer array and a good comparability in between the single flight tubes.

In a next step, the time-of-flight signals have to be converted to the energy domain. Rather different methods to find the correct energy conversion coefficients have been applied for the Ne 1s and Auger data sets. The energy of Ne 1s photoelectrons can easily be varied by adjusting the FEL excitation energy $\hbar\omega_r$, which enables an easy assignment of the time-of-flight peaks to the corresponding kinetic energy $E_{\mathrm{kin}} = \hbar\omega_r - 870.2$ eV. For calibrating the Auger data sets, single Auger lines known from synchrotron spectra [201] had to be assigned to averaged time-of-flight signals. For both electron detection schemes, the energy

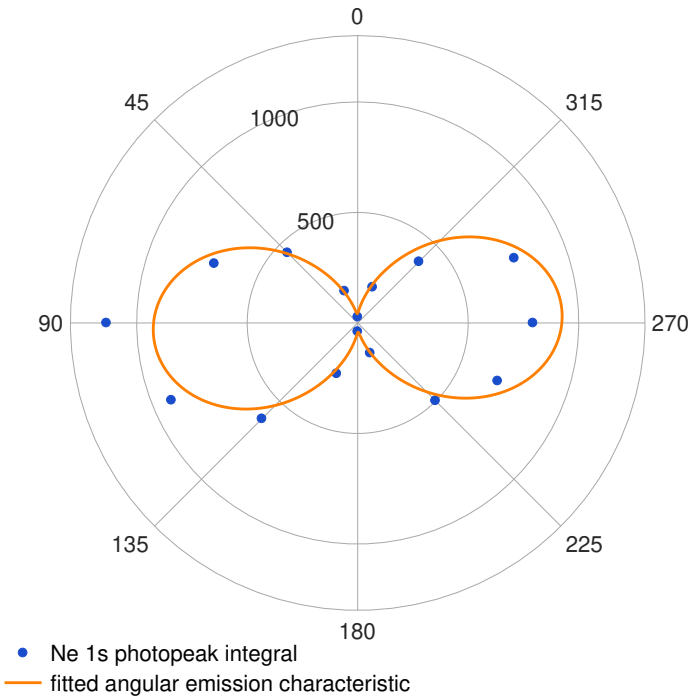

FIGURE 5.5: Angle-dependent Ne 1s peak integral values (blue dots) and fitted ideal dumbbell-shaped emission characteristic (orange line) according to equation 5.2. The linear polarization of the X-ray beam along the horizontal direction, as well as the arrangement of the detectors can be deduced from this figure. Adapted from [86].

conversion has been performed using a hyperbolic fit function, similar to the method described in section 4.3. A more detailed description of the energy calibration is left out here, as it can be found in [86], as well as in the supplementary information of [143].

After the energy conversion, unwished background signal is determined for each shot and each detector at such high kinetic energies, where no physically meaningful signal is expected. It is subtracted subsequently and negative values are set to zero. In figure 5.6, two processed Ne 1s spectrogram-like angular intensity distributions $S(E, \varphi)$ are shown for the case of an unstreaked X-ray shot, where the photoline remains at its central energy of $E_0 \approx 310$ eV with similar intensity for all detectors, and for one particular streaked shot, where the IR vector potential shifts the photoelectron distribution in the angular direction with a maximum at the detection angle of 292.5°. For the Auger data sets, the streaking effect around the central energy of the peak at $E_0 = 803.5$ eV is observed.

5.3.2 Correction of Polarization Ellipticity

As stated already before in the experimental section, the IR laser is unfortunately not perfectly circularly polarized. Consequently, the amplitude of the streaking vector potential varies periodically, which alters the strength of the streaking shift depending on the angle of detection φ. However, the ellipticity is constant and thus the change in amplitude is fixed for a distinct detection angle allowing for a correction of this effect. In order to determine

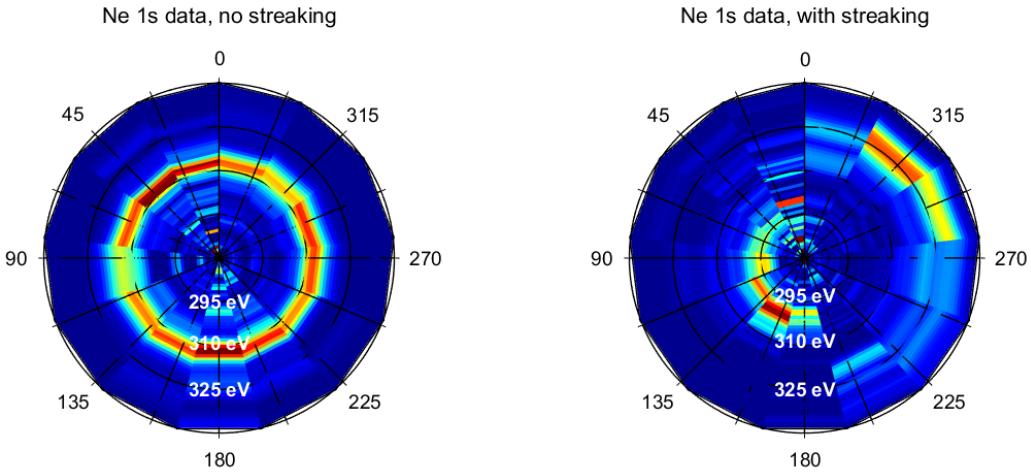

FIGURE 5.6: Single-shot, energy-calibrated and normalized Ne 1s spectrogram-like polar images $S(E, \varphi)$ recorded by the spectrometer array. The spectral intensity is color-coded and shown in a polar plot with the radial axis denoting the kinetic energy of the electrons. In the left panel, the streaking laser is blocked and the photoelectron distributions remains unaffected. In the right panel, the distribution is shifted in energy depending on the X-ray pulse structure, the relative arrival time and the corresponding streaking amplitude.

the polarization ellipse from the streaked electron distributions, a statistical analysis of the maximum detected streaking shift for each detection angle is performed. For this, first a measure for the largest shift to higher kinetic energies in a streaked photoelectron spectrum has to be defined and determined for each single shot and detector. As shown in figure 5.7 a), this so-called cutoff energy E_{cut} is defined as the energy value, where the intensity drops to 10 % of its maximum.

The distribution of the single-shot cutoff energies E_{cut} is analyzed statistically at each detection angle φ for a large number of shots within one experimental run. Looking at the high-energy side of this distribution, the energy value, where the number of occurrence has dropped to 2% of its maximum, is then identified as the overall streaking limit $E_{\mathrm{ell}}(\varphi)$ for a specific detection angle. This procedure is schematically illustrated in figure 5.7 b) and c) for two perpendicular detectors in a Ne 1s experimental run.

For each single experimental run, the angular distribution of $E_{\mathrm{ell}}(\varphi)$ represents the shape and orientation of the elliptical polarization of the IR streaking laser field (shown in the appendix A.2.1). In the following, the normalized polarization ellipse, defined by

$$P_{\mathrm{ell}}(\varphi) = \frac{E_{\mathrm{ell}}(\varphi)}{\max(E_{\mathrm{ell}}(\varphi))}\,, \tag{5.3}$$

is used for an angle-dependent correction of the streaking shift. In order to reduce errors in the further analysis due to noise in the high-energy parts of the spectra, we introduce the following constraint: A shot is discarded, if only one of the determined, angle-dependent cutoff energies $E_{\mathrm{cut}}(\varphi)$ is larger than the corresponding overall streaking limit $E_{\mathrm{ell}}(\varphi)$.

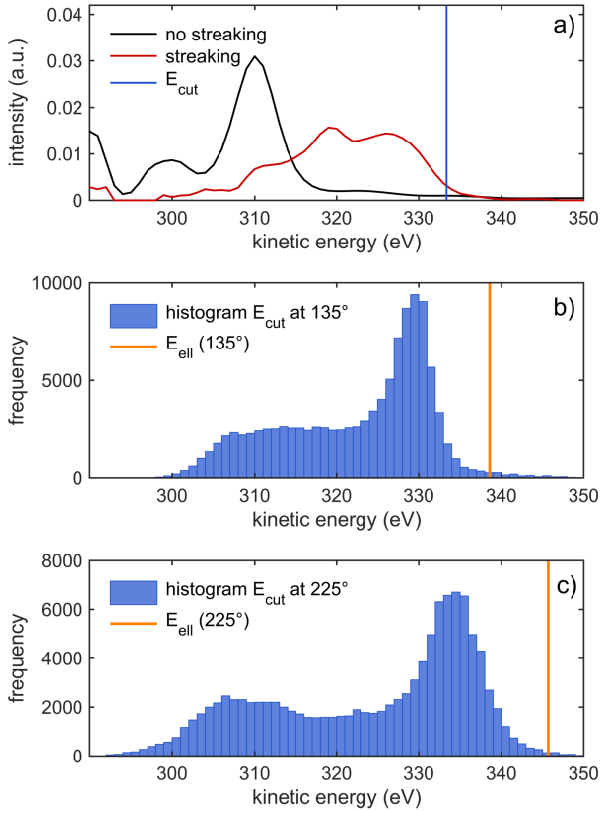

FIGURE 5.7: In panel a), single-shot Ne 1s spectra recorded at one specific detection angle in the unstreaked (black line) and the streaked, energy-upshifted case (red line) are shown. The blue line marks the cutoff energy E_{cut} of the streaked spectrum. In the bottom panels, the distribution of single-shot cutoff energies E_{cut} for all the shots of one experimental run are plotted in a histogram for the two perpendicular detection angles 135° in panel b) and 225° in panel c), respectively. The orange line marks the overall streaking limit E_{ell} for the corresponding detection angle in this run, as defined in the main text.

With the determined normalized polarization ellipse for one run, the actual correction of the elliptical polarization is performed for each single X-ray shot in this run, by calculating the angle-dependent maximum streaking shift according to

$$E_{\mathrm{shift}}(\varphi) = \frac{E_{\mathrm{cut}}(\varphi) - E_0}{P_{\mathrm{ell}}(\varphi)} \,, \tag{5.4}$$

where E_0 is the central energy of the Ne 1s or the Auger peak, when no streaking laser is applied. $E_{\mathrm{shift}}(\varphi)$ is just an auxiliary variable for determining the maximum, ellipse-corrected energy shift a_{ell} within all detectors for every single shot:

$$a_{\mathrm{ell}} = \max\left(E_{\mathrm{shift}}(\varphi)\right) . \tag{5.5}$$

The so-called streaking kick a_{ell} depends on the actual amplitude of the envelope of the streaking laser pulse, which varies from shot to shot due to the arrival time jitter of the X-ray pulse and is the most relevant parameter for the calculation of the X-ray arrival time (detailed derivation in the appendix A.2.2) and for the temporal pulse structure retrieval.

It can be understood as an equivalent to the variable $\bar{\sigma}$ in the complex time–energy retrieval (see section 2.2). In the following, it is used as a scaling factor for obtaining the single-shot upper energy limit in the case of angular streaking with the calculated elliptical polarization $P_{\mathrm{ell}}(\varphi)$:

$$E_{\mathrm{up}}(\varphi) = a_{\mathrm{ell}} \cdot P_{\mathrm{ell}}(\varphi) + E_0 \ . \tag{5.6}$$

The streaking kick ellipse $E_{\mathrm{up}}(\varphi)$ is thus a measure for the maximum energy that is detected at a distinct angle, if the streaking vector potential pointed to this angle at the moment of ionization and the single-shot streaking kick is taken into account.

5.3.3 Retrieval of Pulse Structure

For the retrieval of the FEL pulse structure, we make use of the fact that the number of generated photoelectrons is directly proportional to the X-ray intensity at a given time $I_{\mathrm{X-ray}}(t)$ [205]. The temporal intensity profile of an X-ray pulse can thus be obtained by summing up the photoelectron counts in the corresponding, preprocessed streaking spectrogram-like polar images $S(E, \varphi)$ (see figure 5.6) in a defined ellipse-corrected integration window in the cutoff energy range. The width of the window has to be chosen sufficiently broad in order to neglect integration of noise and hence, to get a meaningful value for the X-ray intensity $I_{\mathrm{X-ray}}(t)$. However, one must take into account that even within the cutoff energy range of a certain detector, a significant part of the signal results from electrons that are energy-shifted by projections of the streaking vector potential pointing to angles in the vicinity of the detector under consideration during the presence of the X-ray pulse. In order to avoid these projection effects and thus to ensure a good resolution of the X-ray pulse structure, the integration window has to be set as narrow as possible. In the following, the derivation of the integration window for the pulse retrieval is presented and schematically illustrated for one particular shot in figure 5.8.

Using the streaking kick ellipse $E_{\mathrm{up}}(\varphi)$ as defined above, we define the angle-dependent, low-energy border of the integration window with

$$E_{\mathrm{low}}(\varphi) = E_{\mathrm{up}}(\varphi) - w_{\mathrm{int}} \ , \tag{5.7}$$

where

$$w_{\mathrm{int}} = \left(1 - \cos\left(\frac{\pi}{5}\right)\right) \cdot a_{\mathrm{ell}} \tag{5.8}$$

is the width of the integration window, which also varies on a single-shot basis depending on the streaking amplitude given by a_{ell}. A projection angle coverage of $\pm\, \pi/5$ rad or $\pm\, 36°$ is considered with the prefactor in the definition of the integration width w_{int} and thus in the lower integration border $E_{\mathrm{low}}(\varphi)$. With this choice, the angular resolution can be estimated to roughly one and a half times the separation between adjacent detectors (22.5°) in each direction. As discussed above, the angle coverage constitutes a compromise between a well-defined integration result and an optimum angular resolution, which directly translates into time resolution according to the angular streaking principle [86].

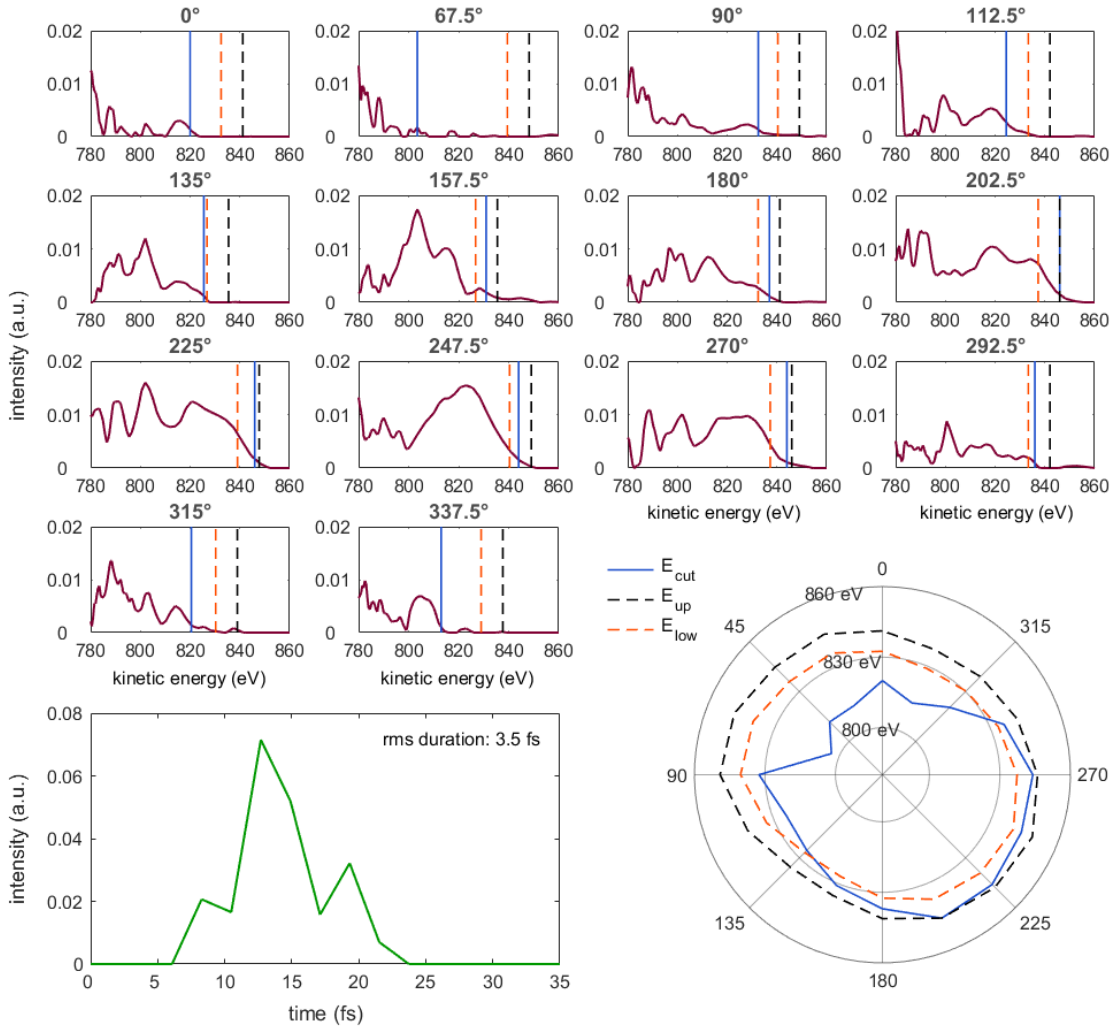

FIGURE 5.8: Demonstration of the FEL pulse retrieval working principle using one exemplary shot from an Auger data set. The top panels show the streaked spectra (red lines) of the 14 individual detectors that have been recorded simultaneously for this shot. The calculated, angle-dependent energy values $E_{\mathrm{cut}}(\varphi)$ (blue line), $E_{\mathrm{up}}(\varphi)$ (black, dashed line) and $E_{\mathrm{low}}(\varphi)$ (orange, dashed line) are marked. These values are displayed additionally in the panel at the bottom, right position in form of a polar plot. The maximum streaking shift at a detection angle of 202.5° is clearly visible. The resulting X-ray intensity $I_{\mathrm{X-ray}}(\varphi)$ is then obtained by integrating the spectral intensity $S(E,\varphi)$ in the range between $E_{\mathrm{low}}(\varphi)$ and $E_{\mathrm{cut}}(\varphi)$, as long as $E_{\mathrm{cut}}(\varphi) > E_{\mathrm{low}}(\varphi)$, whereas it is set to zero in the opposite case. By employing the angular streaking principle, the angle axis is mapped to a temporal axis. The resulting FEL pulse structure $I_{\mathrm{X-ray}}(t)$ is shown in the bottom, left panel. This shot is made up from three SASE spikes and its rms duration is determined to 3.5 fs. Adapted from [86].

According to the definition of the single-shot and angle-dependent cutoff energy $E_{\mathrm{cut}}(\varphi)$, it is the best suitable upper border of the integration window, as the spectral intensity exceeding the cutoff energy can be mainly attributed to noise. Consequently, the integration of spectral intensity for the X-ray pulse retrieval is performed within $E_{\mathrm{low}}(\varphi)$ and $E_{\mathrm{cut}}(\varphi)$, if $E_{\mathrm{cut}}(\varphi) > E_{\mathrm{low}}(\varphi)$, whereas the integral is set to zero else. With the translation from

detection angle to time according to equation 5.1, the temporal X-ray pulse profile can be finally obtained from an angular streaking spectral photoelectron distribution $S(E, \varphi)$ by:

$$\begin{aligned} I_{\mathrm{X-ray}}(t) = I_{\mathrm{X-ray}}\left(\frac{\varphi \cdot \lambda}{2\pi c_0}\right) \sim \int_{E_{\mathrm{low}}(\varphi)}^{E_{\mathrm{cut}}(\varphi)} S(E,\varphi)\, dE \quad &, \quad E_{\mathrm{cut}}(\varphi) > E_{\mathrm{low}}(\varphi) \\ I_{\mathrm{X-ray}}(t) \;=\; 0 \qquad\qquad\qquad\qquad\qquad\quad &, \quad E_{\mathrm{cut}}(\varphi) < E_{\mathrm{low}}(\varphi)\,. \end{aligned} \tag{5.9}$$

With this method, the single-shot X-ray pulse structures for a single run can be retrieved relatively simply and fast, as the main input parameters are the normalized polarization ellipse $P_{\mathrm{ell}}(\varphi)$ and the streaking kick a_{ell}. The presented algorithm is supported by a recently published theoretical description by Kazansky *et al.* [204], where a similar method for an angular streaking pulse reconstruction based on the integration of spectral intensity in the vicinity of the cutoff energy is presented. The best possible time resolution of the retrieval is limited to 2.2 fs, determined by the fixed detector spacing of 22.5° and the IR laser rotation period of 35.3 fs. In contrast, an upper limit of 3.5 fs is derived from the 36° projection angle coverage, as discussed above. Therefore, we assume a mean value of 2.85 fs, situated between these limits, for the temporal resolution of the integration algorithm in the following [86].

The whole retrieval procedure can be employed on single and double X-ray pulse settings for both, the Ne 1s and Auger data sets. For the single X-ray pulse runs, the duration of the retrieved X-ray pulses is of great interest, as it can be directly compared to the provided LCLS estimates. Due to the rich substructure of the SASE pulses, the pulse duration is determined by calculating the rms width of the reconstructed temporal intensity profiles $I_{\mathrm{X-ray}}(t)$ instead of a FWHM duration, which is usually applied for Gaussian-shaped, ultrashort pulses. For the analysis of the FEL double-pulse runs, the algorithm has to be additionally extended with a peak finding routine that is employed to the retrieved pulse structures. In that way, the duration and the separation of the two individual pulses within a single X-ray double-pulse shot may be determined. A comprehensive description of the double-pulse extension of the algorithm, as well as the presentation of the corresponding results can be found in [86].

5.4 Results and Discussion

For a demonstration of the capabilities of the previously described integration algorithm, it has been employed to various data sets with different, nominal X-ray pulse durations. The resulting temporal profiles, as well as the arrival time of the FEL pulses are analyzed statistically in the following. As a benchmark of the obtained results, the speed and the robustness of the reconstruction algorithm are discussed subsequently.

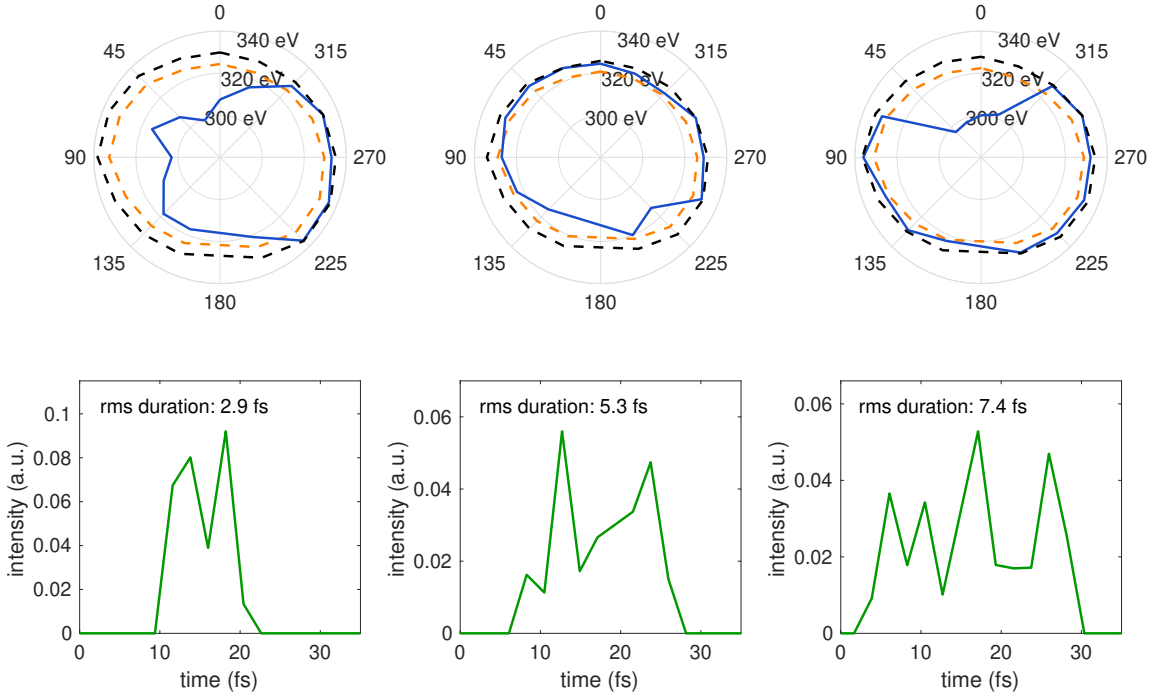

FIGURE 5.9: Pulse retrievals of exemplary X-ray pulses of three experimental single pulse runs with different pulse duration estimates are compared. In the top panels, the measured cutoff energy $E_{\mathrm{cut}}(\varphi)$ (blue line) and the integration algorithm-related variables $E_{\mathrm{up}}(\varphi)$ (black, dashed line) and $E_{\mathrm{low}}(\varphi)$ (orange, dashed line) are shown. The spectral intensity in between the orange and blue line delivers the corresponding temporal pulse structures that are shown in the bottom panels. Adapted from [86].

5.4.1 Statistical Evaluation of Different Experimental Runs

As already described in section 5.2.3, the pulse duration estimates of the FEL have been varied and three different settings in the few-femtosecond regime have been used for angular streaking of either Ne 1s photoelectrons or Auger electrons. In figure 5.9, the polar illustrations of the pulse retrievals and the resulting temporal profiles are shown for three exemplary shots. These are chosen from different Ne 1s data sets with nominal pulse duration estimates of 3.5 fs, 6.5 fs and 10.5 fs. The reconstructions clearly reveal the spiky substructure of the SASE X-ray pulses. The calculated rms duration increases with the number of SASE spikes and it becomes obvious that a FWHM definition of the pulse duration would be misleading.

In a next step, the single-shot integration algorithm is applied to ten thousands of X-ray pulses within the different data sets. The distributions of the determined rms pulse duration and the corresponding mean are shown in figure 5.10. The congruency of the nearly Gaussian-shaped histograms and the similarity of the mean values in between the two electron detection types is substantial. This proves the flexibility and robustness of the underlying algorithm despite small deviations from the LCLS estimate values for the average pulse duration (3.5 fs, 6.5 fs and 10.5 fs).

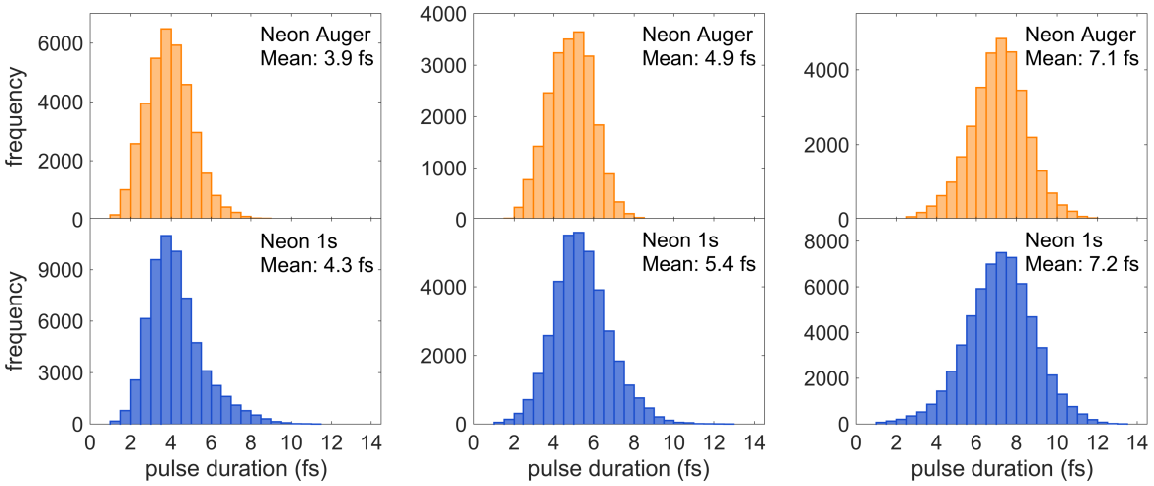

FIGURE 5.10: Distributions and corresponding mean values of the determined rms pulse durations for different FEL settings and detection schemes. From the left to the right panels, the LCLS pulse duration (rms) estimates are increasing from 3.5 fs over 6.5 fs to 10.5 fs. The top panels show the histograms retrieved from the Ne Auger, the bottom panels those of the Ne 1s data sets. Adapted from [86].

These results clearly confirm the expectations that the temporal substructure and the pulse duration vary significantly from shot to shot within one distinct FEL setting. With our single-shot analysis technique, the highly desired temporal characterization of FEL pulses can be realized with a resolution of about 2.85 fs, as discussed above. Due to the non-invasive measurement scheme and the simplicity of our thresholded integration algorithm, the presented pulse characterization technique has the potential to be used as a standard diagnostics tool at FEL facilities. However, for an improvement of the time resolution of X-ray pump–probe experiments, not only the pulse duration is crucial, but also the relative X-ray arrival time. This important quantity can be also determined with our method by means of a transformation of the streaking kick a_{ell} to the relative arrival time within the well-known envelope of the streaking IR laser pulse. The detailed procedure to determine the arrival time can be found in the appendix A.2.2.

The outcome of the arrival time retrieval is illustrated for two exemplary experimental runs in the top panels of figure 5.11. The analysis of all Auger runs yields an average arrival time jitter of 56 fs, which is in very good agreement with the results presented in [143]. The bottom panel of figure 5.11 displays the arrival time and pulse duration for 20 consecutive X-ray shots emphasizing the single-shot applicability of our pulse retrieval method. In that way, few-femtosecond time-resolved X-ray experiments can be realized by implementing the temporal substructure into the analysis and appropriate sorting for only the shortest X-ray spikes. In the following, the capabilities of the integration algorithm are further evaluated and discussed.

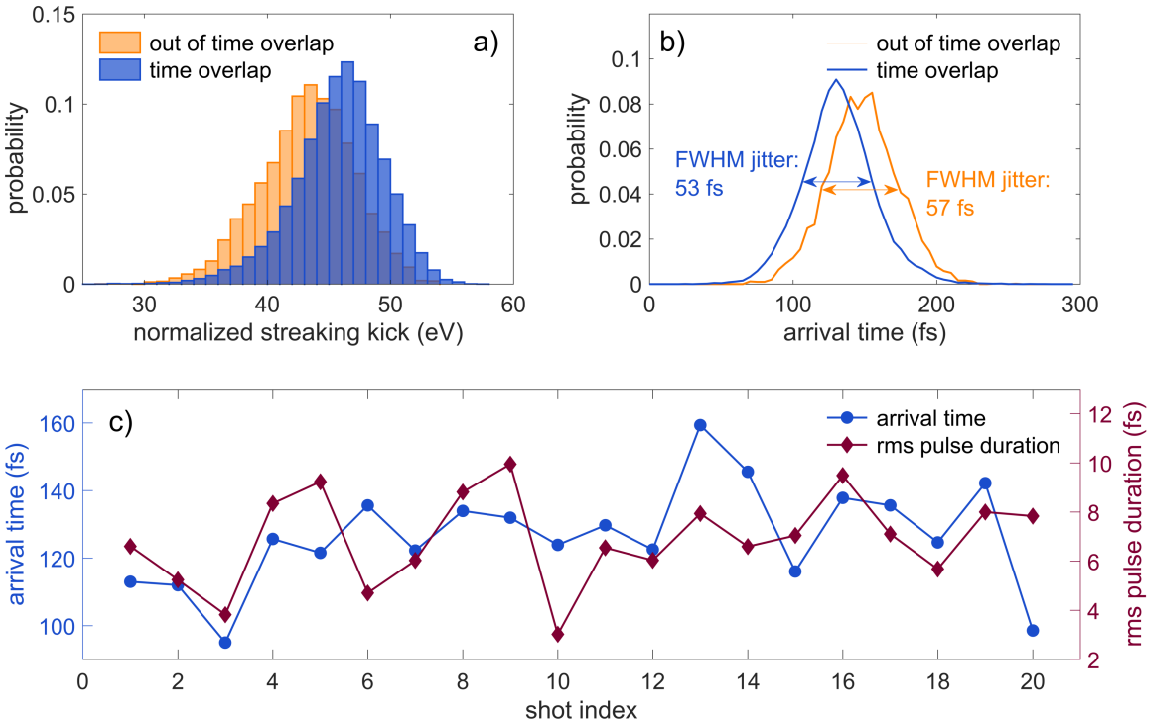

FIGURE 5.11: The relative X-ray/optical arrival time is retrieved from the single-shot streaking kick a_{ell}. The IR intensity-corrected streaking kick distribution is shown in panel a) for two different data sets, where the time overlap between the IR and the X-ray pulse has shifted. The resulting change of the IR streaking amplitude leads to an overall energy shift of the streaking kick distribution. The energy shift is larger for a better time overlap, as the amplitude of the streaking field is maximum at the center of the streaking laser pulse. By using an X-ray/IR overlap scan for a calibration, the streaking kick can be mapped to the arrival time of the X-ray pulse, as shown in panel b), where the relative arrival time is given with respect to the maximum of the IR streaking laser pulse envelope. The width of these distribution allows a determination of the arrival time jitter. In panel c), a random series of 20 consecutive X-ray shots is characterized regarding the arrival time (blue dots) and the pulse duration (red diamonds). Adapted from [86].

5.4.2 Evaluation and Discussion

As discussed before, the results of the integration algorithm are consistent for both electron detection settings and are in good agreement with the provided pulse duration estimates from LCLS. However, to fully validate the reliability of our algorithm, the retrieved pulse profiles have to be further scrutinized. This is realized via a comparison to a well-established pulse characterization method. Thus, we applied the already approved and published complex time–energy reconstruction method [143]) to a full Ne 1s data set, so that a direct comparison on a single-shot basis is feasible. The comparison of both retrievals is shown for exemplary shots in figure A.7 in the appendix. A remarkable congruence of the pulse shapes reconstructed by the complex method and those retrieved by the integration algorithm is observed for these exemplary shots. Also the according rms pulse durations show a reasonable agreement. A detailed, statistical analysis of the comparison is extensively presented in [86] and further corroborates the robustness of the integration algorithm.

Therefore, it can be concluded, that the integration algorithm reliably reproduces the results of the powerful time–energy retrieval with reduced resolution, but with orders of magnitude larger speed. Hence, the applicability as real-time pulse characterization tool has become the unique feature of the integration approach. The aim of a further acceleration of the integration algorithm has been pursued in order to emplace the angular streaking pulse characterization technique as online diagnostics tool also for next-generation, high-repetition rate FEL facilities like the European XFEL with 2.7 kHz [206] or LCLS-II with up to 1 MHz [86, 207]. As described comprehensively in [86], it has been accomplished to optimize the speed of the underlying code by further simplifying the necessary mathematical operations and by translating it from MATLAB™ to the programming language C. On a standard 3.6 GHz workstation, the final version of the algorithm exhibits a runtime of 0.47 µs per shot, which corresponds to a speed of 2.1 MHz.

The angular streaking measurement technique in combination with the presented integration algorithm has thus the potential to be applied as a non-invasive, online diagnostic tool at upcoming MHz-repetition rate XFEL facilities, since the X-ray pulse profiles and also the arrival time can be recorded dependably with a few-femtosecond resolution for each single shot. Used as a smart veto logic, a real-time shot sorting for only the shortest X-ray pulses is feasible, which improves the time resolution of X-ray/optical pump–probe experiments accordingly and helps to reduce the huge amount of data, that has to be processed and stored at high rates. As discussed in [86], not only single X-ray pulses can be studied, but also an extension of the algorithm to a characterization of X-ray double pulses is achieved, which further facilitates high-repetition rate X-ray-pump–probe experiments.

Chapter 6

Conclusion

In the course of this thesis, three major projects, contributing to an advancement of photoelectron streaking spectroscopy, have been realized. The first basic step has been to plan and build up a novel, state-of-the-art attosecond spectroscopy facility at the TUM. Having accomplished this task, the newly developed AS101 experimental beamline had to prove its operability with unprecedented attosecond streaking experiments in the liquid and gaseous aggregate states of water, which have been conducted within a collaboration with the group of Prof. Wörner at the ETH Zurich. Intra-species attosecond photoemission delays of a liquid sample could be determined for the first time in the course of this second project. With a participation at a beamtime at the LCLS X-ray free-electron laser, a third project has emerged that aimed to improve the capabilities of single-shot X-ray pulse characterization by means of employing angle-resolved streaking spectroscopy. The outcome of all these projects — with an emphasis on the attosecond beamline and the photoemission studies in H_2O — is summarized and concluded in this chapter.

Attosecond metrology has evolved to an important spectroscopic tool for the investigation of a large variety of samples and thus, the number of suitable experimental facilities has steadily increased during the last decade. Based on the expertise gathered during this process, a novel beamline for attosecond spectroscopy has been established and optimized with several innovative devices and functionalities. One of these parts is the differentially pumped, conjugated-gradient hollow-core fiber system, which has been newly designed and dimensioned specifically to the output of a commercial, state-of-the-art Ti:Sa amplifier system. This laser source has been installed in September 2015 and from then on routinely operated, maintained and also partly improved. The output of the 3-m long, helium-supplied fiber system has been optimized to a power transmission of up to 60 %, and a nearly Gaussian-shaped supercontinuum spectrum spanning from 400 nm to roughly 1000 nm has been achieved. In combination with an in-vacuum pulse compressor consisting of only two chirped mirrors and a pair of thin wedges, nearly single-cycle NIR pulses with a duration as short as 2.9 fs and a remaining pulse energy of roughly 1 mJ could be generated. These are then available as driving pulses for the HHG process and subsequently for time-resolved (streaking) experiments, which may be alternately performed in two different attosecond high-vacuum experimental setups, one of which is the AS101 beamline. It consists of a high harmonic generation chamber, an XUV spectrometer unit and an UHV end station, which is equipped with a specially designed double-mirror delay assembly and

an advanced TOF detector. All these single devices have been thoroughly reconsidered and optimized regarding the aspects of usability, stability, versatility and throughput. Measurements to characterize the novel beamline using the XUV spectrometer and photoelectron streaking measurements in neon demonstrated the capabilities to produce isolated XUV pulses with durations of several hundreds of attoseconds and photon energies ranging from 80 eV to 160 eV. In a nutshell, we have commissioned a flexible and stable attosecond spectroscopy setup that can be routinely operated by only one scientist in daily business. In 2017, attosecond streaking measurements with gaseous iodine-helium mixtures have been successfully conducted at this beamline. The measured photoemission delays have contributed to reveal the absolute timing of the photoelectric effect in tungsten and iodine [37].

The first demonstration of attosecond streaking at the AS101 beamline, however, has been already accomplished in 2016, only one year after the buildup process had begun. We have achieved the milestone of applying attosecond streaking spectroscopy to liquid samples — for the first time — using an alternative vacuum end station specially designed at the ETH Zurich for this purpose. With a liquid microjet, a thin water filament embedded in an UHV environment is created and used as a target for the ionizing attosecond XUV pulse and the streaking NIR pulse. A large number of streaking spectrograms could be obtained within only two short measurement periods thanks to the comparatively fast acquisition times at the AS101 beamline. With an advanced retrieval algorithm and a thorough statistical analysis of the data sets, the relative photoemission delays of the inner with respect to the outer valence band electrons for both, liquid and gaseous H_2O has been studied on the attosecond timescale. Monotonically decreasing photoemission delays for increasing photon excitation energies have been found for liquid-phase water. The final mean values with 95% confidence intervals — given in brackets behind the mean value — for liquid H_2O are determined to $\Delta\tau_{\mathrm{ov-iv}}$ = 19 (14 , 24) as for E_{XUV} = 80 eV, $\Delta\tau_{\mathrm{ov-iv}}$ = 14 (11 , 18) as for E_{XUV} = 90 eV and $\Delta\tau_{\mathrm{ov-iv}}$ = 12 (10 , 15) as for E_{XUV} = 105 eV. The gas-phase results suggest a more complicated energy dependence with a delay as large as $\Delta\tau_{\mathrm{ov-iv}}$ = 31 (25 , 38) as for E_{XUV} = 80 eV and delays close to zero at higher photon energies: $\Delta\tau_{\mathrm{ov-iv}}$ = -1 (-6 , 4) as for E_{XUV} = 90 eV and $\Delta\tau_{\mathrm{ov-iv}}$ = 9 (-2 , 19) as for E_{XUV} = 105 eV.

In order to gain insights into the underlying electron dynamics of the respective H_2O aggregate states, the physical origin of these delays in the photoemission process has to be further scrutinized. Whereas the gaseous phase delays contain only contributions from the molecular photoionization process itself, it is essential to consider additional effects arising from the electron transport through the dense environment in the liquid phase. Moreover, the interaction of the photo-generated electrons with the infrared field during propagation in the medium has to be taken into account due to the NIR-transparency of liquid water. Very recent theoretical calculations on the molecular photoionization delays performed in our collaborating group in Zurich reproduce the measured delays for the gaseous phase, since substantially small delays with a tendency to zero are predicted for

increasing excitation energies. In order to simulate the liquid-phase delays, the energy-dependent elastic and inelastic differential cross sections, as well as a recently discovered non-local interaction scheme with the NIR field [33, 184], are additionally incorporated into the model in the form of advanced 3D Monte Carlo simulations. Preliminary results already show good accordance with the measured photoemission delays in the liquid phase and confirm the dependency of the delays on the EMFP and IMFP of water. The combination of attosecond metrology in liquid H_2O and these state-of-the-art simulations thus paves the way for providing reliable electron mean free path values, which are to date only available with high uncertainties of up to an order of magnitude.

In addition to these fundamental spectroscopic studies in liquid H_2O accomplished with the streaking technique, also an important, more technical application of this method for the purpose of SASE X-ray pulse characterization has been elaborated within this thesis. In this vein, the idea of two-color angular streaking has been realized experimentally at the LCLS. Hereby, a linearly polarized X-ray pulse and a circularly polarized streaking laser are applied to generate angle-dependent photoelectron spectra, which are simultaneously recorded by a special spectrometer array covering the whole 360° detection plane perpendicular to the beam propagation axis. The temporal profile of a single X-ray pulse is encoded in these angle-resolved spectrogram-like intensity distributions. Due to the novelty of this experimental technique, new methods to retrieve the pulse properties have been developed in order to investigate the stochastically varying substructure of SASE X-ray pulses.

A self-programmed algorithm is applied to numerous data sets acquired for the different measurement schemes, either using neon 1s photoelectrons or secondary Auger electrons, and varying X-ray pulse duration settings. The developed routine allows to determine both, the temporal pulse profile by a thresholded integration of spectral intensity in a well-defined high-energy range, and the relative arrival time between the X-ray and optical pulse. These quantities can be retrieved on a single-shot basis and with an average resolution of 2.85 fs, given by the fixed wavelength of the streaking IR field and the detector spacing. The determined rms pulse durations of the FEL pulses, as well as the arrival time jitter are in good accordance with the estimates from already existing, indirect diagnostics tools. The integration algorithm has been additionally validated with a comparison of the retrieved pulse shapes to those reconstructed by a complex time–energy retrieval with sub-fs resolution, which has been developed in parallel within the collaboration and has recently been published [143]. In contrast to this precise, but time-consuming reconstruction, our algorithm is relying on simpler and faster mathematical operations. Thus, the runtime per X-ray shot could be minimized to roughly half a microsecond. In summary, the SASE X-ray pulse shapes and also the relative arrival time could be retrieved simultaneously, reliably and rapidly with a few-femtosecond resolution. Altogether, a versatile, single-shot FEL pulse characterization method at state-of-the-art XFEL facilities could be demonstrated.

Chapter 7

Outlook

The results obtained in this work, as summarized in the previous chapter, give rise to further perspectives in the field of attosecond metrology in general and more particular, for the investigation of electron transport in liquids, aqueous solutions and ice. Furthermore, future applications of the developed angular streaking pulse characterization technique and possible extensions are elucidated in the following, final chapter of this thesis.

With the availability of the novel AS101 beamline at the TUM, several interesting new projects requiring isolated attosecond pulses can be initiated. For this aim, the versatility of the UHV end station, originally designed for gaseous samples, is a great advantage. A rotatable 3D sample manipulator can be mounted to the chamber and in that way, attosecond spectroscopy at amorphous, crystalline or multilayer solid-state samples can be realized. The first time-resolved experiments on tungsten oxide WO_3 and iron oxide α-Fe_2O_3 in form of compressed powder pellets are conducted at the moment and an extension to homogenous or heterogeneous mixtures of both materials is planned for the near future. These studies aim at the first determination of the ultrashort lifetimes of photo-excited electron–hole pairs in order to improve electron transfer rates in photocatalytic reactions. In this way, the efficiency of charge separation processes in the context of light-to-chemical energy conversion may be improved. Solid-state samples requiring very clean surfaces can also be employed in a second attosecond beamline with a specially designed extreme ultra-high vacuum preparation and spectroscopy end station. This second experimental laboratory will also be operated with the few-fs NIR pulses after the HCF compressor using a large-scale beam transport system. The commissioning is currently in progress and first experiments, for example on graphene, will be conducted soon. Both beamlines provide a flexible and state-of-the-art infrastructure with the capabilities to further push the frontiers of attosecond streaking spectroscopy.

The first measurement of attosecond photoemission delay in the liquid phase of water and the attribution of the obtained results to electron scattering dynamics opens up a new field of photoemission spectroscopy. These unprecedented results in combination with sophisticated 3D Monte Carlo simulations allow to extract the electron mean free path values of H_2O. Thus, a more comprehensive picture of the non-rigid, hydrogen-bonded structure of liquid water can be drawn. These quantities are urgently required for the validation of theories and models that are of greatest importance, i.e. for the study of

radiation damage or many other fundamental processes occurring in aqueous solution. Many chemical reactions and nearly all biological processes take place in liquid water and aqueous solutions. These facts motivate to systematically examine how the aqueous environment modifies the electronic dynamics of a solute on the one hand, and how the solute influences the dynamics of electron transport through the liquid phase on the other hand. Furthermore, it is planned to employ a series of solvated halogen anions with different surface affinity for investigating the manifestation of their depth profiles in the attosecond delay measurements, as well as to study the photoionization delays of a range of small molecules like methanol or ethanol, which form hydrogen bonds of different strengths with water. Not only aqueous solutions are an interesting subject for further scrutinizing the electron transport dynamics in the condensed phase, but also the solid phase of water in the form of hexagonal or amorphous ice. For a direct comparison with the liquid-phase results, the photoemission delays between the inner and outer valence band of ice shall be determined using the same XUV excitation energies. Those two structures exhibit characteristic pair correlation functions, which suggests a difference in the electron transport delays $\Delta\tau_{\mathrm{transport}}$ arising from the varying distances of the scattering sites. Moreover, similar attosecond streaking studies on two different isotopes of water — D_2O and $H_2{}^{18}O$ — are planned. These allow to scrutinize the influence of the scattering cross sections on the photoemission delay by selectively changing the mass-charge ratio of the water molecules. Thus, a systematical investigation of the scattering delay contribution $\Delta\tau_{\mathrm{scatter}}$ in the different isotopes becomes feasible. With this variety of further photoelectron streaking studies, we will be able to reveal a more holistic picture of the attosecond photoemission dynamics in all different aggregate states of water.

The application of angular streaking in the field of FEL pulse characterization also gives rise to some further developments based on the results presented in this thesis. Due to the non-invasive, single-shot measurement scheme and the high-speed integration algorithm, an online diagnostic tool for upcoming XFEL facilities with X-ray pulse repetition rates up to 1 MHz may be realized. Hence, the SASE X-ray pulse shapes and also the relative arrival time can be recorded simultaneously and reliably with few-femtosecond resolution in parallel to ongoing experiments. Used as a smart veto logic, an online pulse sorting for only the shortest X-ray pulses becomes feasible, which directly leads to an improvement of the time resolution of X-ray pump–probe experiments. This helps to reduce the huge amount of data, which has to be processed and stored at high rates. In future beamtimes, it is planned to experimentally prove the applicability of the angular streaking technique for characterizing also hard X-rays with even shorter SASE spikes forming the temporal shape of the pulse. This will be accomplished by changing the target gas and decreasing the wavelength of the circularly polarized streaking field, which reduces the rotation period of the angular streaking clock. Hereby, the flexibility and adaptability of the angular streaking method shall be demonstrated in order to establish it as a standard diagnostics unit with adjustable time resolution and suitable for a wide range of possible X-ray photon energies.

Appendix

A.1 Setup of the AS101 Beamline

A.1.1 Pictures of the Laboratories

Additionally to the beam paths and the panorama photo shown in chapter 3, some photos of the renovated, empty rooms (figure A.1), as well as the fully equipped laser laboratory (figure A.2) and experimental beamline (figure A.3) are shown here. A complete 3D CAD model of the AS101 beamline at its current status is shown in figure A.4.

FIGURE A.1: Empty laboratories directly after the renovation. Both pictures are taken with a view from the central laser laboratory. In the upper panel, the future experimental laboratory of the AS101 beamline can be seen in the background. In the lower panel, the precision air conditioning system is shown at the right and the second experimental laboratory can be seen in the background.

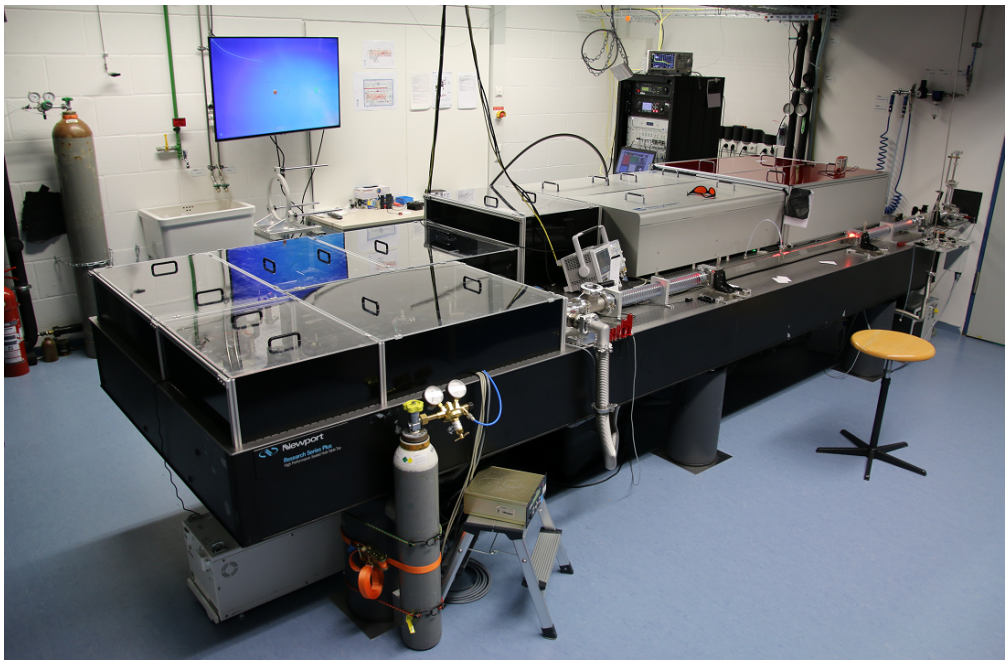

FIGURE A.2: Photo of the laser laboratory. The commercial MOPA system is enclosed within the silver housings in the background. The grating compressor, as well as the beam stabilization and focusing optics are enclosed in the black housing in the front. The hollow-core fiber is situated next to the silver housings.

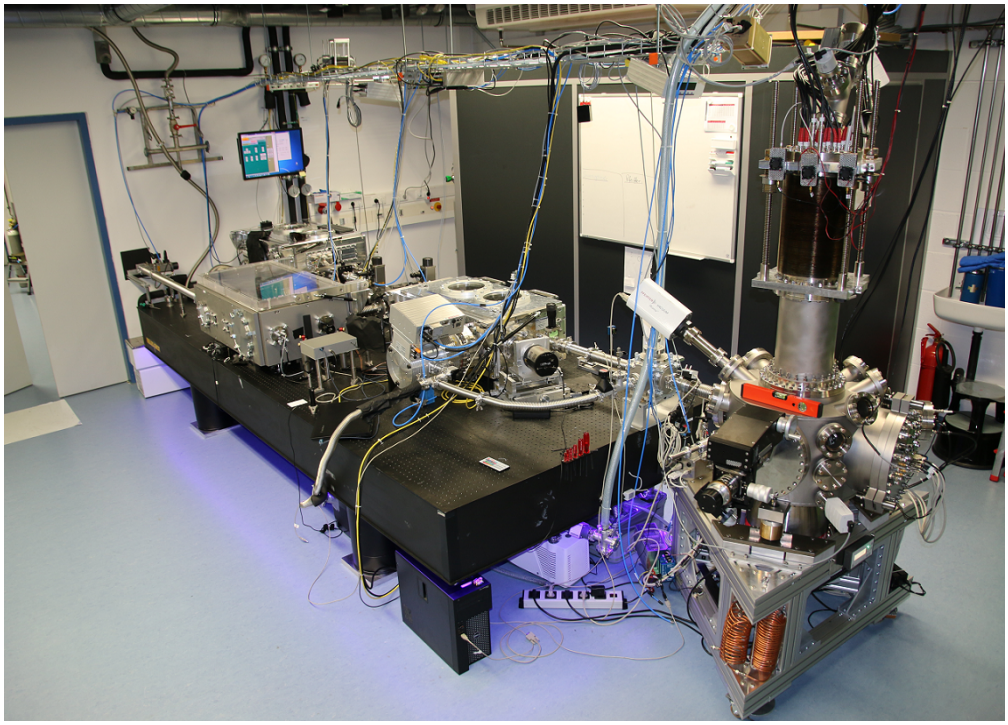

FIGURE A.3: Photo of the experimental AS101 vacuum beamline. In the left part, the pulse compression chamber, as well as the HHG generation and diagnostics units can be seen. The end station of the beamline with the large-scale TOF detector on top is situated next to the laser table. In the background, the black dirt sluice can be seen.

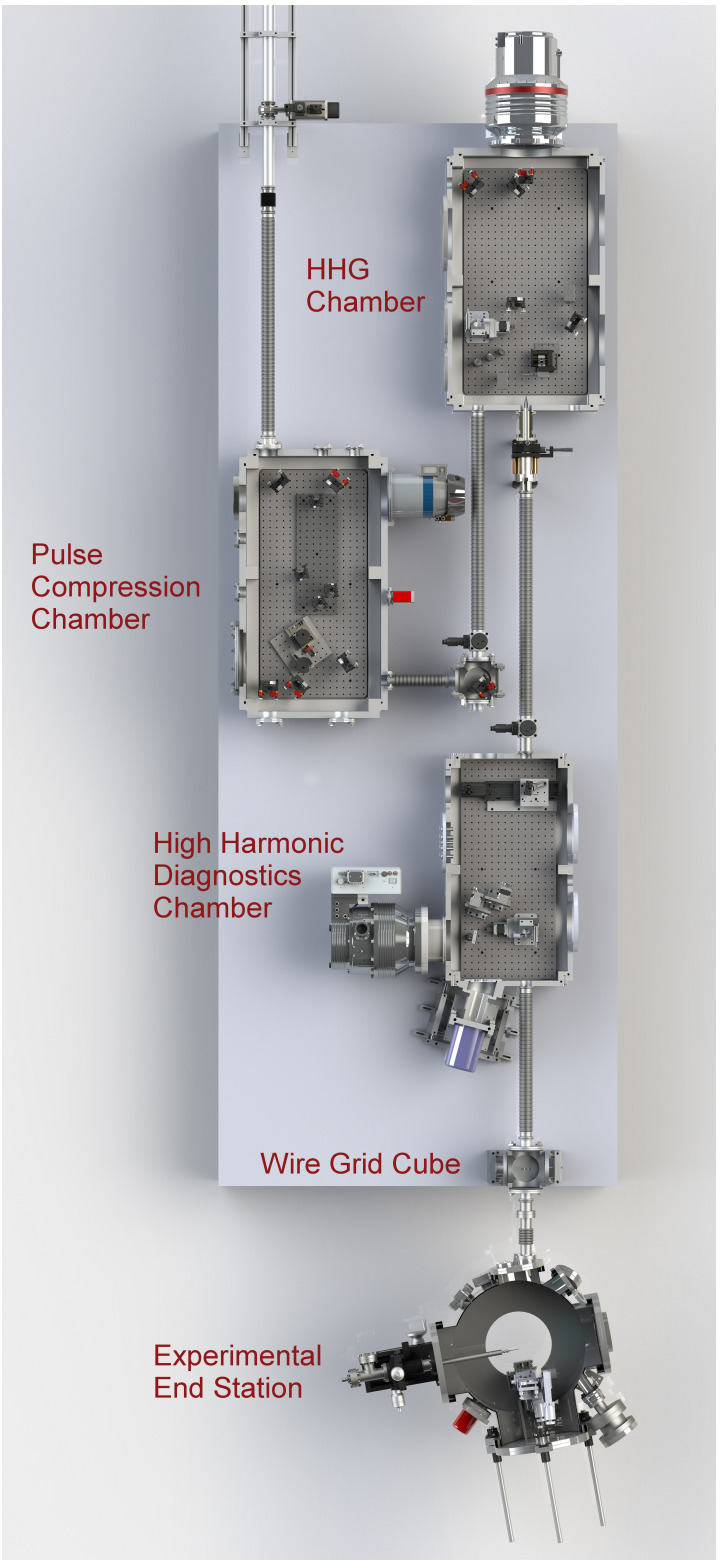

FIGURE A.4: CAD Model of the AS101 XUV vacuum beamline in the experimental laboratory. In this illustration, the beam is entering the pulse compression chamber via the vacuum bellow at the top. Subsequently, it is guided through the HHG chamber, the diagnostics chamber and the wire grid cube to the target interaction zone in the experimental end station. Credits: Andreas Duensing, Chair for Laser and X-ray Physics, Technical University of Munich.

A.1.2 Description of the FEMTOSOURCE™ rainbow™ oscillator

In the following, a detailed description of the FEMTOSOURCE™ rainbow™ oscillator is given, as this device is the fundamental source of CEP-stabilized, femtosecond laser pulses, which are used subsequently in the AS101 beamline. The beam path is illustrated in figure A.5.

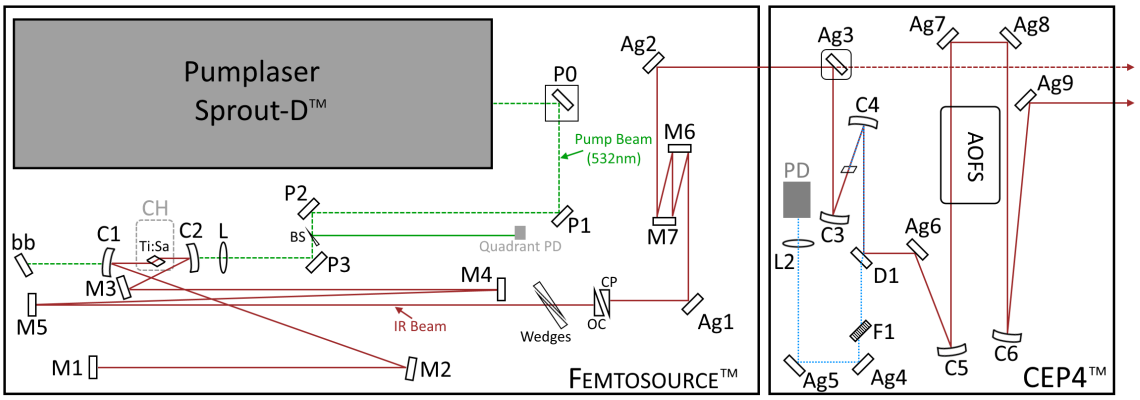

FIGURE A.5: Beam path of the FEMTOSOURCE™ rainbow™ oscillator and the additional CEP4™ SEED CE-phase stabilization unit [107, 208]. The beam path in the CEP4 module has been simplified in this scheme. The abbreviations and the functionality are explained in the main text.

The *Lighthouse Photonics Sprout-D* is a frequency-doubled, diode-pumped Nd:YVO_4 laser and serves as pump source for the oscillator. It is operated at an output power of 3.5 W. With the mirrors P0–P3 and a lens (L), the pump beam is guided and tightly focused into the Ti:Sa active medium and is then stopped by a beam blocker (bb). The crystal holder (CH) is thermally stabilized with cooling water that also cools the whole base plate of the oscillator. A temperature sensor and a heating element allow an even more precise control of the crystal temperature. The pump beam can be stabilized actively with the motorized mirror (P0) and a quadrant photodiode that detects the beam pointing using the reflected parts from a beam splitter (BS). The generated, broadband NIR light oscillates in a resonator consisting of a short arm (M1, M2, C1) and a long arm (C2, M3, M4, M5, OC). C1 and C2 are curved mirrors for focusing the NIR beam into the crystal. The plain mirrors M1 – M5 are negatively chirped and ensure the compensation of dispersion that is introduced by air and the active medium. Additional dispersion control is obtained by two wedges in the resonator placed in Brewster angle geometry. One wedge can be moved parallel to the other, which allows a precise tuning of positive dispersion within the resonator.

The output coupler (OC) is one end mirror of the cavity and transmits a part of the oscillating NIR beam, which is the usable laser output. It is wedged with an angle of 10° at the outer side to prevent unwished back reflections into the cavity. The subsequent compensation plate CP is placed for avoiding angular dispersion. M1 is the other end mirror and is mounted on a linear stage for tuning the resonator length. The stage can be moved by a piezo for introducing a small disturbance, which is triggering the self-mode-locking

of the cavity. More details on the mechanisms of Kerr-lens mode-locking can be found in reference [147] and any modern textbook dealing with ultrafast optics. The silver mirrors Ag1–Ag9 are guiding the NIR beam with the central wavelength of 790 nm and a spectral width of more than 300 nm most efficiently. M6 and M7 are compensating the positive chirp of the output coupler. The mirror Ag3 can be removed to bypass the CEP4™ module. There, a typical output power of 290 mW – 300 mW is measured in the mode-locked operation.

For obtaining a beat signal depending on the carrier-envelope offset frequency f_{CEO}, the NIR beam is focused into a periodically poled lithium niobate (PPLN) crystal, where the difference frequency of the NIR beam is generated and the frequency combs of the fundamental and the difference frequency are mixed in a 0-to-f self-referencing scheme [149–151]. The beat signal (blue dotted line in figure A.5) is passing the dichroic mirror D1 and is then adequately filtered (F1) and focused (L2) onto a photodiode.

The main portion of the NIR beam is reflected by D1 and focused into an acousto-optic frequency shifter (AOFS), which enables to modify the dispersion properties of a birefringent crystal with acoustic waves [152]. Following the feed-forward method [153], the detected carrier-envelope offset frequency is then subtracted from the frequency comb of the NIR beam in the AOFS. This is the so-called fast loop CE-phase stabilization, as it offers the compensation of short-term variations. The fast loop is working only in a small frequency range and therefore, further stabilization mechanisms are necessary, such as feedback loops that adjust the crystal temperature or change the amount of dispersion in the cavity by moving one of two wedges. An additional CEP stabilization mechanism is implemented after the amplification stages. After recollimation of the beam with the curved mirror C6, the train of pulses with stable and constant CE-phase is coupled out and guided to the amplifier system. Due to substantial losses in the PPLN crystal and the AOFS, the power after the CEP4™ unit is reduced to approximately 100 mW corresponding to a pulse energy of E_{pulse} =1.4 nJ.

A.2 Additions to the FEL Pulse Retrieval Algorithm

A.2.1 Elliptical Polarization

The angular shape and orientation of the overall streaking limit $E_{\mathrm{ell}}(\varphi)$, as defined in section 5.3.2 of this thesis is shown in figure A.6 for the different evaluated experimental runs and both electron detection schemes. The similarity of these ellipses confirms the proportionality of the overall streaking limit $E_{\mathrm{ell}}(\varphi)$ to the polarization ellipticity of the IR laser. It should be noted that a sligthly different and more sophisticated method for the determination of the Ne 1s polarization ellipses has been applied, which is described thoroughly in [86].

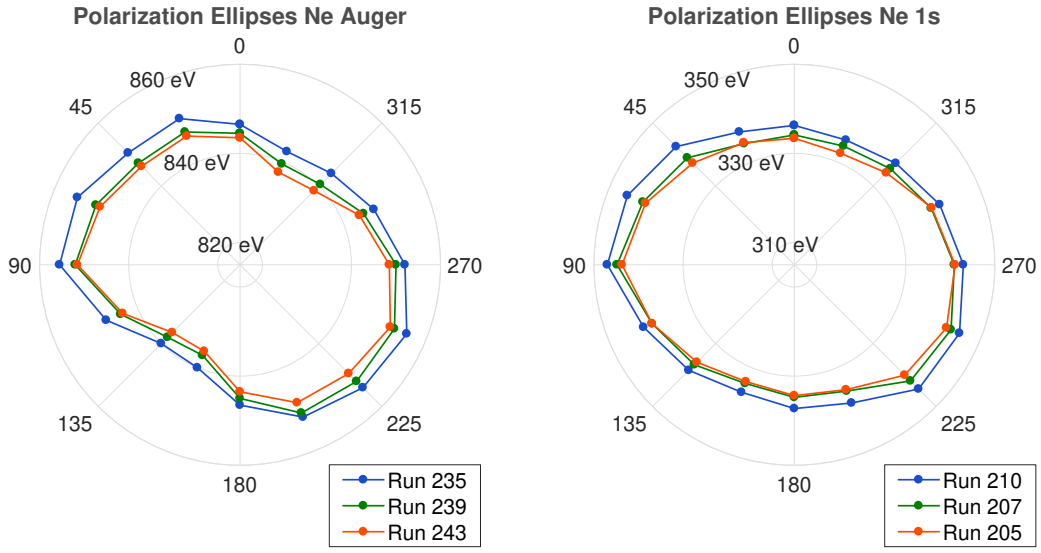

FIGURE A.6: The angle-dependent overall streaking limit $E_{\mathrm{ell}}(\varphi)$ is plotted for different experimental runs within the Auger data sets (left panel) and the Ne 1s data sets (right panel). With a normalization of these ellipses to their respective maximum, the shape and orientation of the elliptical polarization is identified (see equation 5.3) and found to be similar for the analyzed runs. Adapted from [86].

A.2.2 Arrival Time Calibration and Determination

In the following, the single steps to derive the arrival time of X-ray pulses from the single-shot parameter a_{ell}, which is determined in the integration algorithm, are presented. As already mentioned in section 5.3.2, the strength of the streaking energy shift depends on the relative temporal overlap of the FEL pulse with respect to the maximum of the envelope of the IR streaking laser pulse and is thus a quantity, that varies from shot to shot due to the inherent arrival time jitter. The streaking field is characterized by an IR/X-ray delay overlap scan, which yields an IR pulse duration of τ_{IR} = 480 fs (see also [143]). In the retrieval presented in chapter 5, the determined streaking kick a_{ell} represents the single-shot energy shift. Consequently, the variations of the streaking amplitude due to the arrival time jitter are mapped to a distribution of the streaking kick according to

$$a_{\mathrm{ell}} = E_{\mathrm{max}} \cdot \exp\left(-\frac{t_{\mathrm{arrival}}^2}{2\left(\frac{\tau_{\mathrm{IR}}}{2.35}\right)^2}\right) . \tag{A.1}$$

The strongest streaking shift E_{max} = 58 eV is also extracted from the overlap scan and reflects the maximum streaking kick induced by the maximum of the IR laser field envelope. Shot-to-shot power fluctuations of the IR laser have been recorded together with the experimental data and are used to normalize the streaking amplitude. Thus, the arrival time can be determined with the expression

$$t_{\mathrm{arrival}} = \sqrt{-2 \cdot \ln\left(\frac{a_{\mathrm{ell}}}{E_{\mathrm{max}}}\right) \cdot \left(\frac{\tau_{\mathrm{IR}}}{2.35}\right)^2} . \tag{A.2}$$

The arrival time jitter is then estimated by the FWHM of the resulting distribution of t_{arrival} for one experimental run consisting of ten thousands of shots. The results are presented for exemplary runs in figure 5.11.

A.2.3 Comparison of X-ray Pulse Retrievals

In order to validate the reliability of the developed integration algorithm, the retrieved pulse structures are compared to the high-resolution time–energy retrieval presented in [143]. Four X-ray pulses that are well reconstructed with both routines are compared in figure A.7. In order to compensate for the different time resolution of both routines, the results of the complex retrieval have been additionally convoluted with a Gaussian response function. The width of this function is set to 2.85 fs, according to the estimated time resolution of the integration algorithm (see section 5.3.3 and [86]).

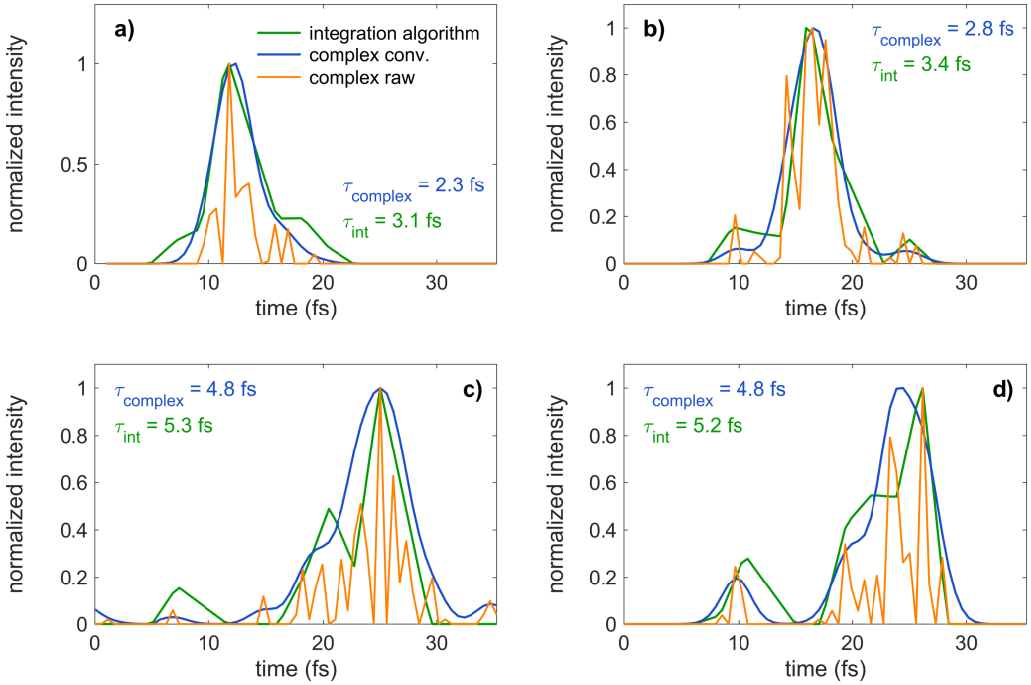

FIGURE A.7: Comparison of the integration algorithm with the complex time–energy retrieval. The panels a) – d) show the single-shot temporal pulse structures retrieved by the integration algorithm (green) and the complex method (orange) for four different X-ray shots. Additionally, the convolution of the complex retrieval with a Gaussian response function (blue) is displayed. The corresponding rms pulse durations of either the integration or the convoluted complex retrieval are additionally given in each panel. Adapted from [86].

Bibliography

[1] A. Einstein. "Zur Elektrodynamik Bewegter Körper". *Annalen der Physik* **322**, 891–921 (1905).

[2] A. Einstein. "Die Grundlage der Allgemeinen Relativitätstheorie". *Annalen der Physik* **354**, 769–822 (1916).

[3] J. E. Barnett. *Time's Pendulum: The Quest to Capture Time–From Sundials to Atomic Clocks*. Basic Books, 1998.

[4] A. D. Ludlow, M. M. Boyd, J. Ye, E. Peik, and P. O. Schmidt. "Optical atomic clocks". *Rev. Mod. Phys.* **87**, 637–701 (2015).

[5] M. Nisoli, S. Stagira, S. de Silvestri, O. Svelto, S. Sartania, Z. Cheng, M. Lenzner, C. Spielmann, and F. Krausz. "A novel-high energy pulse compression system: Generation of multigigawatt sub-5-fs pulses". *Appl. Phys. B* **65**, 189–196 (1997).

[6] E. Goulielmakis, M. Schultze, M. Hofstetter, V. S. Yakovlev, J. Gagnon, M. Uiberacker, A. L. Aquila, E. M. Gullikson, D. T. Attwood, R. Kienberger, et al. "Single-cycle nonlinear optics". *Science* **320**, 1614–1617 (2008).

[7] T. Brabec and F. Krausz. "Intense few-cycle laser fields: Frontiers of nonlinear optics". *Rev. Mod. Phys.* **72**, 545–591 (2000).

[8] M. J. Rosker, F. W. Wise, and C. L. Tang. "Femtosecond relaxation dynamics of large molecules". *Phys. Rev. Lett.* **57**, 321 (1986).

[9] R. Jimenez, G. R. Fleming, P. V. Kumar, and M. Maroncelli. "Femtosecond solvation dynamics of water". *Nature* **369**, 471 (1994).

[10] H. Petek and S. Ogawa. "Femtosecond time-resolved two-photon photoemission studies of electron dynamics in metals". *Progr. Surf. Sci.* **56**, 239–310 (1997).

[11] M. S. Wagner, E. D. Ilieva, P. S. Petkov, R. D. Nikolova, R. Kienberger, and H. Iglev. "Ultrafast hydrogen bond dynamics and partial electron transfer after photoexcitation of diethyl ester of 7-(diethylamino)-coumarin-3-phosphonic acid and its benzoxaphosphorin analog". *Phys. Chem. Chem. Phys.* **17**, 9919–9926 (2015).

[12] A. H. Zewail. "Laser femtochemistry". *Science* **242**, 1645–1653 (1988).

[13] A. H. Zewail. "Femtochemistry: Atomic-scale dynamics of the chemical bond using ultrafast lasers (Nobel Lecture)". *Angewandte Chemie International Edition* **39**, 2586–2631 (2000).

[14] A. L'Huillier and P. Balcou. "High-order harmonic generation in rare gases with a 1-ps 1053-nm laser". *Phys. Rev. Lett.* **70**, 774–777 (1993).

[15] J. J. Macklin, J. D. Kmetec, and C. L. Gordon. "High-order harmonic generation using intense femtosecond pulses". *Phys. Rev. Lett.* **70**, 766–769 (1993).

[16] M. Drescher, M. Hentschel, R. Kienberger, G. Tempea, C. Spielmann, G. A. Reider, P. B. Corkum, and F. Krausz. "X-ray Pulses Approaching the Attosecond Frontier". *Science* **291**, 1923–1927 (2001).

[17] P. M. Paul, E. S. Toma, P. Breger, G. Mullot, F. Augé, P. Balcou, H. G. Muller, and P. Agostini. "Observation of a Train of Attosecond Pulses from High Harmonic Generation". *Science* **292**, 1689–1692 (2001).

[18] M. Hentschel, R. Kienberger, C. Spielmann, G. A. Reider, N. Milosevic, T. Brabec, P. Corkum, U. Heinzmann, M. Drescher, and F. Krausz. "Attosecond metrology". *Nature* **414**, 509–513 (2001).

[19] M. Drescher, M. Hentschel, R. Kienberger, M. Uiberacker, V. Yakovlev, A. Scrinzi, T. Westerwalbesloh, U. Kleineberg, U. Heinzmann, and F. Krausz. "Time-resolved atomic inner-shell spectroscopy". *Nature* **419**, 803–807 (2002).

[20] R. Kienberger, E. Goulielmakis, M. Uiberacker, A. Baltuška, V. Yakovlev, F. Bammer, A. Scrinzi, T. Westerwalbesloh, U. Kleineberg, U. Heinzmann, et al. "Atomic transient recorder". *Nature* **427**, 817–821 (2004).

[21] A. Baltuška, T. Udem, M. Uiberacker, M. Hentschel, E. Goulielmakis, C. Gohle, R. Holzwarth, V. S. Yakovlev, A. Scrinzi, T. W. Hänsch, et al. "Attosecond control of electronic processes by intense light fields". *Nature* **421**, 611–615 (2003).

[22] J. Itatani, F. Quéré, G. L. Yudin, M. Y. Ivanov, F. Krausz, and P. B. Corkum. "Attosecond streak camera". *Phys. Rev. Lett.* **88**, 173903 (2002).

[23] A. L. Cavalieri, N. Müller, T. Uphues, V. S. Yakovlev, A. Baltuška, B. Horvath, B. Schmidt, L. Blümel, R. Holzwarth, S. Hendel, et al. "Attosecond spectroscopy in condensed matter". *Nature* **449**, 1029 (2007).

[24] S. Neppl, R. Ernstorfer, E. M. Bothschafter, A. L. Cavalieri, D. Menzel, J. V. Barth, F. Krausz, R. Kienberger, and P. Feulner. "Attosecond Time-Resolved Photoemission from Core and Valence States of Magnesium". *Phys. Rev. Lett.* **109**, 087401 (2012).

[25] F. Quéré, Y. Mairesse, and J. Itatani. "Temporal characterization of attosecond XUV fields". *J. Mod. Opt.* **52**, 339–360 (2005).

[26] M. Schultze, M. Fieß, N. Karpowicz, J. Gagnon, M. Korbman, M. Hofstetter, S. Neppl, A. L. Cavalieri, Y. Komninos, T. Mercouris, et al. "Delay in Photoemission". *Science* **328**, 1658–1662 (2010).

[27] C.-H. Zhang and U. Thumm. "Attosecond photoelectron spectroscopy of metal surfaces". *Phys. Rev. Lett.* **102**, 123601 (2009).

[28] S. Neppl, R. Ernstorfer, A. L. Cavalieri, C. Lemell, G. Wachter, E. Magerl, E. M. Bothschafter, M. Jobst, M. Hofstetter, U. Kleineberg, et al. "Direct observation of electron propagation and dielectric screening on the atomic length scale". *Nature* **517**, 342 (2015).

[29] R. Locher, L. Castiglioni, M. Lucchini, M. Greif, L. Gallmann, J. Osterwalder, M. Hengsberger, and U. Keller. "Energy-dependent photoemission delays from noble metal surfaces by attosecond interferometry". *Optica* **2**, 405–410 (2015).

[30] Z. Tao, C. Chen, T. Szilvási, M. Keller, M. Mavrikakis, H. Kapteyn, and M. Murnane. "Direct time-domain observation of attosecond final-state lifetimes in photoemission from solids". *Science* **353**, 62–67 (2016).

[31] F. Siek, S. Neb, P. Bartz, M. Hensen, C. Strüber, S. Fiechter, M. Torrent-Sucarrat, V. M. Silkin, E. E. Krasovskii, N. M. Kabachnik, et al. "Angular momentum–induced delays in solid-state photoemission enhanced by intra-atomic interactions". *Science* **357**, 1274–1277 (2017).

[32] M. Nisoli, P. Decleva, F. Calegari, A. Palacios, and F. Martín. "Attosecond electron dynamics in molecules". *Chem. Rev.* **117**, 10760–10825 (2017).

[33] L. Seiffert, Q. Liu, S. Zherebtsov, A. Trabattoni, P. Rupp, M. C. Castrovilli, M. Galli, F. Süßmann, K. Wintersperger, J. Stierle, et al. "Attosecond chronoscopy of electron scattering in dielectric nanoparticles". *Nat. Phys.* **13**, 766 (2017).

[34] A. J. Verhoef, A. Mitrofanov, M. Krikunova, N. M. Kabachnik, M. Drescher, and A. Baltuška. "Attosecond streaking of shake-up and Auger electrons in xenon". In: *EPJ Web of Conferences*. Vol. 41. 2013, 02003.

[35] C. Palatchi, J. M. Dahlström, A. S. Kheifets, I. A. Ivanov, D. M. Canaday, P. Agostini, and L. F. DiMauro. "Atomic delay in helium, neon, argon and krypton". *J. Phys. B: At. Mol. Opt. Phys.* **47**, 245003 (2014).

[36] M. Ossiander, F. Siegrist, V. Shirvanyan, R. Pazourek, A. Sommer, T. Latka, A. Guggenmos, S. Nagele, J. Feist, J. Burgdörfer, et al. "Attosecond correlation dynamics". *Nat. Phys.* **13**, 280–285 (2017).

[37] M. Ossiander, J. Riemensberger, S. Neppl, M. Mittermair, M. Schäffer, A. Duensing, M. S. Wagner, R. Heider, M.Wurzer, M. Gerl, et al. "Absolute Timing of the Photoelectric Effect". *Nature* **561**, 374–377 (2018).

[38] A. Einstein. "Über einen die Erzeugung und Verwandlung des Lichtes betreffenden heuristischen Gesichtspunkt". *Annalen der Physik* **322**, 132–148 (1905).

[39] M. Faubel, B. Steiner, and J. P. Toennies. "Photoelectron spectroscopy of liquid water, some alcohols, and pure nonane in free micro jets". *J. Chem. Phys.* **106**, 9013–9031 (1997).

[40] B. Winter and M. Faubel. "Photoemission from liquid aqueous solutions". *Chem. Rev.* **106**, 1176–1211 (2006).

[41] K. R. Wilson, B. S. Rude, T. Catalano, R. D. Schaller, J. G. Tobin, D. T. Co, and R. J. Saykally. "X-ray Spectroscopy of Liquid Water Microjets". *J. Phys. Chem. B* **105**, 3346–3349 (2001).

[42] K. R. Wilson, R. D. Schaller, D. T. Co, R. J. Saykally, B. S. Rude, T. Catalano, and J. D. Bozek. "Surface relaxation in liquid water and methanol studied by x-ray absorption spectroscopy". *J. Chem. Phys.* **117**, 7738–7744 (2002).

[43] B. Winter, R. Weber, W. Widdra, M. Dittmar, M. Faubel, and I. V. Hertel. "Full Valence Band Photoemission from Liquid Water Using EUV Synchrotron Radiation". *J. Phys. Chem. A* **108**, 2625–2632 (2004).

[44] M. A. Brown, A. B. Redondo, I. Jordan, N. Duyckaerts, M.-T. Lee, M. Ammann, F. Nolting, A. Kleibert, T. Huthwelker, J.-P. Mächler, et al. "A new endstation at the Swiss Light Source for ultraviolet photoelectron spectroscopy, X-ray photoelectron spectroscopy, and X-ray absorption spectroscopy measurements of liquid solutions". *Rev. of Sci. Instrum.* **84**, 073904 (2013).

[45] I. Jordan, M. Huppert, M. A. Brown, J. A. van Bokhoven, and H. J. Wörner. "Photoelectron spectrometer for attosecond spectroscopy of liquids and gases". *Rev. Sci. Instrum.* **86**, 123905 (2015).

[46] I. Jordan. "Attosecond time-resolved photoelectron spectroscopy of liquid systems". PhD thesis. ETH Zurich, 2017.

[47] M. Huppert, I. Jordan, D. Baykusheva, A. von Conta, and H. J. Wörner. "Attosecond delays in molecular photoionization". *Phys. Rev. Lett.* **117**, 093001 (2016).

[48] D. Hutzler. "Time-Resolved Infrared Spectroscopy on Hydrogen Bonded Systems". PhD thesis. Technische Universität München, 2017.

[49] J. M. Sorenson, G. Hura, R. M. Glaeser, and T. Head-Gordon. "What can x-ray scattering tell us about the radial distribution functions of water?" *J. Chem. Phys.* **113**, 9149–9161 (2000).

[50] R. Leberman and A. K. Soper. "Effect of high salt concentrations on water structure". *Nature* **378**, 364 (1995).

[51] S. R. Dillon and R. C. Dougherty. "Raman studies of the solution structure of univalent electrolytes in water". *J. Phys. Chem. A* **106**, 7647–7650 (2002).

[52] Y. Maréchal. "Observing the water molecule in macromolecules using infrared spectrometry: structure of the hydrogen bond network and hydration mechanism". *J. Mol. Struct.* **700**, 217–223 (2004).

[53] D. Hutzler, J. C. Werhahn, R. Heider, M. Bradler, R. Kienberger, E. Riedle, and H. Iglev. "Highly Selective Relaxation of the OH Stretching Overtones in Isolated HDO Molecules Observed by Infrared Pump–Repump–Probe Spectroscopy". *J. Phys. Chem. A* **119**, 6831–6836 (2015).

[54] H. J. Bakker, M. F. Kropman, A. W. Omta, and S. Woutersen. "Hydrogen-Bond Dynamics of Water in Ionic Solutions". *Phys. Scr.* **69**, C14 (2004).

[55] M. L. Cowan, B. D. Bruner, N. Huse, J. R. Dwyer, B. Chugh, E. T. J. Nibbering, T. Elsaesser, and R. J. D. Miller. "Ultrafast memory loss and energy redistribution in the hydrogen bond network of liquid H_2O". *Nature* **434**, 199 (2005).

[56] R. Laenen, C. Rauscher, and A. Laubereau. "Dynamics of Local Substructures in Water Observed by Ultrafast Infrared Hole Burning". *Phys. Rev. Lett.* **80**, 2622–2625 (1998).

[57] E. J. Heilweil. "Ultrafast glimpses at water and ice". *Science* **283**, 1467–1468 (1999).

[58] A. H. Narten, C.-G. Venkatesh, and S. A. Rice. "Diffraction pattern and structure of amorphous solid water at 10 and 77 K". *J. Chem. Phys.* **64**, 1106–1121 (1976).

[59] A. Ben-Naim. *Statistical Thermodynamics for Chemists and Biochemists*. Springer US, 1992, 459–559.

[60] P. Emma, R. Akre, J. Arthur, R. Bionta, C. Bostedt, J. Bozek, A. Brachmann, P. Bucksbaum, R. Coffee, F.-J. Decker, et al. "First lasing and operation of an ångstrom-wavelength free-electron laser". *Nat. Photonics* **4**, 641 (2010).

[61] C. Bostedt, S. Boutet, D. M. Fritz, Z. Huang, H. J. Lee, H. T. Lemke, A. Robert, W. F. Schlotter, J. J. Turner, and G. J. Williams. "Linac coherent light source: The first five years". *Rev. Mod. Phys.* **88**, 015007 (2016).

[62] R. Bonifacio and F. Casagrande. "Instabilities and quantum initiation in the free-electron laser". *Opt. Commun.* **50**, 251–255 (1984).

[63] P. Schmüser, M. Dohlus, J. Rossbach, and C. Behrens. *Free-Electron Lasers in the Ultraviolet and X-Ray Regime*. Vol. 2. Springer, 2014.

[64] T. Tschentscher. "Investigation of ultrafast processes using X-ray free-electron laser radiation". *Chem. Phys.* **299**, 271–276 (2004).

[65] D. Milathianaki, S. Boutet, G. J. Williams, A. Higginbotham, D. Ratner, A. E. Gleason, M. Messerschmidt, M. M. Seibert, D. C. Swift, P. Hering, et al. "Femtosecond visualization of lattice dynamics in shock-compressed matter". *Science* **342**, 220–223 (2013).

[66] L. Young, E. P. Kanter, B. Krässig, Y. Li, A. M. March, S. T. Pratt, R. Santra, S. H. Southworth, N. Rohringer, L. F. DiMauro, et al. "Femtosecond electronic response of atoms to ultra-intense X-rays". *Nature* **466**, 56 (2010).

[67] A. Rudenko, L. Inhester, K. Hanasaki, X. Li, S. J. Robatjazi, B. Erk, R. Boll, K. Toyota, Y. Hao, O. Vendrell, et al. "Femtosecond response of polyatomic molecules to ultra-intense hard X-rays". *Nature* **546**, 129 (2017).

[68] B. Rudek, D. Rolles, S.-K. Son, L. Foucar, B. Erk, S. Epp, R. Boll, D. Anielski, C. Bostedt, S. Schorb, et al. "Resonance-enhanced multiple ionization of krypton at an x-ray free-electron laser". *Phys. Rev. A* **87**, 023413 (2013).

[69] R. Boll, D. Anielski, C. Bostedt, J. D. Bozek, L. Christensen, R. Coffee, S. De, P. Decleva, S. W. Epp, B. Erk, et al. "Femtosecond photoelectron diffraction on laser-aligned molecules: Towards time-resolved imaging of molecular structure". *Phys. Rev. A* **88**, 061402 (2013).

[70] M. P. Minitti, J. M. Budarz, A. Kirrander, J. S. Robinson, D. Ratner, T. J. Lane, D. Zhu, J. M. Glownia, M. Kozina, H. T. Lemke, et al. "Imaging Molecular Motion: Femtosecond X-Ray Scattering of an Electrocyclic Chemical Reaction". *Phys. Rev. Lett.* **114**, 255501 (2015).

[71] N. Coquelle, M. Sliwa, J. Woodhouse, G. Schirò, V. Adam, A. Aquila, T. R. M. Barends, S. Boutet, M. Byrdin, S. Carbajo, et al. "Chromophore twisting in the excited state of a photoswitchable fluorescent protein captured by time-resolved serial femtosecond crystallography". *Nat. Chem.* **10**, 31 (2018).

[72] M. M. Seibert, T. Ekeberg, F. R. Maia, M. Svenda, J. Andreasson, O. Jönsson, D. Odić, B. Iwan, A. Rocker, D. Westphal, et al. "Single mimivirus particles intercepted and imaged with an X-ray laser". *Nature* **470**, 78 (2011).

[73] M. W. Mara, R. G. Hadt, M. E. Reinhard, T. Kroll, H. Lim, R. W. Hartsock, R. Alonso-Mori, M. Chollet, J. M. Glownia, S. Nelson, et al. "Metalloprotein entatic control of ligand-metal bonds quantified by ultrafast x-ray spectroscopy". *Science* **356**, 1276–1280 (2017).

[74] B. Erk, D. Rolles, L. Foucar, B. Rudek, S. W. Epp, M. Cryle, C. Bostedt, S. Schorb, J. Bozek, A. Rouzee, et al. "Ultrafast charge rearrangement and nuclear dynamics upon inner-shell multiple ionization of small polyatomic molecules". *Phys. Rev. Lett.* **110**, 053003 (2013).

[75] C. S. Lehmann, A. Picón, C. Bostedt, A. Rudenko, A. Marinelli, D. Moonshiram, T. Osipov, D. Rolles, N. Berrah, C. Bomme, et al. "Ultrafast x-ray-induced nuclear dynamics in diatomic molecules using femtosecond x-ray-pump–x-ray-probe spectroscopy". *Phys. Rev. A* **94**, 013426 (2016).

[76] C. Gahl, A. Azima, M. Beye, M. Deppe, K. Döbrich, U. Hasslinger, F. Hennies, A. Melnikov, M. Nagasono, A. Pietzsch, et al. "A femtosecond X-ray/optical cross-correlator". *Nat. Photonics* **2**, 165 (2008).

[77] J. M. Glownia, J. Cryan, J. Andreasson, A. Belkacem, N. Berrah, C. I. Blaga, C. Bostedt, J. Bozek, L. F. DiMauro, L. Fang, et al. "Time-resolved pump-probe experiments at the LCLS". *Opt. Express* **18**, 17620–17630 (2010).

[78] N. Hartmann, W. Helml, A. Galler, M. R. Bionta, J. Grünert, S. L. Molodtsov, K. R. Ferguson, S. Schorb, M. L. Swiggers, S. Carron, et al. "Sub-femtosecond precision measurement of relative X-ray arrival time for free-electron lasers". *Nat. Photonics* **8**, 706 (2014).

[79] M. R. Bionta, N. Hartmann, M. Weaver, D. French, D. J. Nicholson, J. P. Cryan, J. M. Glownia, K. Baker, C. Bostedt, M. Chollet, et al. "Spectral encoding method for measuring the relative arrival time between x-ray/optical pulses". *Rev. Sci. Instrum.* **85**, 85040M (2014).

[80] U. Frühling, M. Wieland, M. Gensch, T. Gebert, B. Schütte, M. Krikunova, R. Kalms, F. Budzyn, O. Grimm, J. Rossbach, et al. "Single-shot terahertz-field-driven X-ray streak camera". *Nat. Photonics* **3**, 523 (2009).

[81] S. Düsterer, P. Radcliffe, C. Bostedt, J. Bozek, A. L. Cavalieri, R. Coffee, J. T. Costello, D. Cubaynes, L. F. DiMauro, Y. Ding, et al. "Femtosecond x-ray pulse length characterization at the Linac Coherent Light Source free-electron laser". *New J. Phys.* **13**, 093024 (2011).

[82] I. Grguraš, A. R. Maier, C. Behrens, T. Mazza, T. J. Kelly, P. Radcliffe, S. Düsterer, A. K. Kazansky, N. M. Kabachnik, T. Tschentscher, et al. "Ultrafast X-ray pulse characterization at free-electron lasers". *Nat. Photonics* **6**, 852 (2012).

[83] W. Helml, A. R. Maier, W. Schweinberger, I. Grguraš, P. Radcliffe, G. Doumy, C. Roedig, J. Gagnon, M. Messerschmidt, S. Schorb, et al. "Measuring the temporal structure of few-femtosecond free-electron laser X-ray pulses directly in the time domain". *Nat. Photonics* **8**, 950 (2014).

[84] E. Constant, V. D. Taranukhin, A. Stolow, and P. B. Corkum. "Methods for the measurement of the duration of high-harmonic pulses". *Phys. Rev. A* **56**, 3870 (1997).

[85] P. Eckle, M. Smolarski, P. Schlup, J. Biegert, A. Staudte, M. Schöffler, H. G. Muller, R. Dörner, and U. Keller. "Attosecond angular streaking". *Nat. Phys.* **4**, 565 (2008).

[86] R. Heider. "Attosecond Metrology – Characterization of X-ray Free-electron Laser Pulses via Angular Streaking and Application of Attosecond Spectroscopy on Liquid H_2O". PhD thesis. Technische Universität München, 2018.

[87] G. A. Reider. *Photonik*. Vol. 3. Springer, 2012.

[88] B. E. A. Saleh and M. C. Teich. *Fundamentals of Photonics*. Vol. 2. John Wiley & Sons, Inc., 2007.

[89] J.-C. Diels and W. Rudolph. *Ultrafast Laser Pulse Phenomena*. Vol. 2. Academic Press, 2006.

[90] E. Treacy. "Optical pulse compression with diffraction gratings". *IEEE J. Quantum Electron.* **5**, 454–458 (1969).

[91] R. Szipöcs, K. Ferencz, C. Spielmann, and F. Krausz. "Chirped multilayer coatings for broadband dispersion control in femtosecond lasers". *Opt. Lett.* **19**, 201–203 (1994).

[92] V. Pervak, A. V. Tikhonravov, M. K. Trubetskov, S. Naumov, F. Krausz, and A. Apolonski. "1.5-octave chirped mirror for pulse compression down to sub-3 fs". *Appl. Phys. B* **87**, 5–12 (2007).

[93] P. Tournois. "Acousto-optic programmable dispersive filter for adaptive compensation of group delay time dispersion in laser systems". *Opt. Commun.* **140**, 245–249 (1997).

[94] F. Verluise, V. Laude, Z. Cheng, C. Spielmann, and P. Tournois. "Amplitude and phase control of ultrashort pulses by use of an acousto-optic programmable dispersive filter: pulse compression and shaping". *Opt. Lett.* **25**, 575–577 (2000).

[95] R. W. Boyd. *Nonlinear optics*. Vol. 3. Academic press, 2008.

[96] R. Y. Chiao, E. Garmire, and C. H. Townes. "Self-Trapping of Optical Beams". *Phys. Rev. Lett.* **13**, 479–482 (1964).

[97] P. L. Kelley. "Self-Focusing of Optical Beams". *Phys. Rev. Lett.* **15**, 1005–1008 (1965).

[98] G. Fibich and A. L. Gaeta. "Critical power for self-focusing in bulk media and in hollow waveguides". *Opt. Lett.* **25**, 335–337 (2000).

[99] F. DeMartini, C. H. Townes, T. K. Gustafson, and P. L. Kelley. "Self-Steepening of Light Pulses". *Phys. Rev.* **164**, 312–323 (1967).

[100] M. Nisoli, S. D. Silvestri, O. Svelto, R. Szipöcs, K. Ferencz, C. Spielmann, S. Sartania, and F. Krausz. "Compression of high-energy laser pulses below 5 fs". *Opt. Lett.* **22**, 522–524 (1997).

[101] C. L. Blanc, P. Curley, and F. Salin. "Gain-narrowing and gain-shifting of ultra-short pulses in Ti: sapphire amplifiers". *Opt. Commun.* **131**, 391–398 (1996).

[102] C. V. Shank, R. L. Fork, R. Yen, R. H. Stolen, and W. J. Tomlinson. "Compression of femtosecond optical pulses". *Appl. Phys. Lett.* **40**, 761–763 (1982).

[103] J. G. Fujimoto, A. M. Weiner, and E. P. Ippen. "Generation and measurement of optical pulses as short as 16 fs". *Appl. Phys. Lett.* **44**, 832–834 (1984).

[104] M. Nisoli, S. D. Silvestri, and O. Svelto. "Generation of high energy 10 fs pulses by a new pulse compression technique". *Appl. Phys. Lett.* **68**, 2793–2795 (1996).

[105] B. Walker, B. Sheehy, L. F. DiMauro, P. Agostini, K. J. Schafer, and K. C. Kulander. "Precision Measurement of Strong Field Double Ionization of Helium". *Phys. Rev. Lett.* **73**, 1227–1230 (1994).

[106] E. A. Marcatili and R. Schmeltzer. "Hollow metallic and dielectric waveguides for long distance optical transmission and lasers". *Bell Labs Technical Journal* **43**, 1783–1809 (1964).

[107] M. Wurzer. "Implementation and Characterization of an Attosecond Beamline". Technische Universität München, 2016.

[108] J. S. Robinson, C. A. Haworth, H. Teng, R. A. Smith, J. P. Marangos, and J. Tisch. "The generation of intense, transform-limited laser pulses with tunable duration from 6 to 30 fs in a differentially pumped hollow fibre". *Appl. Phys. B* **85**, 525–529 (2006).

[109] C. Vozzi, M. Nisoli, G. Sansone, S. Stagira, and S. De Silvestri. "Optimal spectral broadening in hollow-fiber compressor systems". *Appl. Phys. B* **80**, 285–289 (2005).

[110] A. L. Cavalieri, E. Goulielmakis, B. Horvath, W. Helml, M. Schultze, M. Fieß, V. Pervak, L. Veisz, V. S. Yakovlev, M. Uiberacker, et al. "Intense 1.5-cycle near infrared laser waveforms and their use for the generation of ultra-broadband soft-x-ray harmonic continua". *New J. Phys.* **9**, 242 (2007).

[111] W. Schweinberger, A. Sommer, E. Bothschafter, J. Li, F. Krausz, R. Kienberger, and M. Schultze. "Waveform-controlled near-single-cycle milli-joule laser pulses generate sub-10 nm extreme ultraviolet continua". *Opt. Lett.* **37**, 3573–3575 (2012).

[112] A. McPherson, G. Gibson, H. Jara, U. Johann, T. S. Luk, I. A. McIntyre, K. Boyer, and C. K. Rhodes. "Studies of multiphoton production of vacuum-ultraviolet radiation in the rare gases". *J. Opt. Soc. Am. B* **4**, 595–601 (1987).

[113] M. Ferray, A. L'Huillier, X. F. Li, L. A. Lompre, G. Mainfray, and C. Manus. "Multiple-harmonic conversion of 1064 nm radiation in rare gases". *J. Phys. B: At. Mol. Opt. Phys.* **21**, L31 (1988).

[114] X. F. Li, A. L'Huillier, M. Ferray, L. A. Lompré, and G. Mainfray. "Multiple-harmonic generation in rare gases at high laser intensity". *Phys. Rev. A* **39**, 5751–5761 (1989).

[115] N. Sarukura, K. Hata, T. Adachi, R. Nodomi, M. Watanabe, and S. Watanabe. "Coherent soft-x-ray generation by the harmonics of an ultrahigh-power KrF laser". *Phys. Rev. A* **43**, 1669–1672 (1991).

[116] C. Spielmann, N. H. Burnett, S. Sartania, R. Koppitsch, M. Schnürer, C. Kan, M. Lenzner, P. Wobrauschek, and F. Krausz. "Generation of Coherent X-rays in the Water Window Using 5-Femtosecond Laser Pulses". *Science* **278**, 661–664 (1997).

[117] J. Seres, E. Seres, A. J. Verhoef, G. Tempea, C. Streli, P. Wobrauschek, V. Yakovlev, A. Scrinzi, C. Spielmann, and F. Krausz. "Laser technology: Source of coherent kiloelectronvolt X-rays". *Nature* **433**, 596 (2005).

[118] S. Neppl. "Attosecond Time-Resolved Photoemission from Surfaces and Interfaces". PhD thesis. Technische Universität München, 2012.

[119] P. B. Corkum. "Plasma perspective on strong field multiphoton ionization". *Phys. Rev. Lett.* **71**, 1994–1997 (1993).

[120] M. Lewenstein, P. Balcou, M. Y. Ivanov, A. L'Huillier, and P. B. Corkum. "Theory of high-harmonic generation by low-frequency laser fields". *Phys. Rev. A* **49**, 2117–2132 (1994).

[121] P. Antoine, A. L'Huillier, and M. Lewenstein. "Attosecond Pulse Trains Using High–Order Harmonics". *Phys. Rev. Lett.* **77**, 1234–1237 (1996).

[122] I. P. Christov, M. M. Murnane, and H. C. Kapteyn. "High-Harmonic Generation of Attosecond Pulses in the "Single-Cycle" Regime". *Phys. Rev. Lett.* **78**, 1251–1254 (1997).

[123] G. Sansone, E. Benedetti, F. Calegari, C. Vozzi, L. Avaldi, R. Flammini, L. Poletto, P. Villoresi, C. Altucci, R. Velotta, et al. "Isolated single-cycle attosecond pulses". *Science* **314**, 443–446 (2006).

[124] A. V. Vinogradov. "Multilayer X-ray optics". *Quantum Electron.* **32**, 1113 (2002).

[125] A. Wonisch, U. Neuhäusler, N. M. Kabachnik, T. Uphues, M. Uiberacker, V. Yakovlev, F. Krausz, M. Drescher, U. Kleineberg, and U. Heinzmann. "Design, fabrication, and analysis of chirped multilayer mirrors for reflection of extreme-ultraviolet attosecond pulses". *Appl. Opt.* **45**, 4147–4156 (2006).

[126] M. Hofstetter, M. Schultze, M. Fieß, B. Dennhardt, A. Guggenmos, J. Gagnon, V. S. Yakovlev, E. Goulielmakis, R. Kienberger, E. M. Gullikson, et al. "Attosecond dispersion control by extreme ultraviolet multilayer mirrors". *Opt. Express* **19**, 1767–1776 (2011).

[127] P. Salieres, T. Ditmire, K. S. Budil, M. D. Perry, and A. L'Huillier. "Spatial profiles of high-order harmonics generated by a femtosecond Cr:LiSAF laser". *J. Phys. B: At. Mol. Opt. Phys.* **27**, 217–222 (1994).

[128] F. Krausz and M. Ivanov. "Attosecond physics". *Rev. Mod. Phys.* **81**, 163–234 (2009).

[129] E. L. Falcão-Filho, V. M. Gkortsas, A. Gordon, and F. X. Kärtner. "Analytic scaling analysis of high harmonic generation conversion efficiency". *Opt. Express* **17**, 11217–11229 (2009).

[130] V.-M. Gkortsas, S. Bhardwaj, E. L. Falcão-Filho, K.-H. Hong, A. Gordon, and F. X. Kärtner. "Scaling of high harmonic generation conversion efficiency". *J. Phys. B: At. Mol. Opt. Phys.* **44**, 045601 (2011).

[131] J. Li, X. Ren, Y. Yin, K. Zhao, A. Chew, Y. Cheng, E. Cunningham, Y. Wang, S. Hu, Y. Wu, et al. "53-attosecond X-ray pulses reach the carbon K-edge". *Nat. Commun.* **8**, 186 (2017).

[132] T. Gaumnitz, A. Jain, Y. Pertot, M. Huppert, I. Jordan, F. Ardana-Lamas, and H. J. Wörner. "Streaking of 43-attosecond soft-X-ray pulses generated by a passively CEP-stable mid-infrared driver". *Opt. Express* **25**, 27506–27518 (2017).

[133] R. Trebino, K. W. DeLong, D. N. Fittinghoff, J. N. Sweetser, M. A. Krumbügel, B. A. Richman, and D. J. Kane. "Measuring ultrashort laser pulses in the time-frequency domain using frequency-resolved optical gating". *Rev. Sci. Instru.* **68**, 3277–3295 (1997).

[134] T. Schultz and M. Vrakking. *Attosecond and XUV Physics*. Vol. 1. Wiley-VCH, 2014.

[135] D. J. Bradley, B. Liddy, and W. E. Sleat. "Direct linear measurement of ultrashort light pulses with a picosecond streak camera". *Opt. Commun.* **2**, 391–395 (1971).

[136] E. Goulielmakis, M. Uiberacker, R. Kienberger, A. Baltuška, V. Yakovlev, A. Scrinzi, T. Westerwalbesloh, U. Kleineberg, U. Heinzmann, M. Drescher, et al. "Direct Measurement of Light Waves". *Science* **305**, 1267–1269 (2004).

[137] M. T. Ossiander. "On the Expansion of Attosecond Streaking Spectroscopy towards Ultrafast Surface Dynamics". Technische Universität München, 2014.

[138] J. Gagnon. "Attosecond Electron Spectroscopy Theory and its Applications". PhD thesis. Ludwig-Maximilians-Universität München, 2010.

[139] E. P. Wigner. "Lower Limit for the Energy Derivative of the Scattering Phase Shift". *Phys. Rev.* **98**, 145–147 (1955).

[140] J. Gagnon, E. Goulielmakis, and V. S. Yakovlev. "The accurate FROG characterization of attosecond pulses from streaking measurements". *Appl. Phys. B* **92**, 25–32 (2008).

[141] D. A. Shirley. "High-Resolution X-Ray Photoemission Spectrum of the Valence Bands of Gold". *Phys. Rev. B* **5**, 4709–4714 (1972).

[142] M. Ossiander. "Attosecond Photoemission Timing". PhD thesis. Technische Universität München, 2018.

[143] N. Hartmann, G. Hartmann, R. Heider, M. S. Wagner, M. Ilchen, J. Buck, A. O. Lindahl, C. Benko, J. Grünert, J. Krzywinski, et al. "Attosecond time–energy structure of X-ray free-electron laser pulses". *Nat. Photonics* **12**, 215–220 (2018).

[144] Z. Huang and K.-J. Kim. "Review of x-ray free-electron laser theory". *Phys. Rev. ST Accel. Beams* **10**, 034801 (2007).

[145] J. N. Galayda, J. Arthur, D. F. Ratner, and W. E. White. "X-ray free-electron lasers—present and future capabilities". *JOSA B* **27**, B106–B118 (2010).

[146] K.-J. Kim. "Three-dimensional analysis of coherent amplification and self-amplified spontaneous emission in free-electron lasers". *Phys. Rev. Lett.* **57**, 1871 (1986).

[147] C. Spielmann, P. F. Curley, T. Brabec, and F. Krausz. "Ultrabroadband femtosecond lasers". *IEEE J. Quantum Electron.* **30**, 1100–1114 (1994).

[148] A. Stingl, M. Lenzner, C. Spielmann, F. Krausz, and R. Szipöcs. "Sub-10-fs mirror-dispersion-controlled Ti:sapphire laser". *Opt. Lett.* **20**, 602–604 (1995).

[149] L. Xu, T. W. Hänsch, C. Spielmann, A. Poppe, T. Brabec, and F. Krausz. "Route to phase control of ultrashort light pulses". *Opt. Lett.* **21**, 2008–2010 (1996).

[150] H. R. Telle, G. Steinmeyer, A. E. Dunlop, J. Stenger, D. H. Sutter, and U. Keller. "Carrier-envelope offset phase control: A novel concept for absolute optical frequency measurement and ultrashort pulse generation". *Appl. Phys. B* **69**, 327–332 (1999).

[151] *CEP4 SEED Module for FEMTOSOURCE rainbow - OPERATORS MANUAL*. V1.3. Femtolasers Produktions GmbH. Fernkorngasse 10, 1100 Vienna, Austria, 2013.

[152] I. C. Chang. "Acoustooptic devices and applications". *IEEE transactions on sonics and ultrasonics* **23**, p2 (1976).

[153] F. Lücking, A. Assion, A. Apolonski, F. Krausz, and G. Steinmeyer. "Long-term carrier-envelope-phase-stable few-cycle pulses by use of the feed-forward method". *Opt. Lett.* **37**, 2076–2078 (2012).

[154] D. Strickland and G. Mourou. "Compression of amplified chirped optical pulses". *Opt. Commun.* **56**, 219–221 (1985).

[155] S. Sartania, Z. Cheng, M. Lenzner, G. Tempea, C. Spielmann, F. Krausz, and K. Ferencz. "Generation of 0.1-TW 5-fs optical pulses at a 1-kHz repetition rate". *Opt. Lett.* **22**, 1562–1564 (1997).

[156] *Femtopower HEHR CEP4 - User manual*. V1.00. Femtolasers Produktions GmbH. Fernkorngasse 10, 1100 Vienna, Austria, 2015.

[157] V. Shirvanyan. "Generation of sub-4-fs, mJ pulses via hollow-core fiber nonlinear pulse compression by the conjugate pressure-gradient method". Technische Universität München, 2015.

[158] M. Nurhuda, A. Suda, K. Midorikawa, M. Hatayama, and K. Nagasaka. "Propagation dynamics of femtosecond laser pulses in a hollow fiber filled with argon: constant gas pressure versus differential gas pressure". *JOSA B* **20**, 2002–2011 (2003).

[159] M. Nurhuda, A. Suda, K. Midorikawa, and H. Budiono. "Control of self-phase modulation and plasma-induced blueshifting of high-energy, ultrashort laser pulses in an argon-filled hollow fiber using conjugate pressure-gradient method". *JOSA B* **22**, 1757–1762 (2005).

[160] M. Nurhuda, A. Suda, M. Kaku, and K. Midorikawa. "Optimization of hollow fiber pulse compression using pressure gradients". *Appl. Phys. B* **89**, 209–215 (2007).

[161] A. M. Duensing. "Generation of High-Power, Few-Cycle Laser Pulses by Spectral Broadening in a Differentially Pumped Hollow-Core Fiber Setup". Technische Universität München, 2016.

[162] M. Pollanka. "Characterization and Optimization of a Hollow-Core Fiber Compressor for Attosecond Experiments". Technische Universität München, 2017.

[163] J. N. Sweetser, D. N. Fittinghoff, and R. Trebino. "Transient-grating frequency-resolved optical gating". *Opt. Lett.* **22**, 519–521 (1997).

[164] A. J. Späh. "Development, Design and Implementation of an Ultra-High Vacuum Chamber for Gas-Phase Attosecond Streaking Spectroscopy". Technische Universität München, 2015.

[165] K. Hütten, M. Mittermair, S. O. Stock, R. Beerwerth, V. Shirvanyan, J. Riemensberger, A. Duensing, R. Heider, M. S. Wagner, A. Guggenmos, et al. "Ultrafast quantum control of ionization dynamics in krypton". *Nat. Commun.* **9**, 719 (2018).

[166] A. Kim. "Attosecond time-resolved photoemission from solid samples". PhD thesis. Technische Universität München, 2015.

[167] B. Temelso, K. A. Archer, and G. C. Shields. "Benchmark structures and binding energies of small water clusters with anharmonicity corrections". *J. Phys. Chem. A* **115**, 12034–12046 (2011).

[168] M. Peper. "Electron Scattering Effects on the Attosecond Photoelectron Spectroscopy of Liquid Water". ETH Zurich, 2016.

[169] N. Ottosson, M. Faubel, S. E. Bradforth, P. Jungwirth, and B. Winter. "Photoelectron spectroscopy of liquid water and aqueous solution: Electron effective attenuation lengths and emission-angle anisotropy". *J. Electron. Spectrosc. Relat. Phenom.* **177**, 60–70 (2010).

[170] M. S. Banna, B. H. McQuaide, R. Malutzki, and V. Schmidt. "The photoelectron spectrum of water in the 30 to 140 eV photon energy range". *J. Chem. Phys.* **84**, 4739–4744 (1986).

[171] S. Hüfner. *Photoelectron spectroscopy: principles and applications*. 3rd ed. Springer Science & Business Media, 2013.

[172] L. B. Skinner, C. Huang, D. Schlesinger, L. G. M. Pettersson, A. Nilsson, and C. J. Benmore. "Benchmark oxygen-oxygen pair-distribution function of ambient water from x-ray diffraction measurements with a wide Q-range". *J. Chem. Phys.* **138**, 074506 (2013).

[173] Q. Du, R. Superfine, E. Freysz, and Y. R. Shen. "Vibrational spectroscopy of water at the vapor/water interface". *Phys. Rev. Lett.* **70**, 2313–2316 (1993).

[174] J. S. Bader, C. M. Cortis, and B. J. Berne. "Solvation and reorganization energies in polarizable molecular and continuum solvents". *J. Chem. Phys.* **106**, 2372–2387 (1997).

[175] Y.-I. Suzuki, K. Nishizawa, N. Kurahashi, and T. Suzuki. "Effective attenuation length of an electron in liquid water between 10 and 600 eV". *Phys. Rev. E* **90**, 010302 (2014).

[176] R. Glauber and V. Schomaker. "The Theory of Electron Diffraction". *Phys. Rev.* **89**, 667–671 (1953).

[177] W. Raith. *Teilchen, Band 4 der Reihe Bergmann-Schaefer: Lehrbuch der Experimentalphysik*. 1992.

[178] S. M. Pimblott, J. A. LaVerne, and A. Mozumder. "Monte Carlo simulation of range and energy deposition by electrons in gaseous and liquid water". *J. Phys. Chem.* **100**, 8595–8606 (1996).

[179] H. Tomita, M. Kai, T. Kusama, and A. Ito. "Monte Carlo simulation of physicochemical processes of liquid water radiolysis". *Radiat. Environ. Biophys.* **36**, 105–116 (1997).

[180] S. Thürmer, R. Seidel, M. Faubel, W. Eberhardt, J. C. Hemminger, S. E. Bradforth, and B. Winter. "Photoelectron Angular Distributions from Liquid Water: Effects of Electron Scattering". *Phys. Rev. Lett.* **111**, 173005 (2013).

[181] A. Zangwill. *Physics at Surfaces*. Cambridge University Press, 1988.

[182] T. X. Carroll, J. D. Bozek, E. Kukk, V. Myrseth, L. J. Sæthre, T. D. Thomas, and K. Wiesner. "Xenon N4,5OO Auger spectrum - a useful calibration source". *J. Electron. Spectrosc. Relat. Phenom.* **125**, 127–132 (2002).

[183] M. Lundholm, H. Siegbahn, S. Holmberg, and M. Arbman. "Core electron spectroscopy of water solutions". *J. Electron. Spectrosc. Relat. Phenom.* **40**, 163–180 (1986).

[184] D. Rattenbacher, I. Jordan, A. Schild, and H. J. Wörner. "Nonlocal mechanisms of attosecond interferometry and implications for condensed-phase experiments". *Phys. Rev. A*, accepted (2018).

[185] S. Nagele, R. Pazourek, J. Feist, K. Doblhoff-Dier, C. Lemell, K. Tökési, and J. Burgdörfer. "Time-resolved photoemission by attosecond streaking: extraction of time information". *J. Phys. B: At. Mol. Opt. Phys.* **44**, 081001 (2011).

[186] J. Feist, O. Zatsarinny, S. Nagele, R. Pazourek, J. Burgdörfer, X. Guan, K. Bartschat, and B. I. Schneider. "Time delays for attosecond streaking in photoionization of neon". *Phys. Rev. A* **89**, 033417 (2014).

[187] D. Baykusheva and H. J. Wörner. "Theory of attosecond delays in molecular photoionization". *J. Chem. Phys.* **146**, 124306 (2017).

[188] Y. Ding, A. Brachmann, F.-J. Decker, D. Dowell, P. Emma, J. Frisch, S. Gilevich, G. Hays, P. Hering, Z. Huang, et al. "Measurements and simulations of ultralow emittance and ultrashort electron beams in the linac coherent light source". *Phys. Rev. Lett.* **102**, 254801 (2009).

[189] A. A. Lutman, Y. Ding, Y. Feng, Z. Huang, M. Messerschmidt, J. Wu, and J. Krzywinski. "Femtosecond x-ray free electron laser pulse duration measurement from spectral correlation function". *Phys. Rev. ST Accel. Beams* **15**, 030705 (2012).

[190] Y. Ding, C. Behrens, P. Emma, J. Frisch, Z. Huang, H. Loos, P. Krejcik, and M. H. Wang. "Femtosecond x-ray pulse temporal characterization in free-electron lasers using a transverse deflector". *Phys. Rev. ST Accel. Beams* **14**, 120701 (2011).

[191] C. Behrens, F.-J. Decker, Y. Ding, V. A. Dolgashev, J. Frisch, Z. Huang, P. Krejcik, H. Loos, A. Lutman, T. J. Maxwell, et al. "Few-femtosecond time-resolved measurements of X-ray free-electron lasers". *Nat. Commun.* **5**, 3762 (2014).

[192] M. Harmand, R. Coffee, M. R. Bionta, M. Chollet, D. French, D. Zhu, D. M. Fritz, H. T. Lemke, N. Medvedev, B. Ziaja, et al. "Achieving few-femtosecond time-sorting at hard X-ray free-electron lasers". *Nat. Photonics* **7**, 215 (2013).

[193] W. Helml, I. Grguraš, P. N. Juranić, S. Düsterer, T. Mazza, A. R. Maier, N. Hartmann, M. Ilchen, G. Hartmann, L. Patthey, et al. "Ultrashort Free-Electron Laser X-ray Pulses". *Appl. Sci.* **7**, 915 (2017).

[194] *LCLS Overview*. URL: https://lcls.slac.stanford.edu/overview.

[195] P. Emma, M. Borland, and Z. Huang. "Attosecond x-ray pulses in the LCLS using the slotted foil method". *SLAC-PUB*, 333–338 (2004).

[196] S. Schorb, D. Rupp, M. L. Swiggers, R. N. Coffee, M. Messerschmidt, G. Williams, J. D. Bozek, S.-I. Wada, O. Kornilov, T. Möller, et al. "Size-Dependent Ultrafast Ionization Dynamics of Nanoscale Samples in Intense Femtosecond X-Ray Free-Electron-Laser Pulses". *Phys. Rev. Lett.* **108**, 233401 (2012).

[197] Y. Ding, C. Behrens, R. Coffee, F.-J. Decker, P. Emma, C. Field, W. Helml, Z. Huang, P. Krejcik, J. Krzywinski, et al. "Generating femtosecond X-ray pulses using an emittance-spoiling foil in free-electron lasers". *Appl. Phys. Lett.* **107**, 191104 (2015).

[198] K. R. Ferguson, M. Bucher, J. D. Bozek, S. Carron, J.-C. Castagna, R. Coffee, G. I. Curiel, M. Holmes, J. Krzywinski, M. Messerschmidt, et al. "The atomic, molecular and optical science instrument at the Linac Coherent Light Source". *J. Synchrotron Rad.* **22**, 492–497 (2015).

[199] E. Allaria, B. Diviacco, C. Callegari, P. Finetti, B. Mahieu, J. Viefhaus, M. Zangrando, G. De Ninno, G. Lambert, E. Ferrari, et al. "Control of the polarization of a vacuum-ultraviolet, high-gain, free-electron laser". *Phys. Rev. X* **4**, 041040 (2014).

[200] M. P. Minitti, J. S. Robinson, R. N. Coffee, S. Edstrom, S. Gilevich, J. M. Glownia, E. Granados, P. Hering, M. C. Hoffmann, A. Miahnahri, et al. "Optical laser systems at the linac coherent light source". *J. Synchrotron Rad.* **22**, 526–531 (2015).

[201] M. O. Krause, F. A. Stevie, L. J. Lewis, T. A. Carlson, and W. E. Moddeman. "Multiple excitation of neon by photon and electron impact". *Phys. Lett. A* **31**, 81–82 (1970).

[202] A. K. Kazansky, I. P. Sazhina, and N. M. Kabachnik. "Angle-resolved electron spectra in short-pulse two-color XUV + IR photoionization of atoms". *Phys. Rev. A* **82**, 033420 (2010).

[203] A. K. Kazansky, A. V. Bozhevolnov, I. P. Sazhina, and N. M. Kabachnik. "Interference effects in angular streaking with a rotating terahertz field". *Phys. Rev. A* **93**, 013407 (2016).

[204] A. K. Kazansky, I. P. Sazhina, V. L. Nosik, and N. M. Kabachnik. "Angular streaking and sideband formation in rotating terahertz and far-infrared fields". *J. Phys. B: At. Mol. Opt. Phys.* **50**, 105601 (2017).

[205] J. Gagnon and V. S. Yakovlev. "The direct evaluation of attosecond chirp from a streaking measurement". *Appl. Phys. B* **103**, 303–309 (2011).

[206] E. A. Schneidmiller and M. V. Yurkov. "Photon beam properties at the European XFEL". *DESY*, (2011).

[207] T. O. Raubenheimer. "LCLS-II: status of the CW X-ray FEL upgrade to the SLAC LCLS facility". *Proc. 37th Int. Free Electron Laser Conf. (FEL 15)*, 618–624 (2015).

[208] *FEMTOSOURCE rainbow - OPERATORS MANUAL*. V1.2. Femtolasers Produktions GmbH. Fernkorngasse 10, 1100 Vienna, Austria, 2014.

Acknowledgements

At this point, I want to take the opportunity to thank all those, who have supported me during my work, as well as in writing this thesis. It was a long way to go and without the help and advice of all of you, it would have been impossible for me to finish my educational career at the Technical University of Munich with this work. In the following, I want to express my special thanks to:

Prof. Dr. Reinhard Kienberger, for providing me the opportunity to conduct my PhD thesis at the Chair of Laser and X-ray Physics E11. During all the years, I always appreciated the familiar climate at this chair and that we could always contact you directly with any concerns, questions or suggestions. Thank you for all your support and advice in the planning phase and for organizing the necessary manpower for the buildup of the new laboratories. You have given me the opportunity to participate in international collaborations at experiments in the USA or Japan, which was also a very enriching experience. Thanks for organizing countless events, festivities and excursions out of the regular working times, where we could forget the issues or better celebrate the proceedings of our work!

Dr. Wolfram Helml, for the supervision of my PhD thesis as well as for being a good mentor and friend. Thank you for letting me participate and work together with you in the beamtimes at the LCLS. I am also very grateful for your theoretical support in form of fruitful discussions and great ideas regarding the extensive angular streaking data analysis during the last years. I also want to thank you for your help and support at the laser maintenance periods and during our streaking experiments. Your help and your expertise have essentially contributed to the outcomes presented in this thesis. I will always remember the great time during, but especially before and after the last beamtime in Japan: Arigatou gozaimasou!

My best friend and direct colleague **Rupert Heider**. During all the years of our studies in physics, the master thesis and now also during our time as PhD students, we have always worked together in an amazing atmosphere and only due to this great collaboration, all the demanding tasks we had to cope with, could be accomplished. Thank you also for always having an amazing time with you out of the laboratory and office, especially in our trips far abroad. I'm looking forward to the next good years of friendship!

Our AS-Lab team: **Andreas Duensing, Markus Wurzer, Michael Mittermair and Alexander Späh**. Rupert and I had big luck in finding such good master students that have become to close PhD student colleagues and good friends over the years. All of you contributed to the successful commissioning of our beamline. Without your help in the numerous nightshifts during the water streaking beamtimes and also with the data analysis, we would not have been able to achieve the unprecedented results that are presented in our theses. I wish you all the best for your theses and I will also support you in all aspects, where you need help or advice!

Special thanks go to **Andreas Duensing** for investing a lot of time and efforts into the creation of the sophisticated 3D CAD models of the beamline that are shown in this thesis.

Our collaboration partners at ETH Zurich: First, I want to thank **Prof. Dr. Hans-Jakob Wörner** for providing the liquid microjet experimental setup and the theoretical support in the field of electron transport in liquid samples. Further, I want to acknowledge **Arohi Jain** and **Dr. Thomas Gaumnitz** for the good experimental teamwork during the beamtimes in Garching.

All the collaborators that participated at the LCLS beamtime and contributed to the successful realization of the experiments and the subsequent data analysis. Special thanks go to **Dr. Ryan Coffee**, **Dr. Nick Hartmann** and **Dr. Gregor Hartmann** for the fruitful discussions and for providing some important ideas and analysis steps that have been essential for the development of the X-ray pulse retrieval algorithm.

Wolfgang Dürichen and **Lukas Loidl**, our workshop team, who always were available when any mechanical requirements or problems occurred during the experiments. Especially during the buildup phase of the laboratory rooms and the beamline, your work and ideas have been of great importance. I also want to thank our secretaries **Susanne Würzinger** and **Stefanie Völkl**, who always have been ready to help when there were any bureaucratic issues to be dealt with.

Maximilian Pollanka, Christian Schröder, Martin Grassl and **Johannes Melcher**, who worked in our laboratory in the course of their bachelor theses and contributed also to the setup and operation of the novel beamline.

All the members of E11 not mentioned before, who have seen to it, that I had a very comfortable working environment. Here, I want to mention also our good office roommate and friend, **Dr. Daniel Hutzler**. Your dry sense of humor always contributed to a relaxed atmosphere in our office. Additionally, I want to thank **Dr. Birgitta Bernhardt, Martin Wörle, Marcus Ossiander, Vahe Shirvanyan, Johann Riemensberger** and **Tobias Latka** for their support and advice regarding theoretical, programming or experimental issues.

All of my friends, the old ones and those I met during the last years. You have encouraged me and enriched my life besides the work.

My family and especially my parents **Anneliese and Josef Wagner**, who always believed in me and supported me in all respects. Without you, I could not have accomplished my studies and my work for this PhD thesis. Thank you that I can always safely count on you!

Exceptionally, I want to thank the most important person in my life, **Fabi**, for all your patience and your support during the hardest times in the last years, especially during the intensive beamtime periods or in the writing phase of this thesis. You have always helped and supported me on my way and helped that I could always keep a clear mind and focus on my goals.